UNIVERSITÉ DE GRENOBLE

THÈSE

Pour obtenir le grade de

DOCTEUR DE L'UNIVERSITÉ DE GRENOBLE

Spécialité : **Physique**

Arrêté ministériel : 7 août 2006

Présentée par

Adrien ALLAIN

Thèse dirigée par Vincent BOUCHIAT

préparée au sein de l'**Institut Néel, CNRS/UJF**
dans **l'École Doctorale de Physique, Grenoble**

Supraconductivité induite dans le graphène dopé par des nanoparticules métalliques

Date de soutenance : le 14 Décembre 2012

devant le jury composé de :

Bernard PLAÇAIS, LPA/ENS	Rapporteur
Dimitri RODITCHEV, INSP/UPMC	Rapporteur
Thierry KLEIN, Institut Néel/UJF	Examinateur
Claire MARRACHE-KIKUCHI, CSNSM/U. Paris-Sud	Examinatrice
Nicolas BERGEAL, ESPCI	Examinateur
Aviad FRYDMAN, Bar-Ilan University	Examinateur
Vincent BOUCHIAT, Institut Néel	Directeur de thèse

À CrouCrou...

Remerciements

Ce travail de thèse a été effectué à l'Institut Néel (CNRS), au sein du Département Nanosciences, dans l'équipe "Systèmes hybrides de basse dimensionnalité". Je tiens à remercier Alain Fontaine et Alain Schuhl, directeurs successifs de l'Institut Néel, ainsi que Joël Cibert et Hervé Courtois, directeurs du département Nanosciences, pour m'avoir accueilli dans leur établissement, où j'ai pu bénéficier d'un environnement de travail tout à fait exceptionnel. Je remercie Bernard Plaçais, Dimitri Roditchev, Claire Marrache-Kikuchi, Nicolas Bergeal, Thierry Klein et Aviad Frydman d'avoir bien voulu être rapporteurs et examinateurs de cette thèse. Je tiens à exprimer toute ma gratitude à Vincent Bouchiat, mon directeur de thèse, pour ses encouragements répétés et ses nombreux conseils. Sa sagesse et son intuition nous ont mené à bon port. Je remercie les membres de l'équipe NanoFab, Thierry Fournier, Thierry Crozes, Bruno Fernandez, Gwenaëlle Julie et Jean-François Motte, sans qui rien de tout cela n'aurait été possible. Un grand merci à Christophe Hoarau et Christophe Thirion pour m'avoir fait profiter de leur expertise en RF. Merci à Wolfgang Wernsdorfer pour le financement. Merci à Laetita Marty, Nedjma Bendiab, Frank Balestro et Eric Eyraud pour leur aide et leurs conseils. Merci à Gianluca Rastelli pour les discussion sur les jonctions Josephson. Merci à Likharev, Barone et Paterno, qui m'ont accompagné tout au long de cette thèse (les livres, pas les auteurs !). Besides...Merci à John pour les corrections d'anglais. Enfin, je salue tous les thésards et stagiaires avec qui nous avons passé tant de bons moments. J'espère que Vitto n'explosera pas la salle de conf avec sa CVD, que Dipankar découvrira le sens de la vie en lisant dans les spectres Raman et qu'Hadi réussira à faire de beaux NEMS en CVD. Merci à Amina, Fabien, Yani, Cornelia, Violetta, Greta, Sven, Johanna, Jean-François, Antoine, Matias, Romain, Sylvain, Shelender, Liu, Mitsuki (aka the Boss) et les autres. Ces trois années en votre compagnie ont été formidables.

Contents

Introduction en français

La notion de dimensionnalité est fondamentale en physique. Les lois mathématiques changent lorsque la dimensionnalité est réduite, ce qui engendre des propriétés physiques différentes. La dimensionnalité n'est pas une propriété intrinsèque du système : elle à trait à une certaine grandeur physique. Un même système peut ainsi voir certaines de ses propriétés régies par des lois bi-dimensionnelles tandis que d'autres le sont par des lois tri-dimensionnelle. En effet, ce qui définit la dimensionnalité du système en regard d'une propriété physique est le rapport entre sa taille et la longueur caractéristique associée à cette propriété. Prenons pour exemple un film mince supraconducteur. Ce film a des propriétés électroniques qui ne sont pas spécifiquement associées à la supraconductivité, comme l'écrantage du champ électrique. La longueur déterminante pour ces propriétés est la longueur de Debye, de l'ordre de la distance inter-atomique. Dans le même temps, ses propriétés supraconductrices varient sur une longueur caractéristique appellée longueur de cohérence supraconductrice ξ, qui peut être de l'ordre de plusieurs centaines de nanomètres.

L'exemple de la percolation dans les systèmes de basse dimensionnalité

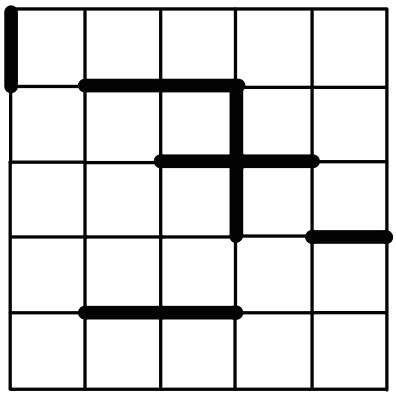

Figure 1 – *Un problème de percolation à 2 dimensions sur une maille carrée. Les lignes en gras représentent les noeuds connectés. Ici, les noeuds sont connectés avec une probabilité* $p = 20\%$.

Pour mieux comprendre l'effet de la réduction de dimensionnalité, nous pouvons prendre l'exemple de la percolation à travers un réseau aléatoire bi-dimensionnel. Considérons le problème le plus simple, c'est-à-dire celui d'un réseau carré de noeuds connectés par des liens (représentés par les lignes en gras sur la Fig.1). La question à laquelle la théorie de la percolation essaye de répondre est la suivante : étant donné que la probabilité pour que deux noeuds voisins soient connectés par un lien est de p, quelle est la probabilité P de trouver un chemin de noeuds connectés à travers le réseau ? Sur une matrice infinie, la solution est simple : il existe une valeur critique p_c, au-delà de laquelle la proba-

bilité $P = 1$, et en-deça de laquelle $P = 0$. La théorie de la percolation donne les valeur de p_c pour différents types de réseaux. Ce qu'elle montre, c'est que les valeurs de la probabilité critique p_c sont de l'ordre de $p_c \approx 15 - 20$ % pour la plupart des réseaux 3D, alors qu'elles valent aux alentours de $p_c \approx 50 - 60$ % pour les réseaux bi-dimensionnels ($p_c = 1/2$ pour le problème particulier décrit Fig.1), et, comme on peut intuitivement s'en douter, pour un réseau uni-dimensionnel (une chaîne), un lien manquant est suffisant pour empêcher la percolation, ce qui revient à dire que $p_c = 1$. A la lumière de la théorie de la percolation, un aspect important des systèmes de basse dimensionnalité devient évident : à mesure que l'on réduit la dimensionnalité d'un système, celui-ci devient plus sensible au désordre.

Système éléctroniques bi-dimensionnels

Parmi les systèmes à dimensionnalité réduite, le cas des gaz d'électrons à 2 dimensions (2D electrons gases, ou 2DEG) [1], c'est-à-dire des systèmes d'électrons dont l'épaisseur est inférieure à l'extension spatiale de la fonction d'onde électronique, est intéressant à plusieurs titres. Tout d'abord, ces système sont très importants d'un point de vue technologique. Du fait de leur faible épaisseur, ces gaz d'électrons ne peuvent pas écranter le champ électrique. Il en résulte que l'on peut facilement influencer la densité de porteurs de charge, et donc leur conductivité. Ce sont des gaz d'électrons à 2D qui sont à la base de la technologie du transistor à effet de champ, et ils constituent en celà un élément central de l'électronique moderne. D'un point de vue plus fondamental, les 2DEG sont intéressants parce qu'ils sont à la limite de la localisation [2]. Dans un métal les interférences quantiques entre les trajectoires électroniques qui s'entrecroisent introduisent une correction négative à la conductivité. Cette correction est donc proportionnelle à ce qu'on appelle la 'probabilité de retour à l'origine'. Or cette probabilité est d'autant plus importante que la dimensionnalité du système est réduite. Ainsi, tandis qu'à trois dimension il existe une valeur seuil de désordre au-delà de laquelle les interférences quantiques entrainent la localisation des états electroniques, à deux dimensions ceux-ci sont toujours localisés, quelque soit le degré de désordre. Ceci a d'importantes conséquences sur la conductivité puisqu'un système d'électrons localisés va tôt ou tard (en diminuant la température) montrer un comportement isolant.

Supraconductivité et localisation

Comme nous l'avons vu, il peut très bien exister des films minces supraconducteurs exhibant des propriétés supraconductrices bi-dimensionnelles tout en étant tridimensionnels du point de vue de la localisation. Cependant un problème fondamental se pose dès lors que le système est aussi bi-dimensionnel du point de vue

de la physique à un électron, car les états électroniques sont alors localisés (le même problème peut d'ailleurs se poser dans un système tri-dimensionnel très désordonné). En effet, comment concilier le fait que d'une part les états électroniques sont localisés, et que d'autre part ils se condensent dans un état collectif superfluide ? Est-ce que les 'paires de Cooper', ces électrons appariés caractéristiques de l'état supraconducteur, peuvent être localisées. Dans ce cas-là, peut-on considérer les fluctuations de la phase supraconductrice comme étant duales des fluctuations de charge dans l'état supraconducteur ? Ou au contraire, est-ce que les paires de Cooper sont 'cassées' lorsque les états électroniques deviennent fortement localisés ? Quel est le rôle de la répulsion électrostatique entre électrons ? Toutes ces questions ont des répercussions, non seulement en physique des solides, mais également dans le domaines des transitions de phase quantiques [3], et elles sont liées à la problématique des supraconducteurs à haute température critique.

Contrairement à ce qui se passe dans un métal normal, dans un superconducteurs les particules élémentaires sont des paires d'électrons, les paires de Cooper. Avec leur spin égal à 1, ces particules obéissent à une statistique de Bose-Einstein et ne sont pas soumises au principe d'exclusion de Pauli. Elles peuvent donc occuper le même état quantique. De ce fait, les mécanismes en jeu et le formalisme pour les décrire changent totalement dans l'état supraconducteur. Par exemple, l'effet d'une réduction de la dimensionnalité est d'un tout autre ordre.

Lorsqu'un système superfluide est confiné à deux dimensions, il acquière un spectre d'excitations à basses énergies sous la forme d'excitations topologiques appelées vortex [4, 5]. Ces vortex sont constitués d'un quantum de flux magnétique autour duquel se forme un tourbillon de supercourant. Le mouvement libre des vortex, associé à des fluctuations de la phase supraconductrice, entraîne de la dissipation qui empêche l'établissement d'un état véritablement supraconducteur (c'est-à-dire pouvant transporter du courant sans voltage). Dans de tels systèmes, les fluctuations quantiques de point zero de la phase supraconductrice peuvent suffire à prévenir l'établissement d'un ordre supraconducteur à longue distance. Dans ce cas, l'état fondamental du système n'est plus supraconducteur mais isolant. Une telle transition dominée par des fluctuations quantiques est dite transition de phase quantique. Il est possible de faire ainsi transiter un système d'un état supraconducteur à un état isolant simplement en faisant varier certains paramètres comme le champ magnétique ou le désordre, qui controlent la force du couplage supraconducteur. La compréhension de cette transition supraconducteur-isolant (TSI) a été un problème important de la physique des solides de ces 30 dernières années, suscitant une grande quantité de travaux. Il apparait que cette transition ne revet pas un caractère unique, mais que de nombreux cas particuliers peuvent se présenter. Ainsi, la possibilité d'étudier cette transition dans un nouveau matériau est une opportunité unique d'en comprendre un peu mieux les mécanismes.

Le graphène, semi-métal bidimensionnel ultime

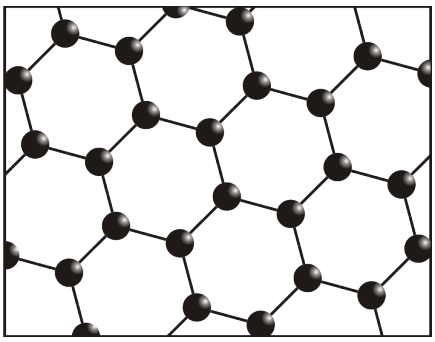

Figure 2 – *Le graphène est un cristal bidimensionnel composé d'atomes de carbone organisés en un réseau hexagonal en 'nid d'abeille'.*

Le graphène est le matériau bidimensionnel par excellence [6] puisqu'il s'agit d'un cristal plan, c'est-à-dire n'ayant qu'un atome d'épaisseur. Les premiers feuillets de graphène mono-couche ont été isolés et contactés électriquement en 2004 [7, 8], provoquant rapidement un enthousiasme sans précédent dans la communauté scientifique. Les raisons à celà sont nombreuses. Tout d'abord, le graphène a montré la mobilité éléctronique la plus haute jamais enregistrée dans un gaz d'électrons 2D à température ambiante ($120,000$ cm^2 V-1.s^{-1}.) [9, 10]. Du fait de sa structure de bande électronique linéaire unique en son genre, les électrons se comportent dans le graphène comme des 'fermions de Dirac sans masse'. Ses conductivités électrique et thermique sont par ailleurs tout à fait remarquables. En outre, le graphène montre des propriétés mécaniques et structurale exceptionnelles, avec un module d'Young comparable à celui du diamant ($\cong$ 1 TPa).

Mais le graphène est surtout un matériau à tout faire. Contrairement à la plupart des autres gaz d'électrons bi-dimensionnels, qui sont des systèmes liés à des interfaces, et donc enterrés à l'intérieur d'hétérostructures épitaxiées, le graphène est à l'air libre et sa surface est facilement accessible. Sa relative inertie chimique en fait une surface se prètant particulièrement bien à la physisorption. Il peut ainsi être ultilisé pour réaliser des matériaux dits hybrides, qui combinent aux propriétés de l'adsorbat la possibilité d'un contrôle electrostatique de celles-ci, rendue possible par la présence d'un effet de champ dans le graphène.

Presentation de la thèse

Durant cette thèse, nous avons étudié les propriétés d'un type particulier de matériau hybride résultant de la physisorption de nanoparticules de métal à bas point de fusion Sn et Pb à la surface du graphène. Nous appellerons ces matériaux hybrides Sn/graphène et Pb/graphène. Lorsqu'on évapore ces métaux sur du graphène, ils démouillent de la surface et forment des îlots de matériau supraconducteur. Si on s'en tient à de faibles épaisseurs, le film est non-percolant, et on réalise ainsi un réseau bidimensionnel désordonné de jonctions Josephson. Le graphène, *via* la tension appliquée sur la grille arrière, permet de controler l'énergie Josephson couplant les ilots. Les propriétés supraconductrices de tels réseaux ont été abordées. Nous

avons notamment observé que la morphologie du réseau joue un rôle dans ces propriétés.

Il est possible d'introduire du désordre de manière controlée dans le feuillet de graphène en l'exposant à une attaque chimique. Les propriétés de transport de ce graphène désordonné ainsi que l'analyse des spectres Raman suggèrent que ce désordre a pour origine une hybridisation partielle de type sp^3 de la maille de carbone. A basses températures ceci permet de rétablir le régime de localisation forte des états electroniques, régime normalement inaccessible dans le graphène du fait de sa structure de bande particulière. Grâce à la tension de grille, nous pouvons ainsi induire une transition entre un régime de localisation faible et un régime de localisation forte.

Lorsque ce graphène désordonné est décoré d'îlots supraconducteurs, ceci permet d'induire une TSI controllée par la tension de grille. Nous touchons ici à la problématique décrite plus haut, c'est-à-dire celle de l'existence de corrélations supraconductrices (ici induites par l'effet de proximité) dans un système d'électrons localisés. Nous avons étudié les propriétés de la TSI et avons caractérisé l'état isolant. Il semblerait que ce soit la percolation entre des domaines de cohérence de phase supraconductrice qui caractérise la transition [11]. Par ailleurs, nous avons observé des signatures claires indiquant la persistence de corrélations supraconductrices dans la phase isolante, avec notamment une résistance plus grande que dans l'état normal. Le graphène décoré à l'étain pourrait s'avérer utile comme banc de test pour les théories traitant de l'émergence d'une phase supraconductrice inhomogène à la TSI dans les films supraconducteurs critiques.

Ce système diffère des réseaux de jonctions Josephson étudiés par le passé en ce qu'il n'est pas constitué de jonctions tunnels, mais de jonctions S-2DEG-S dans lesquelles l'état faiblement ou fortement localisé des électrons du gaz bidimensionnel peut être contrôlé par une grille. Ceci nous a permis de faire varier de manière continue le paramètre de désordre effectif $k_F l_e$ grâce à la grille.

En comparaison d'autres expériences de TSI induites en grille dans des systemes interfaciaux bidimensionnels et des films minces amorphes dans lesquels la transition peut être induite en grille [12, 13, 14], notre système diffère en ce que nous n'influençons pas directement la densité d'état du supraconducteur lui-même, mais plutôt celle du médium dans lequel se propagent les corrélations supraconductrices (le graphène). Notre expérience est donc complémentaire car elle relève clairement de la supraconductivité granulaire.

Par ailleurs, une étude préliminaire a été menée, s'intéressant à la possibilité d'utiliser ces matériaux hybrides pour réaliser des résonateurs mécaniques supraconducteurs. Il s'agit cette fois-ci de tirer parti des propriétés mécaniques exceptionnelles de la membrane de graphène. En effet, sa grande rigidité permet en principe d'obtenir

de hautes fréquences de résonance. L'intérêt de la supraconductivité ici est qu'elle ouvre des possibilités de mesures non perturbatives, qui sont un prérequis pour l'étude de résonateurs mécaniques dans la limite quantique. Nous avons mesuré la résonance de résonateurs mécaniques à base de graphène, et avons été en mesure de fabriquer des membranes suspendues supraconductrices.

Questions abordées dans cette thèse

Sur le graphène désordonné. Jusqu'où pouvons-nous contrôler le niveau de désordre dans une feuille de graphène ? Quelle est la nature de ce désordre ? Quel est le mécanisme de transport à basses températures dans le graphène désordonné ?
Sur les matériaux hybrides Sn/graphène. Quelle est l'influence des nanoparticules métalliques sur les propriétés électroniques du graphène ? Peut-on considérer un tel système comme étant un réseau de jonctions Josephson ? Quel est l'influence de la morphologie des îlots supraconducteurs sur les propriétés de transport globales ? Cette méthode de décoration est-elle compatible avec d'autres matériaux que l'étain ? Jusqu'où peut aller notre contrôle de l'état supraconducteur lorsqu'on utilise du graphène désordonné ?
Sur la transition supraconducteur-isolant. Quel mécanisme conduit à la transition ? Quel est le rôle de la dissipation ? de la percolation ? Est-ce le même mécanisme qui est en jeu dans la limite de faible désordre et dans celle de fort désordre ? Quel est la nature de l'état isolant ? Quels sont les exposants critiques à la transition ? Quel éclairage la littérature sur la TSI dans d'autres matériaux apporte-t-il à notre expérience ? Quel éclairage notre expérience apporte-t-elle sur les autres TSI ?
Sur l'utilisation possible de Sn/graphène dans des résonateurs mécaniques hybrides. Est-il possible d'exploiter ces nouveaux matériaux pour s'attaquer à d'autres problèmes tels que la nanomécanique ?

Principaux résultats et organisation du manuscrit

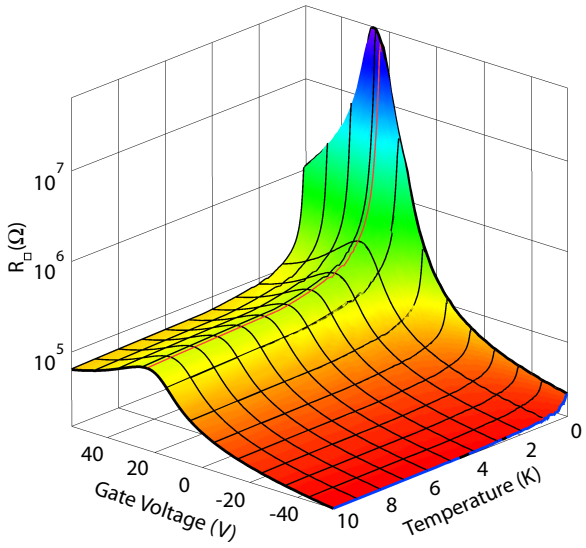

Figure 3 – *Résistance par carré mesurée à basses températures dans du graphène traité chimiquement. Une transition entre un régime de localisation faible et un régime de localisation forte peut être induite par la tension de grille en-dessous de* 1 *K.*

Dans le Chapitre 1, nous verrons quelles sont les propriétés électroniques du graphène et quel est l'effet du désordre sur celles-ci. Nous introduirons une méthode nouvelle pour induire du désordre par voie chimique dans la feuille de graphène. Après une telle attaque, les propriétés de transport et la signature Raman du graphène sont en tous points identiques à ceux des dérivés chimiques comme le graphène hydrogéné (ou graphane), obtenus par plasma. La signature Raman penche également en faveur de défauts de type sp^3 dans la maille de carbone sp^2. Une étude préliminaire à basses températures montre que le mécanisme de transport est de type saut à distance variable ('variable range hopping') avec présence d'un gap de Coulomb au niveau de Fermi. Cette nouvelle méthode pour induire des défauts structuraux permet d'élargir considérablement la gamme de résistances accessibles à la feuille de graphène lorsqu'on fait varier la grille, et va se révéler très utile dans la suite du manuscrit pour contrôler l'établissement de la cohérence de phase supraconductrice.

Dans le Chapitre 2, nous étudierons les propriétés supraconductrices des matériaux hybrides Sn/graphène et Pb/graphène pour le cas de graphène non désordonné. Les particules métalliques induisent un dopage électrostatique, mais elles conservent intact le caractère ambipolaire du transport dans le graphène. Nous montrerons que les propriétés supraconductrices (température de transition, courant critique) sont ajustables par la grille arrière. La densité de courant critique est très grande comparée à celle obtenue dans des jonctions S-g-S classiques. Le système se comporte comme un réseau de jonctions Josephson dans lequel la morphologie des îlots supraconducteurs joue un rôle important.

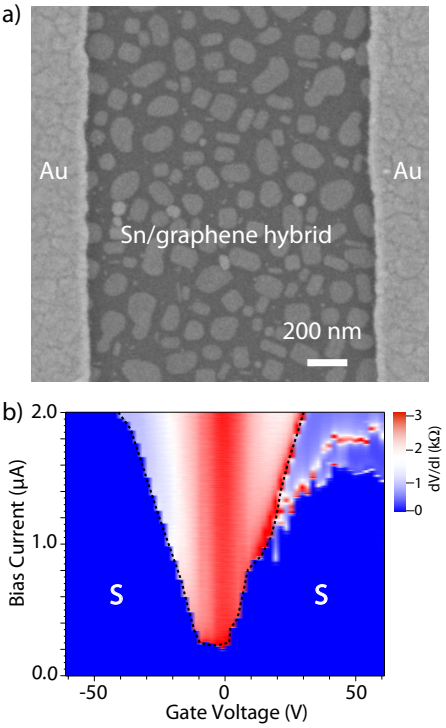

Figure 4 – ***Le matériau hybride Sn/graphène. a)*** *Image MEB montrant la surface du dispositif, avec les contacts en Au.* ***b)*** *Le courant critique en fonction de la tension de grille.*

Plusieurs phénomène restent cependant inexpliqués, notamment le régime dissipatif (pour $I_{bias} > I_c$), qui ressemble à un régime de 'flux-flow' alors que l'échantillon est plus petit que la longueur de pénétration de London $\lambda_\perp$, ou encore l'effet Josephson alternatif, qui ne semble affecter qu'une seule des jonctions dans le réseau.

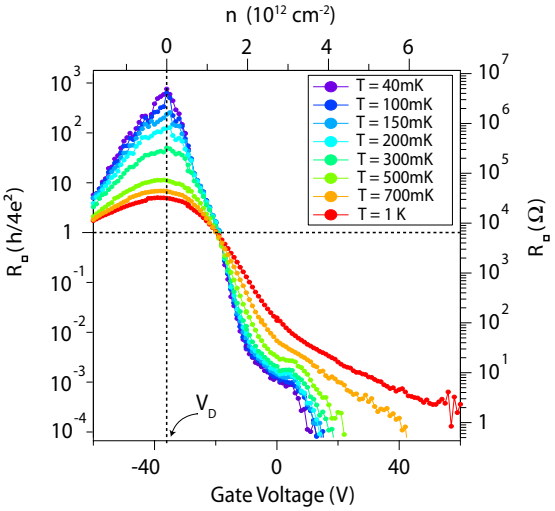

Figure 5 – *Dépendance en grille de la résistance à basses températures dans un échantillon de Sn/graphène désordonné. Le point de croisement aux alentours de $V_g = -20V$ indique une transition de phase quantique, c'est-à-dire une transition indépendante de la température entre un état supraconducteur et un état isolant.*

Dans le Chapitre 3, qui est le cœur de cette thèse, nous nous intéresserons à la TSI induite en grille dans du graphène désordonné et décoré à l'étain. Des feuillets macroscopiques de graphène, synthétisés par CVD (Chemical Vapor Deposition) et dans lesquels du désordre a été introduit comme au Chapitre 1, ont été décorées d'étain comme dans le Chapitre 2. Cette fois-ci, la possibilité d'induire une transition métal-isolant dans le graphène permet un contrôle plus étendu de la cohérence de phase supraconductrice entre îlots. La TSI ainsi induite montre deux régimes de température distincts. A hautes température, la dissipation semble jouer un rôle prédominant, mais un régime de percolation s'établit à mesure que la température est abaissée. La phase isolante a été caractérisée et porte la signature de paires de Cooper préformées. Les exposants critiques ont également été extraits et semblent en accord avec des calculs récents sur la percolation dans les systèmes granulaires.

Dans le Chapitre 4, nous explorerons la possibilité d'utiliser de tels matériaux hybrides pour la réalisation de NEMS (NanoelEctroMechanical Systems) supraconducteurs. Des résultats préliminaires sur la détection de la résonance mécanique dans des membranes de graphène non décorées seront présentés, ainsi que les premières mesures de supraconductivité dans des membranes suspendues de Sn/graphène.

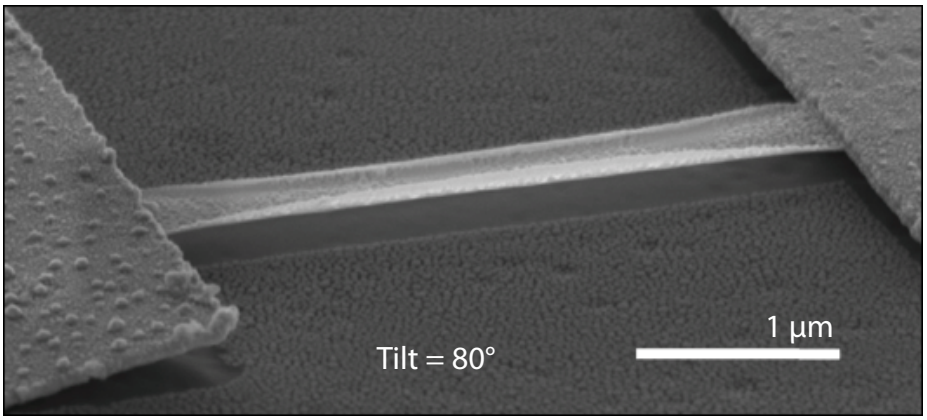

Figure 6 – *Image MEB d'un échantillon suspendu de graphène décoré à l'étain. On observe que les bords de la feuille rebiquent lorqu'on y dépose des matériaux.*

Introduction in english

Dimensionality plays a fundamental role in physics. The mathematical laws governing the physical world are dimensionality-dependent, giving rise to drastic changes in the properties of a system when its size is reduced. The dimensionality of a system is not an intrinsic property. It pertains to a given physical quantity. What matters is the size of the system with respect to the characteristic length of a physical property. The same system can be *at the same time* 2D with respect to one property, and 3D regarding another. Thin superconducting films, for example, can be 2D regarding their superconducting properties when their thickness is less than the superconducting coherence length (typically a few hundred nanometers), while being 3D as far as the properties of single electrons, the characteristic length of which is the Debye length (of the order of atomic distances), are concerned.

The example of percolation in reduced dimensionality

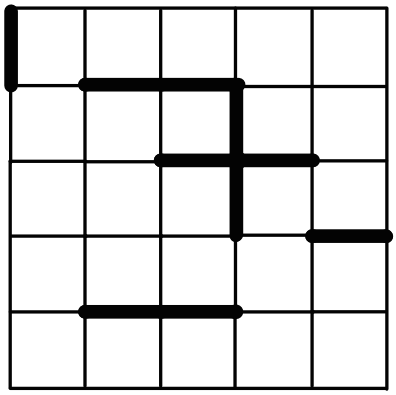

Figure 7 – *Bond percolation problem on a 2D square lattice. Bold lines represent connections bewteen the lattice points. Here, two lattice points are connected with probability* $p = 20\%$.

To better understand how reduced dimensionality affects the physics of a system, let's take the example of percolation through a random two-dimensional network. Fig.7 shows the simplest percolation problem : the bond percolation problem on a 2D square lattice. Nodes on a square lattice can be connected to their neighbours by bonds (represented by thick lines in Fig.7). The question answered by percolation theory is : given that bonds are randomly distributed with a probability p for a bond to connect two neighbouring nodes, what is the probability P that one finds a path of connected nodes across the network ? On an infinite lattice, there is a critical value p_c of the probability p below which $P = 0$, and above which $P = 1$. The percolation theory gives the value of p_c for various lattices in various dimensions. What the theory shows is that 3D systems typically have percolation threshold $p_c \approx 15 - 20$ %, while 2D systems have $p_c \approx 50 - 60$ % ($p_c = 1/2$ for the bond percolation on a square lattice) and, as can be intuitively understood , in 1D, only *one* missing bond is enough to prevent the percolation (which

means $p_c = 1$ in 1D). In the light of percolation theory, one fundamental aspect of low-dimensional systems becomes clear : the smaller the dimensionality of the system, the more it is affected by disorder.

2D electronic systems

Among the low-dimensionality systems, two-dimensional electron gases [1] (2DEG) are of special interest, for both technological and fundamental reasons. 2DEG, because of their geometry, cannot screen the out-of-plane electric field, and therefore their charge carriers concentration can be very easily tuned by gate voltage. This property is the working principle of field effect transistors, and as such it is of great technological importance, being one of the groundings of modern electronics, at the root of today's information technologies. From a more fundamental viewpoint, 2DEG are intriguing because two-dimensional electronic systems are critical regarding localization. The quantum interferences between electron wavefunctions are proportional to the probability of an electron to diffuse back to its origin. Because this probability is higher in 2D, the quantum corrections to the conductivity of 2DEGs are divergent at low temperatures and according to the scaling theory of localization [2], all 2D electronic states are localized, so that sooner or later, any 2DEG is going to become insulating at a certain temperature.

Superconductivity in 2D and the problem of localization

We can bring the problem one step further and ask ourselves what happens in 2D *superconducting* systems, since the collective behavior of the Cooper pair condensate seems contradictory with the theorem of localization in 2D. Can superconductivity take place in a system where the underlying electron wave functions are localized ? Conversely, can Cooper pairs be localized ? In which case, can we consider this state to be the dual of the superconducting state (where the phase fluctuations replace the charge fluctuations) ? Or on the contrary, do the Cooper pairs disappear precisely when the electronic wave functions become localized ? What is the role of Coulomb interactions ? These questions have implications not only in solid-state physics, but also in the field of quantum phase transitions [3] and they are linked to the problematic issue of layered superconductivity in cuprates.

Unlike a normal metal, the elementary charge carriers of a superconductor are the Cooper pairs. Pairs of electrons, with their spin equal to 1, are fundamentally very different from single ones : they are bosons which can occupy the same quantum state and follow a completely different dynamics. When superfluid systems are

confined in 2D, they acquire low-energy topological excitations in the form of vortices of supercurrent [4, 5]. These vortices give rise to a regime of phase fluctuation that hinders the establishment of true superconductivity (zero resistance). In such systems, tuning a parameter, like the thickness or the magnetic field can completely modify the ground state, from a superconducting to an insulating state. Understanding this 'superconductor-insulator transition' (SIT) has been a long-standing issue in condensed-matter physics. A lot of questions in this field remain unanswered or controversial. A immense amount of research has been done over the past 30 years, involving the study of many different materials and their response to different tuning parameters [15]. Over the years, it has gradually become clear that each material and each tuning parameter gives rise to a somewhat unique transition, each case being specific. This complexity makes the establishment of a general theory of the SIT all the more difficult, and the need for its study in hybrid materials, where new parameters can be tuned, relevant and timely.

Graphene, the ultimate 2DEG

Graphene [7, 6] is the ultimate 2D material : a one-atom-thick crystal, which can be made arbitrarily large in the plane. Its isolation in 2004 [8] was soon followed by an unprecedented enthusiasm for its remarkable properties. Graphene was most notably praised for exhibiting the highest room temperature electronic mobility ever reported ($\cong$ 120,000 $cm^2.V^{-1}.s^{-1}$) [10, 9], and for its exotic linear band structure, which gives rise to 'massless Dirac fermions' with interesting properties. Graphene also shows exceptional mechanical robustness with a Young's modulus of 1 TPa (only outperformed by diamond), and outstanding thermal and electrical conductivity. But what makes graphene even more promising is its versatility. Unlike artificial 2DEG that are buried in heterostructures, the top and bottom surfaces of graphene are chemically inert, exposed, and thus easy to functionalize with adsorbates. The latter properties make it the ideal platform for the realization of hybrid devices, which combine the exceptional gate-tunability offered by graphene with the properties of the coupled material.

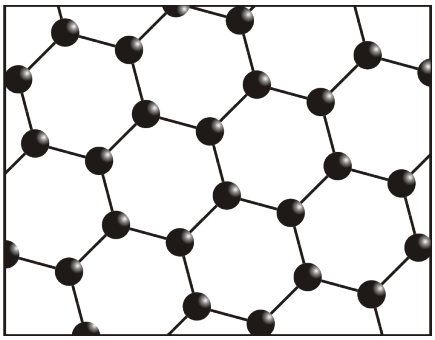

Figure 8 – *Graphene is a 2D crystal composed of C atoms organized into a 'honeycomb' lattice.*

Presentation of this thesis

In this thesis, the properties of one type of hybrid materials based on graphene will be explored: graphene decorated with superconducting nanoparticles of low melt-

ing point metals Sn and Pb, hereafter referred to as Sn/graphene and Pb/graphene. When evaporated over the surface of graphene, Sn atoms self-assemble into a non-percolating array of superconducting islands. Their thickness is low enough for the film not to percolate (that would shunt the graphene and suppress the field effect), while being thick enough to retain their superconducting properties. In doing so they realize a disordered two-dimensional Josephson junctions array (JJA), the Josephson energy of which is gate-tunable. Moreover, we have devised a way to controllably induce disorder in graphene using a chemical method, allowing further control over the superconducting coupling strength. Defect-free graphene, owing to its electronic structure, is robust against localization at low temperatures. Disordered graphene recovers this property and in that case a SIT transition induced in Sn/graphene by changing the gate voltage. The properties of this transition are studied and interpretion of the results in terms of percolation of the superconducting phase-coherent domain [11] is proposed. Graphene decorated with superconducting nanoparticles is a good testbed for theories considering the emergence of inhomogeneities in near-critical films. It differs from previouly fabricated artificial JJA in that the Josephson junctions are not tunnel junctions, but a 'normal' metal crossing over to a localized regime. Moreover, this metal's conductivity, and therefore the crossover temperature, can be gate-tuned. This allowed us to continuously study the establishment of global phase coherence in the system at constant disorder and zero magnetic field. Recent advances in the field of SIT have involved electrostatic control of the transition in two-dimensional crystals and amorphous films [12, 13, 14]. Unlike these experiments, where the carrier density of the superconductor itself was addressed, we tune the carrier density in the graphene 'medium', leaving the density of Cooper pairs in the superconducting adsorbates unchanged. The present study complements the former by revealing the effect of charge carrier density in a new class of granular material. In order to provide a fuller picture, extensive complementary studies of the properties of the metal-insulator transition in *bare* disordered graphene, and of those of the superconducting state in Sn/defect-free graphene are also presented.

Finally, a preliminary study of the feasibility of a hyrbid mechanical resonator made of these Sn/graphene membranes will be presented. For the detection of the quantum state of motion, the superconducting properties of these membranes could be used to design a novel and dissipationless readout scheme.

Questions addressed in this manuscript

- **About disordered graphene.** To what extent can we control the level of disorder in graphene ? What is the nature of the disorder ? What kind of transport mechanism underlies the insulating state at low temperatures ?
- **About Sn/graphene hybrids.** How does a set of nanoparticles sprayed onto the surface of graphene influences its electronic structure and properties ? Can we understand the properties of the hybrid Sn/graphene devices in terms of Josephson junctions arrays ? What is the role of the surface morphology of the Sn islands on the superconducting properties ? Can we use different superconducting materials to make hybrid graphene-based superconductors ? How far can we extend our control over the superconducting state using disordered graphene ?
- **About the Superconductor-Insulator Transition.** What mechanism drives the SIT in Sn/graphene hybrids ? Is it the same mechanism for the cases of weak and strong disorder ? Is dissipation relevant down to low temperatures ? Or is it a percolation transition ? How does this transition compare to transitions in other materials reported in the literature ? What is the nature of the insulating state ? What are the scaling exponents at the transition ?
- **About the possible use of Sn/graphene hybrids for nanomechanics.** Is it possible to harness this new superconducting hybrid to adress other problems, such as nanomechanics ?

Main results and organization of the manuscript

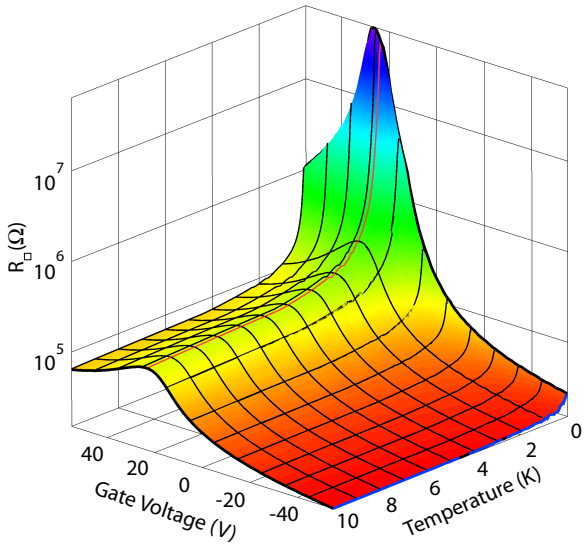

Figure 9 – *Sheet resistance of chemically-treated graphene at low temperature. A transition between weak and strong localization can be induced using the back-gate voltage below* 1 *K.*

In Chapter 1, some of the electronic properties of graphene will be reviewed. A controllable amount of disorder can be introduced in the graphene sheet by a chemical treatment, and these chemically treated graphene sheet behave similar to chemical derivatives of graphene, such as hydrogenated graphene (or graph**a**ne). Raman spectroscopy measurements point towards the presence of sp^3 defects. Preliminary low-temperatures study also support this picture. There is compelling evidence for the presence of a Coulomb gap in the low temperature transport data. This new way of inducing a controllable amount of disorder in graphene allows the fabrication of graphene sheets with a considerably larger range of accessible resistances than in regular graphene. This will be useful in the remainder of the manuscript to control the percolation of superconducting phase ordering.

In Chapter 2, the low temperature properties of hybrid Sn/graphene and Pb/graphene devices obtained using defect-free graphene will be reviewed. Sn nanoparticles induce electrostatic doping, but they do not affect the ambipolar electronic properties of graphene. The resulting hybrid superconductor shows gate-tunable superconducting properties with a very high supercurrent density, as compared to classical graphene SNS junctions. The system behaves like a Josephson junctions array. The influence of the morphology of Sn islands will be put forward. Several interesting features remain unexplained, such as the existence of a flux-flow regime in a sample *a priori* much smaller than the London penetration length $\lambda_\perp$, or the AC Josephson effect, which seems to affect only one Josephson junction in the array.

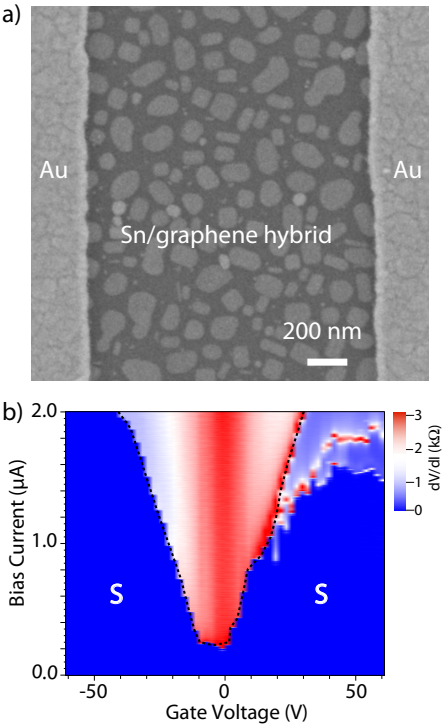

Figure 10 – ***Hybrid Sn/graphene sheet with gate-tunable superconductivity.*** ***a)*** *SEM picture showing the surface of the device with Au contacts.* ***b)*** *Critical current as a function of gate voltage.*

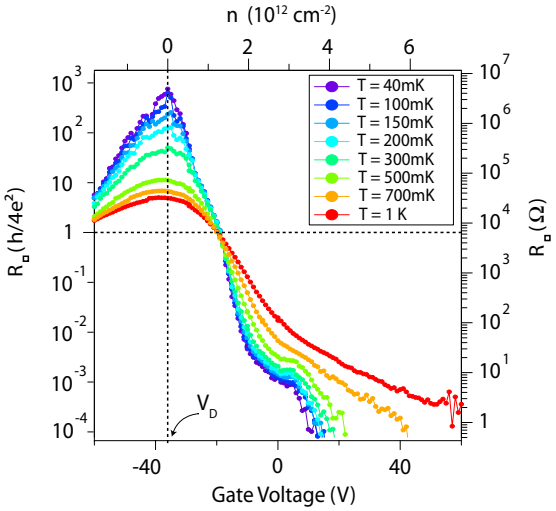

Figure 11 – *Low temperature sheet resistance dependence of Sn/graphene on gate voltage. The temperature-independent crossing point near $V_g = -20V$ is indicative of a quantum phase transition between a superconducting and an insulating state.*

Chapter 3, which is the core of this thesis, will be about the superconductor-insulator transition in Sn-decorated disordered graphene. Macroscopic sheets of disordered CVD graphene like those described in Chapter 1 have been used to fabricate hybrid devices with Sn nanoparticles on the surface, like in Chapter 2. This time, the large dynamics offered by disordered graphene at low temperature allows full control of the superconductiving order. By changing the gate voltage, one can switch from a superconducting to an insulating state. Experimental evidence that this transition is driven by dissipation at high temperatures and by percolation at low temperatures will be shown. The low-temperature transport properties of the insulating state indicate that it is indeed made of localized Cooper pairs. The scaling exponents of the quantum phase transition agrees with recent theoretical work on the percolation of superconducting phase-coherent domains in granular superconductors.

Chapter 4 will explore the possibility of integrating free-standing sheet of Sn/graphene in order to study nanomechanics. Preliminary results on bare graphene mechanical resonators and suspension of Sn/graphene membranes devices will be shown.

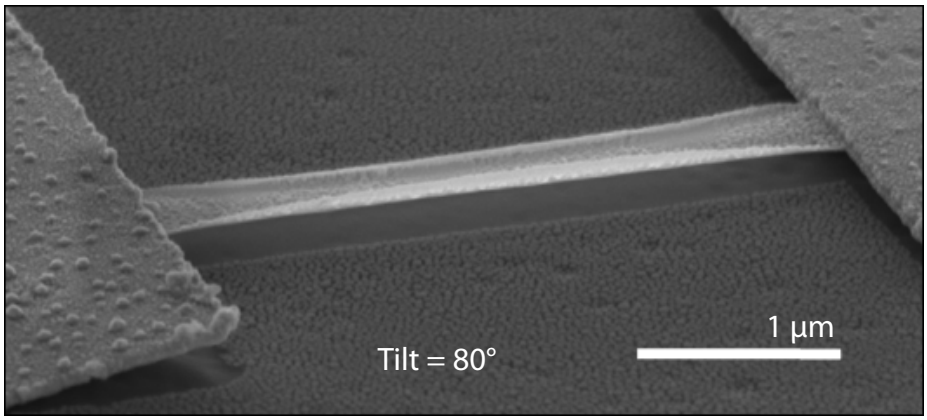

Figure 12 – *SEM picture of a suspended membrane of hybrid material Sn/graphene. A curling of the graphene sheet is observed upon deposition of material.*

1 Disorder and localization in graphene

Introduction en français

Le graphène est l'une des formes allotropiques du carbone. Il est caractérisé par une hybridation sp^2, tout comme le graphite, les fullerènes et les nanotubes de carbone. On peut d'ailleurs considérer le graphène comme le matériau-mère à partir duquel tous ces matériaux peuvent être construits (voir Fig.1.1). Prenons une feuille de graphène. Si on la referme complètement sur elle-même, on obtient un fullerène (structure 0D). Si on la roule comme un tapis, on obtient un nanotube (structure 1D). Enfin, le graphite (structure 3D) n'est rien d'autre qu'un empilement de feuille de graphène (structures 2D). C'est pour cette raison que la structure électronique du graphène a été étudiée bien avant sa découverte, dès 1947 [16, 17]. Ce n'est en effet qu'en 2004 qu'une mono-couche de graphène a été isolée et connectée électriquement pour la première fois [8]. Ces expériences, qui ont mis en évidence l'effet de grille et les propriétés électroniques exceptionnelles du graphène, ont valu à leurs auteurs Konstantin Novoselov et Andre Geim le prix Nobel de physique 2010, et ont donné naissance à un pan entier de la recherche contemporaine en physique des solides.

Parmi les propriétés les plus remarquables du graphène, on notera que :

- Le graphène est un matériau parfaitement bidimensionnel, qui peut maintenant être synthétisé à grande échelle avec une pureté cristalline quasi-parfaite [18]. Cela fait de lui un matériau particulièrement approprié à la production industrielle de dispositifs, qui nécessite des approches de type 'top-down'. Le graphène se distingue en cela des autres nanomatériaux semiconducteurs tels que les nanotubes ou les nanofils.

- Contrairement aux gaz d'électrons bidimensionnels (2DEG), sa surface est exposée et non enterrée, et chimiquement inerte, ce qui le rend facilement accessible électriquement.

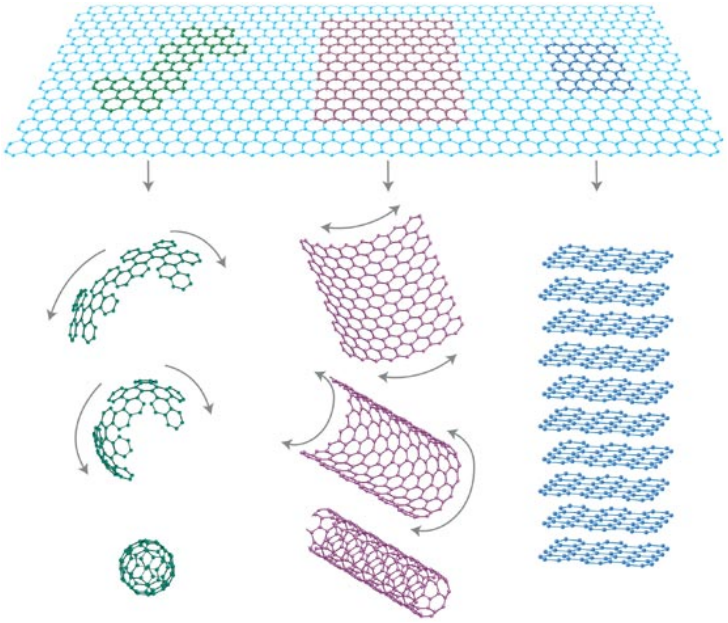

Figure 1.1 – *Les différents allotropes sp^2 du carbone : les fullerenes (0D)(à gauche), les nanotubes (1D)(au milieu) et le graphite (3D) (à droite) dérivent tous d'une manière ou d'une autre du graphène (2D)(en haut). Tiré de [6].*

- La mobilité des porteurs de charge à température ambiante dans le graphène est la plus haute jamais mesurée dans un 2DEG (elle peut atteindre 120 000 $cm^2.V^{-1}.s^{-1}$ à 300 K [10, 9, 19]) (voir Fig.1.2).
- La structure de bande linéaire du graphène est unique. De ce fait, aux basses énergies, les électrons des bandes de valence et de conduction se comportent comme des particules relativistes, ce qui donne lieu à des phénomènes exotiques comme le tunneling de Klein ou un effet Hall quantique anormal. De plus, cette structure de bande est parfaitement symmetrique, ce qui donne un caractère ambipolaire au transport.
- Le graphène peut être fonctionnalisé de plusieurs façons, soit par chimisorption (greffage covalent), soit par physisorption (adsorption, π-stacking), ce qui permet de modifier à volonté ses propriétés électroniques.
- Les conductivités électriques et thermiques [20] du graphène sont parmi les plus hautes connues.
- Enfin, ses propriétés mécaniques sont tout à fait exceptionnelles, avec un poids plume et un module d'Young six fois plus élevé que celui des meilleurs aciers. Les membranes de graphène sont également capables de supporter des déformations élastiques de l'ordre de 25% [21].

La théorie du transport quantique et de la localisation dans le graphène a été traitée par Ando et ses collaborateur à la fin des années 90 [26, 27]. A l'époque il

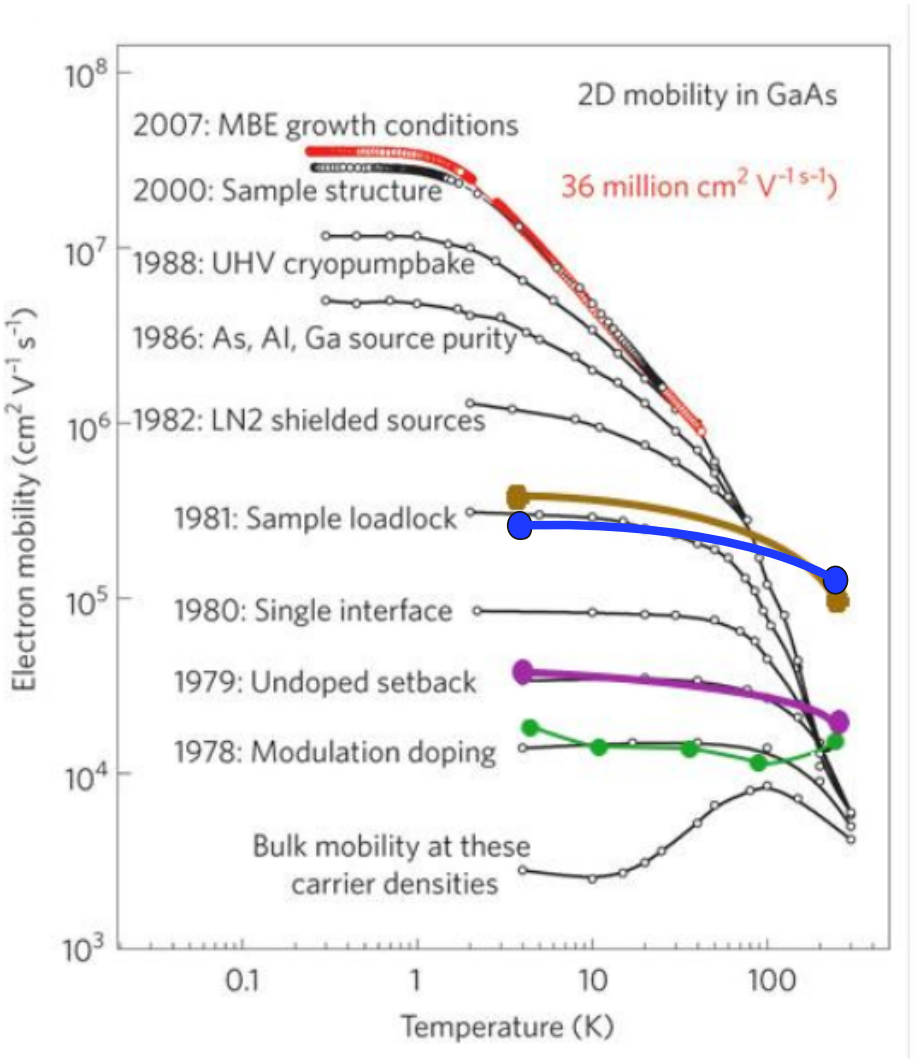

Figure 1.2 – *Records de mobilités électroniques enregistrées dans les 2DEGs en fonction de la température.* ***En noir*** *: dans des hétérostructures GaAs/GaAlAs, évolution au fil des années.* ***En rouge*** *: Etat de l'art actuel dans les hétérostructures GaAs/GaAlAs.* ***En vert****, mobilité enregistrée par [22] dans du graphène CVD reporté sur nitrure de bore hexagonal (hBN).* ***En violet****, graphène exfolié sur hBN, tiré de [23].* ***En brun****, graphène exfolié encapsulé entre deux couches de hBN, tiré de [19].* ***En bleu****, graphène exfolié et suspendu, tiré de [24]. Le graphène est clairement supérieur aux autres 2DEGs à température ambiante. Cette figure est adaptée de [25].*

s'agissait d'en dériver les propriétés des nanotubes de carbone. Contrairement aux 2DEGs classiques, les porteurs de charge dans le graphène possèdent un caractère 'chiral' qui a une influence déterminante sur les interférences quantiques. Tandis que les 2DEGs classiques sont sujet à la localisation faible, le graphène devrait en principe montrer de l'anti-localisation [27]. Peu après les premières expériences de localisations faible dans le graphène [28], une série de travaux théoriques sont parus qui se sont attachés à comprendre l'influence des différents mécanismes de diffusion électronique. Il existe des sous-ensembles d'états électroniques distincts et distants dans l'espace réciproque, appelés vallées, et dont la chiralité est opposée. Il y a une distinction très nette entre les mécanismes de diffusion couplant des états électroniques appartenant à la même vallée, et ceux couplant les vallées [29, 30]. Les mécanismes de diffusion intervallée ont tendance à restaurer la localisation faible dans le graphène, car ils annulent l'effet de chiralité.

Pour pouvoir être intégré dans des circuits réalisant des fonctions logiques, un transistor doit pouvoir être éteint, c'est-à-dire que son courant doit pouvoir être significativement réduit en changeant la tension de grille. Du fait de l'absence de gap dans la densité d'état du graphène, le meilleur ratio I_{on}/I_{off} pouvant être obtenu dans les transistor graphène n'excède pas 10, ce qui est loin d'être suffisant pour ce genre d'applications. En revanche, les dérivés chimiques du graphène, tels que le graphène hydrogéné, possèdent un gap. Récemment, il a été démontré que l'on peut réversiblement hydrogéner le graphène [31], ce qui a poussé beaucoup de gens à s'y intéresser. Bien que la mobilité des porteurs de charge y soit relativement faibles, ces dérivés montrent une résistance qui peut varier de plusieurs ordres de grandeur lorsqu'on change la tension de grille. De plus, l'idée de pouvoir fabriquer des dispositifs purement bidimensionnels par modification chimique locale du graphène est assez enthousiasmante.

Du point de vue du transport à basses températures, le graphène partiellement fonctionnalisé se comporte comme un graphène dans lequel le libre parcours moyen des électrons est réduit et où les processus de diffusion à courte portée entraînent un couplage des états électroniques des différentes vallées. Ceci a pour conséquence que le graphène voit ses électrons devenir localisés à basse température, avec la possibilité d'induire une transition entre les régimes faiblement et fortement localisé par modification de la tension de grille.

Dans ce chapitre, la structure électronique du graphène sera tout d'abord dérivée et étudiée. Nous verrons quelles sont les propriétés qui en découlent. Les techniques de synthèse et de fabrication d'échantillons utilisées dans notre laboratoire seront ensuite décrites. Deux méthodes sont principalement employées pour obtenir du graphène : l'exfoliation mécanique et la croissance par CVD sur cuivre. Une nouvelle manière d'introduire des défauts structuraux dans la maille de graphène a été

découverte et sera étudiée. La signature Raman ainsi que les propriétés de transport à basse température montrent qu'une exposition prolongée de la feuille de graphène à la solution d'attaque utilisée pour graver le substrat de croissance en cuivre ($Na_2S_2O_8$) induit des défaut structuraux et restaure la localisation forte à basse température. Dans l'état isolant, le graphène montre alors des propriétés de transport typiques d'un régime de saut à distance variable de type Efros-Shklovskii.

Introduction in english

Graphene is one member of the family of sp^2 carbon allotropes, along with graphite, fullerenes and carbon nanotubes. Graphene is actually the 'mother' of all these allotropes, as it is the basic unit from which all sp^2 carbon materials can be derived. Roll it and you get a nanotube or a fullerene, stack it and you get graphite (see Fig.1.3). This is why graphene's electronic properties have been studied long before its discovery [16, 17]. However, isolating, connecting and tuning the number and sign of charge carriers by applying an electric field in a *single* sheet of graphene was only achieved in 2004 [8]. Konstantin Novoselov and Andre Geim were awarded the 2010 Nobel prize for this work, which brought into light the phenomenal electrical properties of this one-atom-thick crystal and sparked an intense research activity.

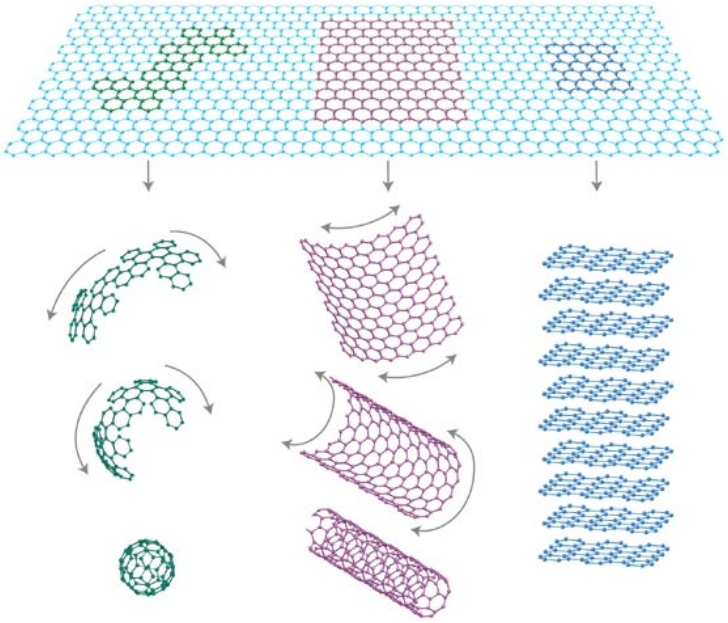

Figure 1.3 – *The sp^2 carbon materials : 0D fullerenes (left), 1D nanotubes (middle) and 3D graphite (right) can all be derived from 2D graphene (top). Taken from [6].*

Among the most notable features that make graphene so attractive, we can cite :

- Graphene is a purely two-dimensional material that can be grown on arbitrarily large surfaces with almost perfect crystalline quality [18], which makes it very suitable for electronic integration using top-down fabrication techniques, as opposed to carbon nanotubes or semiconducting nanowires for example.
- Unlike other 2D electron gases (2DEG), it is chemically stable in the air, exposed and not buried at the interface of heterostructures.
- The room temperature electronic mobility of graphene is the largest ever reported for a 2DEG (it can be as high as $120,000\ \mathrm{cm^2.V^{-1}.s^{-1}}$ at 300 K [10, 9, 19]) (see Fig.1.4).

- It can be functionnalized in many ways, physical (adsorption, π-stacking) or chemical (covalent grafting), to tailor the electronic properties.
- It has a very peculiar and unique electronic band structure, which makes the low-energy charge carriers behave as relativistic or massless particles. This gives rise to exotic phenomena, such as Klein tunneling or an anomalous quantum Hall effect. It is also ambipolar, which means there is a complete symmetry between the conduction and valence band.
- The electrical and thermal [20] conductivities are among the highest reported in any material.
- Graphene also has exceptional mechanical properties, with a light weigth and a Young's modulus 6$\times$ stronger than steel (1 TPa). It forms stable atomically thin membranes that can withstand loads that are hundreds of time its own weight and keep its elasticity with up to 25% relative extension [21].

The question of quantum transport and localization in graphene had been treated theoretically by Ando and his collaborators [26, 27] at the end of the 90's, as a mean to understand the electronic properties of carbon nanotubes. Unlike classical 2DEG, charge carriers in graphene have a 'chiral' character, which drastically influences quantum interferences. Whereas classical 2DEG exhibit weak localization, the chiral character of graphene's electron should lead to anti-localization [27].

Immediately following the early experiments on weak localization in graphene [28], a series of theoretical papers investigated the relative importance of the different scattering mechanisms. They balanced the effects of intervalley and intravalley scattering [29, 30], showing that intervalley scattering can restore weak localization in graphene.

One of the main limitations of graphene in terms of applications is its lack of a band-gap. Because it is a semi-metal, graphene has a small I_{on}/I_{off} ratio, which hampers its use as an electronic switch. The demonstration of the possibility to reversibly hydrogenate graphene [31] to form the large-bandgap graph**a**ne has triggered the recent hype around the chemical derivatives of graphene. Although these materials suffer from a reduced electronic mobility, they exhibit uncomparable gate-tunability of the resistance. The possibility to locally tailor the electronic properties of graphene by chemical functionnalization is also very appealing from a device engineering point of view.

Partially functionnalized graphene behaves like graphene in which a lot of short-range scattering centers have been introduced, restoring weak localization. Transport studies have shown that these devices exhibit transport dominated by variable range hopping, and a crossover from weak to strong localization triggered by gate voltage.

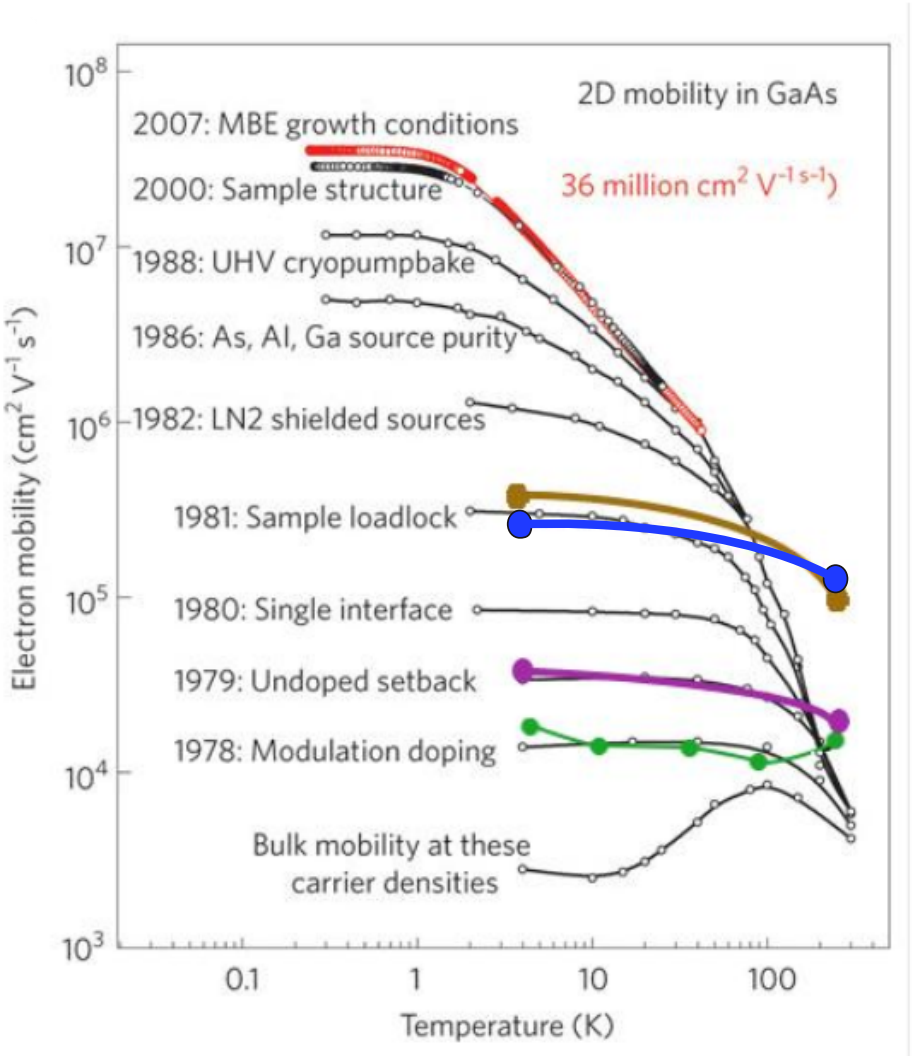

Figure 1.4 – *Comparison between the charge carrier mobilities in the highest mobility 2DEGs.* ***In red and black*** *: in GaAs/GaAlAs heterostructures as the synthesis was improved over the years. Other colors are graphene devices. The red points represent the state-of-the-art in ultra-pure GaAs samples.* ***In green****, the CVD graphene on hBN from [22].* ***In purple****, exfoliated graphene on hBN from [23].* ***In brown****, exfoliated graphene encapsulated in hBN from [19].* ***In blue****, suspended exfoliated graphene from [24]. Graphene has a clear advantage at high temperatures. Figure adapted from [25].*

In this chapter, the electronic structure of graphene will first be derived, and the most salient electronic properties will be discussed. The fabrication methods used in our lab for obtaining graphene will be described. Apart from the traditional mechanical exfoliation, we can grow graphene using chemical vapour deposition (CVD) on Cu substrates, for large-scale production. A new way to induce a controllable amount of disorder in graphene has been discovered : exposing graphene to the acidic solution of $Na_2S_2O_8$, which is used to etch the Cu growth substrate. The Raman signature, as well as the low-temperature transport properties of these disordered graphene sheets are consistent with the presence of a large concentration of lattice defects. The transport properties at low temperature will be emphasized. They show that graphene obtained using this method exhibits an Efros-Shklovskii variable range hopping behavior.

Table of contents of Chapter 1

1.1 Electronic structure of graphene

1.1.1 Crystallographic structure of graphene

Graphene is a 2D crystal of carbon atoms disposed in a honeycomb lattice. Such a crystal has a parallelepipedic Bravais lattice with two atoms per unit cell, named A and B. Two vectors form the basis of the lattice :

$$\mathbf{a_1} = \frac{a}{2}\left(3\mathbf{e_x} + \sqrt{3}\mathbf{e_y}\right), \mathbf{a_2} = \frac{a}{2}\left(3\mathbf{e_x} - \sqrt{3}\mathbf{e_y}\right)$$

where $a = 1.42\ \mathring{A}$ is the distance between nearest neighbours. The reciprocal lattice is formed by the basis vectors :

$$\mathbf{b_1} = \frac{2\pi}{3a}\left(\mathbf{e_x} + \sqrt{3}\mathbf{e_y}\right), \mathbf{b_2} = \frac{2\pi}{3a}\left(\mathbf{e_x} - \sqrt{3}\mathbf{e_y}\right)$$

The first Brillouin zone is hexagonal, with two inequivalent consecutive corners K and K'. These points are of particular importance for the electronic properties of graphene, for at low energies we will restrict ourselves to the vicinity of these points. These points are situated at :

$$\mathbf{K} = \left(\frac{2\pi}{3a}, \frac{2\pi}{3\sqrt{3}a}\right), \mathbf{K'} = \left(\frac{2\pi}{3a}, -\frac{2\pi}{3\sqrt{3}a}\right) \tag{1.1}$$

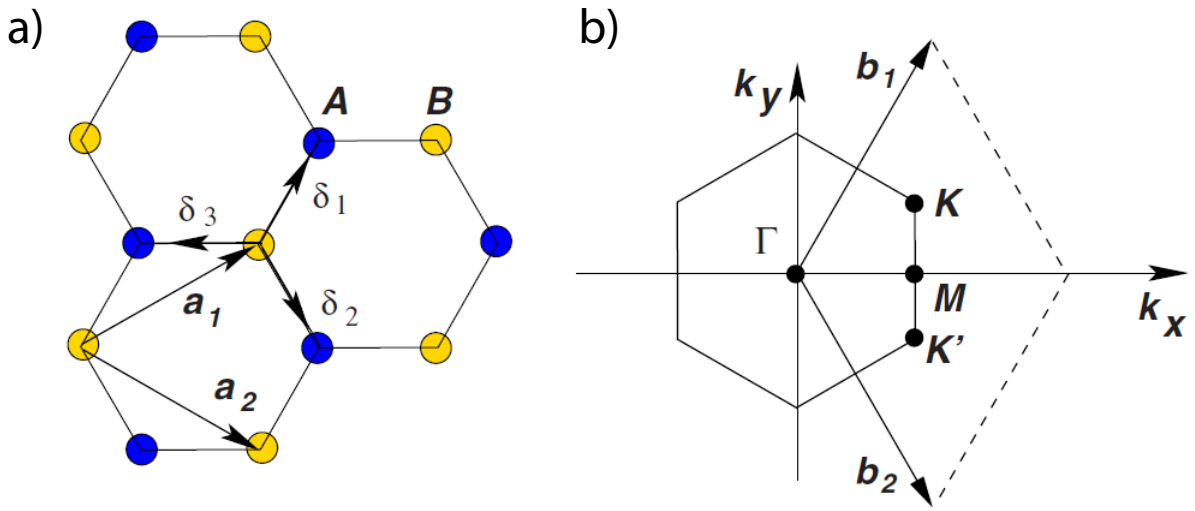

Figure 1.5 – ***Graphene's crystallographic structure. Taken from [32]. a)*** *In the real space. The unit cell is triangular (the basis is formed by vectors* $\mathbf{a_1}$ *and* $\mathbf{a_2}$*), with two atomes (A and B) per unit cell.* ***b)*** *In the reciprocal space.T he basis is formed by vectors* $\mathbf{b_1}$ *and* $\mathbf{b_2}$*. The two especially interesting points K and K' points are shown.*

1.1.2 Band structure of graphene

Carbon atoms possess 6 electrons, occupying the orbitals $1s^2 2s^2 2p^2$ in the ground state. The two $1s$ electrons are core electrons, which are bound to the nucleus. Hybridization of the $2s$ and $2p$ orbitals in the graphene plane gives 3 sp^2 orbitals, while

the out-of-plane $2p_z$ remains unchanged. The remaining 4 electrons will thus occupy these 4 orbitals. Overlap of the orbitals gives rise to energy bands. In the plane, the sp^2 orbitals have a strong overlap, resulting in 3 pairs of bonding and anti-bonding σ/σ^* bands, respectively far below and far above the Fermi energy. These are the so-called 'covalent bonds' responsible for the mechanical strength of sp^2 carbon structures. The $2p_z$ orbitals on the other hand have a smaller overlap and give rise to the so-called π and π^* bands. These two touch at the K and K' points of the first Brillouin zone. These points are called "Dirac points". With 4 electrons per carbon atom to fill these 8 energy bands, only the bottom 4 bands (the bonding bands) are filled, and the Fermi energy of ideal graphene crosses the Dirac points. In other words, the Fermi surface reduces to a set of points in electrically neutral graphene, which means the density of states at the Fermi level $\rho(E_F)$ vanishes (but without exhibiting a bandgap). For that reason, graphene is called a 'semi-metal'.

When considering transport properties, only electrons in the vicinity (within k_BT) of the Fermi energy play a role. In deriving these properties, we can thus restrict ourselves to the π and π^* bands, sometimes referred to as the valence and conduction band, and to low energies : $|E - E_F| < 0.5$ eV.

1.1.3 The Dirac cones

Following the tight-binding approach of Wallace [16] (1947), we can calculate the electronic structure of graphene. At the time, Wallace was aiming at deriving the electronic properties of graphite, a material of interest for the nuclear industry, but his work has been extremely useful to the whole sp^2 carbon community (fullerenes, carbon nanotubes and of course graphene), and has been revived and expanded upon lately, for the study of related structures, such as bilayer and trilayer graphene.

When it is applicable, tight-binding is the easiest method to derive the band structure of electrons in solids. In the tight-binding approximation, we are dealing with essentially unchanged atomic orbitals that have a small overlap with their neighbours. This is basically a perturbation treatment, where the interaction introduces a coupling between two otherwise unchanged levels. Here the coupling takes the shape of a hopping parameter t between nearest-neighbours. This approach is appropriate for the description of the π/π^* bands of graphene, as they originate from out-of-plane orbitals, which naturally have a much smaller overlap than the in-plane orbitals. Note however that in most metals, the tight-binding approach is only used to calculate bands originating from the weakly overlapping core electrons, and is irrelevant for the study of the conduction bands, which are highly hybridized.

Each unit cell contains two atoms A and B with respective p_z orbitals $|\phi_A\rangle$ and $|\phi_B\rangle$ localized at sites $\mathbf{R_j^A}$ and $\mathbf{R_j^B}$, where j is the lattice index. We can write them in the $\mathbf{r}$ representation :

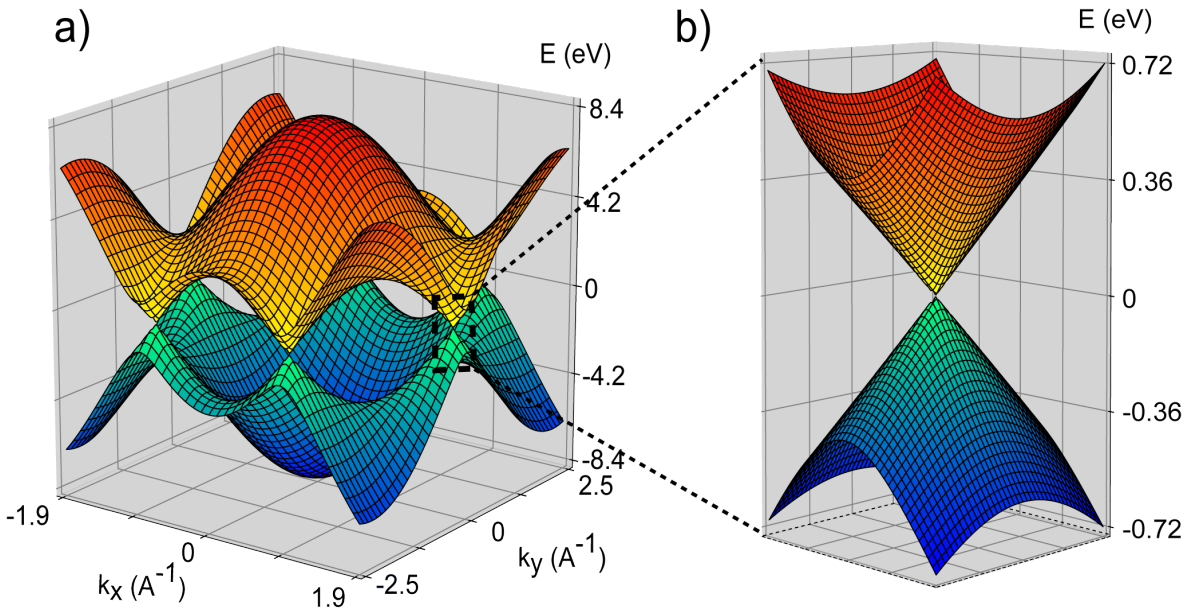

Figure 1.6 – ***a)*** *Graphene band structure (equation (1.5)) obtained from tight-binding calculation with only first neighbours interactions.* ***b)*** *Zoom on one of the K points. At low energies, the dispersion is linear. The valence (blue) and conduction (red) bands touch at the so-called 'Dirac point', but don't overlap, thus making graphene a semi-metal. The peculiar structure near the Dirac point shown in* ***b)*** *is called 'Dirac cone'.*

$$\langle \mathbf{r}|\phi_A\rangle = \phi\left(\mathbf{r}-\mathbf{R_j^A}\right), \langle \mathbf{r}|\phi_B\rangle = \phi\left(\mathbf{r}-\mathbf{R_j^B}\right) \tag{1.2}$$

The test function is a linear combination of all the p_z orbitals in the crystal :

$$\psi^{\mathbf{k}}(\mathbf{r}) = \frac{1}{\sqrt{N}}\sum_j e^{i\mathbf{k}.\mathbf{R_j}}\left(c_A(\mathbf{k})\phi(\mathbf{r}-\mathbf{R_j^A}) + c_B(\mathbf{k})\phi(\mathbf{r}-\mathbf{R_j^B})\right) \tag{1.3}$$

It can be easily verified that this function satisfies the Bloch condition :

$$\psi^k(\mathbf{r}+\mathbf{R}) = e^{i\mathbf{k}.\mathbf{R}}\psi^{\mathbf{k}}(\mathbf{r})$$

In the simplest case where hopping is considered between first neighbours only, the tight-binding Hamiltonian can be written as :

$$H = -t\sum_{<i,j>}\left|\phi_A^i\right\rangle\left\langle\phi_B^j\right| + h.c. \tag{1.4}$$

where $< i, j >$ are couples of nearest neighbours. Solving this Hamiltonian for the test function (1.3) yields the energy eigenvalues :

$$\epsilon_{\pm}(\mathbf{k}) = \pm t\sqrt{3+2\cos\left(\sqrt{3}k_x a\right)+4\cos\left(\sqrt{3}\frac{k_x a}{2}\right).\cos\left(\frac{3k_y a}{2}\right)} \tag{1.5}$$

This energy dispersion if plotted in Fig.1.6a. This very simple model is too simplistic in the sense that it only includes first neighbours hopping. Usually, a more

accurate description includes a hopping term t' between second nearest-neighbours. The value of t' is not well known, but it is of the order of $t' = 0.1t$. However, this expression is sufficient to derive the low-energy spectrum. Expanding this expression in the vicinity of the K and K' points (1.1) we have :

$$\epsilon_{\pm} \approx \pm\hbar v_F ||\mathbf{q}|| \tag{1.6}$$

Where $\mathbf{q} = \mathbf{k} - \mathbf{K}$. This is the so-called Dirac cone structure (see Fig.1.6b). It should always be borne in mind that this is an approximation valid only at low energies ($E < 0.5$ eV), for at higher energies the energy dispersion starts to show the so-called 'trigonal warping'.

When the contributions from the two spins and two valleys are included, the relation between the electronic density n and the Fermi wavevector is :

$$k_F = \sqrt{\pi n} \tag{1.7}$$

This gives us the relation between charge carrier density and Fermi energy using (1.6) :

$$E_F = \pm\hbar v_F \sqrt{\pi n} \tag{1.8}$$

Where $\pm$ is positive for electrons and negative for holes.

1.1.4 Fermi velocity, effective mass and carrier density

Most semiconductors and 2DEG are nearly-free electron systems with a parabolic band structure $\epsilon(\mathbf{q}) = \hbar^2 q^2/(2m)$. The electronic band structure described by equation (1.6) is unique in the realm of electronics. It is linear, symmetric about the Dirac point (valence and conduction band have the same dispersion), and isotropic. The first consequence of that dispersion is that the Fermi velocity :

$$v_F = \frac{1}{\hbar}\frac{\partial|\epsilon_{\pm}(\mathbf{k})|}{\partial\mathbf{k}} = t\frac{3a}{2\hbar} \tag{1.9}$$

is nearly constant and doesn't depend on energy. Near the Dirac points we have $v_F \approx 10^6$ m.s^{-1}. The second important consequence is that the inverse effective mass tensor defined by :

$$[m^*(\mathbf{k})]^{-1}_{i,j} = \frac{\partial^2\epsilon(\mathbf{k})}{\partial k_x \partial k_y} \tag{1.10}$$

is zero, *i.e.* the mass tensor is infinite. This seems somewhat unphysical because particles of infinite mass wouldn't respond to an electric field. Describing graphene's carriers therefore requires to go beyond the semi-classical solid-state physics approach and consider equation (1.6) for what it is : the energy dispersion of ultrarelativistic

particles. As a matter of fact, the Dirac equation $E^2 = m^2c^4 + p^2c^2$ for relativistic particles describes graphene's low energy carriers as well, provided that we take $m = 0$, $c = v_F$ and $p = \hbar q$. Note however that the Fermi velocity in graphene $v_F = c/300$ is too low for electrons to be relativistic. They just happen to mimic relativistic particles because of the peculiar symmetries of the Hamiltonian. This is why electrons in graphene are often termed 'massless Dirac fermions'. Finally, the electronic density of states per unit area is given by :

$$\rho(\epsilon) = \frac{2}{\pi}\frac{|\epsilon|}{\hbar^2 v_F^2} \tag{1.11}$$

1.1.5 Chirality of charge carriers

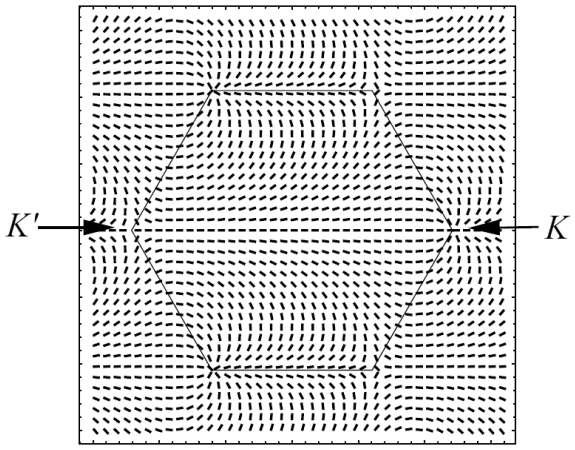

Figure 1.7 – *Orientation of the angle θ_q as a function of $\mathbf{k}$. Taken from [33].*

Let us decompose expression (1.3) on the basis formed by the Bloch functions of the A and B sublattices :

$$\psi^{\mathbf{k}}(\mathbf{r}) = \begin{pmatrix} c_A(\mathbf{k}) \\ c_B(\mathbf{k}) \end{pmatrix} \tag{1.12}$$

For all $\mathbf{k}$, i.e. for all energies, we have :

$$|c_A(\mathbf{k})| = |c_B(\mathbf{k})| \tag{1.13}$$

Because the density of states of wavevector $\mathbf{k}$ equally originates from the A and B sites. In the K and K' valleys, the wavefunctions in momentum space for the conduction and valence band are :

$$\psi_{\pm,\mathbf{K}'}(\mathbf{q}) = \begin{pmatrix} c_A(\mathbf{q}) \\ c_B(\mathbf{q}) \end{pmatrix} = \frac{1}{\sqrt{2}}\begin{pmatrix} e^{-i\theta_q/2} \\ \pm e^{i\theta_q/2} \end{pmatrix} \tag{1.14}$$

$$\psi_{\pm,\mathbf{K}}(\mathbf{q}) = \begin{pmatrix} c_A(\mathbf{q}) \\ c_B(\mathbf{q}) \end{pmatrix} = \frac{1}{\sqrt{2}}\begin{pmatrix} e^{i\theta_q/2} \\ \pm e^{-i\theta_q/2} \end{pmatrix} \tag{1.15}$$

Where $\theta = \arctan\left(\frac{q_y}{q_x}\right)$ and $\pm$ refers to the conduction and valence band. One can see that the presence of two sublattices A and B brings up an additional phase factor θ_q, the symmetry of which mimics that of a spin. We therefore call this vector 'pseudospin'. Fig.1.7 shows the angle θ_q's dependence on $\mathbf{k}$. One can clearly see that the two Dirac points K and K' are inequivalent. We can define a quantity called 'chirality' of an electronic state, which is the projection of the kinetic momentum $\mathbf{q}$ along the direction of the pseudospin. While states of positive energy (electrons) around

the K point have positive chirality, the states around the K' point have negative chirality, and the situation is reversed for states of negative energy (holes). This has important consequences on the transport properties because scattering between electronic states and quantum interference effects will depend on chirality conservation. Electrons with opposite $\mathbf{q}$ vectors within one valley travel in opposite directions (velocity is proportional to the band dispersion), but have opposite chirality θ_q, or said differently, a phase shift of π. This property is called a Berry's phase.

1.2 Transport properties of graphene

In this section, a few general concepts about electron transport and quantum interference effects in graphene devices will be introduced. We will always consider a graphene MOSFET. A MOSFET (Metal-Oxide-Semiconductor Field-Effect-Transistor) is a structure whereby the carrier density in the conducting channel (graphene) can be capacitively controlled by the voltage applied on the gate electrode (a metallic plane separated from the channel by an insulator). The charge carrier density in the graphene sheet is related to the gate voltage through the value of the gate capacitance $C_g = \epsilon_0 \epsilon_r / d$, where ϵ_r is the dielectric constant of the gate dielectric and d is the gate dielectric thickness. Equation (1.8) then relates the Fermi level to the carrier density.

1.2.1 Electron/hole puddles and finite minimum conductivity of graphene

Even though the density of states vanishes at the Dirac point, the conductance never goes to zero upon sweeping the gate voltage in graphene MOSFETs. This has been one of the major debate in the graphene community. Some claim that this is because a universal conductivity $4e^2/\pi h$ should arise in a system of Dirac fermions of vanishing density, *i.e.* near the Dirac point [35]. And indeed this claim finds some support in experiments [36]. However, other people disagree and say that this is an effect of charge inhomogeneities, and that the minimum conductivity, which should be charged-impurity-dependent, only happens to be about $h/4e^2$ in most samples by chance [37, 38]. This picture gained more support when it was experimentally observed that the typical samples on SiO_2 substrates indeed break up into puddles of electron-doped regions and hole-doped regions near the charge-neutrality point [34] (see Fig.1.8). The depth of these puddles was measured to be is on the order of $n_0 = 10^{11}$ cm^{-2}. The origin of these inhomogeneities are most likely charged impurities located in the gate dielectric and hydrocarbon residues on top of graphene. Recently, experiments on double-layer graphene heterostructures unambiguously showed that, when charge inhomogeneities are completely screened out, graphene becomes insulating near the Dirac point [39].

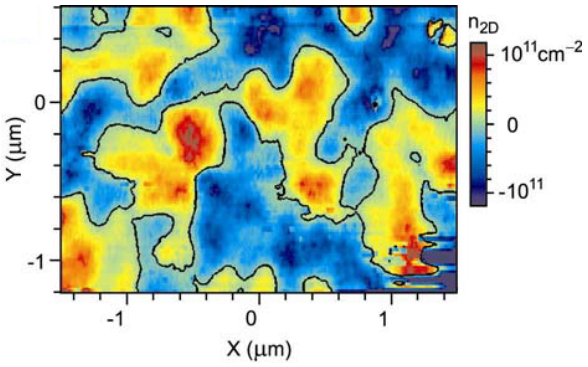

Figure 1.8 – *Figure from [34] showing experimentally measured local charge inhomogeneities near the charge neutrality point in graphene reported on a SiO_2 substrate.*

1.2.2 Drude conductivity and mobility fit

In a simple, yet successful approximation, Drude managed to capture some essential properties of metals by assuming their conductivity results from a dynamical equilibrium between the applied electric field and the friction resulting from scattering events. Let's consider electrons in an electric field **E**. They are uniformly accelerated. Now if we consider that τ is the typical time between two collisions (or scattering events), and that the average velocity is zero after a collision, with a kinetic energy given by the Fermi-Dirac distribution, we find that the *average* velocity with which electrons travel along the electric field, called 'drift' velocity is :

$$v_d = \frac{qE\tau}{m^*} \tag{1.16}$$

where q is the charge and m^* the effective mass of the charge carrier. This leads to the famous Drude formula for electrical conductivity :

$$\sigma = \frac{nq^2\tau}{m} \tag{1.17}$$

Where n is the charge carrier density. An important phenomenological quantity in characterizing a semiconductor is its electronic mobility μ, defined as the ratio between electron drift velocity v_d and the applied electric field E :

$$\mu = \frac{q\tau}{m^*} \tag{1.18}$$

which is proportional to the scattering time τ. We are often going to characterize our graphene devices using this quantity. Now if we write the conductivity as a function of the electron mobility we find :

$$\sigma = nq\mu \tag{1.19}$$

In graphene devices, the carrier density is proportional to the applied gate voltage : $n = C_g(V_g - V_D)/e$, where V_D is the charge neutrality (Dirac) point and C_g the capacitance to the gate. As we have seen in §1.2.1, it never actually vanishes at the Dirac point because of the presence of electron/hole puddles. If we take the root mean square of the density of states in the puddles to be n_0, the total carrier density is :

$$n = \sqrt{\left(\frac{C_g(V_g - V_D)}{e}\right)^2 + n_0^2} \tag{1.20}$$

Finally, the total resistance of the graphene ribbon can be written :

$$R = \frac{L}{W}\frac{1}{e\mu\sqrt{(\frac{C_g(V_g-V_D)}{e})^2 + n_0^2}} \tag{1.21}$$

Where L and W are the device's length and width, respectively. Note that this formula is valid to fit a 4-probes measurement, as it does not include the contact resistance. Whenever a single value of mobility is given for a sample, it is by fitting its field effect curve using relation (1.21), and it means that the scattering rate τ^{-1} is gate-independent.

1.2.3 Scattering mechanism and the conductivity dependence on gate voltage

In exfoliated graphene, the field effect curves often display a linar dependence of conductivity on gate voltage (see Fig.1.9). Given that the number of carriers n is proportional to the gate voltage V_g, this means that the conductivity is proportional to the number of carriers. In other words, it means that the scattering time τ does not depend on gate voltage (equation 1.17). It is a device-dependent constant quantity.

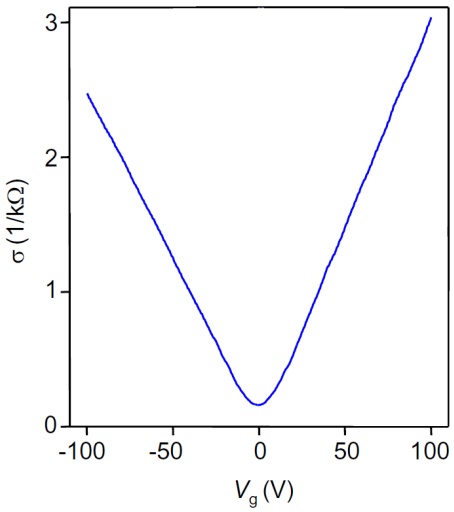

Figure 1.9 – *Typical field effect curve observed in monolayer graphene exfoliated on SiO_2 and patterned into a Hall bar geometry. The conductivity is symmetric and proportional to the gate voltage. Taken from [7].*

Early theoretical works on the scattering of Dirac fermions [37, 40, 41] found that strong (resonant) short-range scatterers (atomic vacancies, sp^3 defects, short-range ripples) and long-range scatterers (charged impurities) induce a totally different gate dependence of the conductivity. They found that samples dominated by short-range scatterers should exhibit a gate-independent conductivity, whereas it should assume a linear dependence on gate voltage for the case of charged impurities. The presence of charged-impurity scattering has strong experimental support and is widely accepted in the community. The correlation between the Dirac peak width and position, which reflects the presence of charged dopants, and mobility, supports this picture [42, 43], as well as the positive influence of the dielectric environment on the mobility [44]. However, there is some controversy as to the relative influence of short-range scatterers. As a matter of fact, the fact that short-range impurities contribute to the resistance in a carrier-density-independant manner, has since then been contested [45, 46]. Short-range impurities such as sp^3 and vacancies should be visible in the Raman spectrum. But careful determination of the transport and elastic scattering times by magnetoconductance [47], as well as mobility studies on high-κ dielectric $SrTiO_3$ substrates [48] tend to support the picture that charged-impurities are not the only sources of scattering in exfoliated graphene. It is possible that other long-range

scattering centers, such as long-range ripples and potential gradients, play an important role in limiting the mobility.

1.2.4 Einstein's relation

If the system size is much larger than the mean free path $l_e = v_F\tau$, the transport regime is called diffusive and the electrical properties can be described using Einstein's relation :

$$\sigma = e^2 D\rho(E_F) \tag{1.22}$$

where D is the diffusion coefficient and $\rho(E_F)$ is the density of states at the Fermi energy. The diffusion coefficient is $D = \frac{v_F^2\tau}{d} = \frac{v_F l_e}{d}$, with d the dimensionality of the system. Using equation (1.11), we find :

$$\sigma = e^2\frac{v_F l_e}{2}\frac{2}{\pi}\frac{|E|}{\hbar^2 v_F^2} = \frac{e^2 v_F l_e}{\pi\hbar^2 v_F^2}\hbar v_F k_F \tag{1.23}$$

$$= 2\frac{e^2}{h}k_F l_e \tag{1.24}$$

What this equation tells us is that when the dimensionless conductance $g = \sigma/G_0 \cong 1$, where G_0 is the quantum of conductance, $k_F \cong l_e$, *i.e.* the electron wavelength is about the same size as the mean free path. In this limit, the plane wave approximation for electrons starts to be irrelevant. In 3D electrons system, this value is critical for the scaling theory of localization [2]. It corresponds to the localization threshold. In 2DEG, this value is not as significant, because any 2DEG will become localized eventually, but it is a good indication of the proximity to the strong localization regime. In the following section, we will see how the electrons get localized at low temperatures in 2DEG and in graphene. It starts with weak localization.

1.2.5 Weak localization

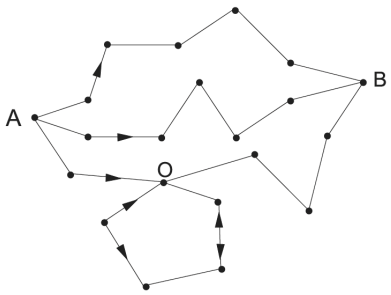

Figure 1.10 – *Different diffusive path from point A to point B. The probability to find the electron in point O is enhanced by quantum interferences.*

Let's consider an electron diffusing in a metal. The probability of diffusion from point A to point B (Fig.1.10) is the square of the sum of the complex amplitudes A_i describing each possible path :

$$P_{AB} = \left|\sum_i A_i\right|^2 = \sum_i |A_i|^2 + \sum_{i\neq j} A_i A_j^* \tag{1.25}$$

The second term in equation (1.25) is the interference term between two paths. During the diffusion

between A and B, the electron wave function acquires a certain phase. The phases acquired over two distinct paths are not correlated. Therefore, the interference term, which is the sum of many $e^{i(\Delta\varphi_1-\Delta\varphi_2)}$ terms, with $\Delta\varphi_i$ being the phase acquired along trajectory i, averages to zero. This is true for all trajectories, except for some special pairs of trajectories. Self-intersecting trajectories (such as represented in Fig.1.10) contain a loop that can be followed in two ways. The phases acquired along the loop are the same for the clockwise and anticlockwise trajectories. Therefore, the two trajectories will interfere constructively at point O (the hermitian product of the phase factors gives 1), increasing the probability to find the electron there. This naturally decreases the probability to find the electron anywhere else, and therefore it decreases the conductivity. This quantum correction to conductivity is thus proportional to the probability for an electron to diffuse back to its starting point, called return probability :

$$Z(t) = \int_\Omega d\mathbf{r} P(\mathbf{r},\mathbf{r},t) = \frac{\Omega}{(4\pi D t)^{d/2}} \tag{1.26}$$

where d is the system's dimensionality and $P(\mathbf{r},\mathbf{r'},t)$ is the probability for an electron to have diffused from **r** to **r'** after time t. The correction to the conductivity then writes :

$$\delta\sigma = \frac{2e^2 D}{\pi\hbar\Omega}\int_0^\infty dt Z(t)(e^{-\frac{t}{\tau_\phi}} - e^{-\frac{t}{\tau_e}}) \tag{1.27}$$

where τ_ϕ and τ_e are the phase coherence and elastic scattering time, respectively. In two dimensions we obtain :

$$\delta\sigma_{d=2} = -\frac{e^2}{\pi^2\hbar}\ln\frac{L_\phi}{l_e} \tag{1.28}$$

We can see from (1.28) that in two dimentions, the correction to conductivity can be arbitrary large if $L_\phi >> l_e$, which will be the case at low temperatures. This is why 2D diffusive systems are always expected to be insulating at $T = 0$ K. The temperature dependence of this correction depends on the temperature dependence of L_ϕ, which in turn depends on the kind of inelastic mechanism involved. It is usually assumed to follow some power law of temperature :

$$\tau_\phi(T) \propto T^{-p} \tag{1.29}$$

Therefore, in two dimensions we have :

$$\delta\sigma_{d=2} \propto \ln T \tag{1.30}$$

Note that equations above are derived from a perturbation treatment in $1/k_F l_e$. They are only valid as long as $g = \sigma/(e^2/h) >> 1$ and for $\delta\sigma/\sigma << 1$.

1.2.5.1 Effect of magnetic field.

In the presence of a magnetic field H, the electrons travelling along a closed loop will pick up an additional phase equal to :

$$\phi = \frac{e}{h} \oint \mathbf{A} d\mathbf{l} = \pm \frac{\pi H S}{\phi_0} \tag{1.31}$$

where $\mathbf{A}$ is the vector potential, S is the loop area, $\phi_0 = h/2e$ the flux quantum and $\pm$ corresponds to the clockwise/anticlockwise case. Applying a magnetic field therefore destroys the quantum interference effect because, each loop having a different surface area, the corrections will average to zero.

1.2.5.2 Effect of scattering mechanisms on localization in graphene

Chirality of the charge carriers in graphene has important consequences [49]. Because electrons rotating in opposite directions inside the same valley always have a Berry phase of π (see §1.1.5), the quantum interference between self-intersecting trajectories of electrons from the same valley should change from constructive to destructive, enhancing the conductivity. On the other hand, by coupling two valleys of opposite chirality, intervalley scattering restores the usual weak localization. A crossover is therefore expected between weak (anti)localization and weak localization as the intervalley scattering rate τ_{iv}^{-1} becomes comparable to the phase-coherence rate τ_ϕ [27]. In early experiments [28], it came as some surprise that graphene often shows no low-field magnetoresistance whatsoever, or at best a strongly suppressed one, suggesting that something had been overlooked. It was soon realized [50] that some defects can disrupt phase coherence within a valley :

- Lattice defects and dislocations
- Surface ripples and curvature of the plane that act as an effective magnetic field
- Large-scale potential gradients

All lead to reduced quantum interferences. This complex dependence is encapsulated in the following formula [30] :

$$\Delta\sigma(B) = -\frac{e^2}{\pi h}\left[F\left(\frac{\tau_B^{-1}}{\tau_\phi^{-1}}\right) - F\left(\frac{\tau_B^{-1}}{\tau_\phi^{-1}+2\tau_i^{-1}}\right) - 2F\left(\frac{\tau_B^{-1}}{\tau_B^{-1}+\tau_i^{-1}+\tau_*^{-1}}\right)\right] \tag{1.32}$$

where $F(z) = ln(z) + \psi(0.5 + 1/z)$, $\psi(x)$ being the digamma function. $\tau_B^{-1} = 4eDB/\hbar$, τ_ϕ^{-1} is the phase-breaking rate, τ_i^{-1} is the intervalley scattering rate and $\tau_*^{-1} = \tau_s^{-1} + \tau_w^{-1}$ is the phase-breaking intravalley scattering rate, which includes the

rate of scattering by dislocations, atomically sharp defects (they induce both intervalley and intravalley scattering) and ripples τ_s^{-1} and the rate of scattering due to the anisotropy of the Fermi surface, the so-called 'trigonal warping' τ_w^{-1}.

In samples obtained by mechanical exfoliation, intravalley scattering predominates over intervalley, which is why we do not see weak localization but a rather metallic behavior. However, in samples with a high density of atomically sharp defects or in narrow samples ($W \leq L_\phi$) where the edges are predominant, weak localization is restored.

1.2.6 Strong localization in 2D systems

In 3D materials, there is a clear distinction between the metallic regime, for $k_F l_e >> 1$, and the localized regime when $k_F l_e << 1$. In the former case ($g > g_c$), the conductivity increases upon increasing the phase-coherent system's size (Fig.1.11). Decreasing the temperature, by increasing the phase coherence length, results in an enhanced conductivity. In the opposite case ($g < g_c$), quantum interferences localize the wave functions. In scaling theory, g_c is called an unstable fixed point.

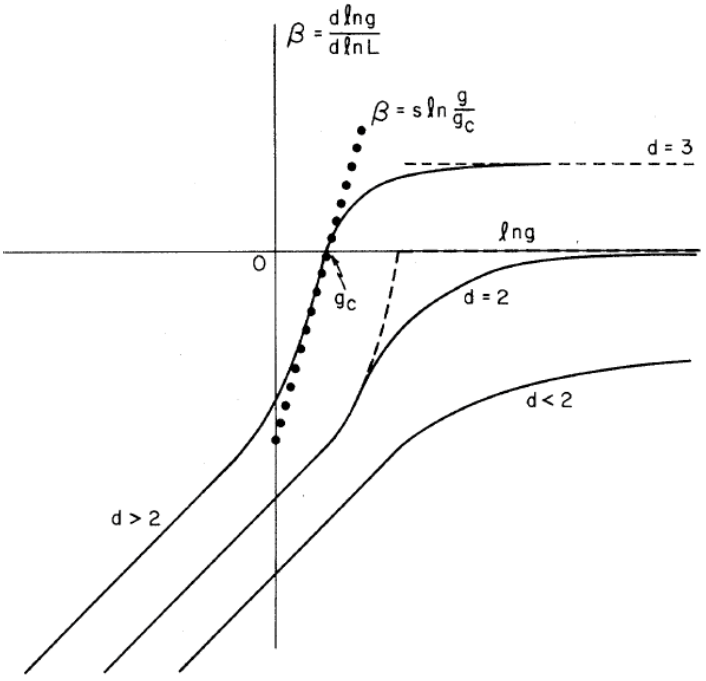

Figure 1.11 – *Scaling diagram of localization at zero temperature. It shows the behavior of β as a function of the conductance $g(L)$ for different dimensionalities. Taken from [2].*

In two dimensions, there is no such unstable fixed point (curve $d = 2$ in Fig.1.11). The weak localization correction (1.28) is always negative and diverges at low temperatures. Therefore, it is said that all electronic states in 2D are localized. The crossover from weak to strong localization in 2D happens when the weak localization correction (equation 1.28) becomes comparable to the conductivity. In 2D, one defines the

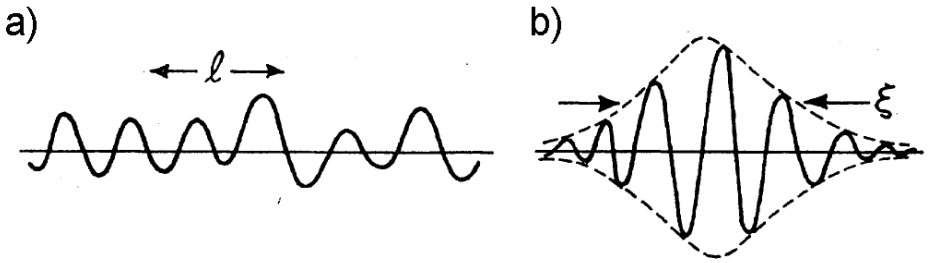

Figure 1.12 – ***Wave functions of electrons are a)*** *Extended and delocalized when the mean free path* $l >> 1/k_F$ *and* ***b)*** *Localized in the opposite case with an exponential decay over the localization length* ξ*. Taken from [51].*

localization length as the critical coherence length $L_\Phi^{crit} = \xi_{loc}$ at which this crossover happens [51] :

$$\delta\sigma \cong \sigma \tag{1.33}$$

Using equation (1.24), we can rewrite equation (1.33) :

$$\frac{e^2}{\hbar\pi^2} \ln \frac{\xi_{loc}}{l_e} = 2\frac{e^2}{h} k_F l_e \tag{1.34}$$

Which gives the localization length in graphene :

$$\xi_{loc} = l_e \exp\left(\pi k_F l_e\right) \tag{1.35}$$

As long as the electron coherence length L_φ, defined by the inelastic scattering events, is smaller than ξ_{loc}, the electrons get scattered from one localized region to another before they can explore it completely. As the temperature is lowered, L_φ grows because the main source of inelastic scattering are phonons. At some point $L_\varphi > \xi_{loc}$ and the electrons become strongly localized. We can see from equation (1.35) that the localization length diverges quite quickly with $k_F l_e$, so that the crossover between weak and strong localization can only be observed within the attainable temperature range ($T > 50$ mK) for samples of conductivity $g \approx 1$ at room temperature.

1.2.6.1 Variable range hopping

When the electronic wave functions are localized, their spatial extent is limited and they decay over the characteristic length ξ_{loc} called the localization length. In this regime, the motion of electrons is dominated by hopping between localized states. Miller and Abrahams [52] showed that the tunneling resistance between two localized sites i and j is :

$$R_{ij} = R_{ij}^0 \exp\left(\frac{2r_{ij}}{\xi_{loc}}\right) \exp\left(\frac{\epsilon_{ij}}{k_B T}\right) \tag{1.36}$$

Where r_{ij} is the hopping distance between sites i and j, and ϵ_{ij} is the energy difference between the electrons on the two sites. The second exponential term reflects the fact that hopping is a phonon-assisted mechanism, and the first term encapsulates the effect of wavefunction overlapping. Should hopping be limited to first neighbours, the conductivity would be activated (Arrhenius-like), like in a band insulator.

However, Mott [53] showed that it is energetically favorable for an electron, when the second exponential term in equation (1.36) becomes too large at low temperatures, to hop towards a remote localized state with an energy closer to his, so as to optimize ϵ_{ij}. As the temperature is reduced, the energy window decreases, and therefore the hopping length tends to increase. This mechanism, where the hopping distance increases with decreasing temperature, is called 'variable range hopping' (VRH).

Let's consider a state i, of energy ϵ_i, where an electron originates. For each temperature, there are an optimum hopping length r_{ij} and energy band $\pm\epsilon_{ij}$ around ϵ_i that minimize the exponential term of equation (1.36) :

$$\frac{2r_{ij}}{\xi_{loc}} + \frac{\epsilon_{ij}}{k_B T} \tag{1.37}$$

The number of suitable states ($\epsilon_j = \epsilon_i \pm \epsilon_{ij}$) the electron finds is proportional to the surface of the circle of radius r_{ij} and to the integrated density of states in the energy band. Assuming a constant density of states $\rho(E)$, the variable range hopping model's assumption is that :

$$r_{ij}^2 \epsilon_{ij} g(E) = \text{constant} \tag{1.38}$$

Which gives the following relationship between hopping length and optimum energy band :

$$r_{ij} \propto (\rho(E)\epsilon_{ij})^{1/2} \tag{1.39}$$

or equivalently :

$$\epsilon_{ij} \propto (g(E) r_{ij}^2)^{-1} \tag{1.40}$$

Now using equation (1.40) one can minimize equation (1.37) with respect to r_{ij} :

$$\frac{2}{\xi_{loc}} - \frac{\text{constant}}{g(E) r_{ij}^3 k_B T} = 0 \tag{1.41}$$

This gives :

$$r_{ij} \propto \left(\frac{\xi_{loc}}{g(E) k_B T} \right)^{1/3} \tag{1.42}$$

The exact value of the average hopping length can be found in [54, 55] :

$$d = \frac{1}{4}\xi_{loc}\left(\frac{T_0}{T}\right)^{1/3} \tag{1.43}$$

Finally, if we inject equation (1.40) and (1.42) into equation (1.36), we obtain :

$$R_{ij} \propto \exp\left(\frac{T_0}{T}\right)^{1/3} \tag{1.44}$$

where :

$$T_0 = \frac{\beta}{k_B g(E)\xi_{loc}^2} \tag{1.45}$$

With β a constant to be determined. A more rigourous derivation gives $\beta = 3$ in 2D [56]. Equation (1.44) is called Mott's law. It can be generalized to d dimensions :

$$R = R_0 \exp\left(\frac{T_0}{T}\right)^{\frac{1}{d+1}} \tag{1.46}$$

We can see that this dependence is weaker than a simpler Arrhenius activation law like equation (1.36), reflecting the fact that electrons find an 'easier' path through the VRH mechanism.

1.2.6.2 Efros-Shklovskii VRH

All localized electron systems do not follow equation (1.44). As a matter of fact, this theory overlooks an important effect : unscreened Coulomb interactions between electrons on occupied localized states renormalize the density of states at the Fermi energy. The calculation of Mott relied on the assumption that $\rho(E)$ is a constant. Efros and Schklovskii [54] showed that Coulomb interactions lead to the following energy-dependent density of states in 2D :

$$\rho(E) = \frac{2}{\pi}\frac{E(4\pi\epsilon_0\epsilon_r)^2}{e^4} \tag{1.47}$$

Where ϵ_r is the relative permittivity. The gap width is defined by the energy at which we recover the unperturbed density of states ρ_0. Using equation (1.47) :

$$\rho_0 \cong \frac{\Delta(4\pi\epsilon_0\epsilon_r)^2}{e^4} \tag{1.48}$$

$$\Delta \cong \frac{\rho_0 e^4}{(4\pi\epsilon_0\epsilon_r)^2} \tag{1.49}$$

Including this renormalization of $\rho(E)$ in the calculation of Mott, E-S showed that this results in a stiffer and dimensionality-independent temperature behavior :

$$R = R_0 \exp\left(\left(\frac{T_0}{T}\right)^{\frac{1}{2}}\right) \tag{1.50}$$

With $R_0 = \frac{h}{e^2}$. This is called the Efros-Shklovskii (E-S) law. The activation temperature T_0^{E-S} is also related to a localization length [54] :

$$\xi_{loc}^{ES} = \frac{2.8e^2}{4\pi\epsilon_0\epsilon_r k_B T_0} \tag{1.51}$$

Where ϵ_r is the relative permittivity of the environment.

Of course, this effect is very dependent on the screening strength. Screening should be absent in insulators, but in real systems puddles of metallic regions can be suspected to subsist, and would provide efficient shielding of the electric field. In addition to that, the presence of a metallic back-gate has been shown to cut off Coulomb interactions at long distances [57]. Therefore, telling if an insulator behaves according to Mott's (1.44) or E-S law (1.50) can bring valuable informations. However, it is often very difficult to distinguish between these two mathematical laws, especially in dimension 2 where they are very close, unless the resistance varies on many orders of magnitude, like in [55].

1.3 Fabrication and characterization of graphene devices

Since the seminal paper by Novoselov *et al.* [8], which introduced the micromechanical exfoliation technique (a.k.a. scotch tape technique), a tremendous effort has been put into the synthesis of graphene, with amazing success. While micromechanical exfoliation gave graphene flakes with excellent electronic and structural properties [7], for graphene to have a significant commercial outlet requires a large-scale synthesis method, even if it was at the expense of crystalline quality. At the time Novoselov and Geim published their work, a team at Georgia Tech. University was already pioneering a novel and promising route towards large-scale production, based on the thermal decomposition of SiC wafers [58] [59]. Although still an active field of research, this technique has had trouble bearing the comparison with the emergence of a chemical vapour deposition technique. The need for very expensive substrates, ultra high vacuum, the lack of control on the number of layers and the inevitable presence of a conducting buffer layer underneath graphene can seriously hamper its potential, although the ultimate crystalline purity of this epitaxially grown graphene could find some niche applications.

Graphene can be obtained by reduction of graphite oxide in solution [60] [61]. This chemical route could potentially be applied for synthesizing cheap and printable conductive coatings. However, the films obtained with this method are in no way comparable to exfoliated graphene in terms of electronic mobility, as they are multilayer, polycrystalline and contaminated by chemical species.

Recent years (2008-2012) have seen a boom in research on the synthesis of graphene by chemical vapour deposition (CVD). The possibility to grow arbitrarily large monolayer graphene with high mobility makes it a potential replacement for the rare and expensive ITO electrodes in touch screens. The CVD growth of graphene has been reported on Ni [62] [63] [64], Cu [65] and Pt [66]. The self-limiting nature of this process allows for the growth of just one layer. Transfer to arbitrary substrates can then be realized using simple methods [67]. The grain size obtained by the most advanced groups now reach 1 mm and beyond [68, 66, 18], with electron mobilities now just as high as those obtained in exfoliated graphene [69].

Finally, an important branch of graphene research is concerned with opening a band-gap in graphene to realize digital electronics devices. To this end, one needs to fabricate graphene nano-ribbons with perfect edges and controllable width. Because plasma-based lithography techniques do not meet the requirements in terms of edge quality , new methods are being devised, such as the chemical synthesis of graphene nanoribbons [70] or the unzipping of carbon nanotubes [71].

In the following sections, some details of the two techniques that we routinely use for the production of graphene in our lab will be explained : mechanical exfoliation

and chemical vapour deposition (CVD) on Cu substrates, as well as the characterization tools and the fabrication processes used for producing electronic devices.

1.3.1 High-mobility devices using exfoliated graphene

1.3.1.1 SiO_2 substrate cleaning

It is known since the first experiments on weak localization in graphene (see note added in proofs of [28]) that rippling and wrinkling is a major source of decoherence and scattering in graphene. Cleaning the substrate is therefore a very important first step in the fabrication of high mobility devices, because trapping impurity between graphene and the substrate not only would induce Coulomb scattering, but it would also significantly wrinkle the sheet. We tried using piranha solution (sulfuric acid+hydrogen peroxyde) to clean the surface prior to exfoliation, but seeing no clear improvement, and given the hassle and danger associated to it, sought alternative routes. We used acetone and soap wash combined with sonication for several minutes. This was followed by 5 minutes O_2 plasma etching of the surface, which in addition to removing eventual organic residues from the surface, seemed to improve the subsequent success rate in getting monolayers.

1.3.1.2 Mechanical exfoliation of graphene flakes

While the sp^2 covalent bond holding the atoms together in a graphene plane is one of the toughest in nature, the van der Waals interaction between two graphene planes in graphite is comparatively pretty weak. This is why graphite is used in pencil, because gentle rubbing against a rough surface (paper) provides enough energy to cleave graphene layers apart. The mechanical exfoliation technique of graphene takes advantage of that property in order to try and thin down graphite layers, until eventually monolayers show up. The procedure is as follows :

- First, drop a chunk of graphite (natural or Kish graphite are preferable over Highly Oriented Pyrolitic Graphite (HOPG)) onto the sticky side of a piece of scotch tape (we use 3M 'magic', for it doesn't leave too much glue residues) (Fig.1.13a).
- Fold the scotch tape on top of the graphite so as to squeeze it, press firmly.
- Gently unfold the tape. The piece of graphite is cleaved in two.
- Repeating this operation will generate some kind of Rorschach pattern (Fig.1.13b). Continue until the scotch tape is fully covered with graphite. Judging when to stop requires some practise. The scotch tape surface should be as densely covered as possible, with graphite fragments as small as possible. It

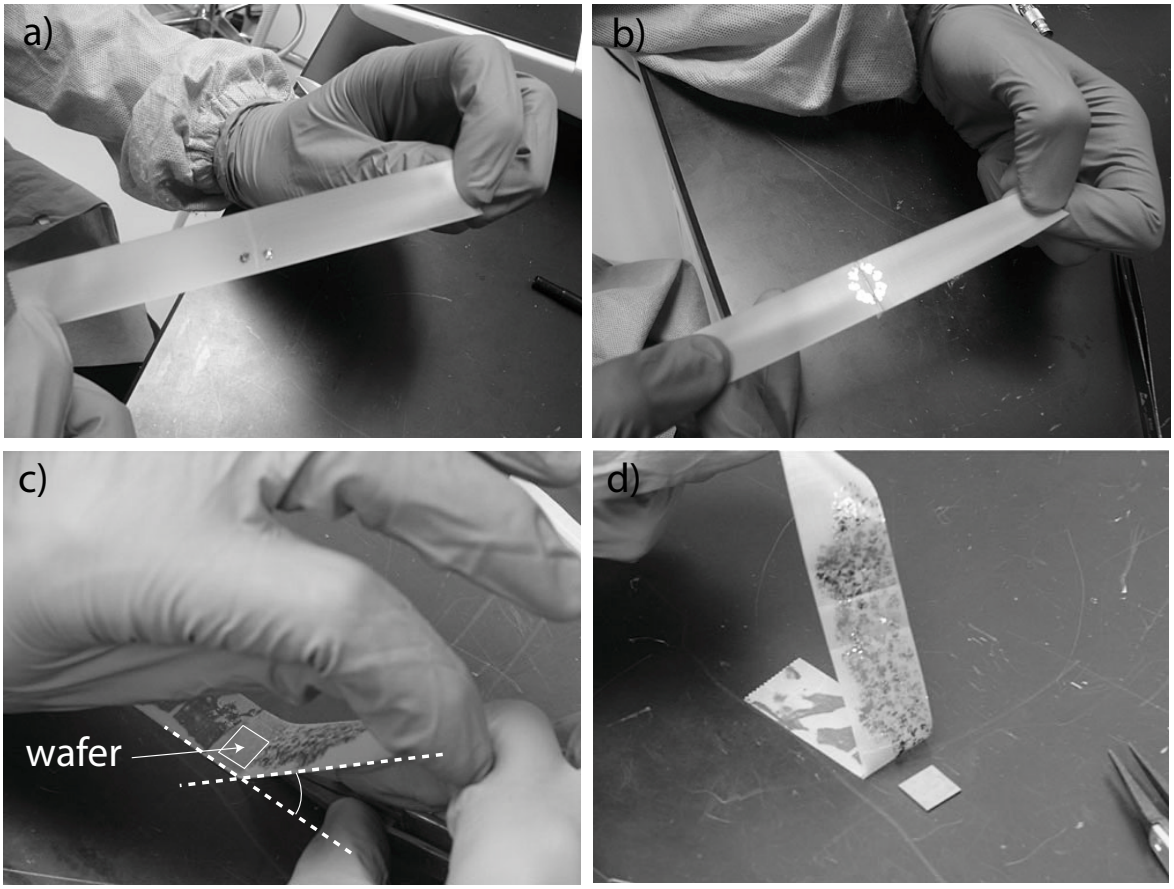

Figure 1.13 – ***Mechanical exfoliation of graphite using scotch tape. Taken from the online tutorial available at*** `http://www.scientificamerican.com/slideshow.cfm?id=diy-graphene-how-to-make-carbon-layers-with-sticky-tape` ***a)*** *Put a piece of graphite on the sticky surface.* ***b)*** *Repeatedly peel it off.* ***c)*** *Stick it onto the substrate and peel off slowly while keeping a small angle with the table.* ***d)*** *The surface of the wafer is now covered in graphite and graphene flakes.*

is important not to have any "bulky" graphite crystal left, for it will not adhere to the substrate surface.

- Remember that each time the scotch tape is unfolded, two fresh graphite surfaces are created, so that the face pointing outside is always clean (there is no glue on graphene).
- Lie down the scotch tape onto a substrate. We used 285 nm SiO_2/Si substrate, which in principle provides the most favourable optical conditions in terms of interferences to get a high contrast for the identification of monolayers [72], but in principle any substrate can be used.
- Gently rubbing the surface helps get rid of spurious bubbles stuck between the tape and the substrate.
- **Slowly** remove the scotch tape by pulling on its end, while keeping a low angle between the tape and the surface (Fig.1.13c).

Looking at the SiO_2 substrate , it is now covered with graphite flakes of various thickness, as is evident from their many different colors (see for example Fig.1.14a). A trained eye can usually tell if a flake is monolayer (Fig.1.14b), but unambiguously proving it necessitates characterization tools, such as AFM and Raman spectroscopy. For exfoliated devices we routinely used Raman spectroscopy to assess the number of layers with certainty.

1.3.2 Chemical Vapor Deposition (CVD) of graphene on Cu and transfer to arbitrary substrate for batch fabrication.

Although mechanical exfoliation yields the best graphene in terms of electronic mobility, it is very time consuming to prepare. Not only must one exfoliate and isolate it using optical microscopy, which is a rather tedious task, but making electric devices requires to address each individual flake using electron beam lithography to pattern electrodes. CVD graphene, on the other hand, allows for batch fabrication of devices that can potentially be as large as one wants. Once a film of graphene has been grown, using UV lithography followed by plasma treatment, one can pattern and etch graphene into stripes and align electrodes on top of them, producing thousands of devices at once. Unlike exfoliated graphene, there is no need to locate CVD graphene : it is covering the whole surface. Since we are no longer bound to using substrates giving a good optical contrast for graphene, CVD graphene can be transferred to arbitrary substrate. Finally, we will see that a controllable defect density can be induced during the fabrication process, which is another way to tailor graphene's electronic properties.

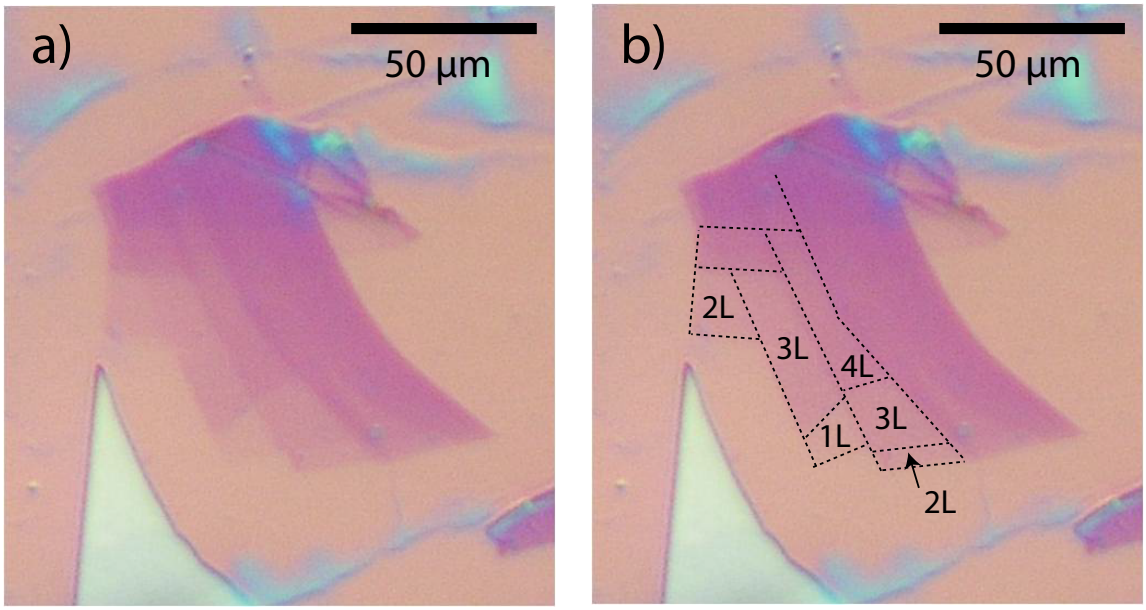

Figure 1.14 – ***Mono- and few-layer graphene as seen by optical microscopy.*** ***a)*** *Image of the SiO_2 wafer after exfoliation. The quantized light absorbtion reflects the quantization of the number of layers. The yellowish flake on the left is graphite.* ***b)*** *By carefully comparing the contrasts, one can assess the number of layers, by assuming that the faintest part corresponds to a monolayer.*

1.3.2.1 CVD growth process

Our home-made CVD oven, shown in Fig.1.15, has been assembled by another PhD student in our group, Zheng HAN, who built the setup and found the appropriate growth parameters. Thanks to him, we are now able to grow state-of-the-art CVD graphene with mobilities comparable to those of exfoliated graphene [73]. The setup has been originally designed to grow graphene on Cu substrates following the recipe first described in [65]. It is made of a furnace surrounding a quartz tube in which the Cu substrate is introduced. H_2, CH_4 and Ar gas can flow in the tube. At the inputs, mass-flow controllers regulate the gas flow. At the output, a screw pump controls the vacuum.

The principle of CVD growth of graphene is that Cu acts as a catalyst : at high temperatures, it cracks methane molecules and traps the carbon atoms at its surface. Once the Cu surface is fully covered, it stops being active as a catalyst. The growth is thus self-limited. Other catalysts, like Ni, can be used. However, Cu has a significant advantage in that it has a very low carbon solubility. Therefore, reduced carbon absorbtion leads to limited segregation during the cooldown, and to a predominantly monolayer coverage. The standard recipe consists of the following steps :

- The screw pump runs at full speed. Its base pressure is about 10^{-2} mbar.
- Ramp the temperature up to 1000°C while flowing H_2

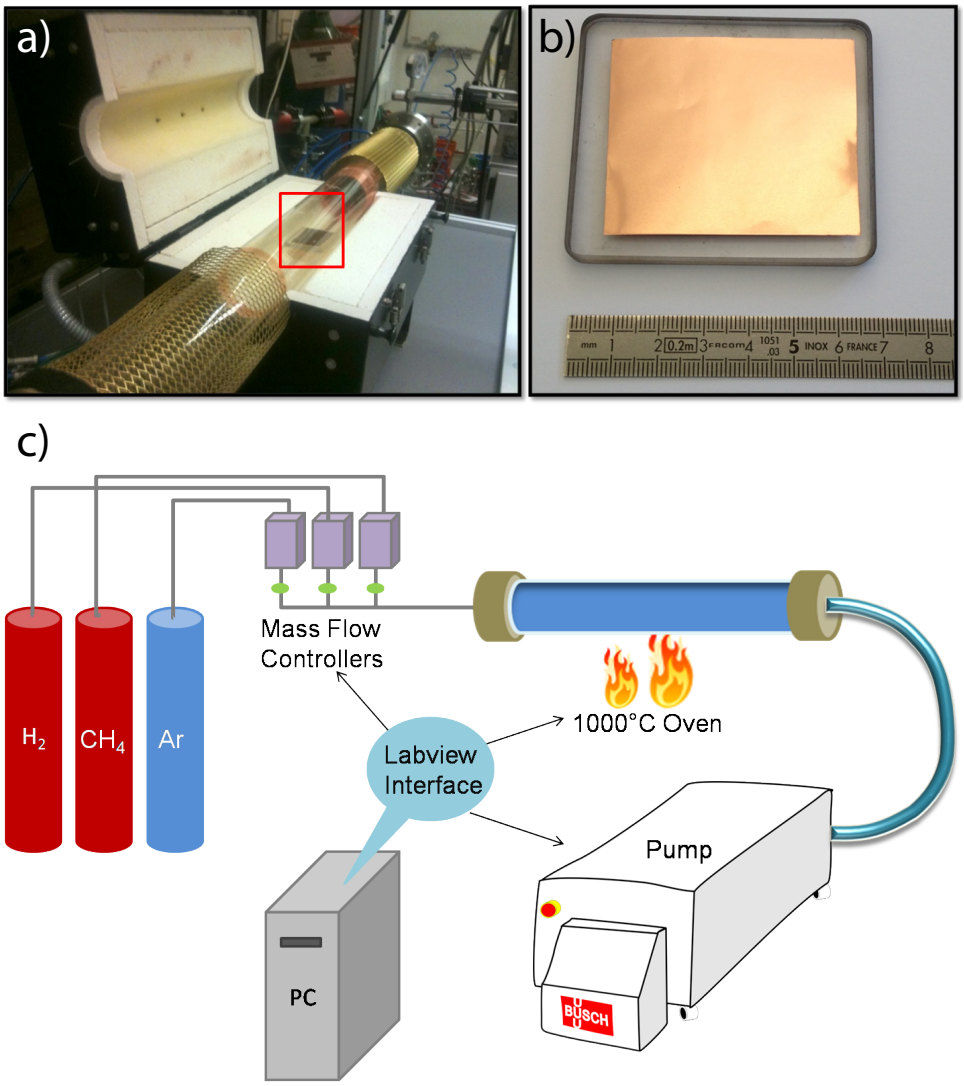

Figure 1.15 – ***Pictures and schematic layout of our CVD setup (Courtesy of Zheng HAN) a)*** *Picture of the CVD oven with the oven top open, revealing the Cu substrate inside the tube (in the red square).* ***b)*** *The substrate holder with a Cu foil on top.* ***c)*** *Cartoon of the setup.*

- Stay at 1000°C 30 minutes while flowing 700 sccm (standard cubic centimeters per minute) of H_2. This allows the Cu surface to reconstruct and form large grains.
- Maintain the H_2 flow and introduce 2 sccm of CH_4 for about 20 minutes.
- Stop CH_4 flow, stop the oven, let H_2 flow until the oven cools down below 500°C.
- Stop H_2 and keep pumping. Wait until $T \leq 200^\circ$ C to open.

A few remarks :

- Using a mixture of H_2 diluted in Ar also works, and it is significantly less dangerous.
- However, the higher the ratio between the partial pressure of H_2 and CH_4, P_{H_2}/P_{CH_4}, the larger the graphene grains will be (up to $P_{H_2}/P_{CH_4} \approx 1000$, after which H_2 starts to etch graphene edges so fast that growth is limited).
- Growth time is inversely proportional to the pressure.
- At higher pressure, graphene grains are more hexagonal, while they tend to be dentritic at low pressures. However, high pressure also gives many multilayered regions.
- Using the standard growth method always results in small patches of second layers appearing at the center of the grains. Using a novel 'pulsed growth' method developped in the group [73], we could get rid of them.

1.3.2.2 Transfer to arbitrary substrate

After the growth, graphene can be transferred from the Cu surface to any substrate. The process is explained in Fig.1.16. Two etching solutions have been used in our studies to remove Cu : $Na_2S_2O_8$ and $(NH_4)_2S_2O_8$. These two solution give very different results : $Na_2S_2O_8$ etches Cu faster, but results in significant alteration of the graphene lattice, as we will see later, while $(NH_4)_2S_2O_8$ is slower but less detrimental to electron mobility.

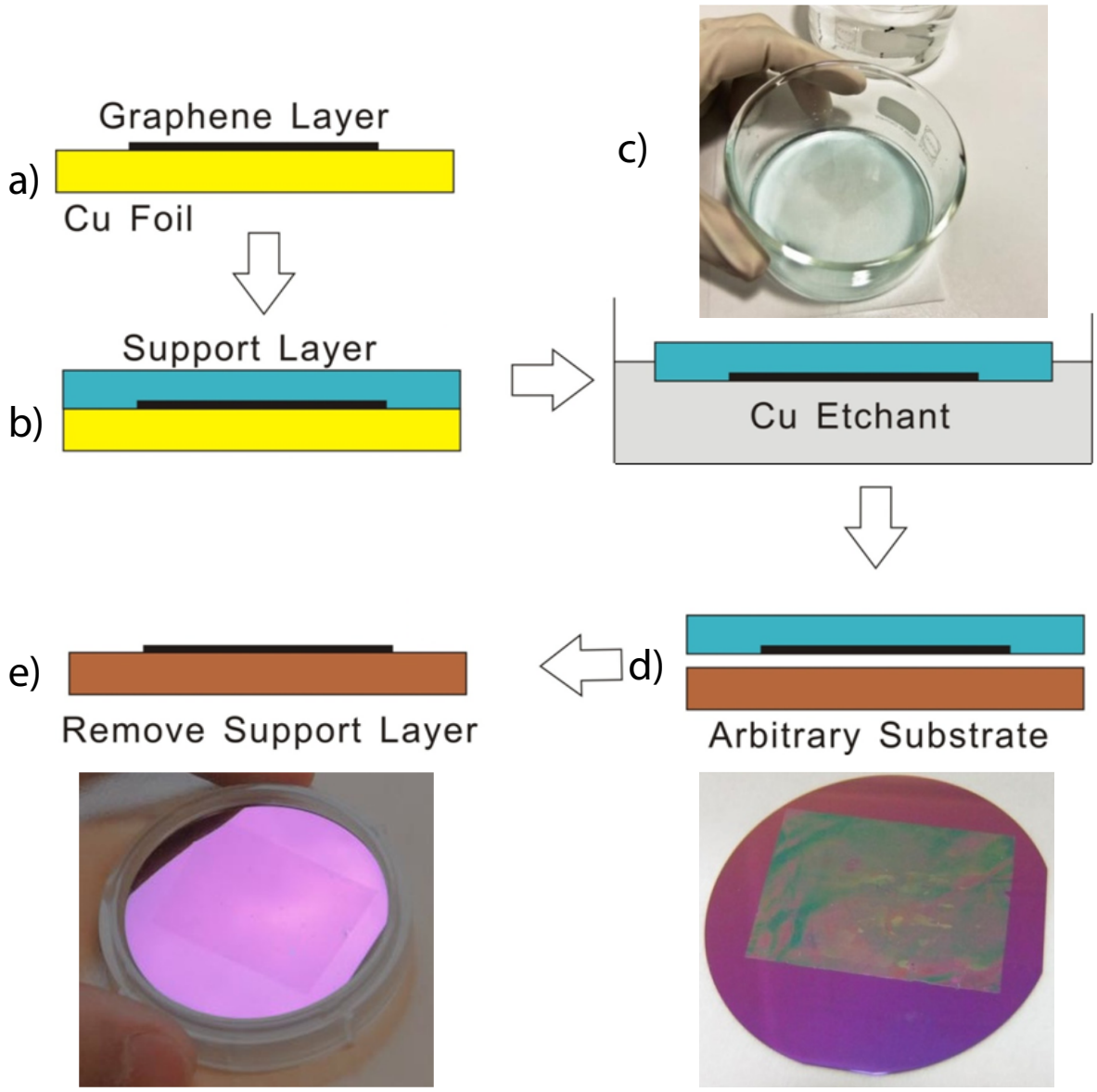

Figure 1.16 – ***Transfer method of Cu-grown CVD graphene onto arbitrary substrate.*** ***a)*** *Graphene on its Cu substrate as it comes after the CVD growth.* ***b)*** *After spin-coating the PMMA support layer.* ***c)*** *The PMMA/graphene/Cu stack is left floating in the Cu etchant, with the Cu face down. Cu is dissolved and PMMA helps maintain the samples afloat and prevents it from balling up. After Cu has been fully removed, transfer to several ($\geq$ 5) successive baths of DI water is necessary to ensure a thorough rinsing of the Cu etchant ions.* ***d)*** *The floating PMMA/graphene is then scooped out with an arbitrary substrate and left to dry on a hot plate for 5 minutes.* ***e)*** *Once all water has dried out, the PMMA is dissolved in acetone.*

1.3.3 Raman spectroscopy and identification of the number of layers

Raman spectroscopy is the study of the phonons, or vibrational modes, of a material, from their interaction with light. It is a very powerful characterization tool, widely used in graphene research. It is non-invasive and relatively easy to set up (as compared to X-ray diffraction for example). When a photon impinges on a material, it excites electrons into virtual, or, if available, into real excited states. The electron then relaxes to the ground state after some time. This elastic process, called Rayleigh scattering, is the dominant process. Sometimes, however, the electron can be scattered by a phonon before it relaxes. It then either loses (Stokes process) or gains (anti-Stokes) energy. The re-emitted photon then has a slightly different color. By measuring the energy spectrum of scattered light one can thus probe the phonon modes energies and their populations. Raman spectroscopy can be technically challenging because the Raman scattering cross section is extremely small compared to elastic scattering. However, when electronic states are available at the laser energy, which is always the case in graphene, the process is called resonant and the Raman intensity can be increased by up to a factor 10^6.

1.3.3.1 Raman setup

A micro-Raman setup is typically composed of a laser, a microscope, a monochromator, a photodiode and a computer. The microscope's objective serves both to focus the incoming laser light onto the surface, and to gather the outcoming light, which is then directed towards the monochromator. The Rayleigh signal, which is orders of magnitude higher than the Raman signal, has to be attenuated using a notch filter. Finally, the photodiode coupled to a monochromator measures the spectrum. Our setup included a piezo-electric sample stage interfaced with the acquisition software, allowing for the precise mapping of Raman bands, with a resolution of 0.3 μm.

1.3.3.2 $\mathbf{q} = 0$ selection rule

Not all phonons can be probed by Raman spectroscopy. Classical conservation rules impose the conservation of energy and momentum :

$$\hbar\omega_s = \hbar\omega_i - \hbar\omega_0 \tag{1.52}$$

$$\hbar\mathbf{k_s} = \hbar\mathbf{k_i} - \hbar\mathbf{q} \tag{1.53}$$

Where ω_i, ω_0 and ω_S are the frequency of the incoming photon, scattering phonon and outgoing photon, respectively, $\mathbf{k_i}$, $\mathbf{k_s}$ and $\mathbf{q}$ are the wavevectors of the photons and phonon, respectively. Since the energy of the phonon is much smaller than that of the photons, $\hbar\omega_0 << \hbar\omega_i$, equation (1.52) becomes $\hbar\omega_s \cong \hbar\omega_i$. This in turn implies that $\hbar\mathbf{k}_s \cong \hbar\mathbf{k}_i$ and $\mathbf{q} \cong 0$.

While typical photon wavevectors are of order 10^7 m^{-1}, the wavevector of phonons can quickly rise to values of the order of 10^{10}. In other words, this condition is equivalent to saying that only phonons of $\mathbf{q} = 0$ can participate in a Raman process. This implies that only optical phonons, which have a finite energy at $\mathbf{q} = 0$, can be probed by this technique.

Two-phonon processes involving a phonon of wavevector $\mathbf{q}$ and another of wavevector $-\mathbf{q}$ also satisfy the conservation rule, as well as processes involving a phonon of wavevector $\mathbf{q}$ and scattering by a lattice defect. Because Raman scattering in graphene is always resonant, the second order processes have a large cross section and are easily visible. This is the case of the 2D band for example.

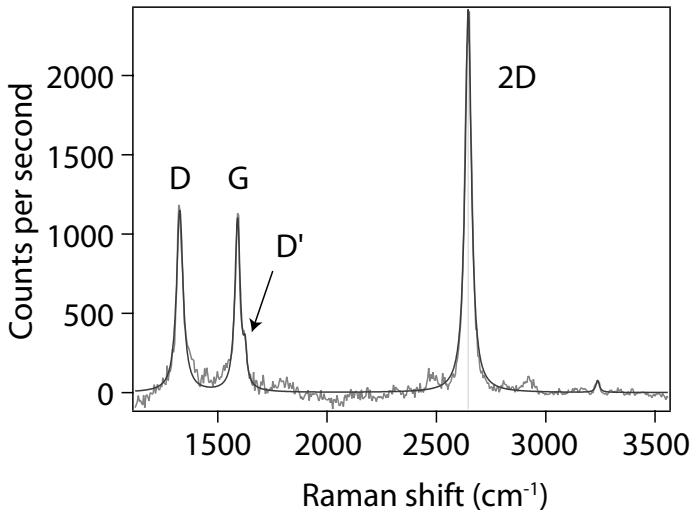

Figure 1.17 – *Raman spectra of disordered graphene showing the D, D', G and 2D bands characteristic of graphitic systems.*

Fig.1.17 shows a typical spectrum obtained on disordered monolayer graphene. A rich literature is dedicated to the study of the many Raman modes of sp^2 carbon allotropes, but here we will restrict ourselves to the three modes that are most comonly used in characterizing graphene. The following bands can be identified :

The G band ($\cong$ 1580 cm^{-1}) is common to all sp^2 carbon allotropes. Fig.1.18 shows the phonon mode which is associated to it.

This mode's energy is insensitive to the laser energy, but anything affecting the C-C bond, such as strain [74], electrostatic doping [75, 76], or temperature [77], will influence it.

The intensity of the G band is directly proportional to the number of graphene layers (up to about 10 layers) [78].

The D band ($\cong$ 1350 cm^{-1}) corresponds to the breathing mode of the aromatic rings.

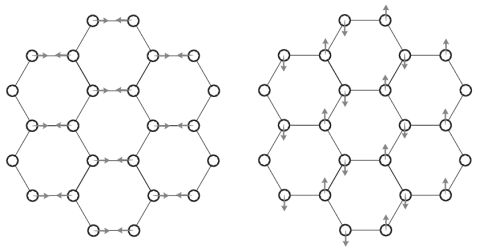

Figure 1.18 – *Phonon modes associated with the G band in carbon sp^2 allotropes. It is degenerate at $\boldsymbol{q} = 0$.*

There are no phonon modes at this energy satisfying the $\mathbf{q} = 0$ selectrion rule, which is why this mode is normally not seen in pure graphene (for example it doesn't appear on the spectrum of exfoliated graphene Fig.1.21b). However, this mode can become apparent owing to second order processes involving scattering on lattice defects with momentum $\mathbf{K}$ (see Fig.1.19).

Tuinstra and Koenig [79] (1970) identified this peak and showed that the ratio of intensity of the modes D and G can be related to the size of graphite nanocrystals L_D by the law : $I_D/I_G \propto 1/L_D^2$. This empirical law has been refined since [80] :

$$L_D^2(\mathrm{nm}^2) = 1.8 \times 10^{-9} \lambda_L^4 \frac{I_G}{I_D} \tag{1.54}$$

Where λ_L is the laser wavelength in nanometers. This observation highlights the role of scattering by lattice edges in this Raman process. Recently, more quantitative studies on graphene with controlled defect density has led to a refined version of the Tuinstra-Koenig law [80] (see Fig.1.20).

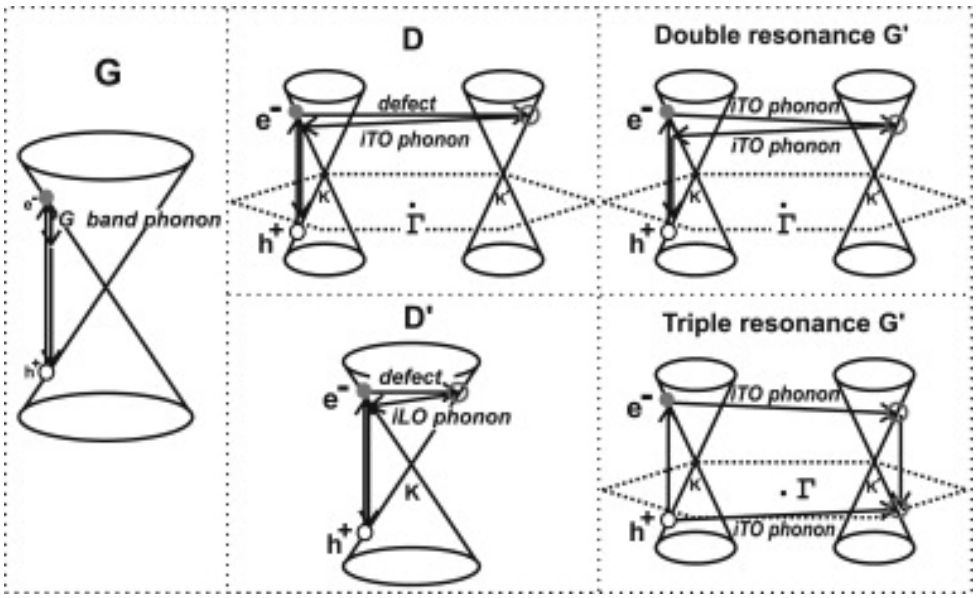

Figure 1.19 – *Scattering processes involved in the different Raman peaks of graphene. Here the 2D band is called G'. Taken from Ref. [81]*

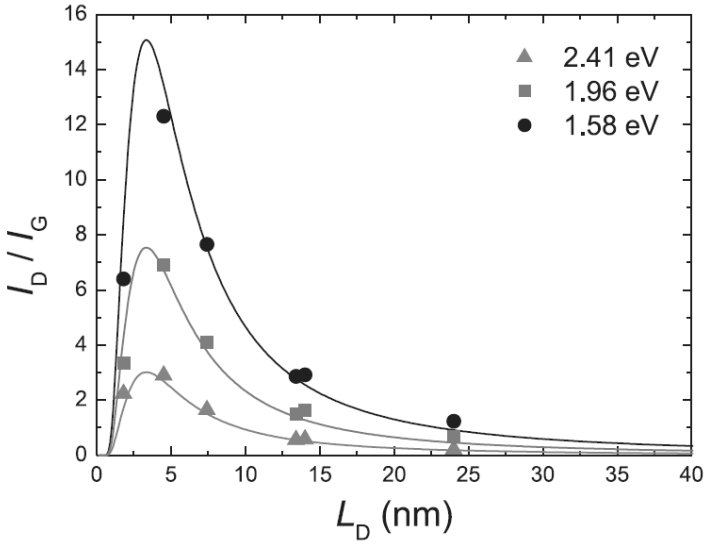

Figure 1.20 – *Ratio I_D / I_G of the Raman peaks intensities as a function of inverse defect density for different laser excitation. The continuous lines are fit to the model of [80]. Equation 1.54 is valid on the right of the maximum (for large L_D). Taken from [80].*

The D′ band ($\cong$ 1600 $\mathbf{cm^{-1}}$) arises from similar processes as those involved in the D band, but for smaller q vectors. It is associated with defects inducing intravalley scattering (see Fig.1.19).

The 2D (also called G′) band ($\cong$ 2650 $\mathbf{cm^{-1}}$) results from the double and triple resonance processes depicted in Fig.1.19 and is sensitive to the number of layers.

In monolayer graphene, because of the symmetry between the valence and conduction bands, the 2D band consists of a single lorentzian. On the other hand, bilayer graphene has not one, but two conduction bands (and two valence bands). Therefore, there are four resonant transitions involving real electronic states, which involve four phonons that give rise to four lorentzians. The same reasoning applies to trilayer, quadrilayer and multilayer graphene. By comparing the lineshape of the 2D bands (Fig.1.21c and d) to the expected shapes given by the literature [81] (Fig.1.21e), one can determine the number of layers with good confidence.

Note that this identification method is only valid if the graphene is Bernal stacked, as is the case for natural or HOPG graphite and the flakes exfoliated from them. In the case of turbostratic stacking (when the layers are randomly oriented on top of each other), electronic coupling between graphene planes is weak and they behave like as many independent monolayers, making this identification technique worthless. CVD graphene notably gives tubrostratic graphene.

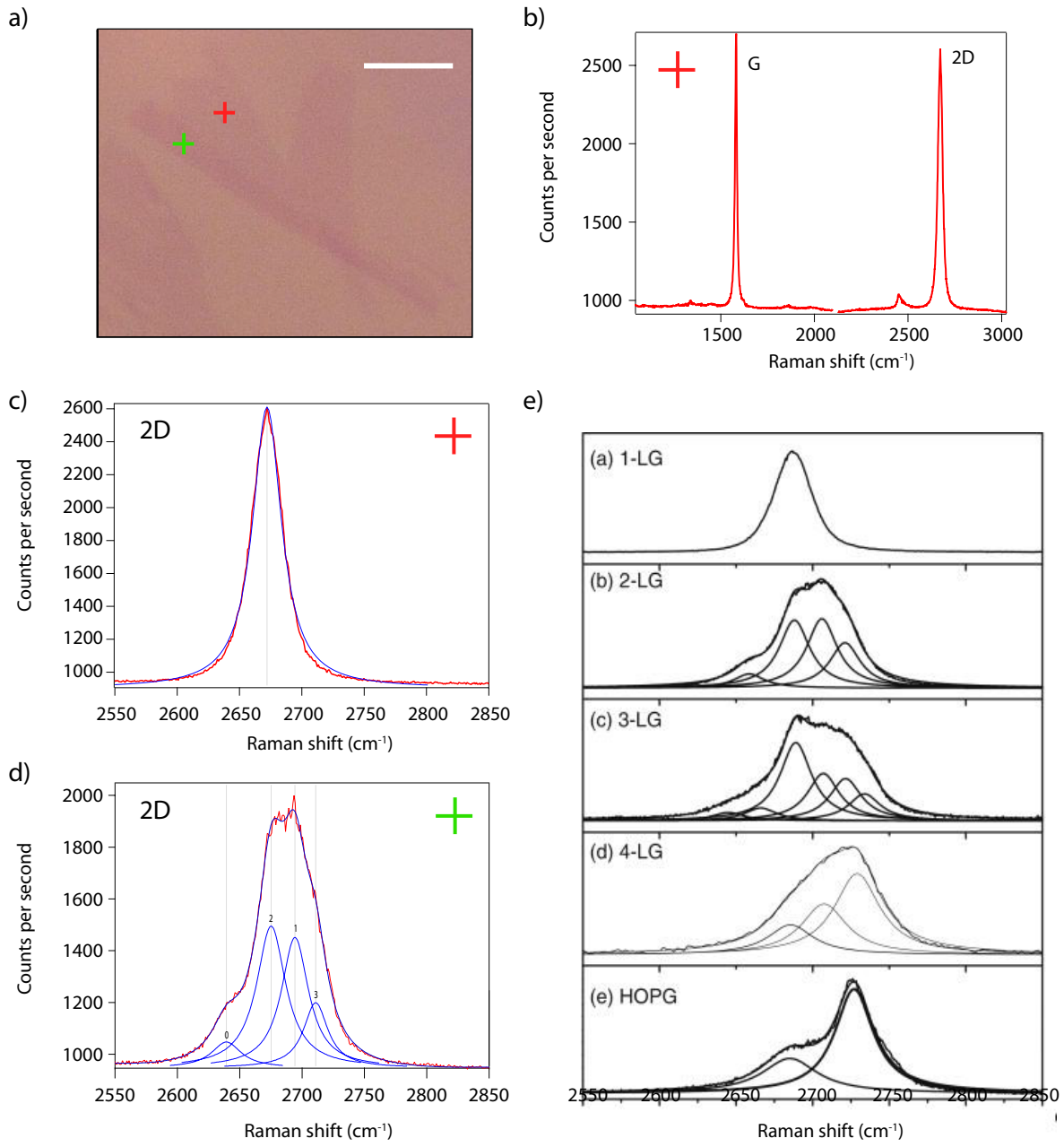

Figure 1.21 – ***Identification of mono- and bi-layer graphene by Raman spectroscopy. Comparison between our spectrum (b, c and d) and the expected lineshape found in the literature (e). a)*** *Optical image of a graphene flake showing two terraces with quantized contrasts. Scale bar is 10 µm.* ***b)*** *Raman spectrum taken on the shallow part of the flake, where it is expected to be thinner (red cross in a), using a green laser ($\lambda = 514$ nm). This is the full spectrum, showing both the G and the 2D band.* ***c)*** *Detailed view of the 2D band for the spectrum taken on the red cross in a. The blue line is a lorentzian fit.* ***d)*** *Detailed view of the 2D band for the spectrum taken on the green cross in a. The broader peak can be fit by four lorentzians.* ***e)*** *Expected lineshapes for the Raman 2D band of monolayer (1-LG), bilayer (2-LG), trilayer (3-LG), quadrilayer (4-LG) graphene and HOPG. Taken from [81].*

1.3.4 Fabrication of electrical devices

Depending on our aim and on the kind of graphene we are using, several lithography techniques are available to contact graphene. For exfoliated graphene, electron beam lithography (EBL) is mandatory, as this technique allows very precise alignment on the small, randomly-placed flakes. For the batch fabrication of micron-scale devices using CVD graphene, we have designed a UV mask. Finally, CVD graphene also allows the fabrication of centimeter-scale devices. For that, a stencil mask was used.

1.3.4.1 E-beam lithography

The resist recipe used for the EBL was a standard one, developped by the Nanofab team in charge of the clean room :

- PMMA 4%.
- Spinning at 4000 rpm with 2000 rpm/s acceleration, for 60s.
- Baking for 5 minutes at 180°C.

This recipe yields a resolution of about 10 nm, with which one can easily design devices as short as 100 nm. The fabricated samples did not require much precision, as they were typically a few microns in length and width, with 1 μm wide electrodes. Therefore, we alternatively used a soft baking at 115°C for 15 minutes, which degrades the resolution, but allows for an easier lift-off.

Alignment method using scratches in the PMMA. Graphene cannot be seen by the scanning electron microscope (SEM) through the PMMA resist, hence some landmark is required for alignment. The usual way around this is to pre-pattern the wafers with regularly spaced metallic markers. Each graphene flake can then be located with respect to the nearest markers. However, this technique has its drawbacks : it involves an additional lithography step, which requires a dedicated UV mask, but more importantly it might contaminate the substrate with resist residues.

In order to exfoliate graphene on a perfectly clean substrate without markers and still be able to find it, we have used an alternative technique, which was taught to the group by Çağlar Girit (now in the Quantronics group in Saclay), the 'PMMA scratches technique'. Fig.1.22 illustrates the process. After exfoliation, pictures of the flake at different magnifications were taken before the resist was spun. After spinning, we took the sample to the probe station, where a powerful optical zoom allowed us to look at the details of the surface. By looking at the graphite flakes, we could locate approximately where the monolayer flake of interest was, and using the tips of the probe station, we scratched PMMA around it, creating four markers, very visible in the SEM, onto which we could align.

Using this method we can get a precision in the alignment on the order of 200 nm.

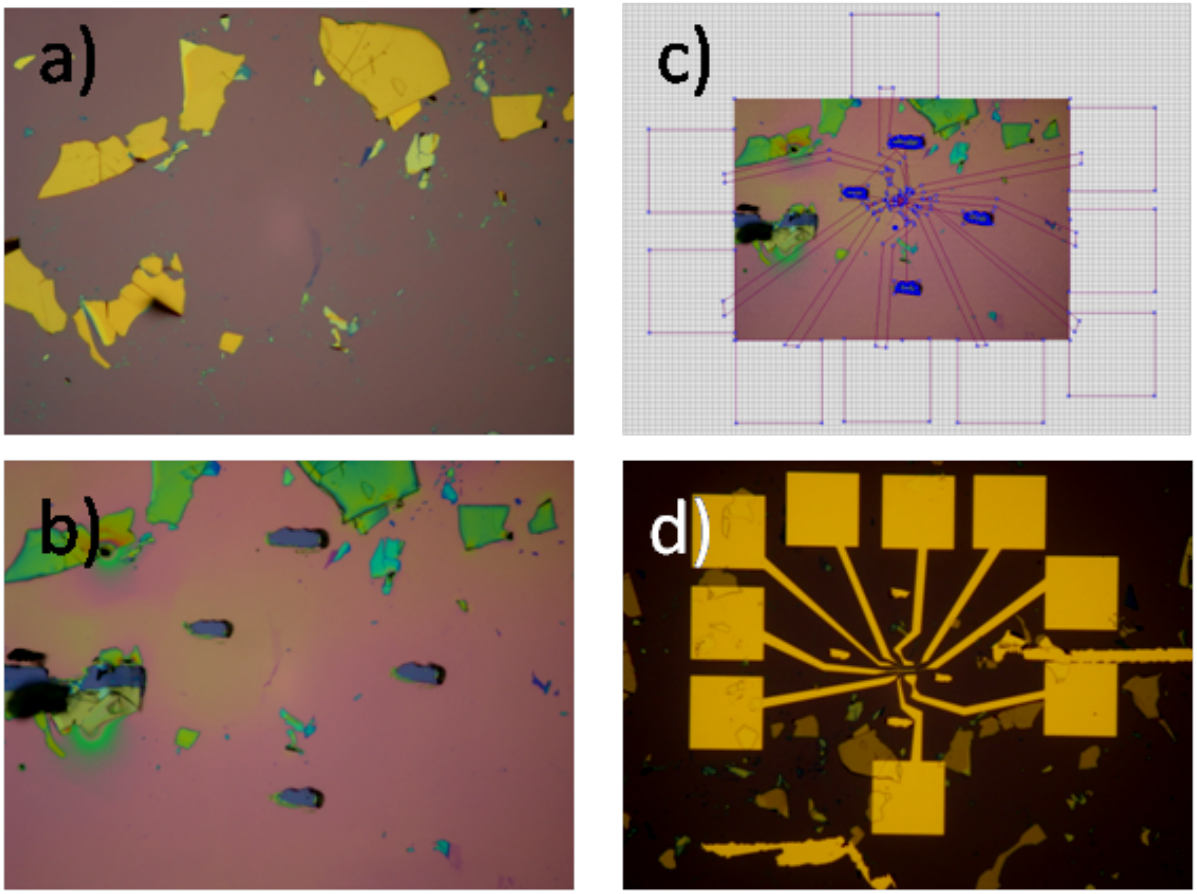

Figure 1.22 – ***Alignment using scratches.*** ***a)*** *A graphene flake is located on the surface of the wafer.* ***b)*** *After spin coating PMMA, the sample is located again in the probe station, and scratches are made nearby using the contact probes.* ***c)*** *The electrodes design includes the scratches as alignment marks. Superimposing the design on top of the SEM image during the alignment procedure helps correct the position.* ***d)*** *The same sample after lift-off.*

1.3.4.2 UV lithography

A set of two UV masks was designed to prepare large batches of CVD graphene-based samples. The masks consist of two layers that can be aligned with respect to each other using alignment marks :

- A layer for graphene stripes of various widths.
- A layer for electrodes with various spacings

Using this we could make many samples with widths and lengths ranging from 0.5 to 5 μm. An example of such devices is shown in Fig.1.23(a and b).

1.3.4.3 Fabrication of centimeter-size devices with stencil masks

For the fabrication of centimeter-scale devices, a set of stencil masks were fabricated. They consist only of a piece of aluminum in which slits have been cut (Fig.1.23c). To adjust to the various sizes of the different samples, scotch tape was used to reduce the slits' sizes. The mask is maintained against the sample surface while the metallic electrodes are evaporated. This technique involves very few steps and allows quick and easy fabrication of devices (Fig.1.23d). The difficulty with such samples lies elsewhere : when the size of graphene is increased, the probability that it covers a pinhole in the gate dielectric becomes large. Therefore, we were very often confronted with problems of gate leakage. A possible workaround is to anneal the substrates in an oven at 500°C under H_2 flow prior to graphene transfer.

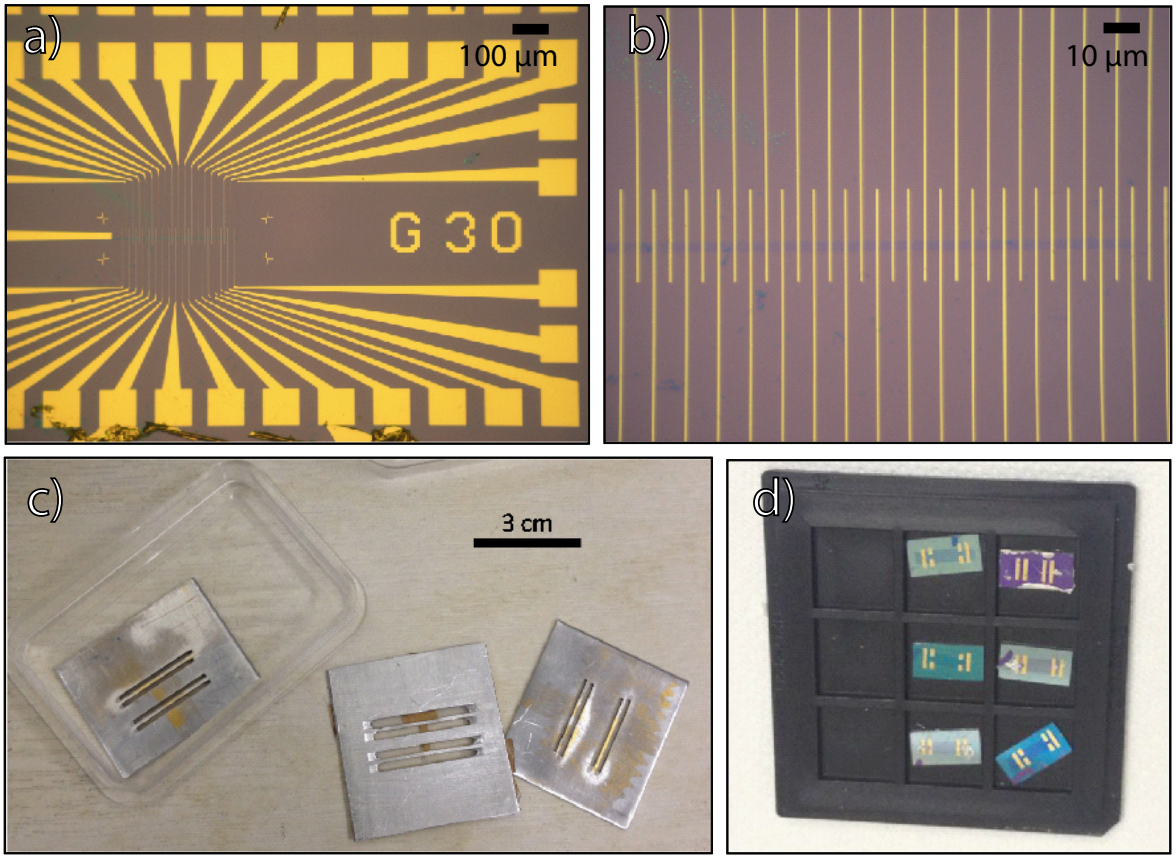

Figure 1.23 – ***Two methods to fabricate samples with CVD graphene. a) and b)*** *Using a set of two UV masks, one to pattern graphene into ribbons, the other to make electrodes.* ***c) and d)*** *Using home-made stencil masks to fabricate centimeter-scale samples.*

1.4 Inducing a controllable amount of disorder in graphene : Raman and transport studies

Several solutions have been tested for the removal of the Cu substrate during the tranfer of CVD-grown graphene (see Fig.1.16). The etchant normally used to fabricate good quality devices is $(NH_4)_2S_2O_8$. We have used $Na_2S_2O_8$ for some time before realizing it was actually degrading graphene's quality. As can be seen in Fig.1.24, the sheet resistivity and Raman D band increase steadily with etchant exposure time. This indicates significant damage to the graphene's crystalline integrity. The nature of the defects induced by $Na_2S_2O_8$ certainly deserves a thorough investigation using elemental analysis and local probes, but such a study is beyond the scope of this manuscript. A preliminary Raman and transport study has been carried out, though, that already sheds light on them.

1.4.1 Lattice defects in graphene

Lattice defects that induce a D band in graphene and sp^2 carbon allotropes can be of the following types [82] : grain boundaries, substitutional atoms, atomic vacancies and sp^3 defects. These defects have a common Raman signature because they disrupt the graphene lattice and can scatter electrons from one valley to the other. In doing so, they allow the second-order Raman processes involving large-wavevector phonons and scattering on a lattice defect, which gives rise to a D and a D' bands in the Raman spectrum (see Fig.1.19). They also restore weak localization by introducing a lot of intervalley scattering, which washes out the effect of chirality of charge carriers.

The goal here is not to give a complete review of defects in graphene, but rather to assess what is the effect of $Na_2S_2O_8$. Therefore, we can already rule out a few of the above-mentioned options. Substitutional defects are atoms such as B and N that occasionally replace a C atom. These defects are usually considered to be growth-related. Moreover, substitutional defects are supposed to induce a shift in the Raman G band, which we did not observe. Grain boundaries are also irrelevant here, as grain boundaries pre-exist in the sample exposed to $Na_2S_2O_8$. That leaves sp^3 defects and vacancies as possible candidates.

Randomly placed adatoms can be covalently attached to the carbon lattice. This perturbs the electronic band structure of graphene, as the π electrons are being removed from the conduction band to participate in the chemical bond. This kind of defect is called sp^3. It comes in different flavors : graphene oxide (GO), hydrogenated graphene (called graph**a**ne), and fluorinated graphene (graFene). Graph**a**ne and graFene derivatives can be created by exposing graphene to plasma. GO can be either exfoliated from oxidized graphite and partially reduced into graphene, or cre-

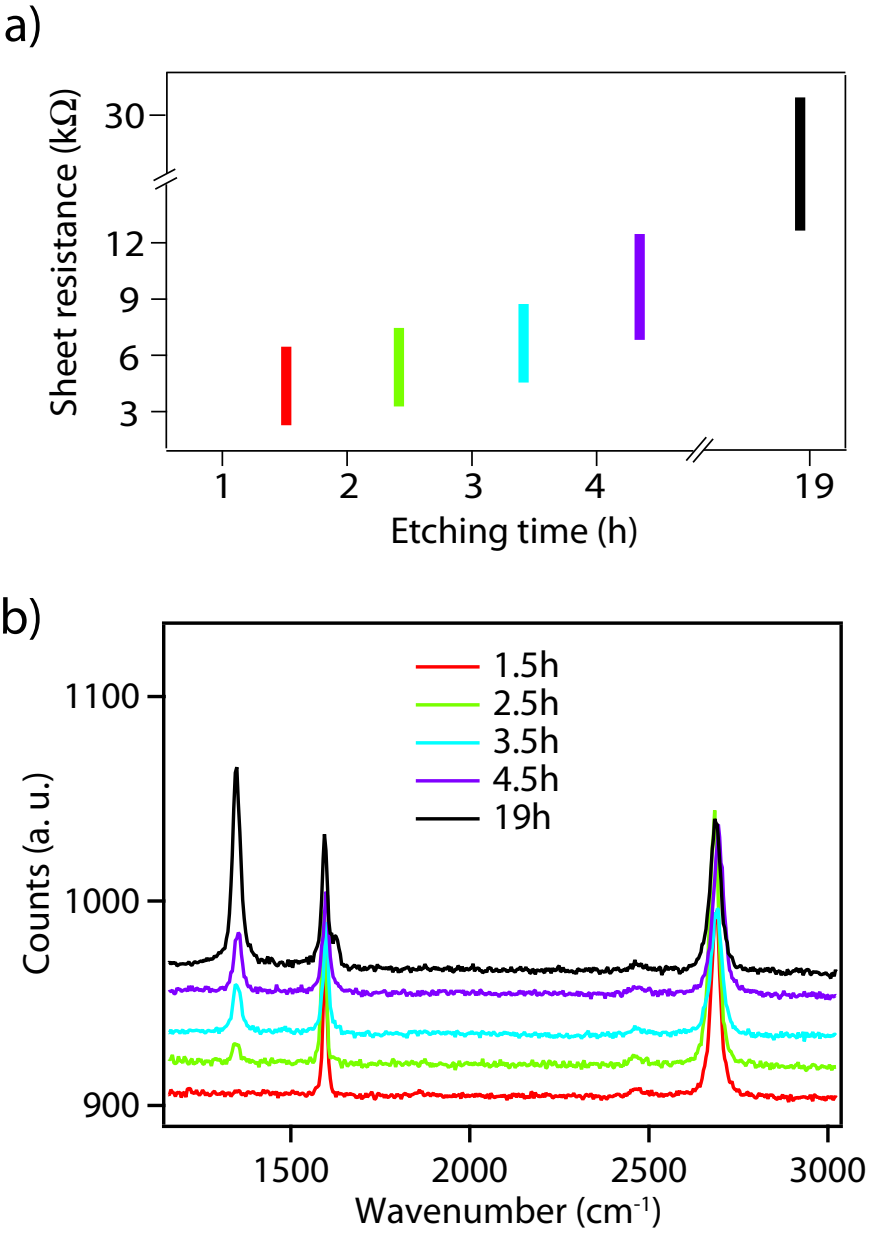

Figure 1.24 – ***Characterization of the effect of prolounged exposure to the Cu etchant $Na_2S_2O_8$.*** ***a)*** *Range of sheet resistivities explored within $V_g = V_D \pm 20$ V as a function of exposure time.* ***b)*** *Raman spectra (green laser) after different times spent in the solution, showing the emergence of a large D band.*

ated using oxygen or ozone plasma. Atomic vacancies can be artificially created in the carbon lattice by bombarding it with Ar^+ or Ga^+ ions.

1.4.2 Raman characterization of the defect density and type of defects

From the ratio between D and G bands in Fig.1.24b, we can estimate the size of crystalline domains using the law of Tuinstra and Koenig [79, 80] (equation 1.54). For the sample that spent 19 h in the solution, the ratio $I_D/I_G = 1.5$ gives a domain size of about $L_D = 3.2$ nm. The same sample shows a resistivity of about 12 kΩ at $V_g = +20$ V. Using Einstein's relation (equation 1.24) we find a mean free path of about $l_e \cong 4.5$ nm. Although this is a crude approximation, these two values are in good agreement. More quantitative analysis is currently being carried out.

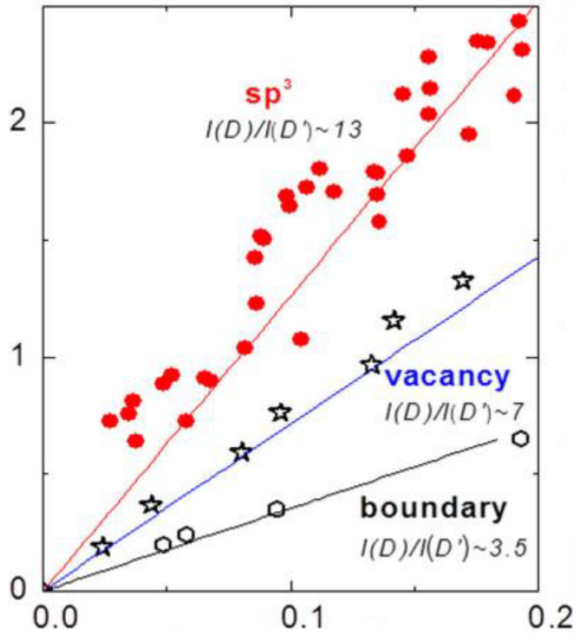

Figure 1.25 – *Ratio of the Raman intensities of the D and D' bands in intentionally defected graphene with sp^3 and vacancies defect, and graphite with grain boundaries. Taken from [83].*

Eckmann *et al.* [83] have compared the ratio between the D and the D' band for different kinds of lattice defects, namely sp^3 defects and vacancies induced by ion bombardment. They found a correlation between the nature of defects and the Raman intensities ratio $I_D/I_{D'}$. For sp^3 defects it seems to fall around $I_D/I_{D'} = 13$, and for the case of vacancies it is closer to $I_D/I_{D'} = 7$ (see Fig.1.25).

We have performed a similar study on our disordered graphene sheet and found that the ratio was systematically higher than 13 (see Fig.1.26). Even on the wrinkles (introduced during the cooldown process due to the thermal expansion coefficient mismatch between Cu and graphene), this ratio is still high (see blue and green spectra on Fig.1.26), indicating that sp^3 defects are the dominant source of scattering.

Therefore we can understand the increased resistivity observed in Fig.1.24 as stemming from short-range scattering on chemically-induced crystalline defects due to the covalent grafting of incoming species. $Na_2S_2O_8$ is more acidic than $(NH_4)_2S_2O_8$, whose counter ion NH_3^+ counteract the acid persulfate. Although not fully characterized yet, our method seems less agressive than the plasma usually used to covalently graft atoms, since no knock-on damage is expected in our case.

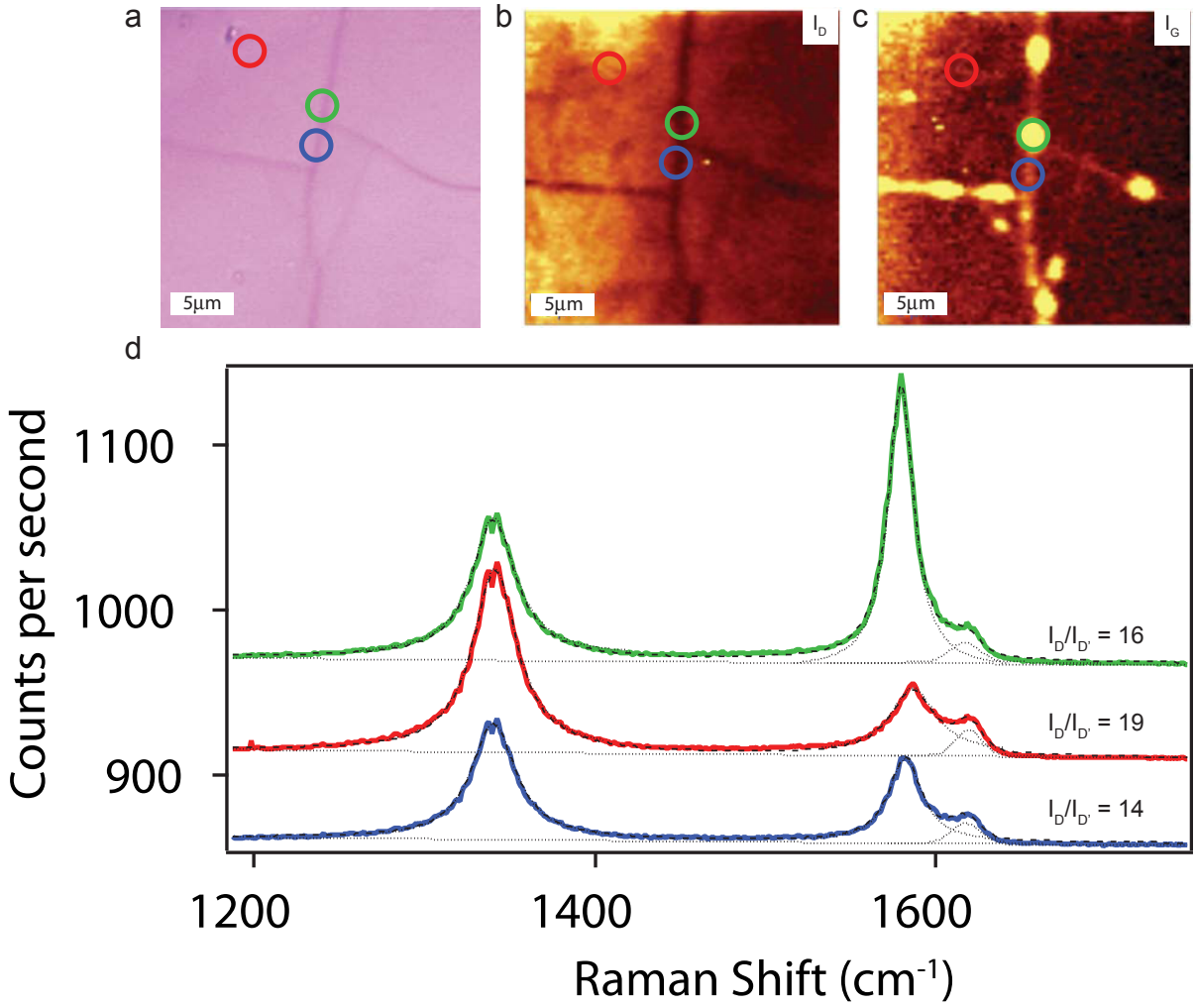

Figure 1.26 – ***Ratio of the Raman D and D′ bands.*** ***a)*** *Optical microscope image.* ***b)*** *Raman mapping of the D band.* ***c)*** *Raman mapping of the G band.* ***d)*** *Spectra obtained in the three positions depicted by the three circles in a, b and c.*

This new way of producing disordered graphene turned out to be very useful, as it allows us to controllably engineer the range of resistivity values accessible by changing the gate voltage. In the next sections, a preliminary study of the low-temperature transport properties of this new kind of disordered graphene will be shown, with special emphasis on the strong localization regime.

1.4.3 Transport properties of microscopic disordered graphene

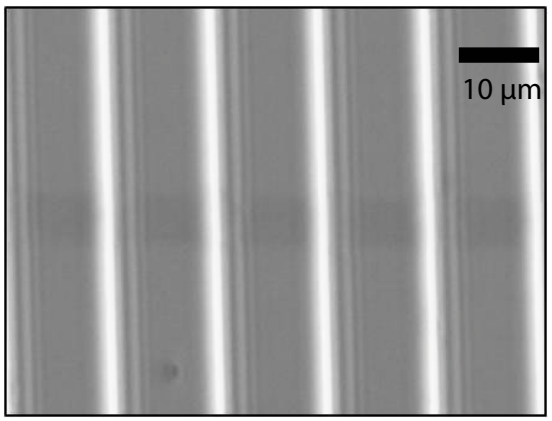

Figure 1.27 – *Optical microscope image of the samples studied in this section.*

In this section, the low temperature transport properties of CVD-grown graphene samples treated with $Na_2S_2O_8$ and patterned into micro-ribbons using a UV mask will be discussed. Different samples will be compared, characterized by their degree of disorder, which can be quantified by the dimensionless resistivity at room temperature. Clean graphene exhibits a maximum sheet resistivity of the order of $\frac{e^2}{4h}$ at room temperature, while the more disordered sample can go beyond this value. We will see that, at low temperatures, these samples exhibit a transport gap centered at the Fermi energy and a variable range hopping (VRH) dependence on temperature of the Efros-Shklovskii kind.

1.4.3.1 Room temperature electric field effect curves of samples with various levels of disorder

Fig.1.28 shows the field effect curves of two graphene field effect transitors made with CVD graphene : one has had the Cu substrate removed using the 'good' etchant $(NH_4)_2S_2O_8$ and is clean (in blue), and the other using the 'bad' etchant $Na_2S_2O_8$ and is disordered (in red). These two curves were measured at room temperature and under vacuum, using an AC current bias excitation and lock-in detection, and in a four probes geometry, so that contact resistance can be ruled out.

The curves were fitted using equation (1.21) to extract the electronic mobility μ and residual carrier density n_0. In fitting the red curve (disordered graphene), the only way to get a working fit was to add a contact resistance R_c to account for the upshift in the resistivity. Off course since this is a 4-probe measurement, there is no contact resistance involved. Instead, we can assume that scattering by short-range neutral lattice defects gives a carrier density-independent contribution to the resistivity in a way similar to a contact resistance. Following [40, 44, 84], one can write :

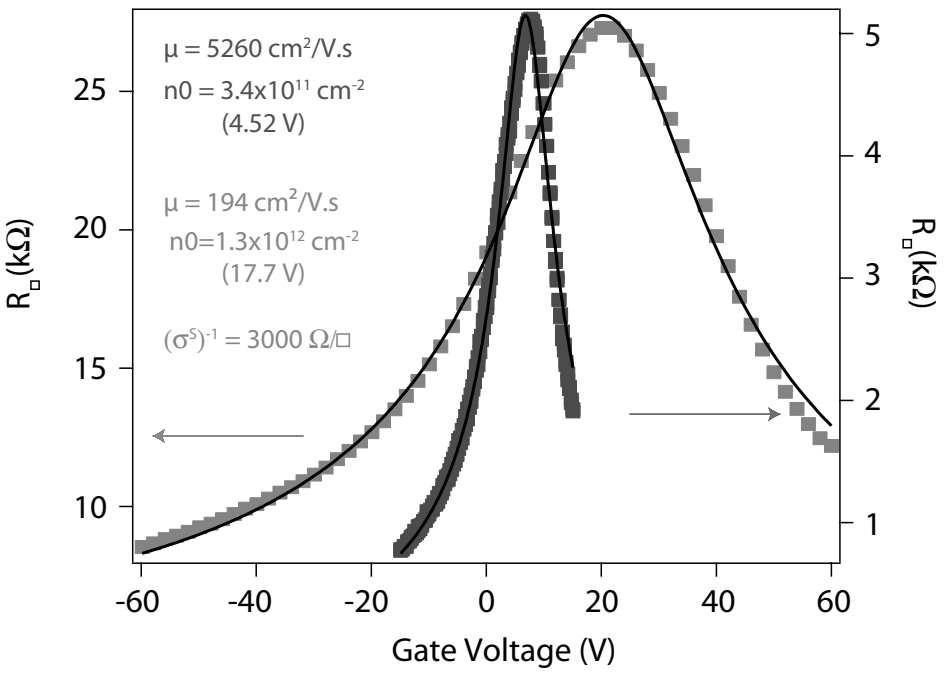

Figure 1.28 – *Field effect curves (sheet resistance as a function of back-gate voltage) at room temperature for two CVD graphene samples.* ***Blue points*** *: Clean sample. The Cu substrate has been etched with $NH_4S_2O_8$.* ***Red points*** *: disordered sample which has spend time in the $Na_2S_2O_8$ solution.* ***Black lines*** *: are fits to equation (1.21). The values of the fitting parameters are indicated.*

$$\sigma^{-1} = ((n - n_0)e\mu)^{-1} + (\sigma^S)^{-1} \tag{1.55}$$

Where n is the carrier density induced by the gate voltage, n_0 is the residual charge carrier density near the Dirac point (rms density of electron and hole puddles) and $\sigma_s \propto n_{imp}$ is the contribution from short-range scatterers, proportional to their density.

The fact that short-range scatterers introduce a constant resistance is controversial [46], and our limited knowledge of the nature of the induced defects does not allow us to estimate their density from this measurement. Along with the moblity, the residual carrier density near $V_g = V_D$ (as measured by the Dirac peak width) is also indicated.

In the clean CVD-grown sample, the higher mobility with respect to the disordered CVD sample, is correlated with a narrower Dirac peak. This indicates that $Na_2S_2O_8$ *also* introduces charged impurities, the effect of which is both to reduce the mobility and increase the charge inhomogeneity. As a matter of fact, we observed a steady shift of the Dirac point position towards the right upon increasing the exposure time (not documented here). Charge inhomogeneities also increased, giving an ever broader Dirac peak.

In conclusion, it seems that both the neutral short-range **and** charged-impurity scattering are significantly enhanced by the exposure to $Na_2S_2O_8$. We note that this is not incompatible with the presence of sp^3 defect, which are most likely charged,

inducing both types of scattering at the same time. A more quantitative study is needeed to draw any conclusion on that matter.

1.4.3.2 Weak localization between 300 K and 4 K

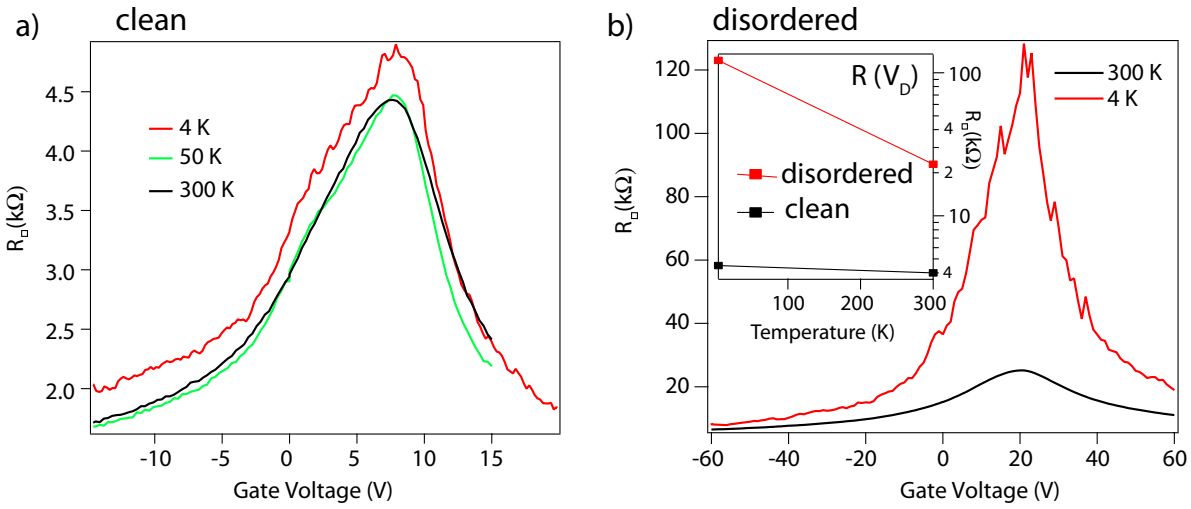

Figure 1.29 – ***Absence of weak localization in clean graphene, as opposed to disordered one. Field effect curves at various temperature.*** ***a)*** *For clean graphene (same sample as the blue curve in Fig.1.28).* ***b)*** *For disordered graphene (red curve in Fig.1.28).* ***Inset*** *: Evolution of the resistivity maximum between room temperature and 4 K for clean and disordered graphene.*

Fig.1.29 shows the evolution in temperature in the clean and disordered samples from Fig.1.28. We can see that the clean sample Fig.1.29a exhibits only a small correction to its conductivity at 4 K, which is a signature of graphene with a low intervalley scattering rate. On the other hand, the disordered sample Fig.1.29b shows a divergent resistivity, especially near the Dirac point.

Fig.1.30 shows the temperature dependence of another CVD graphene treated with $Na_2S_2O_8$, but exhibiting a rather low room temperature resistivity in the range 2.5 kΩ - 8 kΩ and a wide Dirac peak ($\cong$ 20 V), indicating mild disorder (intermediate case between the blue and the red curve in Fig.1.28). As the temperature is reduced, we can see that the resistivity increases logarithmically, indicating the occurence of weak localization in the sample.

Here, we see that the rate of conductivity change $d\sigma/d(\ln T) \approx 20.5\ \mu\text{S.ln(K)}^{-1}$ is independent of gate voltage (the right and left vertical scales in Fig.1.30b are only offset by a constant). This is in rather good agreement with equation (1.28) for a normal 2DEG with no effect of chirality of the charge carriers :

$$\frac{d\sigma}{d(\ln T)} = \frac{d\delta\sigma}{d(\ln T)} = \frac{e^2}{\pi^2\hbar} = 26\mu\text{S.}\ln\left(\text{K}\right)^{-1} \tag{1.56}$$

This temperature dependence indicates that our disordered CVD graphene presents a significant amount of atomically sharp defects, which restore the weak

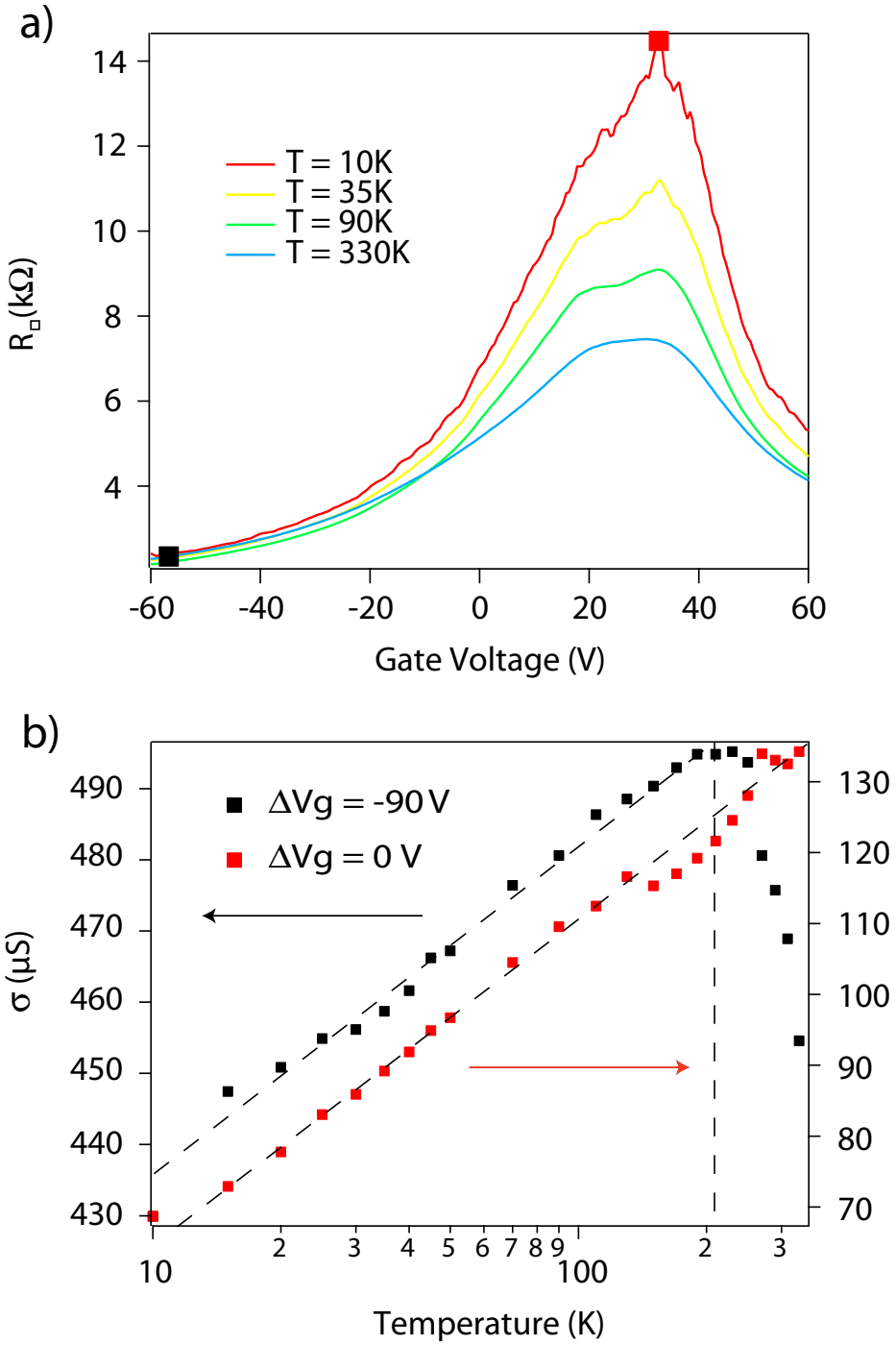

Figure 1.30 – ***Temperature dependence of a weakly disordered CVD graphene FET. a)*** *Sheet resistivity versus gate voltage at different temperatures.* ***b)*** *Conductivity plotted versus temperature for 2 gate voltages indicated in plot a). The logarithmic dependence on temperature is outlined. At high temperature, a region of enhanced conductivity due to reduced phonon scattering is identified in the high doping region.*

localization normally absent in graphene. In order to study the strong localization regime at lower temperatures, we need to use a different sample, however, so that the crossover is within reach of the experimental apparatus (the minimum temperature attainable is 30 mK). In the next section, we will study the disordered sample shown in Fig.1.29b and in red in Fig.1.28.

1.4.3.3 Strong localization near the Dirac point in disordered CVD graphene

This disordered sample has a room temperature sheet resistance close to $R_Q = h/e^2$ (red curve in Fig.1.28), indicating that the sample is near the localization crossover. We will study the characteristic of the strongly localized regime. The sample's dimensions are $L \times W = 2.8\ \mu\text{m} \times 1.6\ \mu\text{m}$.

Remarks concerning the measurement of insulators

Characterizing an insulator is not as straightforward as measuring the resistance of a metal. First of all, because the resistance becomes very large, the current-biased scheme we have used so far is no longer relevant. Just like the current source mode is the natural way to measure superconductors, which will always have an impedance lower than the internal impedance of the voltage source, the voltage source mode is the natural way to measure insulators. This is why we measure insulators by biasing the sample in a 2-probes, voltage-biased geometry, using an AC+DC voltage bias and a current amplifier.

Moreover, because the I(V) characteristics of insulators are highly non-linear, proper characterization requires the measurement of the full I(V) curve. The differencial resistance is strongly dependent on the excitation amplitude, and we have to make sure that our excitation level is low enough to lie within the gapped region. Using tiny voltage excitations, noise becomes a predominant issue, and care must be taken to shield the system properly, shorten the wires to the maximum, and use the full potential of the lock-in detection.

Finally, at very high impedances, lock-in detection suffers from the high intrinsic RC constant of the electrical circuit, which makes it necessary to work at ever lower frequencies. For our large CVD samples (several mm^2 in area), the capacitive coupling to the back-gate ground plane is so big that above typically $R > 10\ \text{M}\Omega$, we have no choice but to work in DC. This way resistances as high as $10\ \text{G}\Omega$ can be measured.

The insulating state near the Dirac point ($V_g = 16$ V) was characterized down to 60 mK by recording the I(V) characteristics with an AC excitation voltage of 100 μV.

What we can see on Fig.1.31 is that, after a monotonous decrease, the differential conductivity starts to exhibit a strongly non-linear and non-monotonic behavior. While the high-bias part saturates and goes up slightly, the zero-bias region starts to dive quickly. The gap appears around zero bias near 1 K and from the crossing points between the lowest curve and the curve at 1.2 K, where high-bias conductivity is minimum, we can define the gap width $2\Delta = 1.7$ meV. Even though a systematic study on samples of different lengths hasn't been carried out, we can rule out the possibility that this gap originates in a Schottky barrier [85] or in the band structure. If this was the case, the gap would appear as the thermal energy decreases below the gap value. Here, there is a clear mismatch between the gap energy and the thermal energy : $T_\Delta = \Delta/k_B \cong 10$ K$>> T_{cross} \cong 0.7$ K. Instead, this gap is probably indicative of strong Coulomb interactions that renomalize the density of states near the Fermi level.

Taking the differential resistance at the bottom of the gap for each temperature, one can try to analyse the hopping mechanism at play. Plotting the log of the resistance against $T^{\frac{1}{2}}$ or $T^{\frac{1}{3}}$ does not allow us to differentiate between Mott and E-S, as in both case we see straight lines with a kink (Fig.1.32 shows it for E-S). The kink indicates that a crossover takes place around $T_{cross} = 0.7$ K, which corresponds to the appearance of the dip in the differential conductance. This probably means that the crossover happens between a regime of Mott VRH (equation 1.44) to a regime of E-S VRH (equation 1.50). This hypothesis is in line with the fact that E-S regimes are usually observed at lower temperature, and give a stiffer divergence of the resistance. Moreover, the fitting function shown in Fig.1.32 for the lower temperatures part crosses the resistance axis near the quantum of resistance, which means there is a good agreement with the prefactor in equation (1.50). This fact is a hallmark of the E-S regime [55, 86].

Now that we have some indications that there is a transition from Mott VRH to E-S with lowering temperatures, we can try to deduce the localization lengths and see if it holds. Between 10 K and $1.2 - 0.7$ K , we can fit the points using equation (1.44) for the Mott VRH mechanism, and we find an activation temperature of $T_0^{Mott} = 12.1$ K. Then, we have to assess the density of states. Following the procedure used in [87], we assume that the graphene has an average residual carrier density of $n_0 = 2.10^{16}$ m^{-2}, which gives us the Fermi energy $E_F = \hbar v_F \sqrt{\pi n_0}$. Using equation (1.11), we arrive at the density of states $\rho(E_F) = 1.5 \times 10^{36}$ J^{-1}.m^{-2}. Finally, using equation (1.45) we arrive at :

$$\xi_{loc}^{Mott} = 109 \text{ nm} \tag{1.57}$$

Using equation (1.43), we find the following hopping length :

$$d = 70 \text{ nm} \tag{1.58}$$

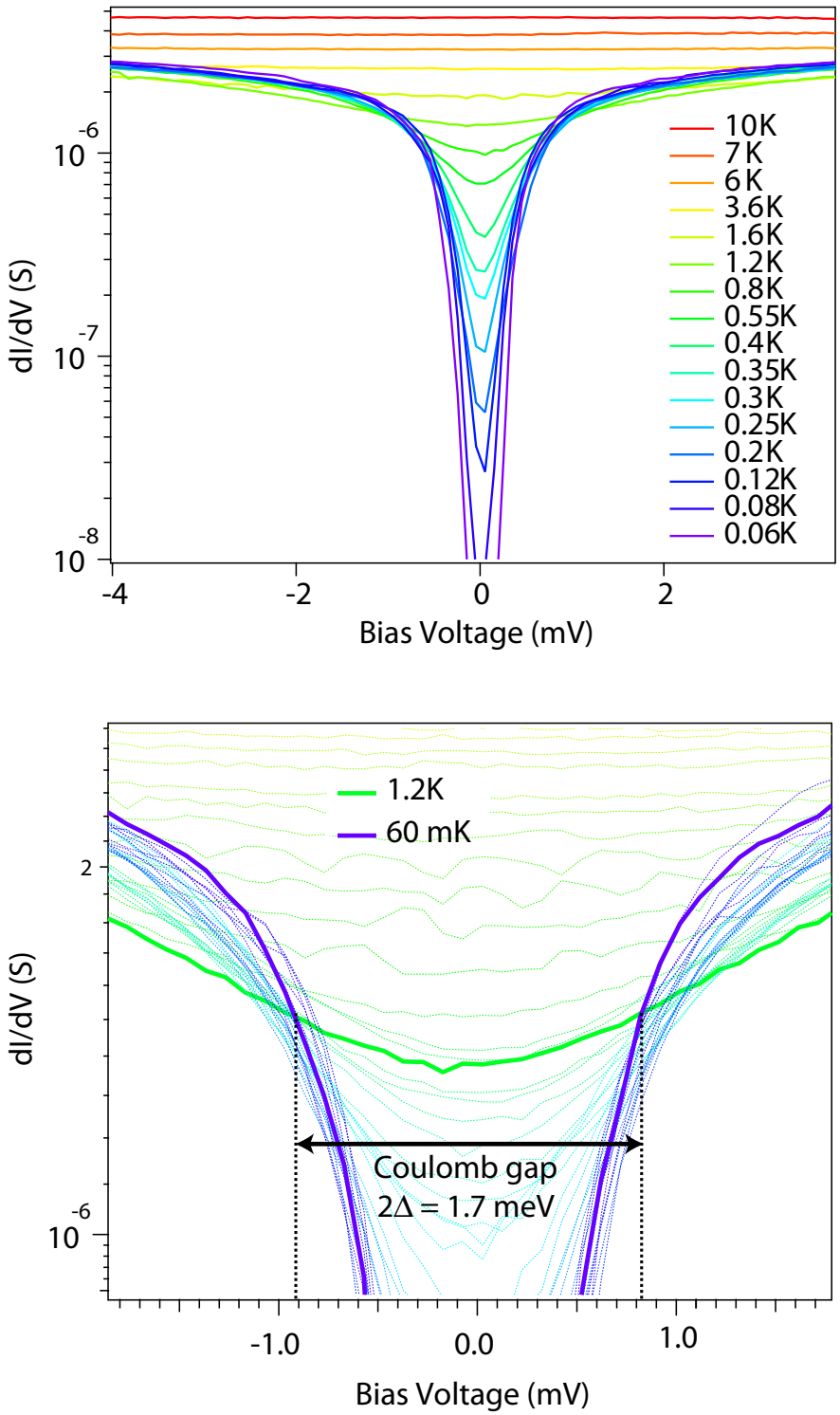

Figure 1.31 – ***Differential conductance*** $\frac{dI}{dV}(V)$ ***for different temperatures near the Dirac point*** ($V_g = 16$ ***V). a)*** *A dip centered at zero appears at low temperatures.* ***b)*** *This 'Coulomb gap' is approximately* $\Delta \cong 0.85$ *meV.*

We turn now to the low temperature regime (where the gap strengthens). The Efros-Shklovskii theory predicts that the Coulomb interactions will give a gap in the density of states (equation 1.49) [54] :

$$\Delta^{E-S} = \frac{\rho_0 e^4}{(4\pi\epsilon_0\epsilon_r)^2} \tag{1.59}$$

Where ρ_0 is the density of states outside the gap and the relative permittivity. Using the value $\epsilon_r \cong 15$ measured in graphene [88] and the value of density of states derived previously we find a gap $\Delta^{E-S} \cong 2.2$ meV. Note that this value is the local gap in the DOS and that we measure the transport gap, which should be larger. The E-S fit shown in Fig.1.32 gives the activation temperature $T_0^{E-S} = 9.85$ K. This value corresponds to a localization length (equation 1.51) :

$$\xi_{loc}^{ES} = 316 \text{ nm} \tag{1.60}$$

Which is in slight disagreement with the value of $\xi_{loc}^{Mott} = 109$ nm found in the Mott VRH regime.

As was stated earlier, the Mott to E-S crossover temperature is $T_{cross} = 0.7$ K. The transport gap that appears has a width of $\Delta/k_B = T_\Delta \cong 10$ K. Here we have to remember this is not a tunneling experiment but a transport one. We are not probing the local Coulomb gap $k_B T_{CG}$ but a series of N gapped localized states. The relevant energy is the voltage applied to each localized state V_{loc}. The transport is suppressed when $eV < \Delta = N \times eV_{loc} = N \times k_B T_{CG}$. According to Rosenbaum [89], we should have $T_{cross} \cong 2T_{CG}$, so that $T_{CG} = 0.35$ K is the Coulomb gap of one localized state (quantum dot). We measure $T_{cross} = \frac{1}{14.2} T_\Delta$, which means we have $N = 2\frac{T_\Delta}{T_{cross}} = 28.4$ dots in series. This means that the average distance between dots is 91.5 nm. This value is in relatively good agreement with the localization and hopping length obtained earlier, confirming that a gap appears in the localized states. However, the gap value does not agree with the Efros-Shklovskii theory (equation 1.59).

To conclude, the low-temperature transport regime bears signatures of the Efros-Shklovskii mechanism. First of all, the resistance starts to increase faster and the gap strengthens. Second, the width of this gap can be accounted for by considering that the charging energy of a localized state is of order 0.35 K. This value is much smaller than what is predicted by the E-S model (equation 1.59). The localization length in the E-S regime is also found to be anomalously large. Looking back at the lengths derived from the Mott VRH regime (10 K - 1 K), we see that the hopping distance d is smaller than the localization length ξ_{loc}^{Mott}. This means we are only *marginally* localized, with electrons hopping between largely overlapping states. This could explain the discrepancy. As a matter of fact, we can expect that in that case, the Coulomb interaction is strongly renormalized and that Efros-Shklovskii equations do not strictly apply to this limit of intermediate disorder. Alternatively, the disagreement could be due to

the inherent inapplicability of the VRH model to graphene, as was recently argued by Liang and Sofo [90].

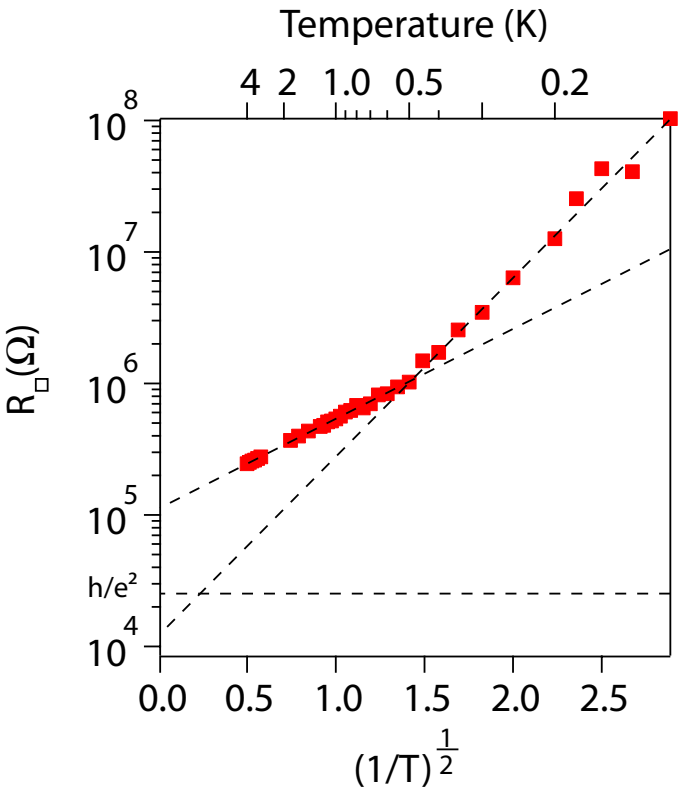

Figure 1.32 – *Maximum sheet resistivity plotted on an Efros-Shklovskii plot. The oblique dashed lines are fits to equation (1.50). The horizontal one indicates the quantum of resistance.*

1.4.3.4 Variable range hopping in graphene with vacancies and sp^3 defects

The low-temperature transport properties of disordered graphene lattices has become a very active field of research recently. The case of sp^3 disordered graphene have been studied quite extensively. Mott variable range hopping (VRH) (equation 1.46) has been observed in reduced graphene oxide [91, 92, 93, 87, 86], graFene [94, 95] and graphane [31, 96, 97]. Some of the most recent papers actually found evidence of an Efros-Shklovskii (E-S) type VRH regime (equation 1.50) in all three of them : reduced graphene oxide [86] (shown in Fig.1.33), graphane [97] and graFene [95]. As for atomic vacancies in graphene, fewer studies are available [98, 99]. Only a couple of them did investigate the low temperature transport. Zhou *et al.* [100] found a Mott variable range hopping regime as well.

In the vast majority of these studies, the samples are much more disordered than in our case, so that a VRH regime can be observed starting from room temperature. This allows a better characterization and is a possible improvement in our study. However, we felt bound to study samples exhibiting the same gate-tunable transition from weak

to strong localization at low temperature as the one exhibited by the samples used in Chapter 3.

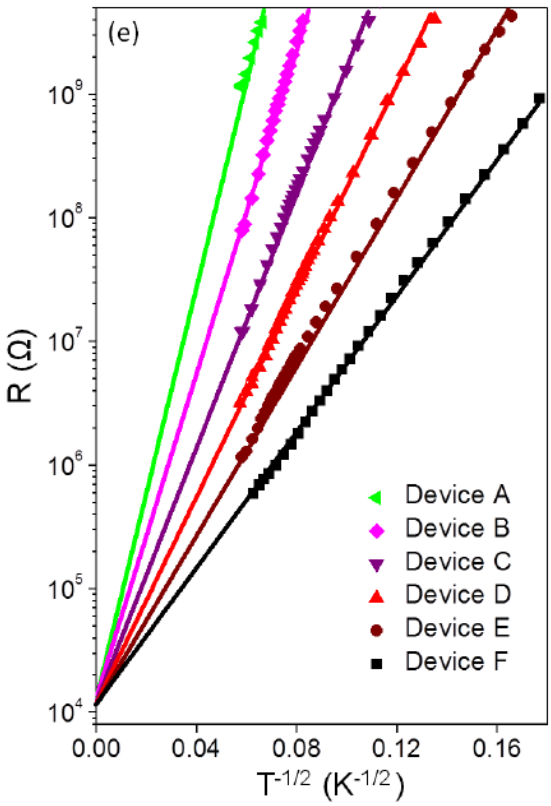

Figure 1.33 – *Fit to the E-S VRH in graphene oxide sheets at various levels of reduction. Taken from [86].*

1.4.4 Transport in macroscopic disordered CVD graphene

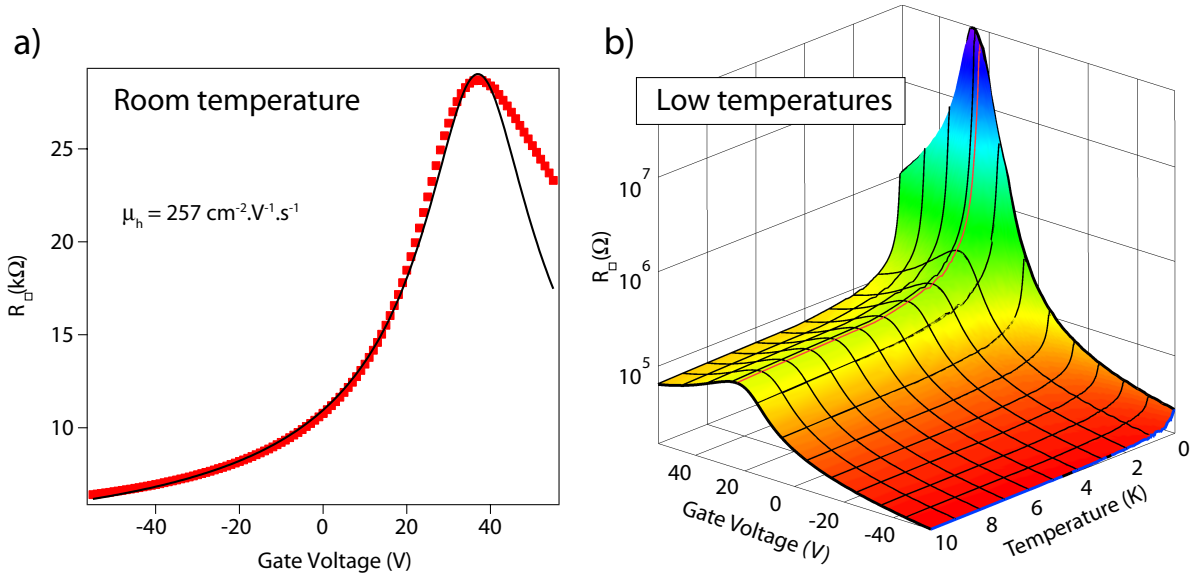

Figure 1.34 – ***Resistance of the macroscopic disordered sample SAM-54.*** ***a)*** *Room temperature field effect curve. The mobility fit (equation 1.21 gives a hole mobility of* $\mu_h \cong 257\ cm^{-2}.V^{-1}.s{-}1$. ***b)*** *Low temperature 3D map of the sheet resistance as a function of gate voltage and temperature.*

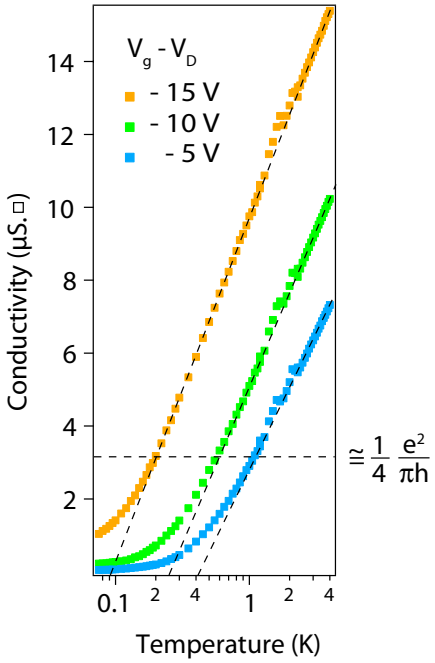

Figure 1.35 – *Crossover between weak and strong localization in sample SAM-54 at different gate voltages. The oblique dashed line are fit to equation (1.28) and the horizontal one indicates where the conductivity stops following the weak localization law.*

Sample of size L larger than the phase-coherence length L_Φ are very convenient for transport measurements at low temperature because they don't suffer from universal conductance fluctuations (UCF). This is particularly interesting when trying to fit the magnetic response to the weak localization theory (equation 1.32). As a matter of fact, Tikhonenko *et al.* [101, 102] had to resort to some averaging procedure to go around this problem in their microscopic samples. Macroscopic samples can also reveal what happens on a larger scale in disordered graphene. This prompted us to use a macroscopic sample of dimensions $L \times W = 9\ \text{mm} \times 5\ \text{mm}$: sample SAM-54.

Sample SAM-54 studied here has a room temperature field effect curve very similar (see Fig.1.34a) to that of the microscopic sample studied in the previous section (Fig.1.28), so that one can assume they have the same level of disorder. Fig.1.34b shows that it also becomes strongly localized at low temperature near the Dirac point.

Interestingly, it seems that the resistance does not increase quite as fast with decreasing temperatures as in the microscopic sample. Fig.1.35 shows the crossover regime between weak and strong localization at low temperatures for 3 different gate voltages. It is apparent that the slopes of the weak localization correction (the oblique dashed lines) are different for the 3 gate voltages. This observation is in stark contrast with that made in Fig.1.30b that the weak localization is gate-independent in microscopic samples. Another observation that can be made is that the conductance at which the crossover happens (horizontal dashed line) is actually about a factor of 4 lower than the expected value [103]. We haven't measured this crossover in the microscopic samples to compare, however.

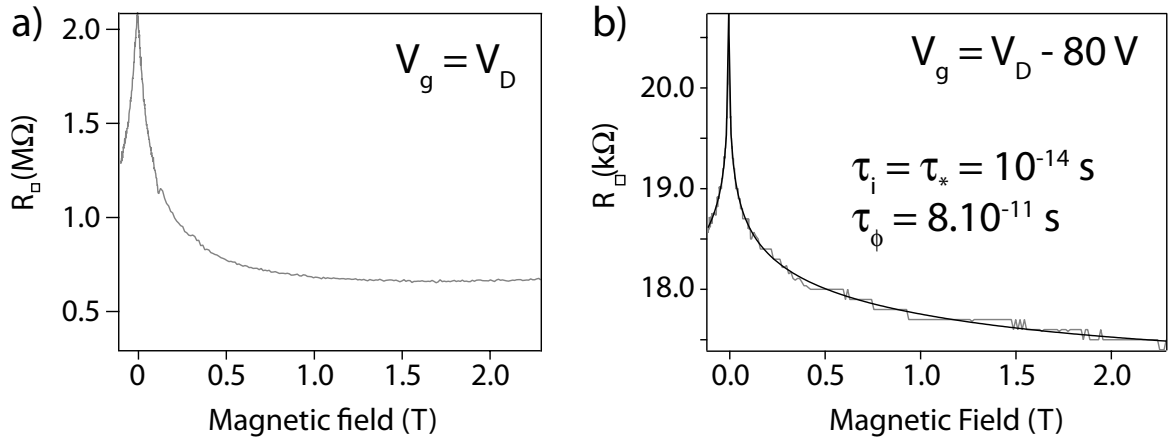

Figure 1.36 – ***Magnetoresistance of sample SAM-54, measured at*** $T = 200$ ***mK. a)*** *At the Dirac point in the strongly localized regime.* ***b)*** *Far from the Dirac point in the weakly localized regime. The black line is a fit to equation (1.32).*

Finally, we measured the magnetic response of that macroscopic sample (Fig.1.36), and here again the result is a bit puzzling. The magnetoresistance was recorded at a single temperature $T = 200$ mK. Fig.1.36a shows the magnetoresistance taken at the Dirac point, where the sample is already in the MΩ range, and Fig.1.36b shows it in the region far from the Dirac point, where the sample is still weakly localized.

After many attempts, the curve in Fig.1.36b was simply impossible to fit the weak localization theory of McCann [30] (equation 1.32). However, by changing the aspect ratio of the sample from $L/W = 1.8$ to $L/W = 10.5$, the fitting worked quite well and gave reasonable values. The value of the phase coherence time τ_Φ is in good agreement with the values found in [101]. The intervalley τ_* and intervalley τ_i scattering times are found to be both smaller than 10^{-14} s. This corresponds to mean free paths smaller than 10 nm. Basically, the scattering rates are so high that only the first term on the RHS of equation (1.32) is of significance.

Near the Dirac point (Fig.1.36a), the large decrease of the resistance is expected with a magnetic field, as we are in the strongly localized regime. Similar results have been observed by [87, 94, 96] in different graphene derivatives. In our case

the magnitude of the observed negative magnetoresistance was not as enormous as theirs, possibly indicating a strong influence of Coulomb interactions in the localization mechanism.

1.4.4.1 Discussion

There seems to be corroborating evidence, from the value of the critical resistance at the WL-SL crossover (Fig.1.35), and from the magnetoresistance fitting (Fig.1.36), that the effective aspect ratio of our sample is about a factor of 4 larger than the geometric aspect ratio. In macroscopic sheets of disordered CVD graphene, one can easily imagine that the profusion of geometrical defects arising from tears and gaps at grain boundaries can result in such a renormalization of the aspect ratio. However, there could be another reason. As a matter of fact, among the small samples made by UV lithography, neighbouring samples which appeared structurally intact, often exhibited very different resistivities. Moreover, the gate-dependence of the weak localization slope in the macroscopic sample (Fig.1.35) indicates that this renormalization factor is in fact gate-dependent, a fact that rules out a pure 'geometric' effect. A non-homogeneous atomic disorder, like the one shown on the Raman map of Fig.1.26b, where the D band has spatial variations, may explain such a behavior, if the variability is large enough on a large scale.

Conclusion du Chapitre 1

Dans ce chapitre, nous nous sommes penchés sur les propriétés du graphène 'nu'. Nous avons étudié ses propriétés d'un point de vue théorique et expérimental. Du graphène obtenu de plusieurs manières, soit par exfoliation mécanique de cristaux de graphite, soit par croissance CVD, a été caractérisé. L'un des avantages du graphène CVD est qu'il permet de fabriquer des échantillons de taille bien supérieure à la longueur de cohérence de phase des électrons, ce qui est pratique pour s'affranchir des effets de fluctuation universelle de la conductance. Nous avons démontré une nouvelle approche permettant d'introduire du désordre dans le graphène, par une réaction chimique dont nous ignorons pour l'instant la nature, mais qui semble introduire des défaut structuraux de type sp^3 dans la maille. Nous avons jaugé le désordre ainsi introduit par des mesures de spectroscopie Raman ainsi que par les propriétés de transport à basses températures de ces feuilles de graphène.

Les conclusions suivantes peuvent être tirées de ce chapitre :

- Une relation claire et reproductible entre le temps d'exposition à la solution acide et le degré de désordre a été mise en évidence, à la fois par des mesures de spectroscopie Raman, et par des mesures de résistance. Ces deux expériences semblent montrer que le désordre est induit à une échelle atomique. Bien que la nature des défauts nous soit encore inconnue, il semblerait qu'il s'agisse de défauts de type sp^3.

- Les échantillons les plus désordonnés (ceux qui ont passé le plus de temps dans la solution) montrent un régime de localisation forte à basses températures (typiquement sous 1 K) et près du point de neutralité de charge. Une transition du régime de localisation forte à un régime de localisation faible est induite par l'augmentation progressive de la densité de porteurs de charge lorsqu'on fait varier la tension de grille. On a ainsi réalisé une transition métal 2D-isolant controllée électrostatiquement.

- Dans le régime fortement localisé, les interactions électron-électron se manifestent à la fois sous la forme d'un gap de Coulomb dans la densité d'état, ainsi que dans le régime de saut à distance variable de type Efros-Schklovskii. Cependant, les longueurs de localisation que nous avons pu extraire de ces données sont en léger désaccord les unes avec les autres.

- Nous avons maintenant à notre disposition une méthode relativement reproductible qui nous permet d'induire à volonté du désordre dans le graphène. Ce graphène au désordre controllé est un bon matériau de départ, une bonne platforme électronique, sur laquelle nous allons pouvoir construire des matériaux hybrides. Nous verrons en effet au Chapitre 3 que les matériaux hybrides

supraconducteurs décrits au Chapitre 2 acquièrent des propriétés intéressantes lorsque du graphène désordonné est substitué au graphène exfolié. En effet, la possibilité d'induire une transition métal-isolant dans la platforme graphène permet un contrôle plus poussé des interactions supraconductrices dans le matériau hybride.

Conclusion of Chapter 1

In this chapter, we have addressed the problem of electrons transport in 'bare' graphene devices, both from a theoretical and an experimental point of view. Graphene samples from different sources, mechanical exfoliation of Kish graphite, and CVD growth, have been characterized. The latter source of graphene offers the great advantage to allow the fabrication of macroscopic devices, where mesoscopic fluctuation are absent. A useful and original way of controlling the electronic disorder using a chemical treatment during the transfer of CVD graphene onto measurement substrates has been discovered. The amount of disorder has been assessed by Raman spectroscopy and electronic measurements at room and low temperatures.

Several conclusions can be drawn from this chapter :

- A clear and reproducible relationship between the exposure time to the acidic etchant and the amount of disorder was assessed by both the intensity of the Raman D-band and the sheet resistance of the graphene layer. Both experiments tend to prove that the disorder induced by the etchant is at the atomic scale. It is likely an sp^3 hybridization of the carbon atoms, even though its exact nature is still unknown.

- For the most disordered samples (obtained by long exposure to the etchant), a regime of strong localization of electrons is observed at low temperature (typically below 1 K) near the charge neutrality point. A sharp transition towards the weakly localized regime occurs by rising the charge carrier density with the gate voltage, in an electrostatically controlled insulator-to-2D metal transition.

- The strongly localized regime is characterized by the presence of a Coulomb gap, resulting in an Efros-Shklovkii dependence on temperature. However, the derived the localization lengths and Coulomb gap we derived are not completely consistent.

- We now have at our disposal a method to provide graphene with controllable electronic disorder, a material which will act as a well defined starting point (a so called "electronic platform") for the fabrication of hybrid devices. This will be studied in Chapter 3. We will indeed see in Chapter 3 that the amount of disorder within the graphene "medium" linking superconducting nanoparticles is a critical parameter to tune the superconductor-insulator transition.

Gate-tunable Josephson effect in Sn/graphene hybrids

2

Introduction en français

Bien qu'il existe des prédictions théoriques selon lesquelles le graphène possède une supraconductivité intrinsèque lorsque son niveau de Fermi atteint la singularité de van Hove [104, 105], ceci n'a pas encore été démontré expérimentalement. En revanche, induire du supercourant par effet de proximité est relativement facile dans le graphène [106, 107]. Dans les années 90, beaucoup d'efforts ont été faits pour réaliser l'effet de proximité dans des gaz d'électrons bidimensionnels (2DEG) [108]. Epitaxier des hétérostructures et venir les contacter électriquement avec des matériaux supraconducteurs représente d'énormes difficultés techniques. Cependant le jeu en vaut la chandelle car, la technologie des semiconducteurs aidant, ces dispositifs offrent une grande souplesse et un contrôle inégalé du supercourant. Ils ouvrent ainsi de nouvelles perspectives, avec par exemple la possibilité de réaliser des dispositifs supraconducteurs sensibles à la lumière, ou mieux encore, des circuits logiques supraconducteur reposant sur le contrôle électrostatique du supercourant. Par ailleurs, ils permirent d'observer des effets tels que la quantification de la conductance ou les interférence quantiques dans le régime supraconducteur. L'émergence du graphène est intéressante de ce point de vue. En effet, le 2DEG du graphène est à l'air libre et son interface avec les métaux est caractérisée par une faible barrière Schottky, ce qui signifie que l'on peut y induire du supercourant relativement aisément.

Le graphène est également un matériau assez exotique, dans lequel il est intéressant en soi d'étudier l'effet Josephson. Du fait de son libre parcours moyen relativement important, il peut en principe former des jonctions Josephson ballistiques [109]. De plus, un nouveau type de réflection d'Andreev, dite 'spéculaire', a été prédit à l'interface graphène/supraconducteur [110]. Enfin, ce système permet l'étude de l'effet Hall quantique des paires de Cooper [111].

L'idée de coupler un réseau de particules supraconductrices à la surface du graphène pour induire de la supraconductivité sur des distances arbitrairement larges

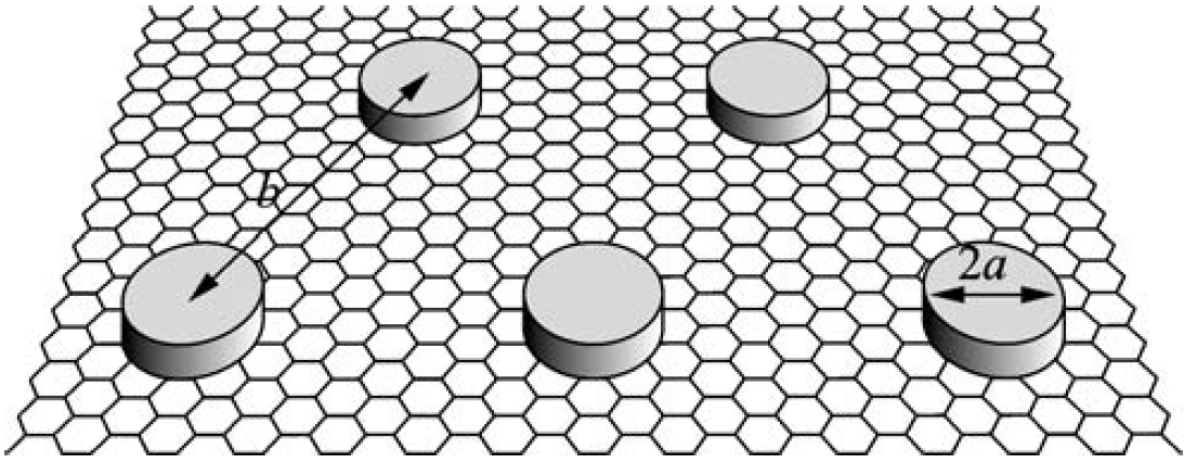

Figure 2.1 – *Vue schématique d'un réseau de nanoparticules supraconductices décorant la surface du graphène (la maille du graphène n'est pas à l'échelle). Les paramètres géométriques gouvernant les propriétés supraconductrices sont le rayon a des ilôts et la distance les séparant b. Tiré de [112].*

a été proposée par Feigel'man *et al.* en 2009 [112]. Reconnaissant que le graphène était compatible avec la supraconductivité, ils proposèrent alors d'utiliser celui-ci comme matériau 'hôte', médiateur du transport cohérent de paires de Cooper entre les îlots supraconducteur. Du fait de la densité d'état très faible du graphène comparé aux métaux classiques, l'effet de proximité inverse ne devrait pas affecter les particules supraconductrices outre mesure. Ils prédirent que ce réseau de jonctions SNS montrerait une température de transition variable en grille et qui dépendrait des paramètres suivants : le rayon a des îlots, la distance b les séparant, et enfin la résistance de l'interface supraconducteur/graphène.

Kessler *et al.* ont montré en 2010 que de tels systèmes hybrides peuvent être fabriqués simplement en évaporant un métal à bas point de fusion, l'étain, sur la surface du graphène. Si l'épaisseur déposée est suffisemment fine alors le métal démouille et forme des îlots qui ne percolent pas. Le matériau hybride préserve les propriétés intrinsèques du graphène, notamment la possibilité de faire varier la conductance par la tension de grille. Pendant ce temps, les îlots d'étain forment un réseau désordonné auto-assemblé de jonctions Josephson. Le supercourant observé est particulièrement fort, ce qui est assez remarquable car celà signifie que la barrière Schottky à l'interface Sn/graphene n'est pas trop importante. L'étude de la température de transition dans ces systèmes à montré qu'ils se comportent comme des films minces bidimensionnels, c'est-à-dire qu'il suivent une loi de type Berezinki-Kosterlitz-Thouless (BKT), dépendante en grille.

Dans ce chapitre, nous irons un peu plus loin dans l'étude des propriétés supraconductrices de ces matériaux hybrides. Nous observerons d'abord l'effet de l'étain sur les propriétés électroniques du graphène, ainsi que les différentes morphologies

qui peuvent résulter de l'évaporation de l'étain sur différents types de surfaces. Les deuxièmes et troisièmes parties du chapitre introduiront les concepts liés à l'effet Josephson, ainsi que le formalisme utilisé pour traiter les réseaux de jonctions Josephson. Ces notions seront utilisées dans les sections 4 et 5, où nous étudierons successivement des matériaux hybrides formés avec de l'étain et du plomb. Nous porterons une attention particulière à l'effet de la morphologie sur les propriétés supraconductrices.

Introduction in english

Although it has been predicted that graphene supports intrinsic superconductivity [104, 105], experimental realization is still lacking. However, inducing superconductivity by proximity effect is relatively easy in graphene [106, 107]. In the 90's, a significant experimental effort was put in realizing the proximity effect in 2D electron gases (2DEG) [108]. The technical challenge represented by the growth and subsequent electrical contacting of these buried 2D gases was only equalled by the superior control that semiconductor technology could provide over the supercurrent. Novel quantum effects, like sensitivity to light, quantization and gate control of the supercurrent were observed. The emergence of graphene brings in this respect new and exciting perspectives. Unlike these artificial heterostructures, graphene is a naturally occuring 2DEG with its surface chemically inert, open to the air and and readily accessible. This make it possible to directly induce a supercurrent by proximity by evaporating superconducting contact on it.

Graphene-based Josephson junctions are appealing because they could potentially be made ballistic [109], but also because a new kind of so-called 'specular' Andreev reflection has been predicted [110], and because they allow the study of the interplay between the Josephson and the quantum Hall effect [111].

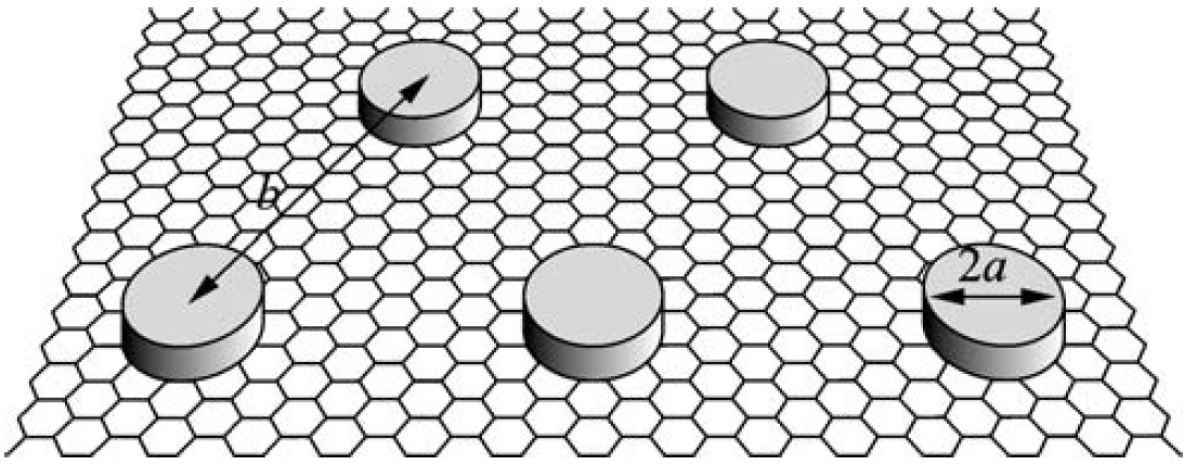

Figure 2.2 – *Schematic picture (not to scale) of an array of superconducting nanoparticles on the surface of graphene. The geometrical parameters governing the superconducting properties are the island radius a and the inter-islands spacing b. Taken from [112].*

The idea to couple an array of superconducting particle to graphene dates back to a paper by Feigel'man *et al.* [112], published in 2009. Aknowledging the robust proximity effect previously observed in graphene Josephson junctions [106], they proposed to use graphene as a 'host' material mediating the phase-coherent transport of Cooper pairs between superconducting nanoparticles. Because graphene has a very

low density of states compared to bulk metals, it should not adversely affect the intrinsic superconducting properties of the nanoparticles, like a normal metal would. The resulting array of SNS Josephson junctions would exhibit gate-tunable superconducting properties that would also depend on parameters such as island radius a and inter-island spacing b (see Fig.2.2).

Kessler *et al.* [113] showed that such a hybrid system can be formed when a thin layer of low-melting-point Sn is evaporated over the surface of graphene. The hybrid material preserves the intrinsic gate-tunability of graphene, while the Sn islands organize into a self-assembled array of Josephson junctions. Quite remarkably, the Schottky barrier at the Sn/graphene interface does not seem to hinder the supercurrent much. The hybrid device exhibits a gate-tunable Berezinskii-Kosterlitz-Thouless (BKT) superconducting transition temperature and properties.

In this chapter, the superconducting properties of this hybrid material will be studied in more details. The effect of Sn on the electronic properties of graphene will be dealt with first, as well as the different Sn islands morphology that can be obtained in different conditions. The second and third part of this chapter will introduce concepts related to Josephson junctions and Josephson junctions arrays, that will be useful in the fourth and fifth parts, where the superconducting properties of hybrids made by combining graphene with Sn and Pb will be studied. Special emphasis will be put on the effect of surface morphology of the Sn islands on the superconducting transition temperature and critical current.

Table of contents of Chapter 2

2.1 Graphene decorated by tin nano-particles : a hybrid material

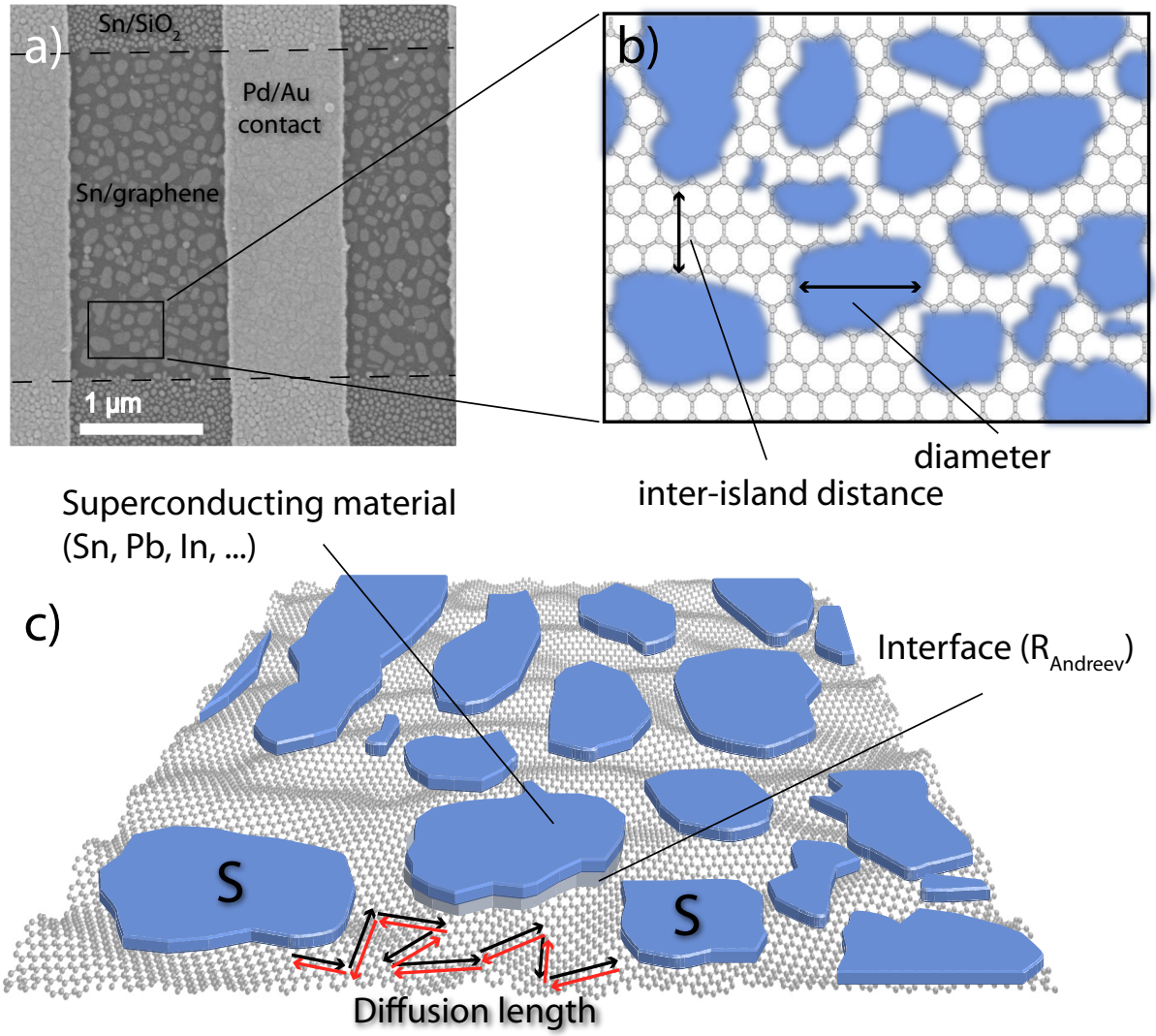

Figure 2.3 – ***Relevant physical quantities in the hybrid system.*** ***a)*** *SEM picture of the Sn/graphene system.* ***b)*** *and* ***c)*** *Schematic pictures introducing the different relevant physical quantities.*

In this section I will describe how hybrid Sn/graphene devices can be obtained by self-assembly of an array of Sn islands on the exposed surface of graphene. The resulting system behaves like a hybrid material combining the gate-tunable properties of graphene with the superconductivity of Sn nanoparticles. Fig.2.3 introduces the important physical quantities that will influence the hybrid properties.

2.1.1 Device fabrication and characterization

2.1.1.1 A few words about tin

As one of the constituents of bronze, tin has been known to men for thousands of years. With a very low melting point (232°C), it is very soft and malleable. Combined with the fact it doesn't rust, it makes a good material for alloying and a good anti-corrosive plating in food container. In air, tin forms the dioxide SnO_2, which is impervious to oxygen, thus forming a 'crust' of a few nanometers that prevents further oxidation. Tin is also a type-I superconductor with a critical temperature $T_C = 3.72$ K and a critical field $H_C = 30$ mT [114].

2.1.1.2 Self-assembly of tin nanoparticles on graphene

Because of its low melting point, tin does not fully wet surfaces and tends to form droplets. on graphene, even a film as thick as 50 nm will still not be continuous if it is evaporated at room temperature. Fig.2.4 shows SEM images of the various conformation of a nominally 10 nm thick Sn film on different graphene (Fig.2.4a-c) and SiO_2 (Fig.2.4d) surfaces. Sn evaporation is done by Joule evaporation under 10^{-6} mbar at room temperature.

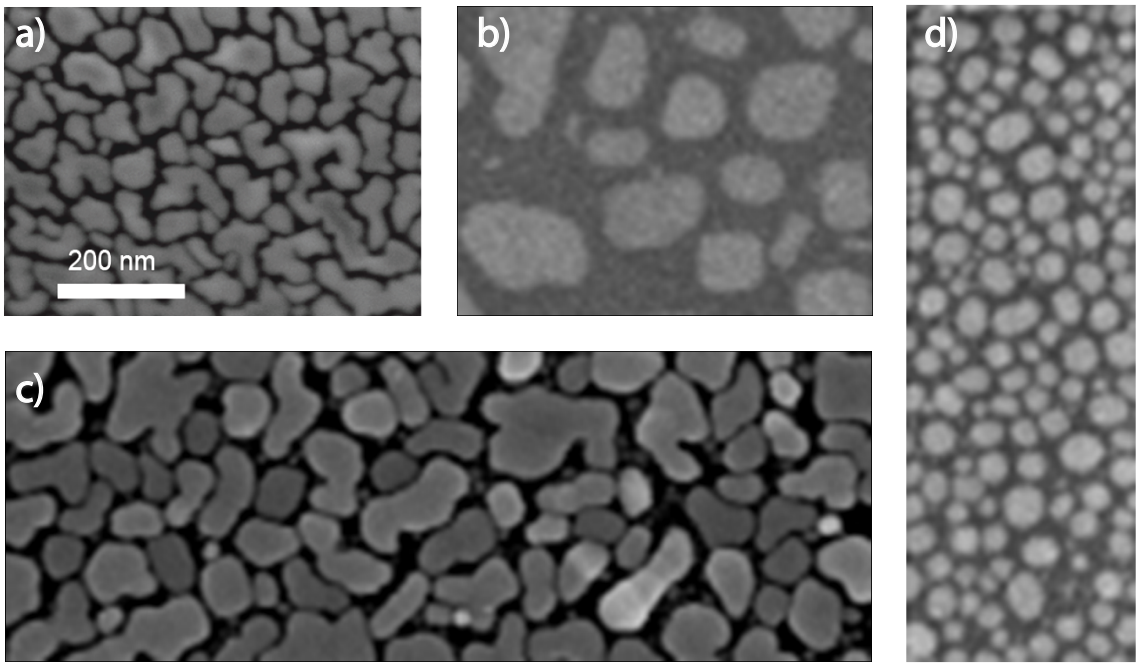

Figure 2.4 – ***Sn grains on various graphene substrates and on SiO_2.*** ***a)*** *on exfoliated graphene previously exposed to PMMA.* ***b)*** *on freshly cleaved graphene.* ***c)*** *on CVD graphene previously transferred to SiO_2 using a PMMA support layer.* ***d)*** *on the SiO_2 substrate. All images are on the same scale.*

The conformation of Sn on graphene surfaces can be divided into two categories correponding to Fig.2.4a and Fig.2.4c on the one hand, and to Fig.2.4b on the other hand. Fig.2.4a shows an exfoliated graphene sample, on top of which Sn has been evaporated *after* the patterning of electrodes. Fig.2.4c shows a sample made of CVD-grown graphene. Sn was evaporated after the graphene sheet was transferred to the SiO_2 substrate. In both cases, the surface of graphene has been exposed to PMMA prior to Sn deposition. They are both characterized by bulbous Sn islands and low inter-island spacings. The Sn islands on exfoliated graphene have a more homogeneous distribution of shapes and sizes, while on CVD graphene, there seems to be a greater variability in the electrical coupling between Sn islands and the graphene sheet, as evidenced by the varying SEM contrasts of different islands.

Fig.2.4b shows the surface of an exfoliated graphene flake where Sn decoration was done just after the exfoliation, on a supposedly much cleaner surface. The grains are bigger and rounder, and the gaps between them are much larger. This is probably due to a better mobility of Sn atoms on the cleaner surface. Finally, Fig.2.4d shows how the Sn islands conform onto the SiO_2 substrate. The rough surface of SiO_2 gives rise to a denser array of smaller islands. Note that all of these arrays are non-percolating. This is not the case if the evaporation is done at lower temperature, in which case a continuous film forms, while evaporation at higher temperature gives large hemispheric Sn 'domes' that tend to decorate the edges and defects of graphene.

The samples shown in Fig.2.4 have been analysed using ImageJ to extract the surface coverage of Sn nanoparticles in the different limits. The results are summarized in Table2.1

Figure	Sample type	Surface coverage
2.4a	Exfoliated graphene, dirty surface	80 %
2.4b	Exfoliated graphene, clean surface	43.8 %
2.4c	CVD graphene, dirty surface	69.6 %

Table 2.1 – *Surface coverage of Sn islands obtained on different graphene surfaces characterized by their cleanliness. The coverage values were obtained by analysing SEM images of a few microns square using the software ImageJ.*

On exoliated graphene, the deposition of Sn on clean and dirty surfaces give rise to very different surface coverages. While the Sn assembles into a tight array on the dirty surface, it results in a much looser conformation on clean surfaces.

On graphene, tin islands typically form pancakes of lateral size on the order of 100 nm. The spacing between islands doesn't seem to depend on the thickness, but rather on the surface cleanliness. Typical spacings range from 25 nm in 'dirty' surface devices (Fig.2.4a and c) to 50 nm in the 'clean' case (Fig.2.4b). We note that grain sizes and spacings are more homogeneously distributed in the former case.

2.1.1.3 Enhanced optical contrast of decorated flakes

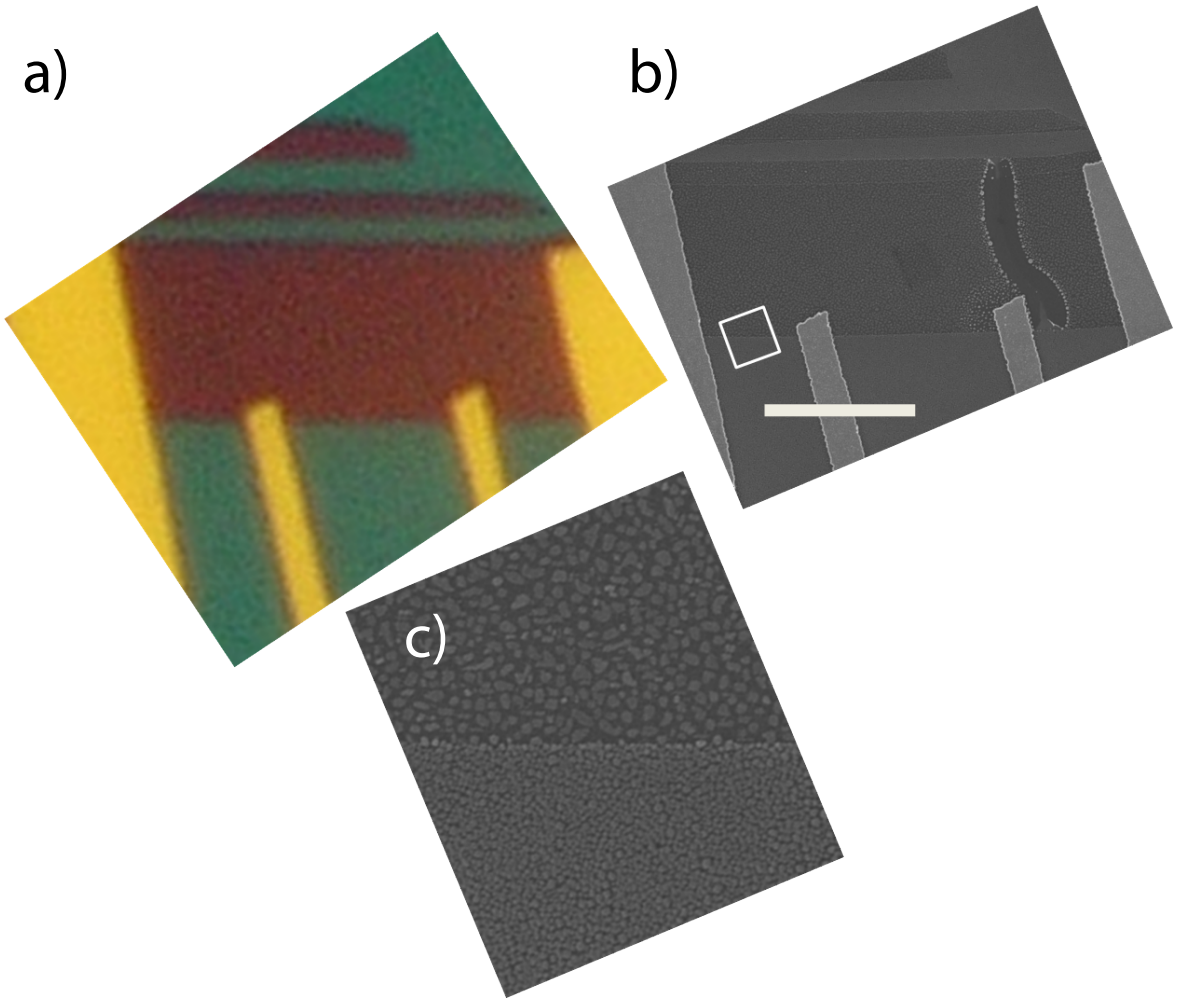

Figure 2.5 – ***Enhanced optical contrast in Sn decorated graphene. a)*** *optical and* ***b)*** *SEM images of the same graphene device.* ***c)*** *Zoomed view of the white square in b) showing the graphene boundary. The scale bar is 5 µm.*

Graphene flakes decorated with Sn have a very strong optical contrast, as compared to bare graphene. As can be seen on Fig.2.5, where an SEM and an optical image of the same device are put side by side, this contrast originates in the strongly surface-dependent conformation of Sn islands.

2.1.2 How tin influences the electronic properties of graphene

When graphene is in contact with a metal, their Fermi energies align. According to the work function mismatch between Sn ($\Phi_{Sn} = 4.42$ eV) and graphene ($\Phi_g = 4.5$ eV), this should dope the graphene sheet with electrons to the tune of 0.08 eV (see Fig.2.6a). Using equation (1.8) this corresponds to a charge density (and gate voltage with 285 nm of SiO_2 dielectric) :

$$n = 5.2 \times 10^{15} \mathrm{m}^{-2} \equiv 6.9\mathrm{V} \tag{2.1}$$

However, this value is wrong because it overlooks the effect of the interfacial potential. Giovannetti *et al.* [115] showed that this potential has two components : the contribution due to the charge transfer Δ_{tr} (Fig.2.6b), which can be modeled by a plane capacitor, and the contribution from chemical interactions Δ_c between graphene and the metal (Fig.2.6c).

The chemical interaction potential can be calculated using density functional theory (DFT). It depends strongly on the metal-graphene distance and only weakly on the metal under consideration, so that basically there are three situations, depending on the equilibrium metal-graphene distance d :

- For $d \cong 2$ $\mathring{A}$, the band structure of graphene is completely altered by the metal. This is the case for example with Ni, Co and Pd.
- For $d \cong 3.3 - 3.4$ $\mathring{A}$, the band structure of graphene remains intact, but the chemical potential Δ_c is the main contributor to the surface potential, shifting the Fermi level towards the conduction band by about 0.9 eV (see Fig.2.6c). This is the case for Al, Ag, Cu, Au and Pt.
- Finally, if $d \geq 5\mathring{A}$, the Fermi level shift can be inferred from simple work function mismatch considerations, provided that the potential step due to the charge dipole is accounted for.

2.1.2.1 Room temperature field effect

Fig.2.7 shows the field effect measurement of a graphene sheet prior to and after deposition of 10 nm of Sn. After deposition, the typical ambipolar transport characteristics with maximum resistivity at the charge neutrality point is conserved. This indicates that the Sn does not influence the band structure of graphene. The electron mobility is strongly reduced, with a pronounced electron-hole asymmetry. Importantly, it was repeatedly observed [116] that the resistivity maximum does not decrease upon Sn deposition. Had the graphene been short-circuited by the Sn islands, which have a very low and gate-independent resistance, the overall resistivity would have dropped. Notice that because the Sn islands are electrically disconnected and at a floating potential, tuning the carrier density in graphene is accomodated by the Sn/graphene interfacial potential. Therefore, even though the Fermi level in graphene is pinned to that of Sn, the carrier density can be tuned throughout the sample (Fig.2.6). We are really dealing with a coupled hybrid system.

Kessler *et al.* [113] studied the effect of Sn on the field effect curves and showed that the induced doping was approximately constant, regardless of the initial doping.

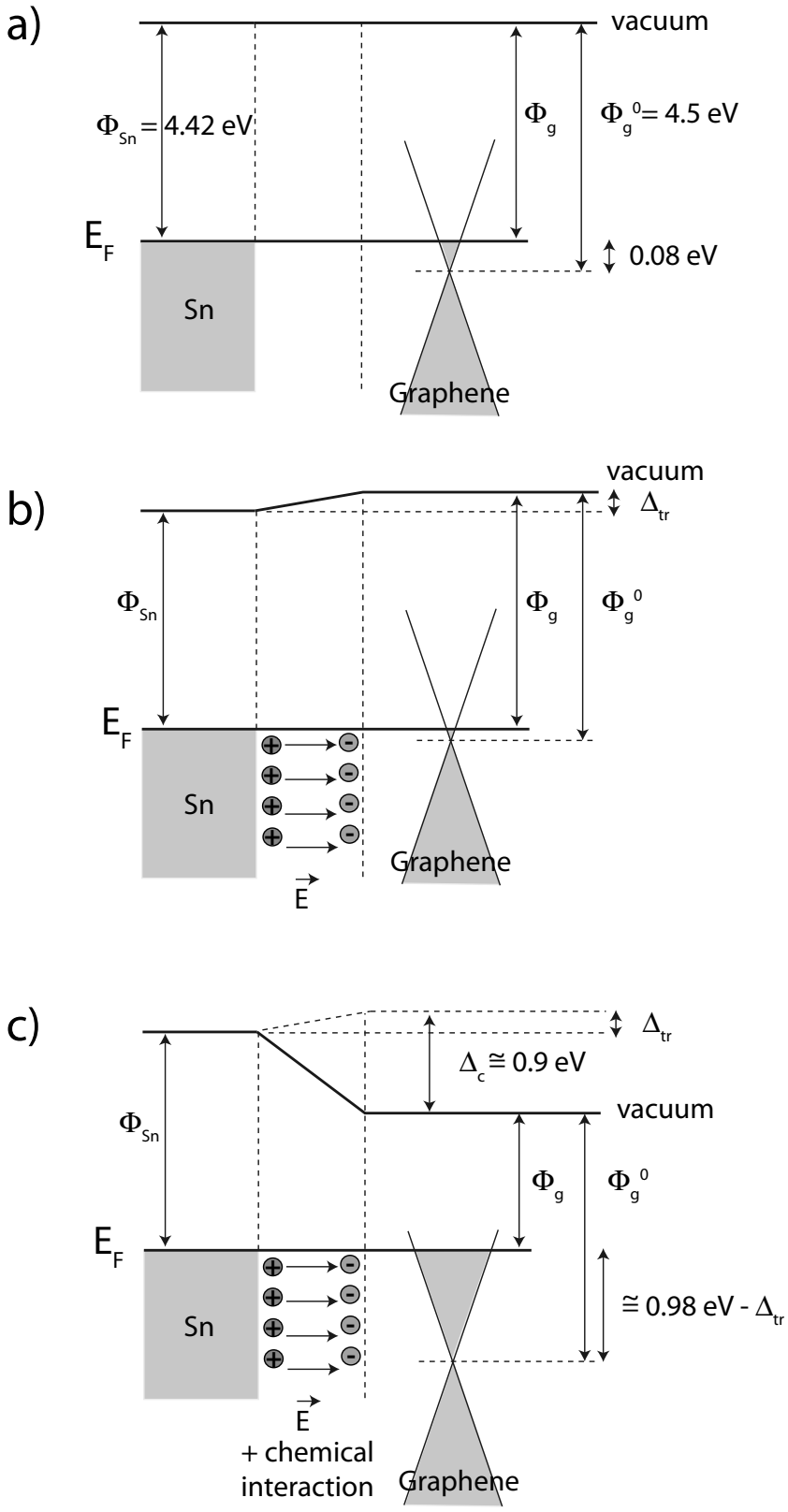

Figure 2.6 – ***Electrostatic doping in graphene in contact with Sn. Adapted from [115]. a)*** *The work function mishmatch should give electron doping in graphene.* ***b)*** *However, the interface dipole reduces this quantity.* ***c)*** *The main contribution comes from chemical interactions and gives large electron doping.*

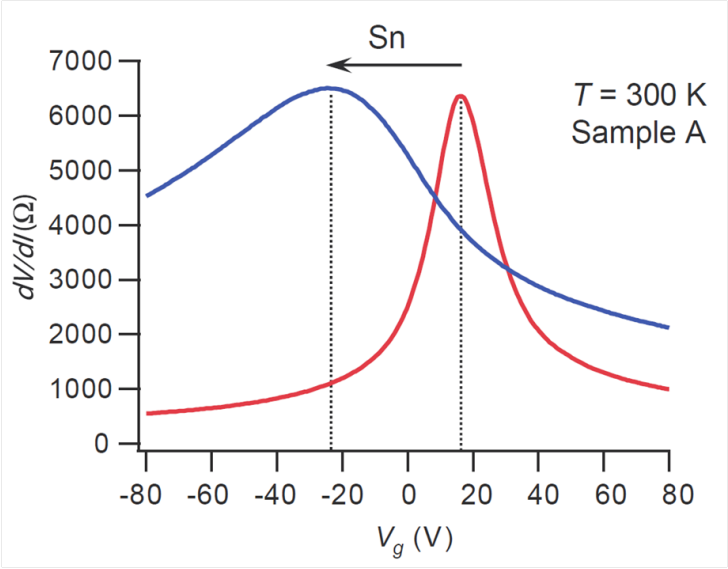

Figure 2.7 – *Field effect curve of a device before (red) and after (blue) Sn deposition. Taken from [113].*

Fig.2.7 shows that the neutrality point shifts towards lower gate voltages after Sn deposition, indicating electron doping. The amount of doping inferred from the Dirac point shift, after renormalization to the coverage was $9 \pm 2 \times 10^{12}$ cm^{-2}, which is in agreement with the results of [115] for the case of a weakly-interacting metal such as Al, Ag, Cu and Pt, within a factor of two of accuracy. The uncertainty about the metal/graphene distance for the case of Sn can account for this uncertainty, especially if impurities are present at the interface.

2.1.2.2 Raman study

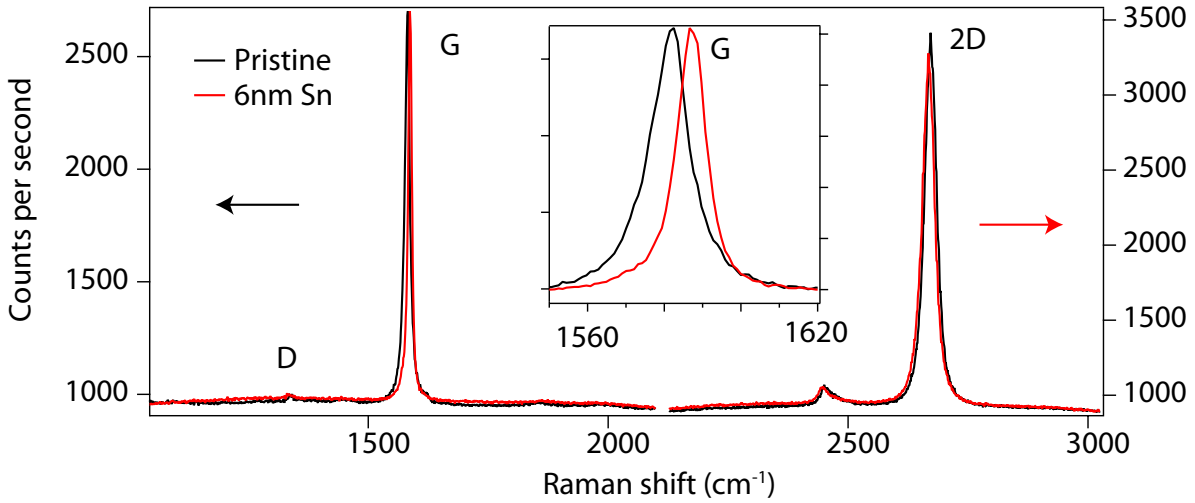

Figure 2.8 – *Raman spectra before (black) and after (red) deposition of 6 nm of Sn. The inset shows a zoom on the G band.*

Another way to assess the effect of Sn adsorbates on the electronic properties of graphene is to record the Raman signal. Using 532 nm laser excitation, we compared

the Raman spectra of several graphene flakes before and after deposition. Fig.2.8 shows one typical spectrum. The first observation is that there is no D band appearing, indicating that the graphene's structural integrity is not affected by Sn (the small D band visible in Fig.2.8 was already present before deposition). This is different from the result obtained by Li *et al.* [117] on noble metals Ag, Au and Pt-decorated graphene, where the decoration procedure, involving plasma, was more aggressive and resulted in structural defects in the graphene lattice.

We recorded the position and full width at half maximum (FWHM) of the Raman G band before and after decoration with various amounts of Sn. The inset of Fig.2.8 shows the evolution of the G band upon deposition of 6 nm. There is a clear blue shift of the band accompanied by a reduced full width at half maximum (FWHM). This is probably not an effect of stress, since it is not associated with any significant shift in the 2D band [74]. Instead, it probably indicates that the Fermi level has been shifted. After Sn deposition, the graphene is doped even more, resulting in a higher frequency of the mode. Its Fermi level, once lying near the Dirac point (large FWHM) has now shifted away from it (small FWHM). More results on several samples decorated with 1 nm to 6 nm of Sn are reported in Fig.2.9a. We observed a systematic anti-correlation between the sign of the G band position shift and the sign of the FWHM change. This is in line with our understanding that this effect is due to doping. Fig.2.9b shows data acquired by Yan *et al.* [75] showing the evolution of the G band with doping. The behavior of our samples indicates a systematic *n*-doping with Sn decoration.

A more comprehensive study would have necessitated a controlled environment. As a matter of fact, day-to-day variations in the atmospheric conditions are likely responsible for the large variability in the measured position of the G band in the pristine samples, which ranged from 1579 to 1592 cm^{-1}. In addition to that, an analysis of the surface coverage dependence on the amount of Sn deposited should have been carried out.

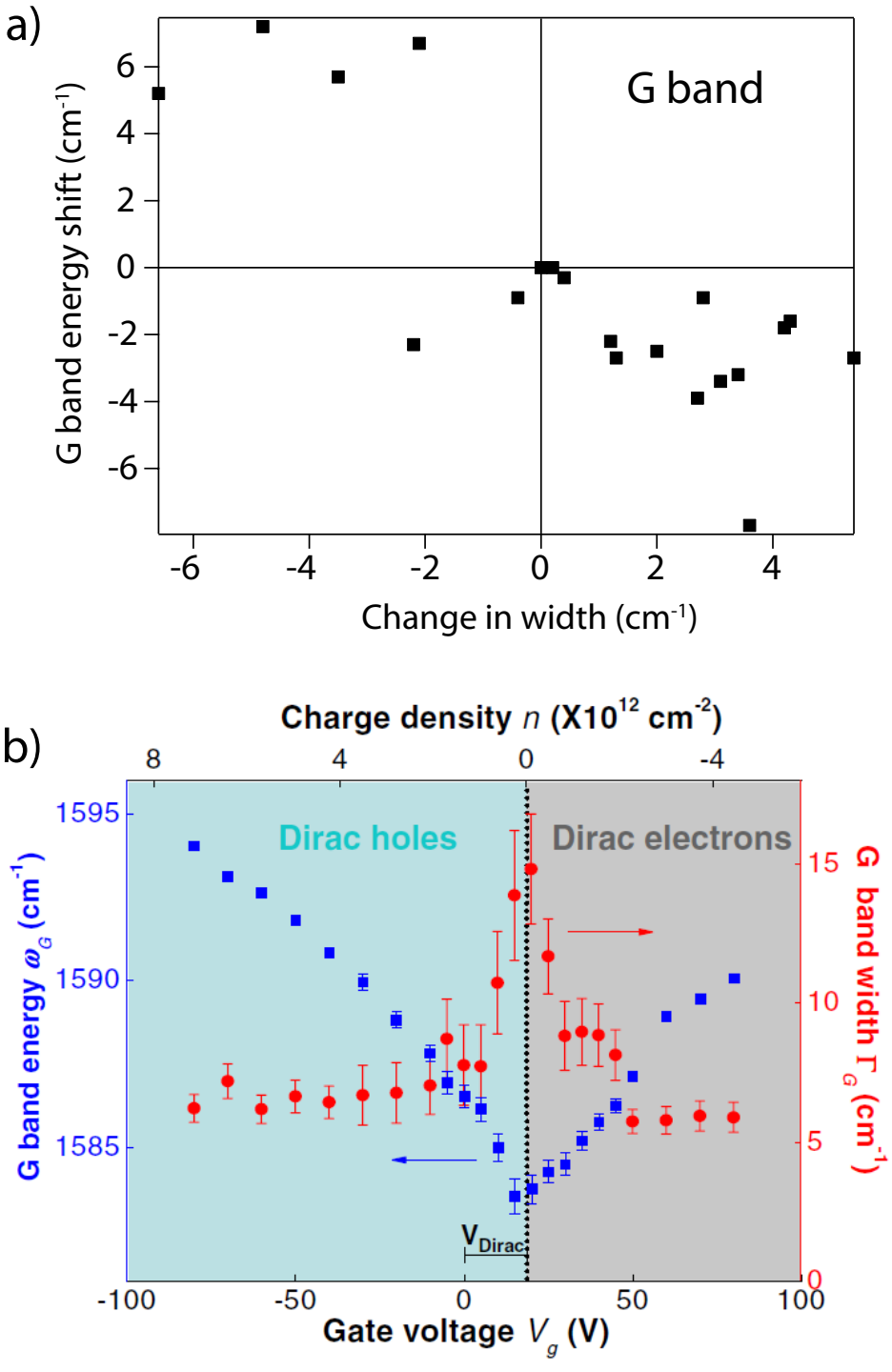

Figure 2.9 – ***Effect of Sn on the position and width of the G band. a)*** *observed shift in the position and width of the Raman G band of graphene after decoration with Sn.* ***b)*** *Experimental data from [75] showing the evolution of the G band upon electrostatic doping.*

2.2 The Josephson effect

In this section, concepts related to the superconducting proximity effect and DC/AC Josephson effect will be introduced. The mechanism of Andreev reflections in SNS Josephson junctions and the particular case of graphene will be addressed.

2.2.1 DC Josephson effect

The Josephson effect is the occurence of a supercurrent through a thin tunnel barrier separating two superconductors [118, 119]. Such a Superconductor-Insulator-Superconductor (SIS) structure is called a Josephson junction and it has remarkable properties. The I(V) characteristic of such a device follows very simple mathematical rules. Suppose that two superconductors of wave function $\Psi_L = \Delta_L e^{j\phi_L}$ and $\Psi_R = \Delta_R e^{j\phi_R}$ for the left and right electrode, respectively, are connected via a thin insulating junction. The supercurrent in the junction is related to the difference in the phases of the two superconducting electrodes :

$$I_S = I_C \sin(\varphi) \tag{2.2}$$

Where $\varphi = \varphi_L - \varphi_R$ is the superconducting phase difference, and I_C, the 'critical' current, is a junction-dependent quantity. When the junction carries a voltage, this voltage is also related to the superconducting phase difference :

$$V = \frac{\hbar}{2e}\frac{\partial \varphi}{\partial t} \tag{2.3}$$

Where V is the voltage drop over the Josephson junction. These relations are non-linear and allow for the realization of complex functions. Two Josephson junctions in parallel form what is called a superconducting quantum interference devices, or 'SQUID' [120], which is the ultimate magnetic flux detector.

SIS junctions are not the only systems exhibiting these properties. Similar behavior is observed whenever two superconductors are weakly coupled electrically. There are many ways to realize this 'weak link'. It can be a thin ($\approx$ 1 nm) insulating layer (SIS structure), a normal metal (SNS), a superconductor with a lower critical temperature (SS'S), a ferromagnet (SFS), a molecule, a carbon sp^2 allotrope, a simple 'neck' in a bulk superconductor (Dayem bridge), a point contact, and any structure whereby a region of strong superconducting phase gradient/supercurrent density is created.

Whenever such a structure is encountered, some modified version of the Josephson relations (2.2) [121], and (2.3) apply.

Although very similar in their manifestation, the microscopic processes involved in the Josephson effect differ in the different varieties of Josephson junctions. While a microscopic understanding of the SIS structures was reached early on [122], the tunneling formalism wasn't adapted to treat the various configurations in which the

Josephson effect is encountered. In particular, the properties of long SNS junctions at arbitrary temperatures have only been fully understood in the late 90's [123].

2.2.2 Properties of SNS Josephson junction

Here the properties of S-(Normal metal)-S (SNS) junctions will be described. A couple of relations that will be used later in the manuscript will be derived. The specific properties of graphene-based Josephson junctions (S-g-S) will be touched upon next.

2.2.2.1 Proximity effect and Andreev reflections

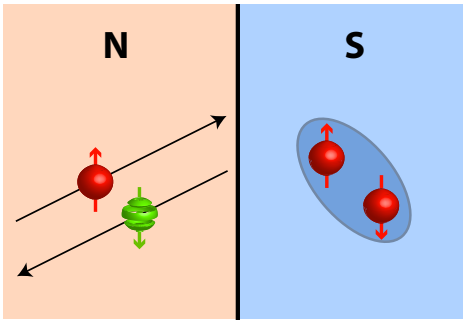

Figure 2.10 – *Schematic picture of an Andreev reflection.*

In SIS structures, the Josephson effect can be understood as a tunneling process, which probability decreases exponentially with distance. This is why only very thin SIS structures can exhibit a measurable supercurrent. SNS structures behave quite differently. Even though there is no pairing potential for Cooper pairs inside the normal metal, proximity supercurrent survives on length scales much larger than the coherence length in the superconductors, typically over microns. The mechanism involved cannot be limited to tunneling. The question at hand here is how charge transfers through a S/N interface. De Gennes [124] showed that superconducting correlations 'leak' inside a normal metal in contact with a superconductor. How is it possible for an electron at the Fermi energy in the normal metal to enter the superconductor, where there is an energy gap ? The microscopic picture was proposed by Andreev [125].

Andreev reflections occur at the interface between the normal metal (N) and the superconductor (S) (see Fig.2.10). The electron coming from the normal metal is retro-reflected as a hole with oposite $\mathbf{k}$ vector, opposite spin and opposite energy with respect to the Fermi level. The outcome of this process is a net charge transfer of $2e$, an energy transfer of $2E_F$, zero momentum transfer and zero spin transfer. This is equivalent to transmitting a Cooper pair.

It should be noted here that the momentum conservation is an approximation, only valid if the superconducting gap Δ is much smaller than the Fermi energy E_F, meaning that it cannot affect the kinetic energy of the incident electron significantly.

The electron and the reflected hole travel along time-reversed paths, which means the Andreev reflection correlates electron-hole pairs ('Andreev pairs') inside the normal metal. As such, it is equivalent to the *diffusion* of Cooper pairs in the normal metal. The Josephson effect emerges when the phase-coherence of the Andreev pair is conserved until the hole is reflected back as an electron, thus closing the loop.

2.2.2.2 Coherence length in the normal metal

Although a rigourous derivation of this quantity involves quantum mechanics [124], we can arrive at the same result using a more qualitative and intuitive approach [126].

Because of the band dispersion relation, the reflected hole may not have exactly the same wave vector as the incoming electron. They only have exactly opposite **k** vectors directly at the Fermi energy (see Fig.2.11). As a result of this **k** vector mismatch, electron and hole will acquire a phase shift which will eventually break the Andreev pair at an energy-dependent distance from the N/S interface [126], which depends on the diffusion coefficient :

$$L_\epsilon = \sqrt{\frac{\hbar D}{\epsilon}} \tag{2.4}$$

What this means is that the Andreev pair loses coherence when the influence of the superconductor cannot be felt anymore, *i.e.* when the Thouless energy :

$$E_{Th} = \frac{\hbar D}{L_\epsilon^2} \tag{2.5}$$

becomes smaller than the pair energy ϵ.

This energy-dependent superconducting coherence length in the normal metal is bounded by the (single-electron) phase-breaking length L_ϕ. To describe the Josephson effect, one should only consider the whole electron distribution at thermal equilibrium [126]. The relevant energy scale is therefore the thermal energy and the decoherence length is the thermal length :

$$L_T = \sqrt{\hbar D / 2\pi k_B T} = \xi_N \tag{2.6}$$

From now on we will refer to that quantity as the superconducting coherence length in the normal metal ξ_N.

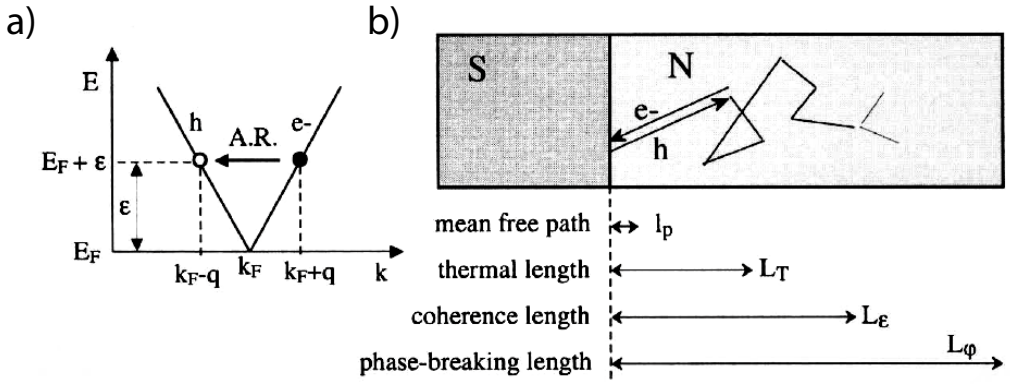

Figure 2.11 – ***Coherence of the Andreev pair in a normal metal.*** ***a)*** *The incident electron and reflected hole have a slight wave-vector mismatch* $2q$. ***b)*** *Relevant length scales in the normal metal. At the coherence length* L_ϵ*, the electron and hole have acquired a phase difference of order* π*. Taken from [126].*

2.2.2.3 Critical current in short and long SNS junctions

Two things determine the critical current of an SNS junction. First, if the junction length L is larger than the coherence length $\xi_N(T)$, the critical current is exponentially reduced. Second, once $\xi_N(T) > L$, what limits the critical current is the number of available Andreev states. The number of such states is proportional to the density of state, *i.e.* inversely proportional to the normal state resistance, and to the energy range up to which they can form. We have seen that the Thouless energy sets an upper limit to that range. Andreev pairs with an energy higher than the Thouless energy $E_{th} = \hbar D/L^2$ do not remain coherent across the sample. The superconducting gap of the electrodes $\Delta(T)$ is another bound. Above that energy, the electrons do not undergo an Andreev reflection, but directly enter the superconductor. Therefore, if the Thouless energy E_{Th} of one junction is larger than the zero temperature superconducting gap Δ_0 of the electrodes, what will eventually limit the critical current is the superconducting gap, whereas in the opposite case it will be the Thouless energy. This is what Fig.2.12 shows, where we can see that, in the left branch (long junctions), the critical current is proportional to the Thouless energy ϵ_c.

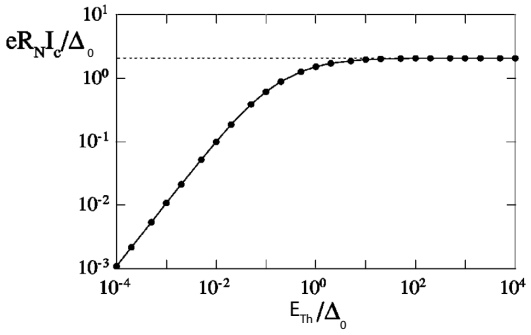

Figure 2.12 – *Evolution of the $R_N I_C$ product as a function of the Thouless energy ($\propto L^{-2}$) at $T = 0$ K. Taken from [127].*

This shows that there is an important distinction between the so-called 'short' junctions $L << \xi_N(T_C) \equiv E_{Th} << \Delta_0$, and the long ones. In the short junctions, the critical current is immediately limited by the superconducting gap $\Delta(T)$. They behave in temperature exactly like constrictions in a superconductor, which means they follow the Kulik-omel'yanchuk (K-o) dependence [128], which is close to the Ambegaokar-Baratoff (A-B) dependence for tunnel junctions. This is what is shown in Fig.2.13. Fig.2.13a shows the temperature dependence of SNS junctions of various lengths. one can see that the shortest junctions have the same dependence as the one predicted by K-o for constrictions (Fig.2.13b), which is close to the A-B dependence in the high temperature regime. The zero temperature critical current for a short SNS junction is given by :

$$I_{c0}^{K-o} = 1.3\frac{1}{R_N}\frac{\pi}{2}\frac{\Delta(0)}{e} \tag{2.7}$$

For long SNS junctions, it is given by [127] (see Fig.2.12) :

$$eR_N I_c(0) = 10.82E_{Th} \tag{2.8}$$

Whereas the K-o theory does not give any simple expression for the temperature dependence of a short SNS junction, a good high temperature approximation is the A-B law :

$$I_c^{A-B}(T) = \frac{1}{R_N}\frac{\pi}{2}\frac{\Delta(T)}{e}\tanh\left(\frac{\Delta(T)}{2k_BT}\right) \tag{2.9}$$

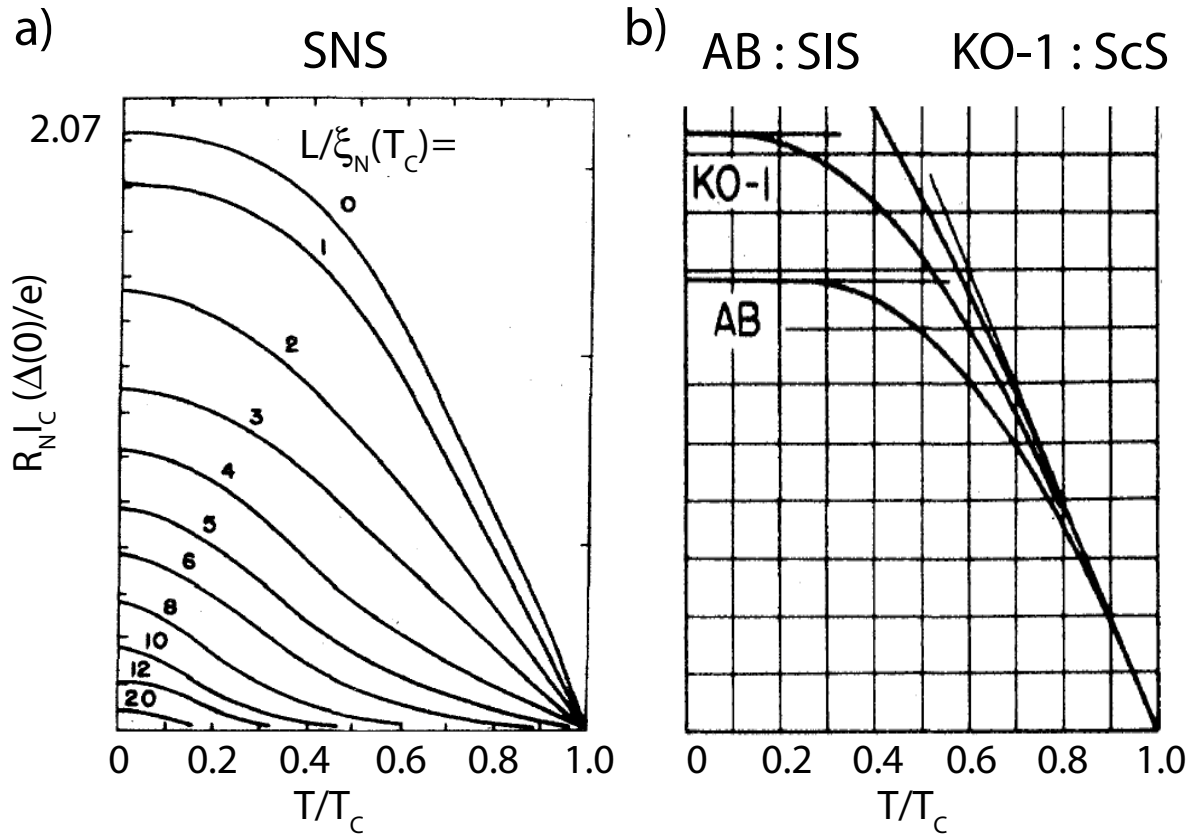

Figure 2.13 – ***Temperature dependence of the I_CR_C product of different Josephson weak links.*** ***a)*** *SNS junctions of different lengths.* ***b)*** *SIS junctions (A-B theory [129]) and constrictions ScS (K-o theory [128]). Taken from [130].*

Finally, the temperature dependence of long SNS junctions is a bit more complicated. As long as $\xi_N(T) < L$, their critical current is exponentially reduced [123, 127] :

$$I_c^{SNS}(T) \propto T^{3/2}\exp\left(-\frac{L}{\xi_N(T)}\right) \tag{2.10}$$

Using equation (2.6), this gives :

$$I_c(T) \propto T^{3/2}\exp(-\sqrt{T}) \tag{2.11}$$

Then when they reach $\xi_N(T) = L$, their critical current increases with the superconducting gap but quickly saturates at the Thouless energy (equation 2.8).

2.2.3 Josephson effect in graphene

Andreev reflection process couples electronic states with opposite $\mathbf{k}$ vectors. Equation (1.14) shows that in graphene, the electronic states with opposite $\mathbf{k}$ vectors (where $\mathbf{k} = \mathbf{K} + \mathbf{q}$), *i.e.* belonging to different valleys, are time-reversal symmetric, providing for a robust proximity effect in graphene. This situation has to be contrasted with that of electrons with an opposite $\mathbf{q}$ vector, that is to say electrons travelling in opposite direction, but belonging to the same valley. In the latter case, chirality plays an important role. This essential difference explains why backscattering can be suppressed in an sp^2 carbon lattice where the disorder only couples states within a valley [49], whereas Andreev reflection is not. The measurement of the first graphene-based Josephson field effect transistor (JoFET) was reported in 2007 by Heersche *et al.* [106], and confirmed the existence of a robust proximity effect in graphene. They demonstrated the existence of a gate-tunable and ambipolar supercurrent in graphene JoFET (see Fig.2.14). The gate-tunable conductivity of monolayer graphene translates naturally into the gate-tunable maximum supercurrent, similarly to what was done in S-2DEG-S junctions [108]. Interestingly, the supercurrent survives even near the charge neutrality point. This is interesting, because when the Fermi level of graphene is close to the Dirac point, the electron and reflected hole should belong to different bands. This process breaks the time-reversal symmetry and should give rise to a novel kind of 'specular' Andreev reflection.

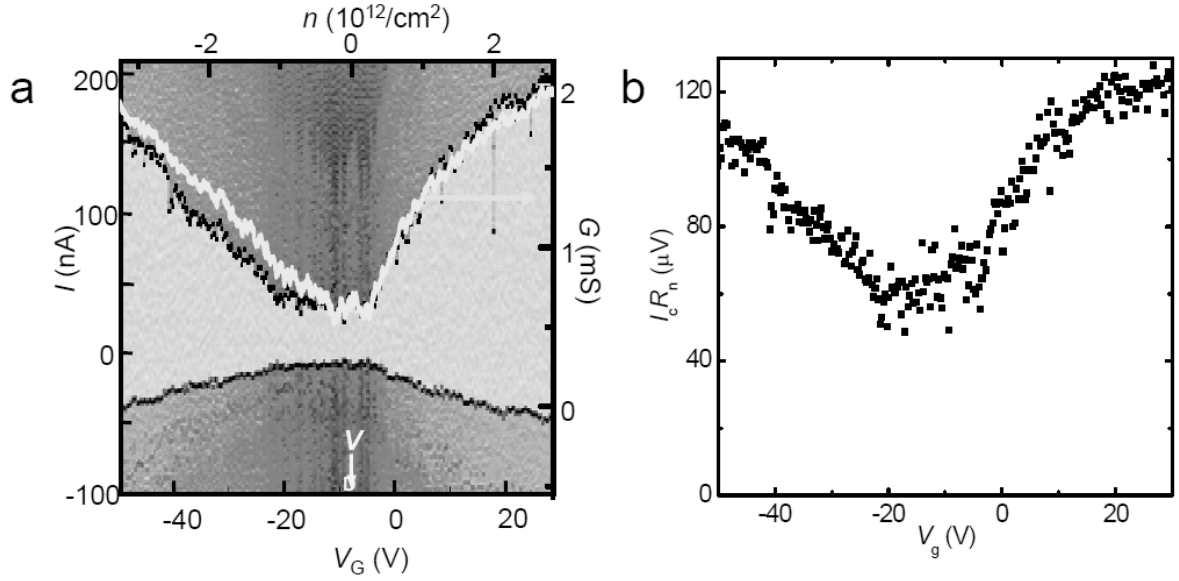

Figure 2.14 – ***Gate-tunable supercurrent in graphene Josephson junctions. Taken from [106]. a)*** *Differential resistance map as a function of gate voltage and bias current. The yellow part corresponds to superconductivity. The blue line is the normal state conductance.* ***b)*** *$I_C R_N$ product extracted from the data in a).*

2.2.3.1 Experiments on S-g-S junctions

Graphene Josephson junctions can be fabricated simply by evaporating superconducting contacts on top of the graphene surface. Unlike most 2DEG heterostructures (with the notable exception of InAs inversion layers [131]), graphene can be directly connected by metal contacts. Ti or Pd underlayers are usually used to ensure that the Schottky barrier is minimized. Despite this, even Pt, a metal which should give a rather large interface barrier with graphene [115], turns out to be compatible with supercurrent after improving the contact by current annealing [132].

Several experiments on S-g-S junctions are reported in the literature. In all experiments, a sturdy gate-tunable supercurrent was observed, even in the vicinity of the Dirac point (see Fig.2.14).

A significant effort was put into fabricating short junctions in order to probe the ballistic regime [106, 107, 132]. However, so far no clear signature of this regime has been obtained, and the transport in these devices seems to be diffusive.

With their very large electron mobility and ease of contact, graphene Josephson junctions are also the ideal testbed for studying the interplay between the quantum Hall effect and superconductivity [111, 133].

2.2.3.2 Specular Andreev reflection

Fig.2.15 pictures how the Andreev reflection is realized in graphene. Fig.2.15a, b and c show the Andreev retro-reflection process, which is similar to what happens in other metals. Like the incoming electron, the reflected hole belongs to the conduction band. The term 'retro-reflection' comes from the trajectory of the reflected hole, which retraces approximately that of the incident electron (Fig.2.15c). The peculiarity of graphene emerges when the Fermi level is near the Dirac point. In that case (Fig.2.15d and e), the reflected hole is taken in the valence band. The particle velocity, proportional to $\frac{\partial E}{\partial k}$, changes sign when one changes from conduction to valence band, therefore the hole is not retro-reflected anymore, but specular-reflected [110].

To observe the specular Andreev reflection, the Fermi level must lie within a narrow energy band around the Dirac point, for the electron-hole pair is formed *at most* a distance Δ_0 from the Fermi energy, where Δ_0 is the superconducting gap. Using the relation $\Delta_0 = 1.76\, k_B T_C$ and taking $T_C = 3.7$ K for the case of Sn, this means the Fermi energy must be within :

$$\Delta_0^{Sn} = 0.56 \text{ meV} \tag{2.12}$$

of the charge neutrality point. Using relation (1.6) and $q = \sqrt{\pi n}$ this means the doping must be smaller than :

$$n^{\max} = 2.57 \times 10^{11} \text{ m}^{-2} \tag{2.13}$$

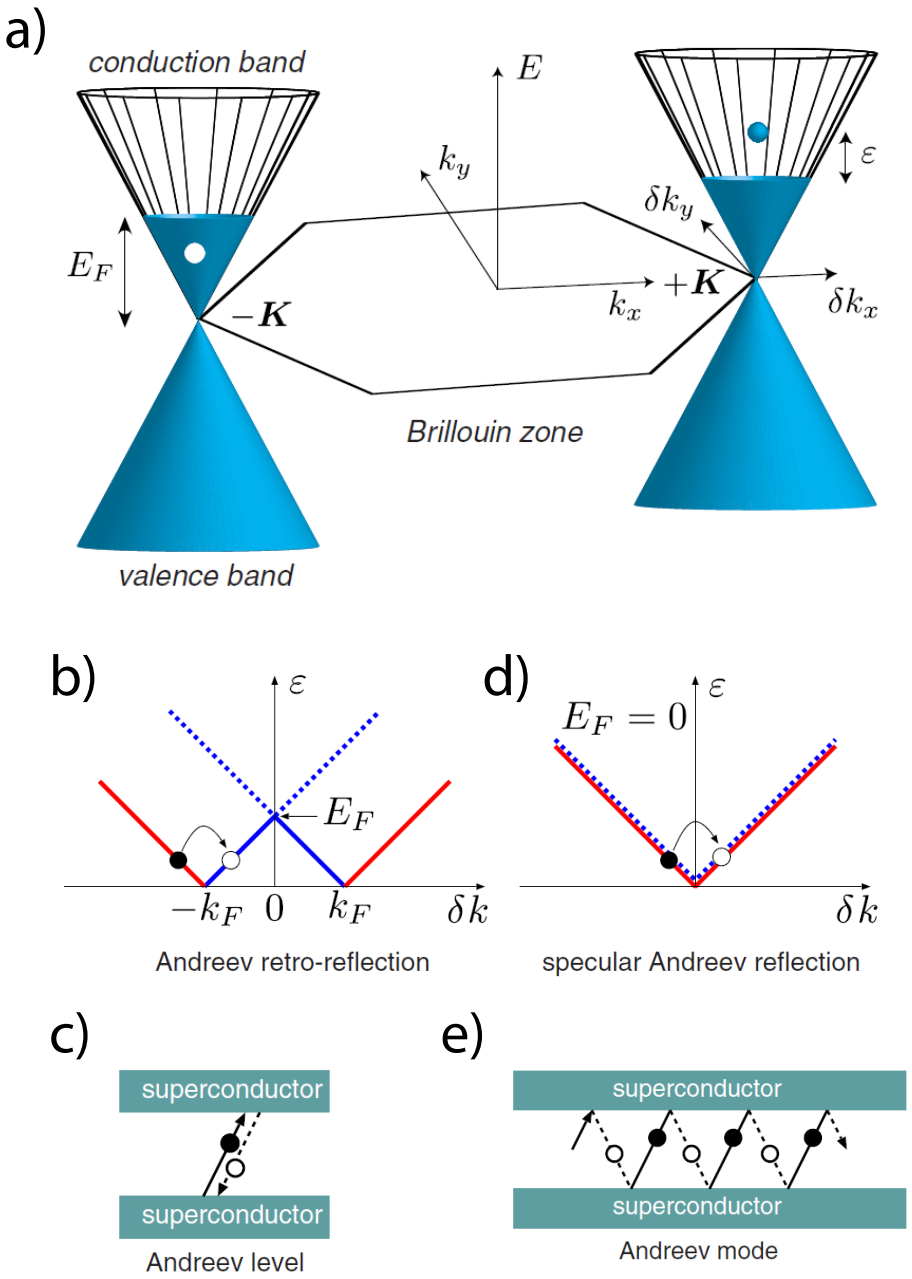

Figure 2.15 – ***Andreev reflection in graphene.*** ***a)*** *Band structure of (electron-doped) graphene showing how an electron and a hole excitations with opposite* $\boldsymbol{k}$ *vectors are converted into each other by the (classical) Andreev reflection.* ***b)*** *The same process is depicted on a simple diagram where the two valleys are superimposed. The blue line is the left valley in a), and the red line is the right valley.* ***c)*** *Trajectories of the retro-reflected Andreev pair in the real space.* ***d)*** *Specular Andreev reflection process, taking place only when the Fermi level* E_F *is close enough to the Dirac point.* ***e)*** *Specular Andreev reflection in the real space. Taken from [134].*

This carrier density actually corresponds to a gate voltage of 0.34 mV with our typical gate capacitance. This value is orders of magnitude smaller than typical carrier density inhomogeneities in graphene (see Fig.1.8). The lowest reported values for the residual carrier density in graphene are on the order of 10^{14} m^{-2} [39]. Although it is very interesting, these stringent conditions make this effect difficult to harness.

Nevertheless, this does not mean it has no influence on the supercurrent. As was shown by Komatsu *et al.* [133] (see Fig.2.16), specular Andreev reflections at the boundary between electron-doped and hole-doped regions in globally neutral graphene could be responsible for the anomalous suppression of supercurrent in the vicinity of the Dirac point in long S-g-S junctions.

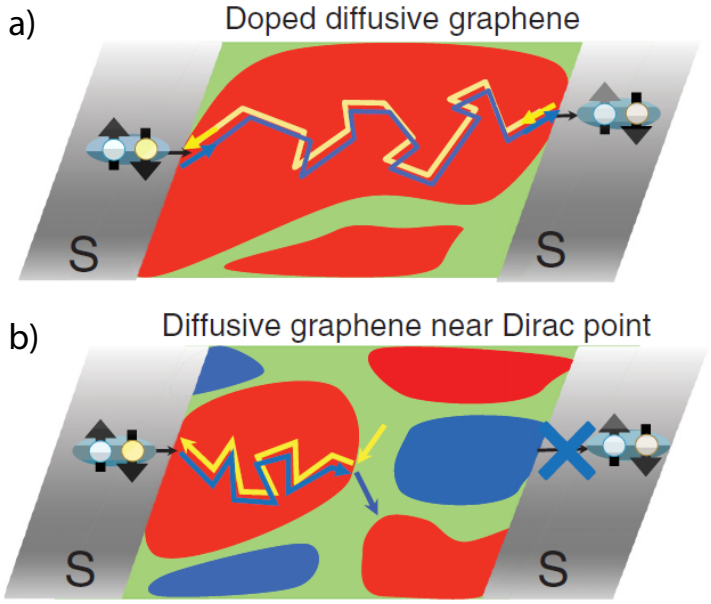

Figure 2.16 – ***Effect of specular Andreev reflection in a long diffusive S-g-S junction.*** ***a)*** *Far from the Dirac point, the Andreev pair travels coherently like in a normal metal.* ***b)*** *Specular Andreev reflection of the Andreev pair at the interface between electron and hole puddles hinders the coherent transport.*

2.2.4 AC Josephson effect

Here a few relations will be derived concerning the response of a Josephson junction to an AC excitation. We will take the simplest case of a tunnel junction, where equation (2.2) and (2.3) are exact. The properties derived here apply to SNS junctions as well, as long as the current-phase relationship is single-valued. It will be shown that when an AC voltage (but this also applies to an AC current) is passed through a Josephson junction at frequency f, plateaus develop in the DC $I(V)$ characteristic of the junction at constant values of voltage, proportional to the frequency f.

If a voltage is present at the ends of a Josephson junction, the phase will vary according to equation (2.3) :

$$\varphi = \varphi_0 + \frac{2eV}{\hbar}t \tag{2.14}$$

Equation (2.2) becomes :

$$I = I_1 \sin(\varphi_0 + \frac{2eV}{\hbar}t) \tag{2.15}$$

For an applied DC voltage, the rotation of the phase implies that the supercurrent now oscillates at frequency $2eV/\hbar$. If one applies an AC voltage instead, $V(t) = V_0 + v\cos\omega_r t$, the phase evolves as :

$$\varphi(t) = \omega_f t + \frac{\omega_f}{\omega_r}\frac{v}{V_0}\sin(\omega_r t + \varphi_0) \tag{2.16}$$

where we have defined $\omega_f = (2e/\hbar)V_0$.

The current $I(t) = I_1 \sin(\varphi(t))$ can be expressed as :

$$I(t) = I_1[\sin(\omega_f t + \varphi_0)\cos(a\sin\omega_r t) + \cos(\omega_f t + \varphi_0)\sin(a\sin\omega_r t)] \tag{2.17}$$

where

$$a = \frac{\omega_f}{\omega_r}\frac{v}{V_0} = \frac{2ev}{\hbar\omega_r} \tag{2.18}$$

Introducing the Fourier-Bessel expansions :

$$\cos(a\sin\omega t) = \mathrm{J}_0(a) + 2\sum_{k=1}^{\infty}(-1)^k \mathrm{J}_{2k}(a)\cos(2k\omega t) \tag{2.19}$$

$$\sin(a\cos\omega t) = 2\sum_{k=0}^{\infty}(-1)^k \mathrm{J}_{2k+1}(a)\cos[(2k+1)\omega t] \tag{2.20}$$

where $\mathrm{J}_k(x)$ are Bessel functions of the first kind of order k, we can re-write the expression for the current :

$$\begin{aligned} I(t) =& I_1[\mathrm{J}_0(a)\sin(\omega_f t + \varphi_0) + 2\sum_{k=1}^{\infty}\mathrm{J}_{2k}(a)\cos(2k\omega_r t)\sin(\omega_f t + \varphi_0) \\ &+ 2\sum_{k=0}^{\infty}\mathrm{J}_{2k+1}(a)\sin[(2k+1)\omega_r t]\cos(\omega_f t + \varphi_0)] \end{aligned} \tag{2.21}$$

Using trigonometric relations :

$$I(t) = I_1\left[\mathrm{J}_0(a)\sin(\omega_f t + \varphi_0) + \sum_{l=1}^{\infty}\mathrm{J}_1(a)\left[\sin[(l\omega_r + \omega_f)t + \varphi_0] + (-1)^{l+1}\sin[(l\omega_r - \omega_f)t + \varphi_0]\right]\right] \tag{2.22}$$

This expression shows that, whenever the relation :

$$\omega_f = \frac{2e}{\hbar}V_0 = \pm n\omega_r \tag{2.23}$$

is satisfied, *i.e.* whenever a DC voltage $V_0 = \pm n\omega_r\hbar/2e$ is present, a DC supercurrent can flow. Its magnitude is given by :

$$I_n = I_1 \mathrm{J_n}\left(\frac{nv}{V_0}\right)\sin\varphi_0 \tag{2.24}$$

Lets consider that an AC voltage of a given amplitude v and at a given frequency ν is being applied to the sample (either directly or shined by an antenna). We bias the sample with a constant low current. Since no voltage is applied, the condition (2.23) is fulfilled, with $n = 0$. A DC supercurrent :

$$I_0 = I_1 \mathrm{J_0}\left(0\right)\sin\varphi_0 \tag{2.25}$$

can thus flow. As the bias is increased, the phase φ_0 accomodates the biased current until it reaches the maximum value $I_0 = I_1\left|\mathrm{J_0}(0)\right|$. A finite voltage then appears. When the voltage reaches $V_J = \dfrac{hf}{2e}$, equation (2.23) is satisfied again and any additional current biased inside the junction will be taken up by Cooper pairs and induce no more voltage drop : we have reached a plateau. In a current-biased experiment, what equation (2.23) tells us is that whenever the Josephson frequency ω_f matches an harmonic of the AC voltage frequency it locks on it, and any additional current is transported by Cooper pairs. This means that when an external radiation is present, pair tunneling processes are possible, in which a pair absorbs or radiates n photons of frequency ω_r. The maximum probability for this process is realized when the relation (2.23) is satisfied.

2.3 Josephson junction arrays

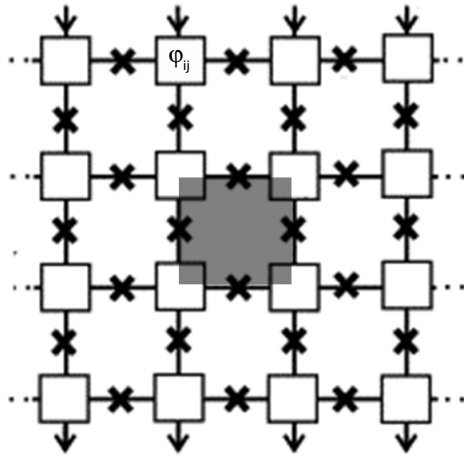

Figure 2.17 – *Schematic picture of a Josephson junction array. Each superconducting island is defined by its superconducting phase φ_i. The shaded region in the center represents the unit 'cell' of the array.*

In this section, the formalism of Josephson junctions arrays will be briefly introduced. We will see that a particular kind of superconducting transition arises, characterized by the presence of vortex-antivortex pairs.

Let's consider an array of superconducting islands connected by Josephson junctions in a square array (Fig.2.17). Each superconducting island has a phase φ_{ij} and the phases of neighbouring islands are coupled to each other by the energy $U = E_J(1 - \cos\Delta\varphi_{ij,kl})$, where :

$$E_J = \Phi_0 I_c / 2\pi \tag{2.26}$$

is the Josephson energy, $\phi_0 = h/2e$ is the flux quantum and I_c is the junction's critical current. The total energy of the system therefore can be written [135] :

$$H = E_J \sum_{ij} \sum_{(k,l)\in \mathrm{nn}} (1 - \cos\Delta\varphi_{ij,kl}) \tag{2.27}$$

Where 'nn' stands for 'nearest neighbours'. Under zero magnetic field, the ground state of the system (energy minimum) corresponds to all the phases being aligned.

2.3.1 Berezinskii-Kosterlitz-Thouless transition

A simple topological excitation can be constructed by adding one flux quantum Φ_0 inside one cell (Fig.2.18). The presence of this magnetic flux adds the following constraint : the superconducting phase along any contour line enclosing the magnetic flux undergoes a 2π rotation. This results in concentric rings of supercurrent trying to screen out the magnetic flux.

The energy of this so-called 'vortex' is the total kinetic energy of these supercurrents [135] :

$$E = \pi E_J \ln\frac{R}{a} \tag{2.28}$$

where a is the lattice constant and R is the outer radius of the vortex. This radius will be

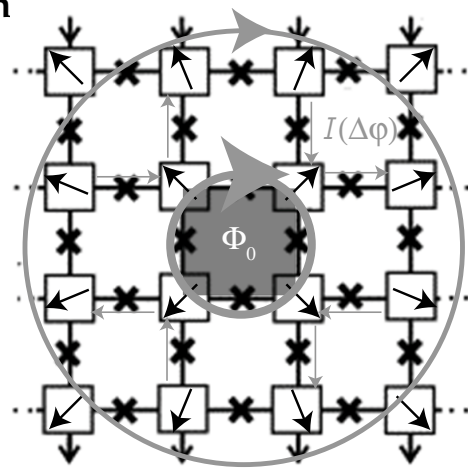

Figure 2.18 – *The presence of a magnetic flux quantum in the central cell puts a contraint on the phases (arrows). The resulting rings of supercurrent try to screen out the magnetic flux.*

bounded, either by the sample size, or by the screening length $\lambda_\perp$. At zero magnetic field, the condition of no net flux imposes that there can only be as many positive vortice as negative ones (with opposite flux).

The presence of free vortices in the system is associated with dissipation. This is because, when current is biased through the sample, the vortices start to move in response to the Magnus force (see box). As is well known, an electromotive force results from a change of flux, which is the case when a vortex moves. Therefore, applying a current in the presence of free vortices engenders dissipation.

Magnus force exerted by a current of charge on a magnetic flux

The Magnus (or gyroscopic) force is the force, perpendicular to its motion, that a spinning body experiences in a fluid. By analogy, we call Magnus force the force exerted by the current on a magnetic moment. Its origin lies in the Lorentz force. Although the Lorentz force describes the force exerted by a magnetic field on a moving charge, we can take the alternative view. Considering the biased current as the irremovable quantity, and the third law of Newton, the reciprocal force thereby exerted on the magnetic moment $\mathbf{m} = m\mathbf{e_z}$ by the charge carrier speed density $\mathbf{v} = v\mathbf{e_x}$ is :

$$\mathbf{F} = \mathbf{v} \wedge \mathbf{m} = F\mathbf{e_y} \tag{2.29}$$

It is perpendicular to the direction of the current.

Let's consider two vortices of opposite sign (vorticity). If we take the path integral of the phase on a contour enclosing the two vortices, it is equal to zero, because no net flux threads that surface. Therefore, the energy of this vortex pair is bounded by the pair size R_{12} :

$$E_{12} = 2\pi E_J \ln \frac{R_{12}}{a} \tag{2.30}$$

Since this energy increases with increasing distance, it gives rise to an *attractive* force. Therefore, vortex and anti-vortex are bound together and no free vortices exist at zero temperature. At finite temperatures, vortex pairs can be thermally excited, with activation energy $\cong 2\pi E_J$. Therefore, the critical temperature T_{BKT} at which vortex-antivortex pairs start to proliferate is given by :

$$k_B T_{BKT} = \frac{\pi}{2} E_J(T_{BKT}) \tag{2.31}$$

Where $E_J(T_{BKT})$ depends on the temperature through the dependence of I_c. There is a trade-off between the increased entropy resulting from the presence of free vortices, and their energy cost. The equilibrium corresponds to a minimum in the free

energy $F = E - TS$. In the regime of free vortices proliferation, flux-flow dissipation leads to an ohmic ($V \propto I$) characteristic. The resistance, which is proportional to the vortex population, grows as :

$$R(T) \propto \exp\left(\frac{b}{\sqrt{T - T_{BKT}}}\right) \tag{2.32}$$

Below T_{BKT}, the finite energy barrier correponding to the vortex-antivortex binding energy needs to be overcome before the sample can dissipate energy through vortex motion. The biasing current overcomes that barrier when the opposite Magnus force exerted on the vortices and anti-vortices breaks them apart. This gives rise to a non-linear V(I) characteristics : $V \propto I^{a(T)}$, with $a(T_{BKT}) = 3$ and growing. At T_{BKT}, the exponent a jumps from 1 to 3. This is considered to be the hallmark of the BKT transition.

2.3.2 London penetration length

It is important to remember that the BKT results [4] are only strictly applicable to neutral superfluids, like helium films. However, Beasley *et al.* [5] showed that, if the supercurrents are small, their effect on the vector potential is negligible, and the dynamics of vortices is governed by the superfluid velocity field only, as if the superfluid was electrically neutral. This condition can be restated as the absence of screening, or in other words, as the London penetration length $\lambda_\perp$, which is the length over which the magnetic field gets screened by supercurrents, being larger than the typical size R_{12} of a vortex-antivortex pair. In thin superconducting films, $\lambda_\perp$ is renormalized : $\lambda_\perp = \lambda^2_{\text{bulk}}/d$, where d is the film's thickness. Similarly, in Josephson junction arrays (JJA), the London penetration length is given by [136] :

$$\lambda_\perp \cong \frac{\Phi_0}{2\pi\mu_0 I_c} \tag{2.33}$$

The exact value depends on the inductance of a cell, which in turn depends on the array geometry.

2.3.3 AC Josephson effect in Josephson junctions arrays

When a microwave radiation is applied to an array of $M \times N$ identical Josephson junctions, giant Shapiro steps equal to N times the amplitude of Shapiro steps for a single junction develop [137] :

$$V_n = n\frac{N\hbar\omega}{2e} \tag{2.34}$$

where N is the array size in the direction of current flow. In real arrays, where all the junctions are never exactly the same, such giant Shapiro steps can still be

observed, because of the mutual phase locking of adjacent Josephson junctions [138]. If the different junctions are too different, however, it is expected that each of them will develop its own steps in the V(I) characteristic, so that the overall voltage response will be smeared out.

2.4 Superconducting properties of Sn/graphene hybrids

In the following section, the low temperature properties of hybrid Sn/graphene superconducting field effect transistors will be discussed, starting with the intrinsic superconducting properties of the Sn nanoparticles. Then, the BKT theory for Josephson junctions array will be used to account for the superconducting transition temperature. The critical current and AC Josephson effect will also be addressed. When possible, a comparison will be made between the properties of different surface morphologies : the tight arrays, like those prepared by Kessler *et al.* [113] (Fig.2.19a), and the loose arrays fabricated on ultra-clean surfaces (Fig.2.19b) (see Table 2.1). The critical current and the AC Josephson effect data seem to indicate that the properties of the array are dominated by its weakest link. Some facts are so far not fully understood, most notably the behavior of the voltage-carrying state, which resembles a flux-flow regime.

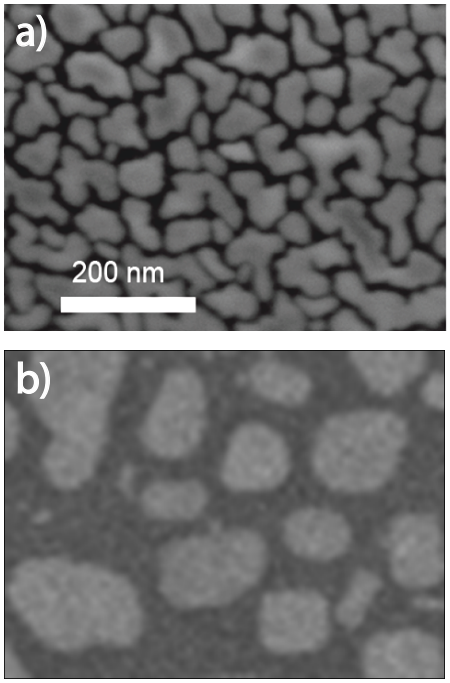

Figure 2.19 – ***Two cases are addressed.*** ***a)*** *Tight array of Sn islands, which results from the evaporation on a dirty surface.* ***b)*** *Loose array when Sn is evaporated on freshly cleaved graphene.*

2.4.1 Superconducting properties of Sn nanoparticles

2.4.1.1 Critical temperature

The question of superconductivity in the confined environment of the Sn islands is dealt with first. One can indeed wonder what happens when the grains are smaller than the superconducting coherence length of Sn $\xi_0^{Sn} \cong 230$ nm. Anderson [139] showed that the intrinsic superconducting properties of the grains remain unaffected as long as the superconducting gap Δ_0 is greater than the average energy-level spacing in the grain. Because of the confinement, the energy-level spacing is inversely proportional to the volume V : $\delta \propto V^{-1}$. For the case of Sn, an energy-level spacing of 1 K is reached in spherical grains of diameter $d = 10$ nm (see Fig.1 in [140]). In our case, the typical island's volume would be about $10\text{ nm} \times \pi \times (50\text{ nm})^2$, giving a volume about 150 times larger, which means an energy-level spacing on the order of 10 mK, much smaller than the T_C. Sn/graphene hybrids always start exhibiting superconductivity-related behavior around 3.7 K, which is the bulk T_C of Sn, confirming that the intrinsic superconducting properties of Sn are unchanged.

2.4.1.2 Critical magnetic field

Before diving into the results and discussions, how the devices respond to a magnetic field at low temperature will be briefly shown. This gives a better vision of the intrinsic properties of Sn islands in our system, and brings support to the fact that the system behaves like an array of Josephson junctions.

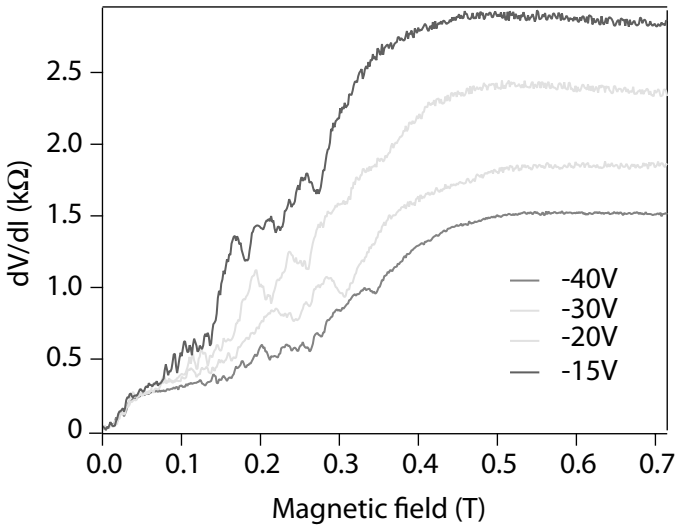

Figure 2.20 – *Differential resistance as a function of magnetic field for various gate voltages at $T = 100$ mK.*

Fig.2.20 shows the magnetic field response of the system for several different gate voltages near the base temperature of the dilution fridge ($T = 100$ mK). It can be seen that the sample recovers its normal state resistance at magnetic fields of the order of $B_C \approx 0.5$ T. This value is much larger than the bulk critical field of Sn, which has been measured to be of the order of 30 mT [114]. Although it is known that quantum confinement can enhance the superconducting gap [141], this is not sufficient an explanation for such a large increase. Especially since the T_C is unchanged, as will be demonstrated later. This enhancement of B_C has already been observed in Sn/SnO_x core-shell nanospheres [142] and can be qualitatively accounted for using the theory of Beloborodov *et al.* [143] for granular superconductors. Let's consider a Sn island of radius $r = 100$ nm and height $h = t/c \cong 20$ nm, where $t = 10$ nm is the nominal thickness evaporated and $c \cong 0.5$ is the surface coverage. The mean free path in a nanometer-sized cristal can be approximated to be $l_e \cong 3h$ [144]. According to [143], the necessary magnetic field to completely suppresse the gap in grains of radius r (in the case of cylindrical grains, the correction factor is of order 1 [145] is :

$$B_C = \frac{\Phi_0}{r}\sqrt{\frac{15}{\xi_0 l_e}} = 0.65 \text{ T} \tag{2.35}$$

Another striking feature in Fig.2.20 is that, at intermediate magnetic fields, the dif-

ferencial resistance shows a pseudo-periodic modulation of the resistance with magnetic field. This effect is well documented [135] and arises due to magnetic frustration of the superconducting phase lattice by the magnetic field. A similar effect was observed by NGuyen *et al.* [146] in a superconducting thin film of Bi in which a regular array of holes was patterned. The periodic feature is related the number of flux quantum per unit cell. In our case, the array is quite disordered (see Fig.2.21b), which is why we see intricate features. Nevertheless, we can identify some periods. Fig.2.21a shows it at a gate voltage of $V_g = 10$ V, where it is quite obvious. The magnetic field is a flux per unit area. Therefore, we can attribute the periodicity in magnetic field $B_p = 73$ mT to the addition of one flux quantum per unit cell and deduce the area of that unit cell :

$$A = \frac{\Phi_0}{B_p} \tag{2.36}$$

Where $\Phi_0 = 2.07 \times 10^{-15}$ Wb is the flux quantum. We find $A = (170 \text{ nm})^2$, which indeed matches the typical dimension of the area enclosed by Sn islands in our system, as is shown in Fig.2.21b, thus supporting the interpretation of the data in the framework of Josephson junctions arrays. Note that for larger samples (and in particular the samples that we'll use in Chapter 3), the disorder averages out this effect.

2.4.2 Critical temperature T_{BKT} in Sn/graphene hybrids

In this part, the BKT transition observed in the two kinds of arrays depicted in Fig.2.19 will be compared : the case of tight arrays of islands (Fig.2.19a) that were studied by Kessler [113, 116], and looser array that results from the evaportation on a very clean surface (Fig.2.19b). First, it is of interest to estimate the value of the screening length $\lambda_\perp$ in these systems.

For the tight array (Fig.2.19), which presumably has junctions with a higher critical current, we can calculate an upper bound to the critical current of a single Josephson junction in order to get a lower bound for the value of $\lambda_\perp$. Assuming that the critical current of the Josephson junction formed between two islands is given by equation (2.7), where the normal state sheet resistivity of graphene is of order 1 kΩ and the typical aspect ratio of the junction is $W/L = 5$, we obtain :

$$I_c \leq 5.73 \times 10^{-6} \text{ A} \tag{2.37}$$

Using this value we can calculate the lower bound to the screening length using equation (2.33) :

$$\lambda_\perp \geq 46 \ \mu\text{m} \tag{2.38}$$

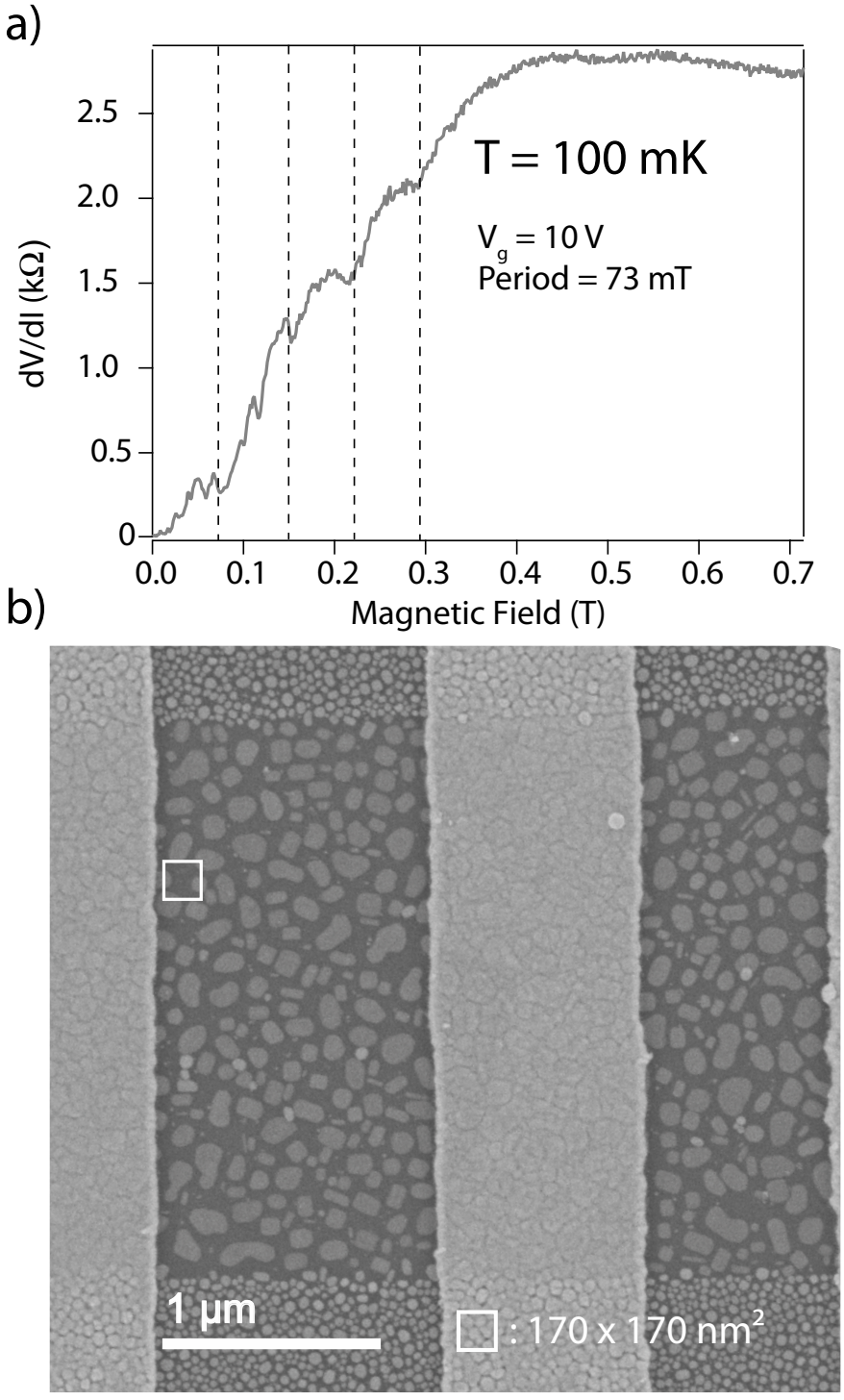

Figure 2.21 – ***Hint of magnetic frustration. a)*** *Differential resistance as a function of magnetic field for a gate voltage $V_g = 10$ V. The periodic modulation in magnetic field can be associated with an area.* ***b)*** *SEM picture of the sample. The squared region corresponds to the area deduced from the periodic modulation in a).*

Both samples are much smaller than the London penetration length, so the range of logarithmic interaction between vortices (validating the BKT treatment) will not be bounded by the screening length, but rather by the sample size (which gives rise to finite-size effects as we will see later). The 'tight array' sample had dimensions $L \times W \cong 10\ \mu\text{m} \times 5\ \mu\text{m}$. The 'loose array' is shown in Fig.2.21b.

2.4.2.1 Tight array of islands

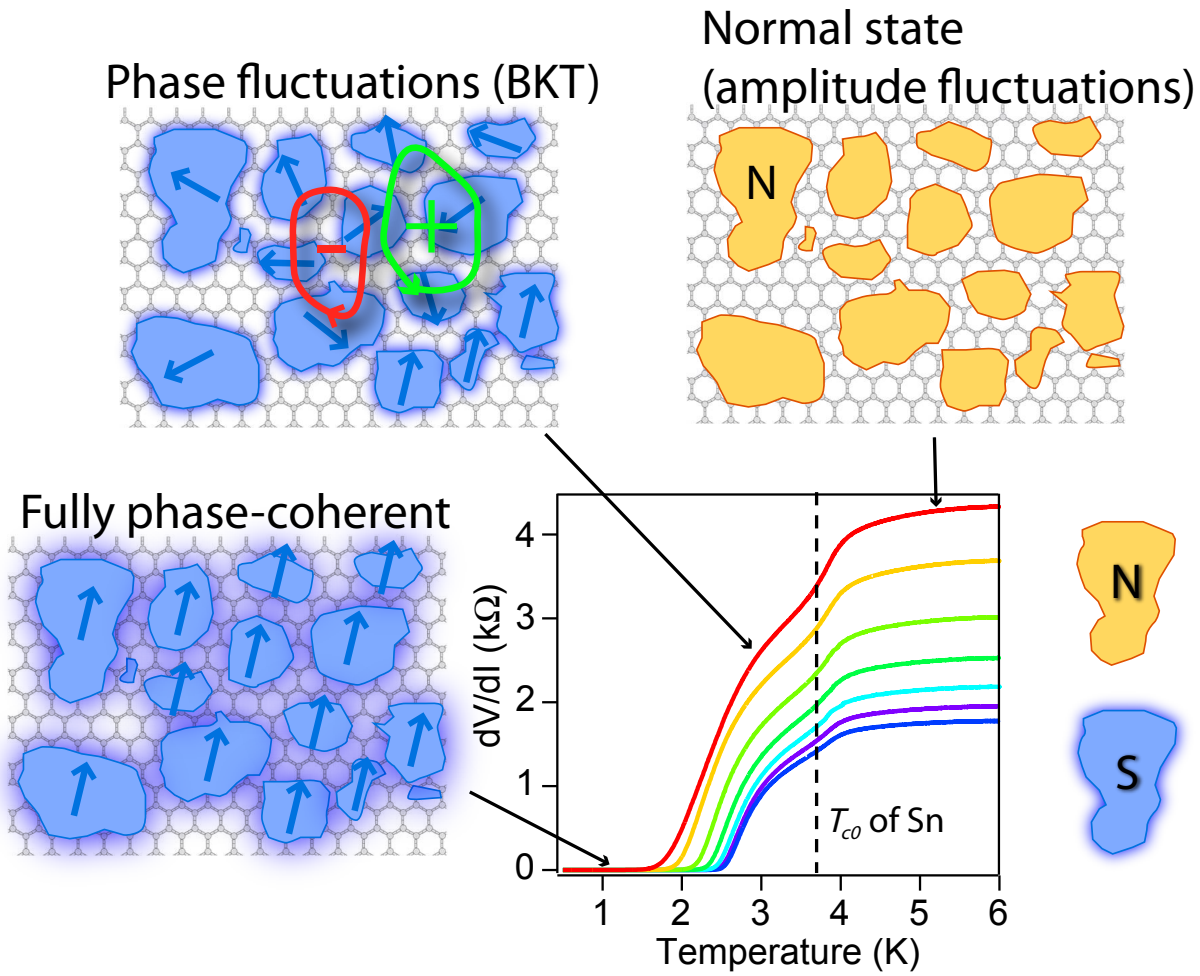

Figure 2.22 – ***Establishement of phase coherence in the tight array.*** *Differential resistance as a function of temperature for different gate voltages in the tight array. The blue arrows represent the superconducting phase, and the glow the proximity effect. Partial drop of the resistivity is associated with the superconducting temperature of Sn islands. In the BKT region, the system is characterized by phase fluctuations.*

Fig.2.22 shows the superconducting transition in tight arrays. The behavior is very similar to other reported BKT transitions in thin superconducting films and networks of weak links [147, 148]. The onset of superconduconductivity in the Sn islands around $T_{c0}^{Sn} = 3.7$K is accompanied by a partial drop in the sheet resistivity. This is due to the immediate influence of the Sn island's superconductivity on the graphene regions situated underneath. The fact that proximity effect already takes place right at T_{c0}^{Sn} is a sign that the tunnel barrier at the Sn/graphene interface is rather low. The fraction of the total resistance represented by this drop is constant but depends on the carrier type (see Fig.2.23). This is an important observation, because it means the height of the potential barrier at the Sn/graphene interface does not depend on gate voltage.

Full superconductivity (zero resistance) sets in at a lower temperature, reflecting

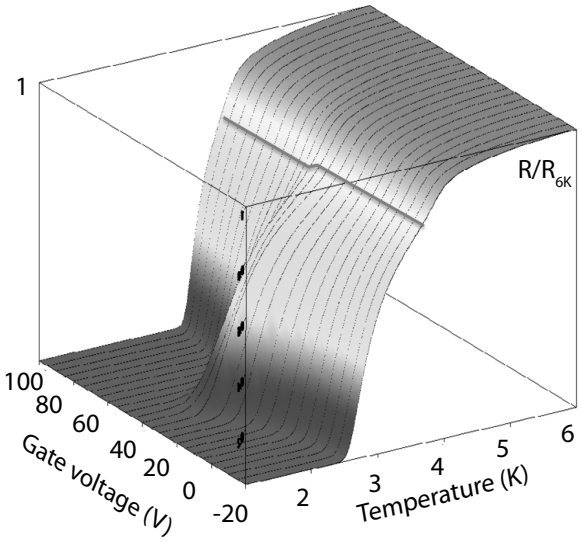

Figure 2.23 – *Differential resistance as a function of gate voltage and temperature, normalized to the value at 6 K. The partial drop of resistance at T_{c0}^{Sn} is outlined. Its value depends on the carrier type.*

the existence of a phase-fluctuant intermediate state. In this regime, the resistance can be fitted using equation (2.32) to yield the critical temperature T_{BKT} of the film.

Using the equations derived in [5] and [149], Kessler *et al.* [113] related the vortex unbinding temperature T_{BKT} to the film's normal state resistance :

$$\frac{T_{c0}}{T_{BKT}}\left[\frac{\Delta(T_{BKT})}{\Delta(0)}\tanh\left(\frac{\Delta(T_{BKT})}{2k_BT_{BKT}}\right)\right]=\frac{\epsilon_\nu R_N}{R_0} \tag{2.39}$$

Where $\Delta(T)$ is the superconducting gap, R_N is the normal state resistance, $R_0 = 8.96\ \text{k}\Omega$ and ϵ_ν is an effective dielectric constant describing the screening of the vortex-antivortex attraction and is used as the only fitting parameter, finding a remarkable agreement with equation (2.39) (Fig.2.24b).

2.4.2.2 Loose array

Fig.2.25 shows the same BKT transition in the sample with a loose array of superconducting islands (Fig.2.19). Whereas the overall behavior is very similar to the previous case of tight array, we notice that the plateau preceding the BKT transition in Fig.2.25c and d is getting broader, and the critical temperature T_{BKT} gets lower. This cannot be an effect of normal state resistance, for it was similar in both samples. Looking at equation (2.39), we can identify the origin of this discrepancy.

This formula (2.39) was derived for the case of superconducting thin films [5, 149]. Using it here amounts to considering that the hybrid Sn/graphene system as an intrinsic superconducting thin film, regardless of the effect of island spacing on the critical current and screening length, which is improper for the case of Josephson junctions array.

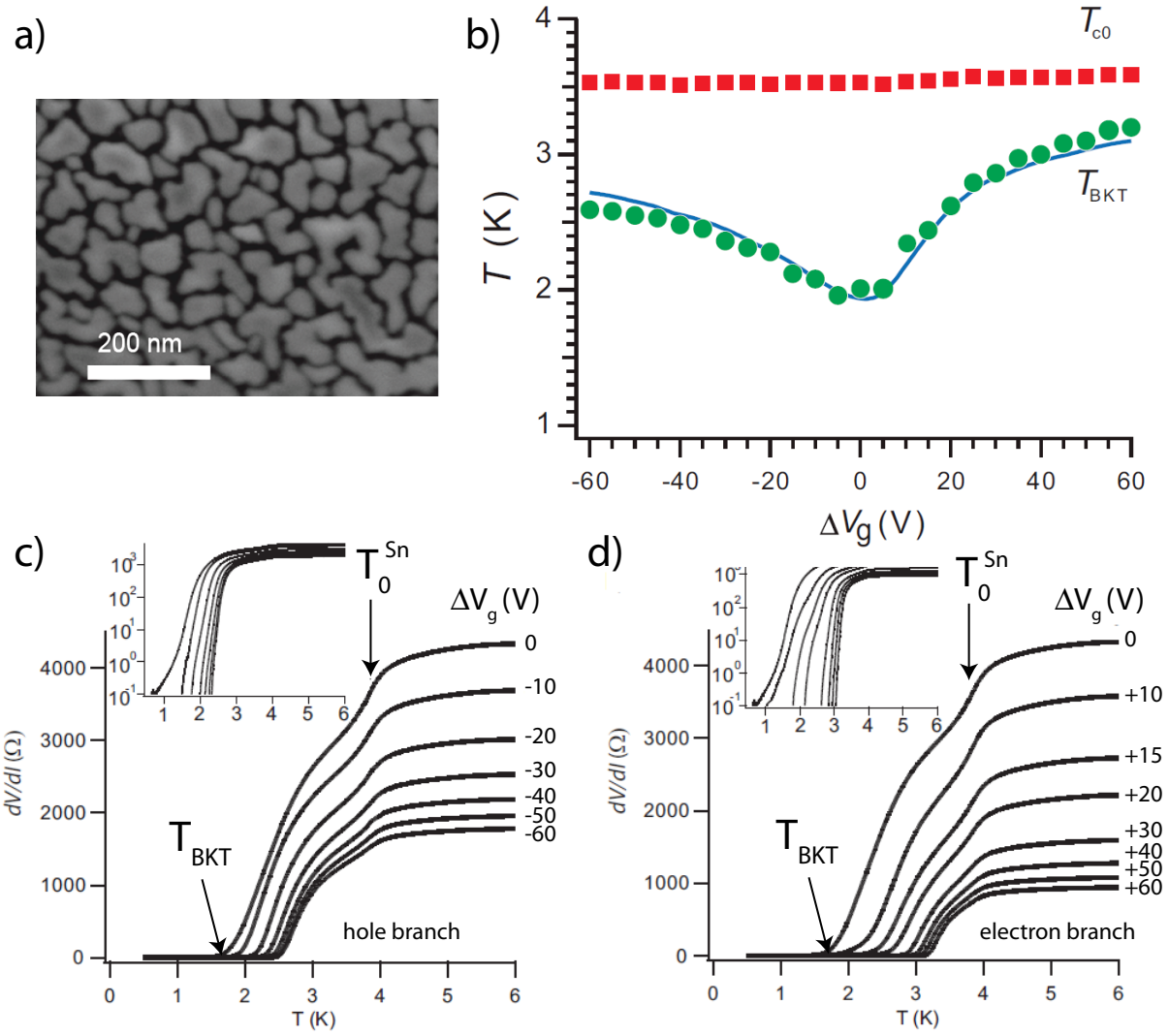

Figure 2.24 – ***BKT transition in Sn/graphene devices. Case of a tight array.*** ***a)*** *SEM image of the sample's surface, showing the high surface coverage and small inter-island gap in the tight array.* ***b)*** *Critical temperatures extracted from the temperature data shown in c and d. Red squares corresponds to the first resistance drop indicated in c and d. This value matches the bulk critical temperature of Sn T_{C0}^{Sn} and marks the onset of superconducting fluctuations. Green dots correspond to the temperature T_{BKT} which corresponds to zero resistivity (see c and d). The blue line is a fit to equation (2.39).* ***c)*** *and* ***d)*** *Differential resistance as a function of temperature recorded at different gate voltages ($\Delta V_g = V_g - V_D$). T_{BKT} marks the onset of zero resistivity. Taken from [116].*

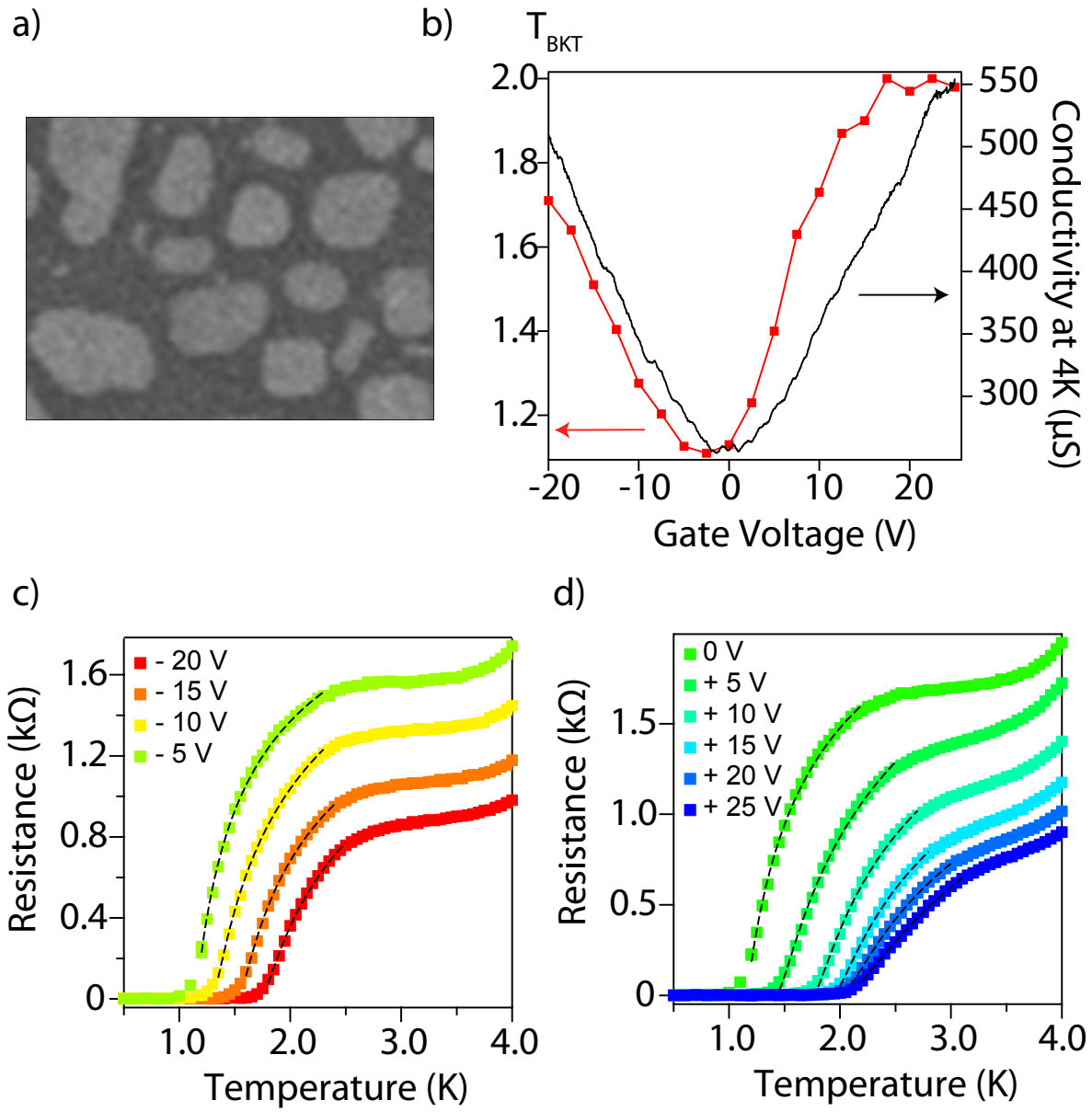

Figure 2.25 – ***Superconducting transition of the graphene sample decorated with a loose array.*** ***a)*** *SEM picture of the surface morphology.* ***b) Red*** *: T_{BKT} extracted from the curves in c and d.* ***Black*** *: conductance at 4 K in the normal state.* ***c)*** *Differential resistance as a function of temperature for different gate voltages on the electron side. Dashed lines are fit to equation (2.32).* ***d)*** *Same thing on the hole side.*

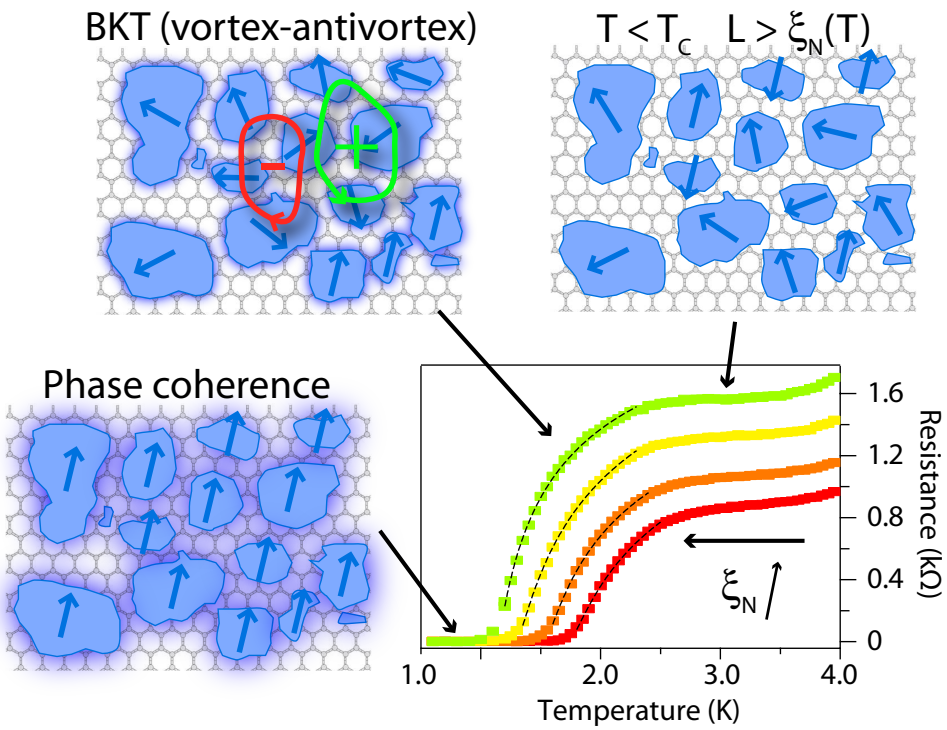

Figure 2.26 – ***Establishment of the phase coherence in the loose array*** T_{c0}^{Sn}. *This time the normal state above* T_{c0}^{Sn} *is not represented. In an array of SNS junctions of lengths greater than* $\xi_N(T_C)$*, a plateau corresponding to the percolation of the proximity effect shows up, before the actual BKT transition can take place.*

Actually, Lobb *et al.* demonstrated [136] that if one expresses the BKT temperature as a function of the Josephson energy (equation 2.31), then express this energy as a function of the A-B critical current (with equations 3.2 and 2.9), one finds the same relationship as (2.39), meaning that this relationship is readily applicable to an array of **tunnel** Josephson junctions with little renormalizations. Now as we have seen in Fig.2.13, the high temperature dependence of the critical current of a short SNS junction is very close to that of a tunnel junction, which is probably why Kessler *et al.* found such a good agreement with (2.39). However, as was already pointed out by Lobb [136], if the array is made of long SNS junctions with critical currents exponentially decaying with length (2.10), the behavior can differ from the standard thin film limit, as depicted in Fig.2.26.

Eley *et al.* [**?**] observed such an effect in arrays of Nb islands on a Au film with varying inter-island spacings (see Fig.2.27). We can estimate the critical length for a short junction in our case, neglecting the influence of the Andreev resistance. The condition is [127] :

$$E_{Th} = \Delta_0 \tag{2.40}$$

This gives a junction length of :

$$L_{short} = \sqrt{\frac{\hbar D}{\Delta_0}} \tag{2.41}$$

Using equation (1.24), for example at $V_g = -20$ V, where the sheet resistivity is 2 kΩ (aspect ratio $L/W \cong 1/2$), the mean free path can be estimated to be of the order of $l_e \cong 30$ nm. This gives us $L_{short} \cong 120$ nm. The typical junction lengths in the tight array are $\cong 20$ nm, as seen from SEM images, and somewhere aroung $50 - 60$ nm in the loose array. These values are somewhat smaller than the value we derived for the short junction length, but this discrepancy could be explained by the presence of a tunnel barrier at the Sn/graphene interface.

Effect of the Andreev resistance

So far, the effect of the resistance of the interface between Sn and graphene, the so-called 'Andreev resistance' hasn't been mentioned. The effect of this potential barrier is to restore some normal reflections at the S/N interface (as opposed to Andreev reflections), thereby decreasing the critical current. One expects that an array with a larger Andreev resistance will tend to show a larger plateau preceding the BKT transition, as if the junctions were longer.
In the case of Sn/graphene, the samples which supposedly had the cleanest surface (the loose arrays, evaporated on freshly cleaved graphene) showed a plateau. Conversely, samples made with CVD graphene, which should have had a higher interface barrier, show a BKT transition immediately following the superconducting transition of Sn islands. This indicates that the graphene's surface cleanliness has a marginal effect on the Andreev resistance, as compared effects relating to the island's morphology.

Fig.2.25b plots together the conductivity at 4 K and the BKT transition temperature obtained in our loose array. Apart from the slight Dirac point mismatch, which we can also explain by the larger island spacing's effect on doping, what we see is that there is no way to fit the whole curve using (2.39) : unlike the previous case, we cannot superimpose the two curves. The best we can do is to fit either the electron or the hole side. This indicates again that the Schottky barrier (Fig.2.23), which hampers the supercurrent, is different on the electron and the hole side, so that they have a different Andreev resistance. While this may not result in a substantial change for the case of very short junctions, if the junctions are already in the long-junction limit, this could have a more drastic effect.

Equation (2.39) is not suited to fit our transition. However, we can still rely on the more general form (2.31) :

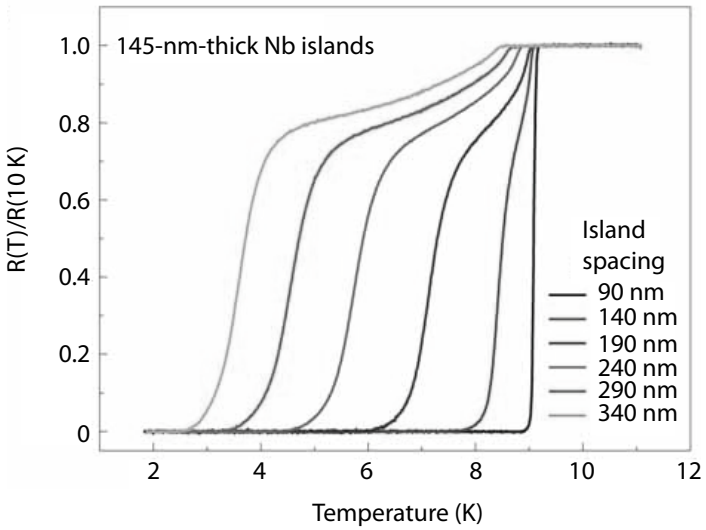

Figure 2.27 – *Normalized resistance as a function of temperature in regular arrays of Nb islands on a Au surface for various array parameters. The BKT transition temperature depends on the inter-island spacing. Taken from [***?** *].*

$$T_{BKT} = \frac{\pi\hbar}{4ek_B} I_c(T_{BKT}) \tag{2.42}$$

Calculating the critical temperature from this relation, however, would require too many assumptions. What we can do instead, is turn the problem around and use this relationship to estimate the effective critical current of a single junction at the transition temperature $Ic(T_{BKT})$. The result of this transformation is plotted in Fig.2.28.

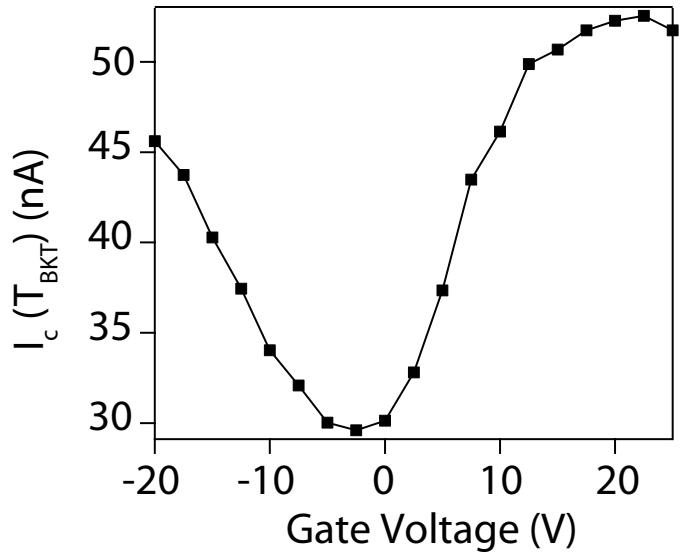

Figure 2.28 – *Calculated critical current at the critical temperature T_{BKT} as a function of gate voltage.*

2.4.3 V(I) characteristic near the transition

As explained in §2.3.1, the V(I) characteristic should undergo a drastic change at the vortex-unbinding temperature T_{BKT}, the exponent $a(T)$ in $V(I) = I^{a(T)}$ jumping from 1 to 3. This is the only irrefutable proof that a superconducting transition is driven by vortex-antivortex physics. For a good example of this jump, see [148].

2.4.3.1 Exponent jump smearing due to inhomogeneities

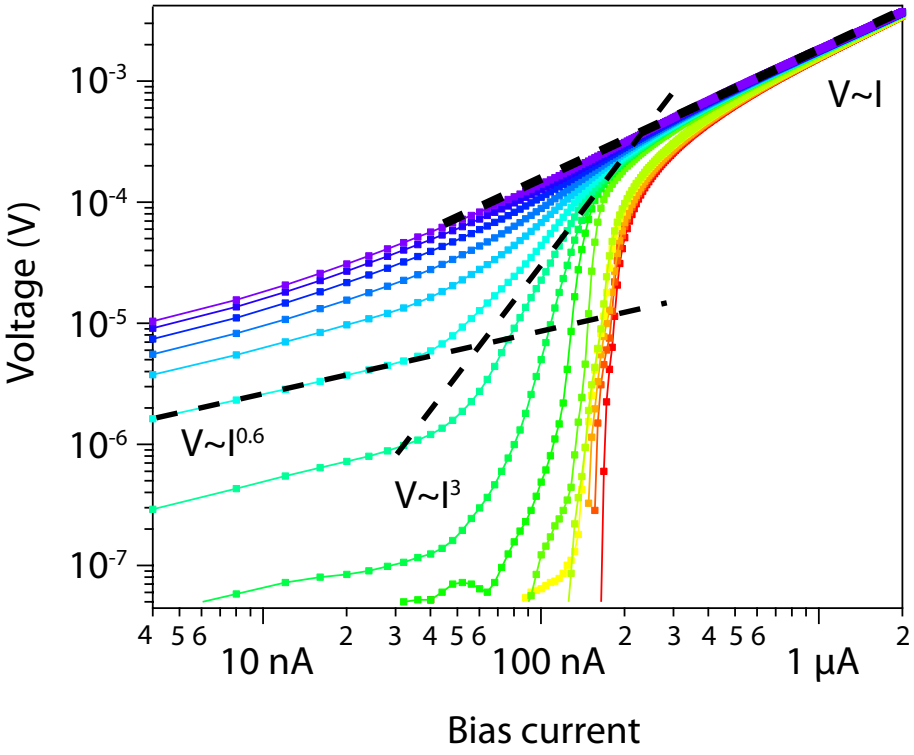

Figure 2.29 – *Log-log plot of the V(I) characteristic for various temperatures around the superconducting transition temperature T_{BKT} for $V_g = 0$ V.* ***Red curve*** *: $T = 100$ mK,* ***Purple curve*** *: 1.5 K. By steps of 100 mK. The dashed lines indicate ohmic behavior ($V \propto I$) expected at high temperatures and at low currents, and $V \propto I^3$ expected at the BKT transition. The behavior at low bias is actually sublinear ($V \propto I^{0.6}$).*

Unfortunately, none of our devices showed a clear jump, but rather a smooth increase (see Fig.2.29). This is not uncommon, as this signature is only rarely clearly observed in real samples [147, 150]. Even a very clean and ordered system like the one of Eley *et al.* shows a very small jump (Supplementary information of [**?**]).

This has been explained [151] to stem from inhomogeneities in the sample. Local fluctuations in the critical current give rise to different local transition temperatures. The result is equivalent to having several BKT systems in series with slightly different critical temperatures. This gives a broadened transition in temperature, but it also

rounds the apparent exponent $a(T)$. In our case, the system is clearly of inhomogeneous nature, so that it is not surprising *not to* observe any jump. In these conditions, qualifying the transition as 'BKT' could seem a bit abusive, but in the absence of an alternative picture, it seems like a reasonable explanation, for the shapes of the superconducting transitions are pretty close.

2.4.3.2 Finite-size effect on the V(I) characteristic

Fig.2.29 shows the V(I) characteristics of a loose array at various temperatures ranging from 100 mK to 1.5 K. We can clearly distinguish a regime of low current ($I_b \leq 40$ nA), where temperature-independent characteristic is sublinear : $V \propto I^{0.6}$, a steep increase of the voltage $V \propto I^{a(T)}$ at intermediate bias current, with a temperature-dependent $a(T)$, and a high bias 'normal' state where the behavior is ohmic ($V \propto I$). Ohmic behaviors at low bias have been reported several times [152, 150]. It is usually ascribed to finite-size effects [152, 153, 154]. When the size of a critical vortex-antivortex pair, which is inversely proportional to the biased current, gets larger than the sample, the activation energy decreases and an ohmic behavior develops at low bias (see Fig.2.30).

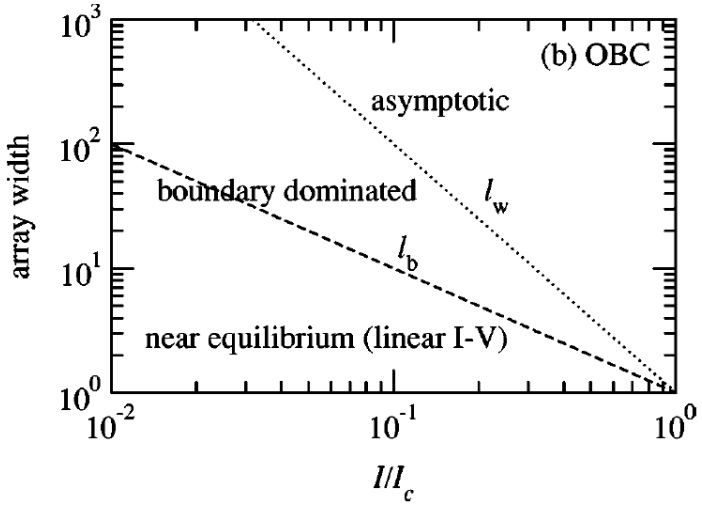

Figure 2.30 – *Phase diagram taken from [153] showing that reduced array width (in number of junctions) gives an ohmic behavior at low bias (in units of total critical current).*

The temperature-independent sublinear increase in voltage lasts up to about 40 nA, which is approximately $I_c/4$. According to Fig.2.30 this would correspond to a width of about 5 junctions. As seen from Fig.2.21b, the number of junctions in the width is on the order of 10. Finally, we note that the low bias behavior is not actually ohmic but instead follows $V \propto I^{0.5-0.6}$. This has been observed on three different samples and remains unexplained. It could be due to some Coulomb blockade being gradually overcome as the bias increases.

2.4.4 Critical current

2.4.4.1 Critical current at low temperatures

Fig.2.31 shows the switching current at low temperatures for the tight and the loose array. They both show a gate-tunable switching current. Once renormalized by the sample width, the switching current density is higher in the tight array by a factor of 3 in the highly doped region, and by a factor of 7 near the Dirac point. The switching current is more strongly reduced near the Dirac point in the loose array than in the tight array, reflecting the increased influence of specular Andreev reflections (see§2.2.3.2). This observation is in line with what we saw of the temperature transition. The junctions are longer, so that the critical current saturates at a lower value. Both arrays show asymmetric behavior with respect to zero, although the asymmetry seems reversed. Maybe this is a problem of polarity of the gate voltage in one of the measurements. With a Dirac point around $+40$ V, where it is expected to be near -40 V, one can assume that the polarity was reversed in the tight array experiment. If this is the case, then the two maps look similar at first sight.

However, looking at the curves Fig.2.31b, e and f reveals a fundamental difference. While the tight array shows a staircase-like series of switching events with increasing bias current, as is expected for a chain of weak links with various switching currents, the loose array displays a surprising single switching event over a large range of gate voltages (see Fig.2.32). It directly returns to the total normal state resistance R_N, as if it was a single Josephson junction. Only for gate voltages $V_g > +15$ V does it show multiple switching like tight array.

We interpret this as a heating effect. Once the weakest link (the supercurrent bottlneck) starts to dissipate, it warms up the whole sample which switches on an avalanche effect. This bottlneck is gate-dependent. For some gate voltages, the bottleneck is well coupled to a heat sink (the electrodes for example) and the avalanche does not occur. The reason why this happens only in the loose array can be attributed to the higher proportion of the surface that starts to dissipate above the switching current.

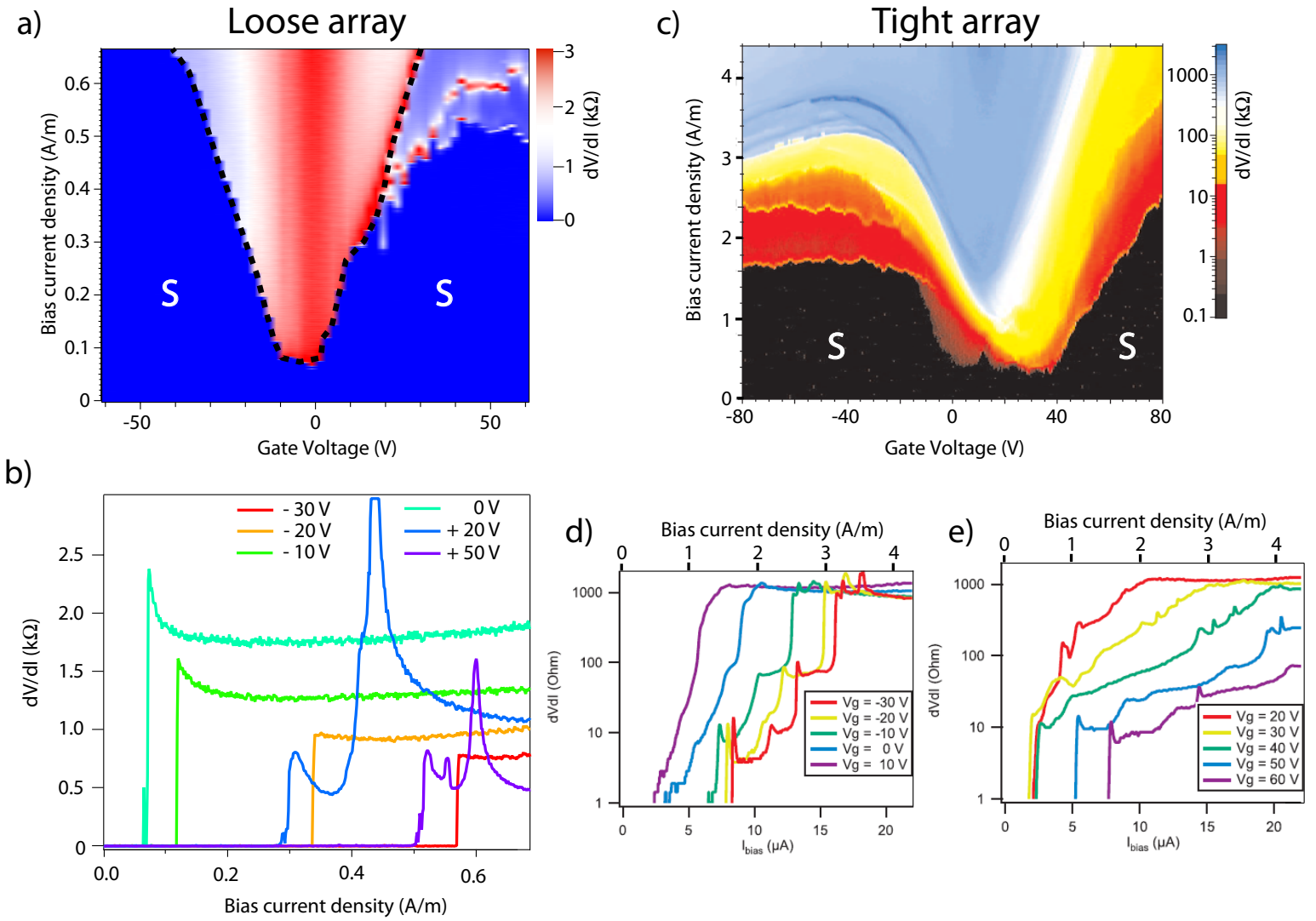

Figure 2.31 – ***Gate dependence of the switching current at*** $T = 50$ ***mK. a)*** *and* ***b)*** *For the case of the loose array.* ***c), d)*** *and* ***e)*** *For the case of the tight array, taken from [116]. Differential resistance as a function of bias current density and gate voltage. Data for the tight array are plotted on a log scale. The dashed line (loose array) outlines the critical current at which the samples becomes fully normal (see Fig.2.32). 'S' stands for 'superconducting'. The loose array shows a reduction by a factor 3 to 7 of the critical current density.*

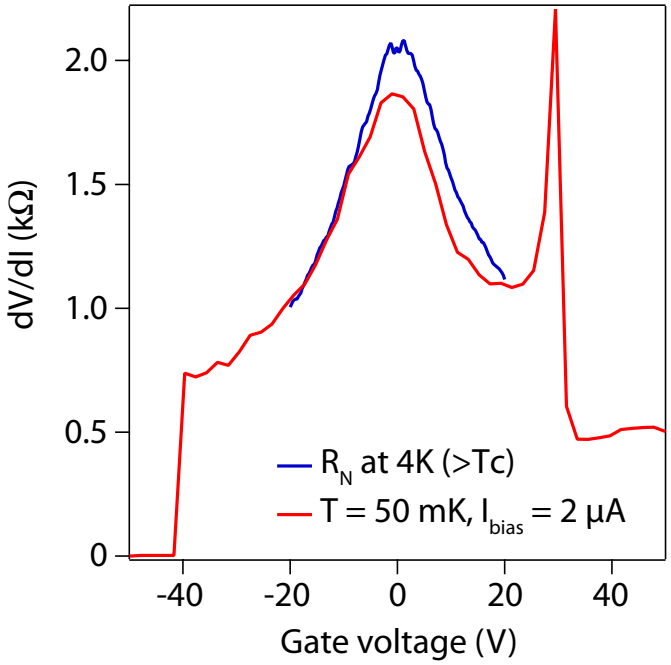

Figure 2.32 – *Differential resistance as a function of gate voltage, measured above the critical temperature (blue curve) and above the critical current (red curve) at $T = 50$ mK. The red curve is just an horizontal cut of Fig.2.31 at 2 μA. For $V_g > +40$ V, the sample is still superconducting and the curve doesn't reflect the normal state. The peak near -30 V is also such an artefact.*

2.4.4.2 Temperature dependence of the critical current

We studied further the temperature dependence of the switching current in the loose array. Fig.2.33 shows the numerically integrated V(I) curves at different temperatures for a gate voltage $V_g = -20$ V, where the sample undergoes full switching at the switching current. Two regimes can be distinguished : above 1.2 K (first four curves), it seems that decreasing the temperature will gives rise to an increasingly sharp slope at the switching current, similar to what is observed in resistively shunted Josephson junction, where the voltage tends to follow [135] :

$$V = R(I^2 - I_{c0}^2)^{1/2} \tag{2.43}$$

However, as we can see on Fig.2.33 (dashed line), this dependence does not fit the voltage well. Moreover, when the temperature is reduced below 1.2 K, the behavior changes. The voltage becomes increasingly linear, with an offset DC supercurrent surviving deep inside the voltage-carrying state and no hysteresis. Such a behavior was first observed by Clarke [155] and is usually ascribed to what is called 'flux-flow' dissipation (see Fig.2.34). In wide ($W >> \lambda_{bot}$) SNS junctions and Josephson junctions arrays [156] , the sample starts to dissipate before the depairing current is reached. This is caused by the self-field that is generated by the supercurrent, which creates

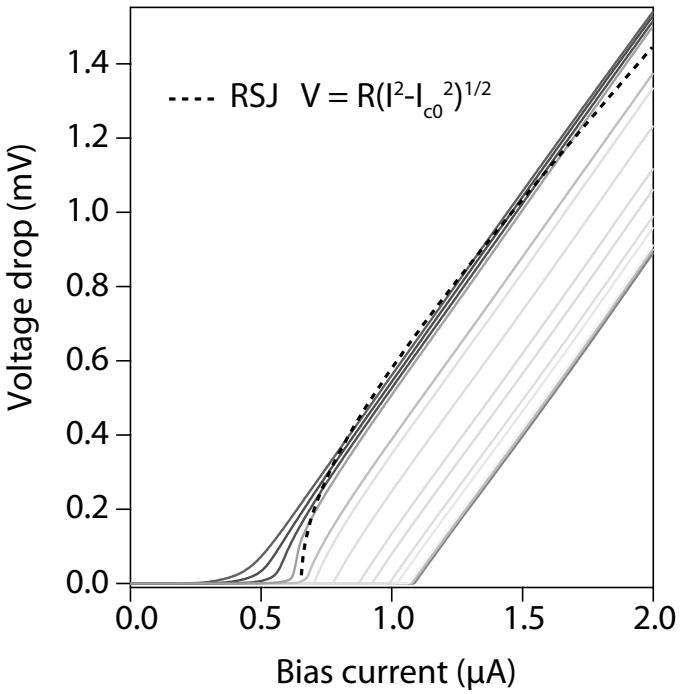

Figure 2.33 – *V(I) characteristic of the loose array at $V_g = -20$ V for different temperatures. The sample is current-biased.* ***Purple curve*** *: 1.5 K,* ***Red curve*** *: 100 mK. By steps of 100 mK.*

vortices that start moving and dissipate under the Magnus force. Flux-flow typically gives a finite slope at the switching current, and an ohmic behavior.

This result is puzzling and contradicts the previously derived lower bound on the length $\lambda_\perp$ (equation 2.38), which was much larger than the sample width of 3 μm. So, this is probably not flux-flow. For the moment, we have no clear idea, but this could be an effect of sample inhomogeneity.

Finally, Fig.2.35 shows the temperature dependence of the critical current for various gate voltages. It clearly doesn't increase exponentially as would be expected for long SNS junctions, but rather follows a Ambegaokar-Baratoff-like dependence (equation 2.9). This confirms our intuition that the onset of the BKT transition corresponds approximately to coherence length $\tilde{\xi}_N(T)$ reaching the junction length, so that below T_{BKT} the critical current already grows like $\Delta(T)$. Regarding the influence of gate voltage on the temperature dependence, an asymmetry can be detected, but it is not related to the charge carrier sign.

If one compares the curves at $+10$ V with the one at -15 V, they pretty much overlap. However, the same cannot be said about the curves at $+20$ V and -20 V : even though they have the same critical current at 1.5 K, the -20 V curve goes to higher critical current at base temperature. We can relate the temperature behavior to the fact that we are in the single switching or multiple switching region of gate voltage (see Fig.2.31a). This confirms that we are dealing with two different supercurrent 'bottlencks' that have slightly different lengths.

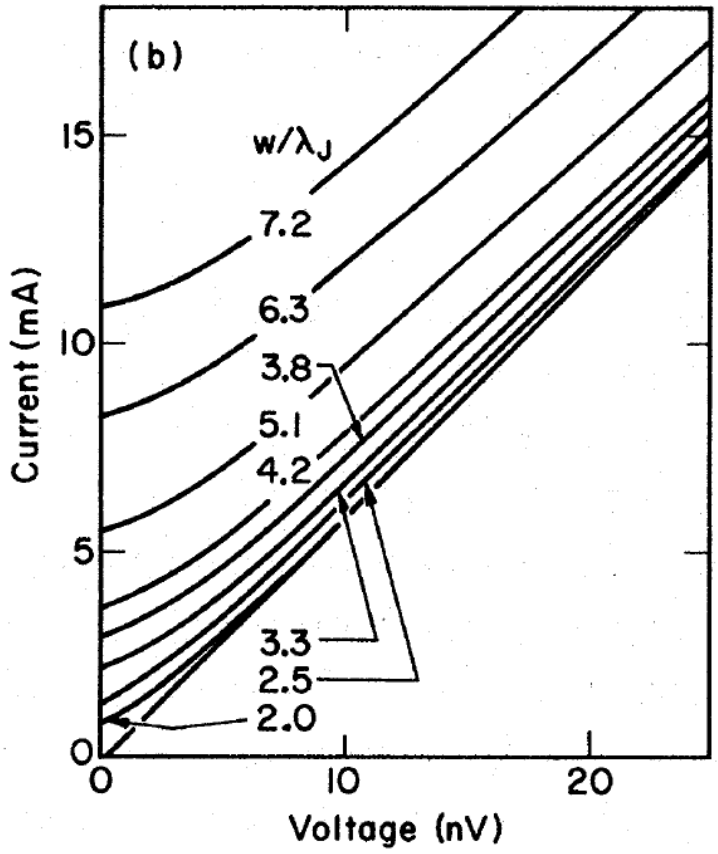

Figure 2.34 – *I(V) characteristic of a wide SNS junction measured by Clarke, showing flux-flow dissipation when the screening length becomes smaller than the junction width. Taken from [155].*

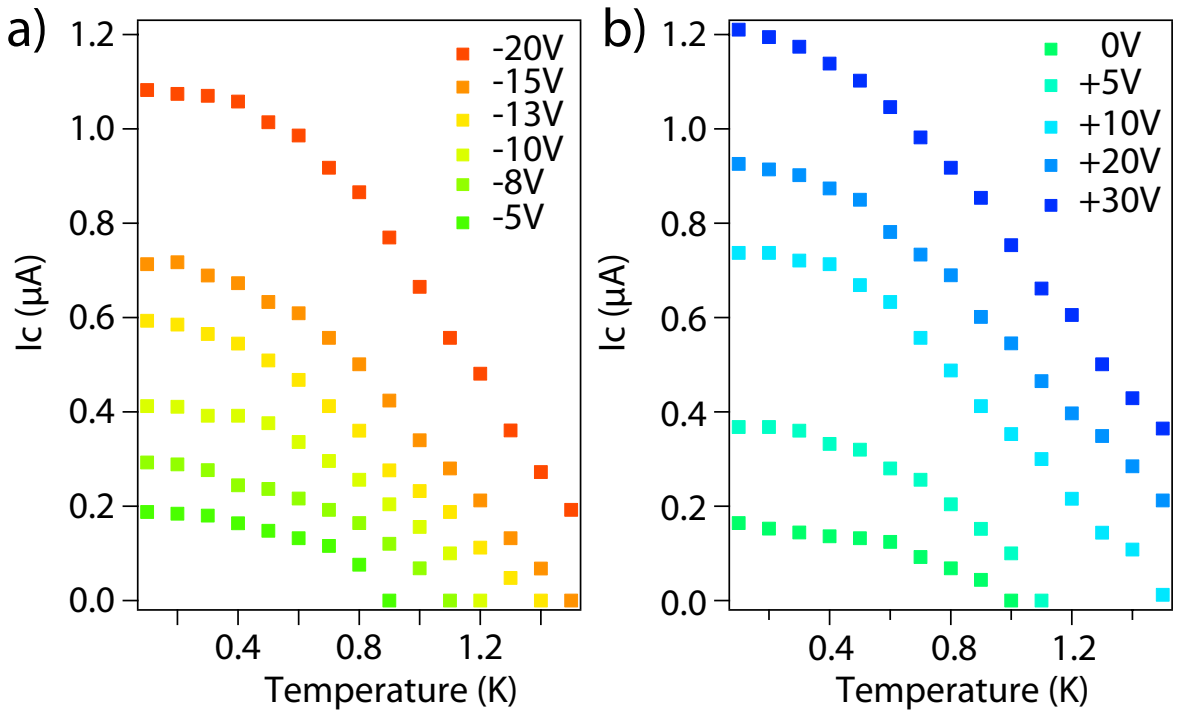

Figure 2.35 – ***Temperature dependence of the critical current. a)*** *on the hole side (single switch).* ***b)*** *on the electron side.*

2.4.4.3 I_cR_N product

The critical current I_c of a Josephson junction is inversely proportional to its normal state resistance R_N. Therefore, the relevant quantity that should be considered when assessing the strength of a critical current is the I_cR_N product. All the predictions for the maximum supercurrent we have seen in §2.2.2.3 are actually calculations of this product in different limits.

It should be borne in mind that we are probing an array of Josephson junctions, the total normal state resistance R_N of which is **not** the same as the local normal state resistance r_n of a single junction. The fact that the device switches in an avalanche actually prevents us from reading the value of the local r_n of the bottleneck junction. The results presented here should not be misinterpreted. We are not drawing any conclusion from the absolute value of the I_CR_N, which is obviously overestimated. The values taken from the K-o-1 and K-o-2 are only put here as a reminder to demonstrate that the I_cR_N product is impossibly high, implying that a bottleneck indeed switches first.

Fig.2.36a presents the I_cR_N product of our loose array, obtained by multiplying the critical current at $T = 50$ mK by the normal state resistance at 4 K. There is a surprising agreement between the product above +15 V and the value predicted by the K-o theory for short diffusive ($l_e << L << \xi_N$) SNS junctions. In order to dissipate any confusion, the results on another sample with a different aspect ratio are shown on Fig.2.36b. Here, the value of the I_cR_N product is clearly too high to be physical. Therefore, we conclude that this agreement with K-o was fortuitous. Regardless of the irrelevance of the absolute value of the I_cR_N product here, we can draw some conclusions from this, if we assume that the local r_n and measured total R_N are proportional.

Looking at the shapes of the I_cR_N, now, they are asymmetric, suggesting that the bottleneck junction is not the same on the electron side and on the hole side. This confirms what we already saw in the temperature dependence.

An intriguing feature is also the shape of the I_cR_N product in sample 51-1 (Fig.2.36b). It shows interesting fluctuations that are reminiscent of the predicted behavior for ballistic graphene Josephson junction (Fig.2.36c). The first minimum after the Dirac point should arise around $E_FL/\hbar v_F \cong 5.5$ (Fig.2.36c). The first minimum in Fig.2.36b occurs at about 30 V from the Dirac point. This would correspond to a junction length of :

$$L \cong 5.5\frac{\hbar v_F}{\hbar v_F\sqrt{\pi\frac{C_gV_g}{e}}} \cong 20 \text{ nm} \tag{2.44}$$

This value is in reasonable agreement (within a factor of 2) with the typical value of the junction's lengths in our system. However, this observation is in disagreement with our assumption that the junctions are longer than the coherence length !

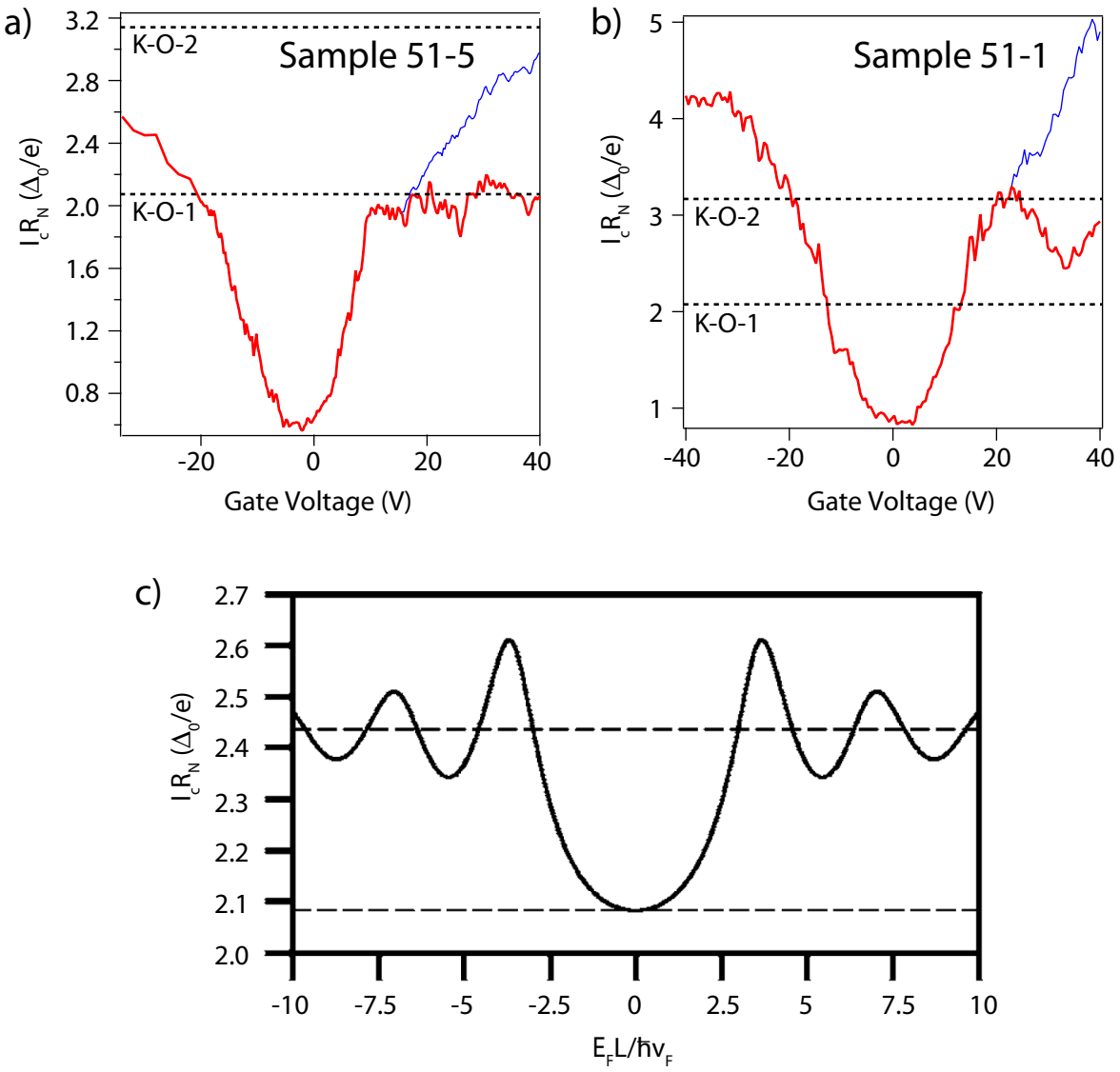

Figure 2.36 – I_cR_N ***product in the loose array.*** ***a)*** *In the sample that has been studied so far. The red line is the switching current. The blue line corresponds to the second switching event observed on the positive voltage side. Dashed lines indicate the theoretical predictions for the I_cR_N product of a short diffusive SNS junction ($l_e << L << \xi_N$) (K-o-1) and for a ballistic junction ($L << l_e$) (K-o-2) [130].* ***b)*** *The same quantity calculated in another sample with a similar sheet resistance, but a different aspect ratio.* ***c)*** *Theoretical prediction for the I_cR_N product of a ballistic junction made of graphene by Titov and Beenakker [109].*

Finally we note that like in all other experiments on the proximity effect in graphene, the $I_c R_N$ is anomalously reduced near the Dirac point, which could be due to the specular Andreev reflection [133] (see §2.2.3.2).

2.4.5 AC Josephson effect

Finally, we have measured the response of the same loose array to microwave radiations at low temperature. Because the electric lines in the dilution refrigerator are highly filtered, an AC current cannot be directly applied to the sample. Instead, we used an antenna hanging just above the sample, through which we applied a microwave voltage. The electric field created by the antenna in turn induces an oscillating current in the Josephson junction, the amplitude of which depends on the (position-dependent) coupling between the microwave field and the sample. Before going any further, it is important to note that the sample suffered from being heated up to 300 K and then cooled down again before the measurement. As a result, the single switching behavior was lost, and instead we had a two-step transition characterized by a much smaller critical current $I_c^* \cong 600$ nA $< I_{c0}$ and an intermediate resistance $R_N^* \cong 130\ \Omega$ at $V_g = -40$ V (see Fig.2.37).

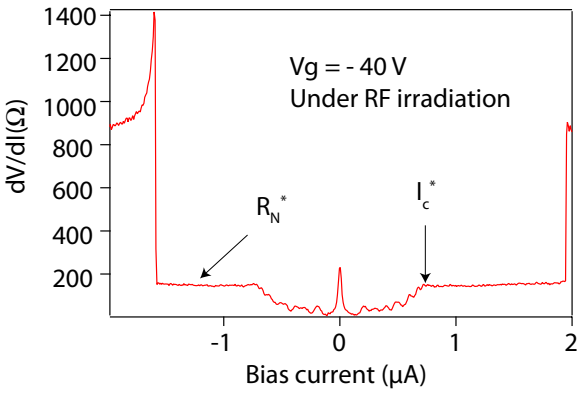

Figure 2.37 – *Differential resistance as a function of bias current in the loose array for $V_g = -40$ V under microwave irradiation. The sample has changes after a temperature change and now shows a two-step switching in current with a low intermediate resistance.*

Fig.2.38a shows the differential resistance of the sample under microwave irradiation, as a function of bias voltage and radiation amplitude, at gate voltage $V_g = -40$ V. The blue regions in the color map correpond to zero differential resistance, *i.e.* voltage plateaus, as can be seen in Fig.2.38b, where vertical line from Fig.2.38a at constant microwave power is numerically integrated. As can be seen in Fig.2.38b, the voltage plateaus occur at values very close to twice what is expected for a single Josephson junction under irradiation : $V_n = \frac{n\hbar\omega}{2e} = n \times 4.14\ \mu$V. The double value is due to the fact that we are actually looking at a power at which the width of the zero-th plateau (equation 2.25) is minimized so that we see the direct transition from plateau -1 to $+1$ (a clearer example of this will be shown later in Fig.2.44).

On the one hand, these steps correspond well to what is predicted for a single Josephson junction. On the other hand, the full switching critical current I_{c0} does not show any modulation, except for a slight reduction at large microwave power. Since

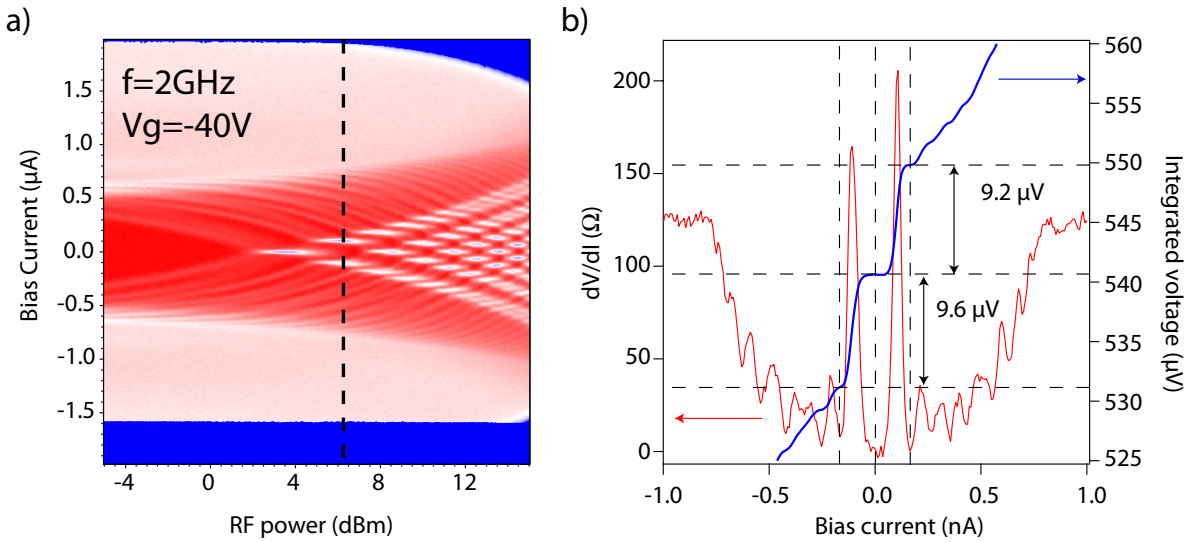

Figure 2.38 – ***AC Josephson effect in the loose array at*** $T = 50$ ***mK for*** $V_g = -40$ ***V and microwave frequency*** $f = 2$ ***Ghz. a)*** *Color map of the differential resistance as a function of bias current and microwave power. Blue regions corresponds to* $dV/dI = 0$. ***b) Red curve*** *: line cut taken from a) (dashed line).* ***Blue curve*** *: numerically integrated voltage drop, showing the Shapiro steps.*

that reduction is only observed in the switching and not in the retrapping current, we attribute it to heating. This behavior is a bit puzzling because in a disordered array of N Josephson junctions in length, one would expect that the contributions from each junction add up, giving a smeared out AC Josephson effect. Here, apparently, only one junction (the bottleneck) shows Shapiro steps.

2.5 Superconducting properties of Pb/graphene hybrids

As a comparative study, it is very interesting to see the effect of changing the superconducting material. Here we chose to use Pb, which shares a lot of properties with Sn. It is impervious to oxidation, superconducting and has a low melting point. Therefore, similar samples can be prepared using Pb. In this section, we will study the superconducting properties of a sample of exfoliated graphene on top of which 30 nm of Pb are deposited by Joule evaporation.

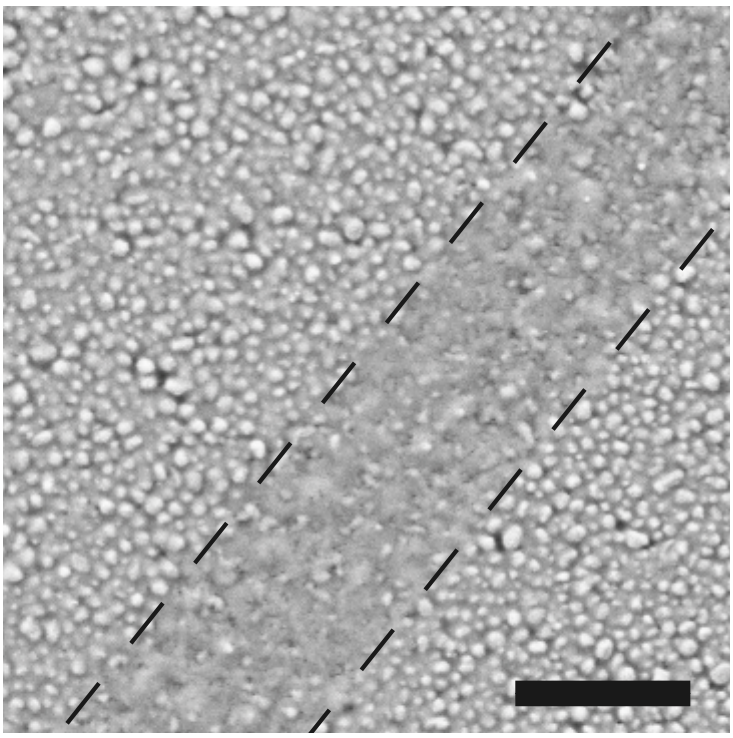

Figure 2.39 – *SEM picture of Pb/graphene sample. The dashed lines outline the graphene flake edges. The scale bar is 1 µm.*

As can be seen on Fig.2.39, the conformation of Pb on graphene is very different from Sn. Here we do not show the sample, because it was destroyed by electrostatic discharge after the measurement, but this piece of graphene was on the same chip. Unlike Sn, Pb seems to form a continuous granular layer on top of graphene. Therefore, changing the material has a double effect : it changes both the superconducting and the morpholgy parameters.

This sample (sample Pb-09) still shows gate tunability of the resistance, as shown in Fig.2.40. This proves that the Pb layer does not form an electrically continuous layer. The position of the Dirac point after Pb deposition is much more remote on the negative side than in typical Sn/graphene samples, indicating stronger electron doping. This is in line with the lower work function of Pb $\Phi_{Pb} = 4.25$ eV and the seemingly higher surface coverage. Note that for this sample it was impossible to go

beyond the Dirac point. Below -80 V, the field effect becomes increasingly flat and shows no sign of decrease down to -120 V.

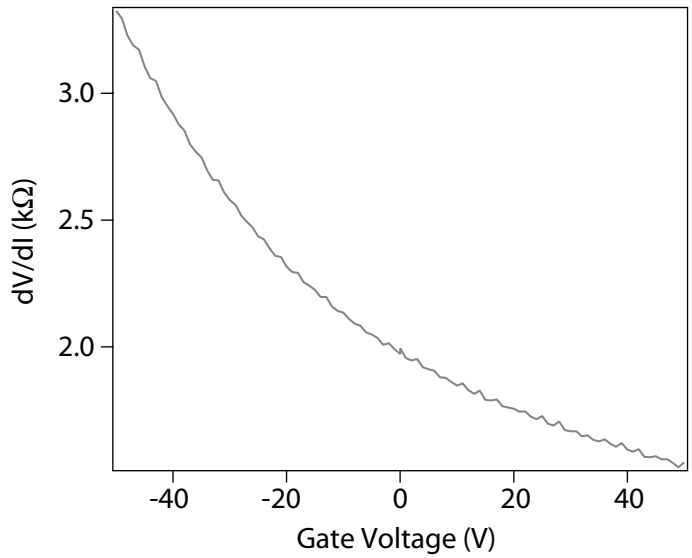

Figure 2.40 – *Field effect curve of sample Pb-09 at room temperature showing gate tunability of the resistance.*

2.5.1 Superconducting transition

At first sight, the superconducting transition of the Pb/graphene sample is similar to the transition in Sn/graphene samples (see Fig.2.41a). The transition starts at a gate-independent temperature T_{c0}, and reaches zero at a gate-dependent temperature T_{BKT}. A notable difference, though, is that here the temperature $Tc0$ is lower than the critical temperature of bulk lead T_{c0}^{Pb} : $T_{c0} \approx 5.8$ K $< T_{c0}^{Pb} = 7.2$ K. This could be an effect of confinement in ultra-small Pb grains. It has been shown [141] that unlike Sn nano-particles, Pb nano-particles exhibit a reduced superconducting gap when their size is reduced below 15 nm. However, SEM pictures do not allow us to draw any conclusion about this. Second, we see that the BKT transition happens after a plateau, like in the loose array studied previously. This time, though, it could be due to a higher Andreev resistance. As a matter of fact, Pb is known to be more readily oxidized than Sn. Moreover, the reduced T_C probably indicates a deep oxidation, resulting in the confinement of the superconducting core of Pb grains.

The tail of the superconducting transition is also interesting. It seems that for the low resistance curves ($V_g > 0$ V), below a certain temperature, the superconducting transition becomes gate-independent. This is seen clearly on Fig.2.41b, where residual resistance R/R_N versus temperature is plotted. It appears to become gate-independent for $T < 3.5$ K. This is probably due to device inhomogeneity.

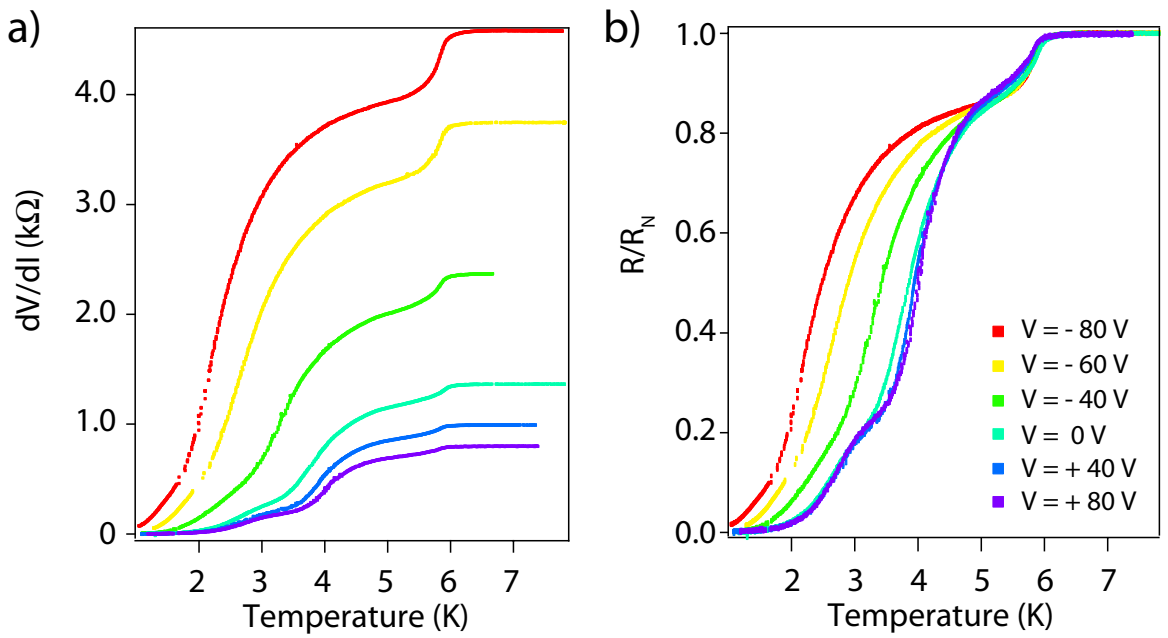

Figure 2.41 – ***Gate-dependent superconducting transition in sample Pb-09.*** ***a)*** *Differential resistance as a function of temperature for various gate voltages.* ***b)*** *The same data renormalized to the normal state resistance* $R_N = R_{7K}$.

2.5.2 Magnetic field dependence

The Pb/graphene sample showed an extreme sensitivity to magnetic field. As can be seen in Fig.2.42, a 1 mT offset from zero already induces a significant decrease of the switching current. Therefore, measuring the switching current requires a careful cancellation of the offset magnetic field.

The very distorted 'Fraunhofer-like' pattern of Fig.2.42 is probably the result of the inhomogeneous supercurrent distribution in the sample. Nevertheless, from the width of the central peak we can extract an order of magnitude for the junction area. Using equation (2.36) we find a junction area of A≈(1.5 μm)^2, which is a factor of 4 smaller than the actual device size of $L \times W = 2\ \mu\text{m} \times 3\ \mu\text{m}$.

2.5.3 Critical current

To measure the critical current, we directly measured the voltage using a Nicolet Accura 100 digital oscilloscope. A triangular voltage signal at a frequency of order 100 Hz was sent from a waveform generator to the bias resistor and fed into the sample, providing the current bias. The oscilloscope was reading the input signal on channel 1 and the output voltage (after amplification) on channel 2. Using the XY visualization option, we could observe the evolution of the V(I) curve in real time. The large number of switching events per second (100 Hz) provides fast averaging of the signal and reduces the noise drastically. This technique allows much faster measurements and real-time observation of the V(I) curve, which is handy in order

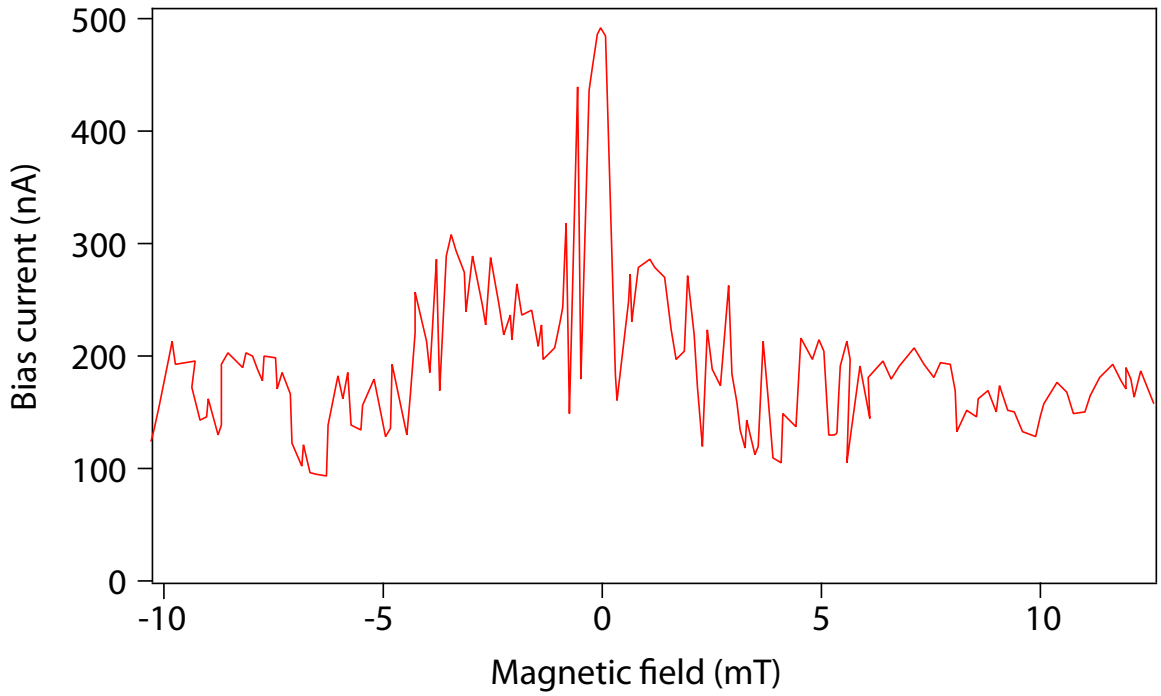

Figure 2.42 – *Switching current at T = 100 mK and V_g = 0 V, as a function of magnetic field.*

to cancel the offset magnetic field (we can visualize for what field the critical current becomes maximum).

Some V(I) curves at different gate voltages are shown in Fig.2.43. Similarly to Sn/graphene samples, we observe that the critical current increases as we increase the gate voltage away from the Dirac point. This time, hysteretic behavior is observed. However, the transition is not direct but happens stepwise. As can be seen on the $V_g = -50$ V curve (blue curve in Fig.2.43), the normal state differential resistance (see Fig.2.40) is not directly recovered after the first switching event. Instead, a series of switching associated with increasing differential resistances dV/dI is observed. The first value of dV/dI after switching scales approximately like the normal state resistance.

2.5.4 AC Josephson effect

Fig.2.44a shows the AC josephson effect of sample Pb-09 at $T = 100$ mK, $V_g = +100$ V and with a microwave excitation frequency of 3 Ghz. The observed steps develop from the critical current of the first switching event observed in the previous section. The voltage steps correspond precisely to the expected values for a single Josephson junction : $V_J = \frac{hf}{2e}$ (see Fig.2.44b and c). In this case too, the Shapiro steps seem to appear only at the weakest link.

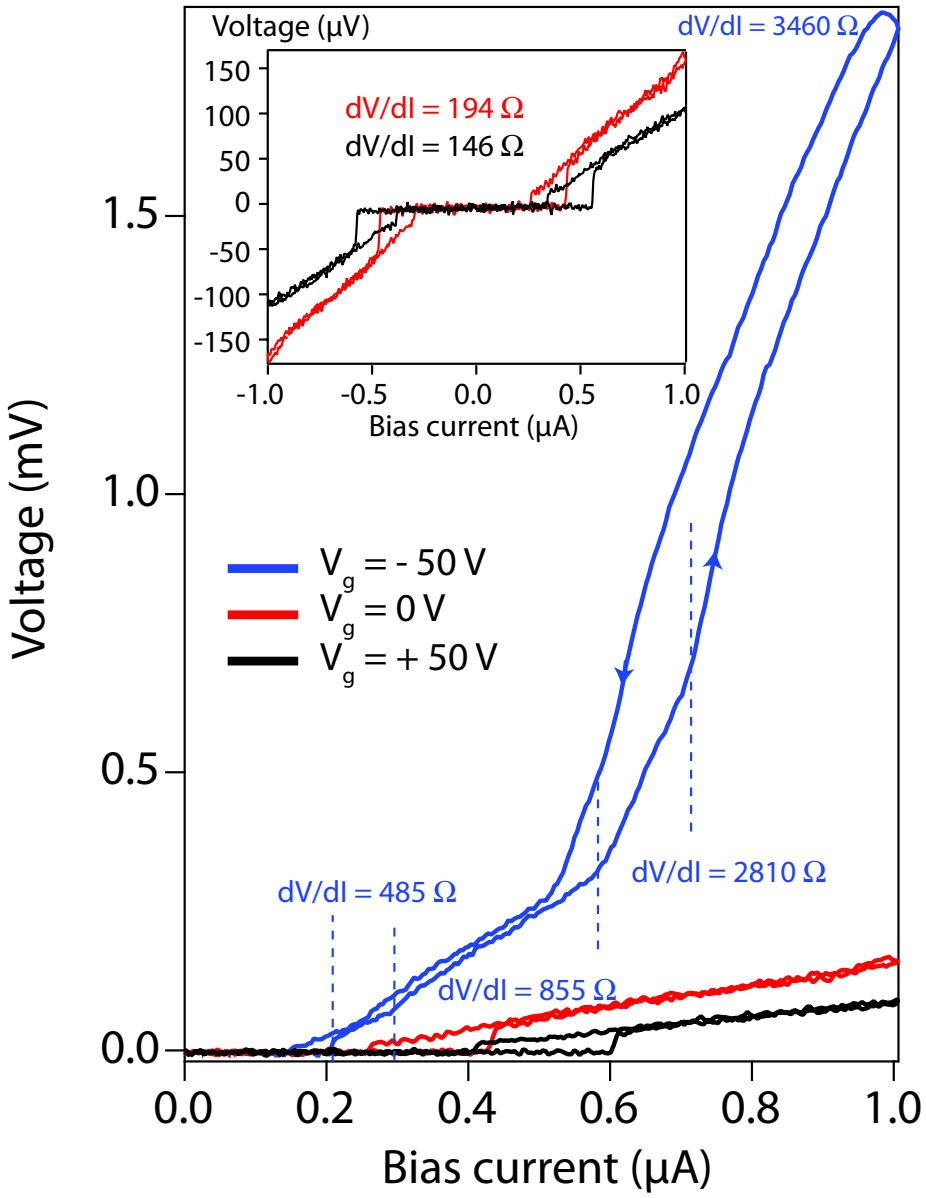

Figure 2.43 – *Voltage drop measured as a function of applied DC current for three different gate voltages.* ***Inset*** *: zoom on the bottom two curves. Dashed lines outline the different regimes of differential resistance dV/dI in the blue curve. The corresponding values of dV/dI are indicated.*

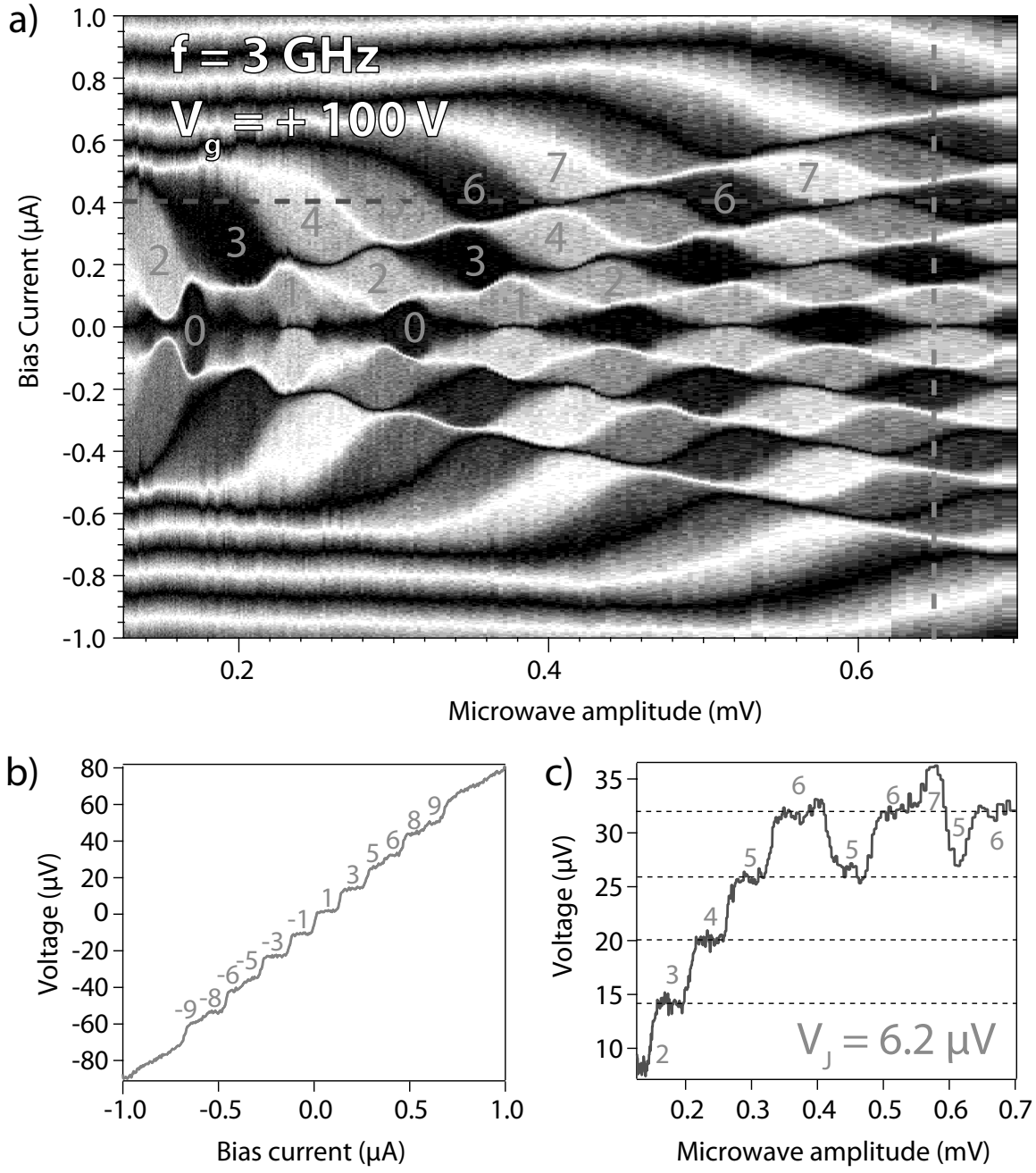

Figure 2.44 – ***AC Josephson effect in Pb-09.*** ***a)*** *Color map of the voltage measured across the junction as a function of bias current and microwave amplitude. The sequence of voltage plateaus is identified by numbers.* ***b)*** *Vertical cut along the blue line in a). The numbers identify the plateaus in the sequence.* ***c)*** *Horizontal cut along the blue line in a), revealing a set of single steps.*

Conclusion du Chapitre 2

Dans ce chapitre, nous avons caractérisé l'influence des billes d'étain sur les propriétés électroniques du graphène, à l'aide de mesures de transport à température ambiante ainsi que par spectroscopie Raman. Nous avons pu voir que le dépôt d'étain n'affectait pas la qualité cristalline du graphène. Nous avons ensuite exploré les propriétés supraconductrices de ces matériaux hybrides à basses températures. Deux métaux à bas point de fusion ont été utilisés pour fabriquer ces échantillons : le plomb et l'étain. Ces deux matériaux se sont révélés capables de rester supraconducteurs et de former une interface suffisemment transparente avec le graphène pour pouvoir induire de la supraconductivité, que l'on peut alors contrôler avec la tension de grille.

La transition vers un état de résistance nulle suit la loi de Berezinskii-Kosterlitz-Thouless (BKT) en température, caractéristique de la supraconductivité bidimensionnelle. Ceci est dû aux fluctuations de la phase supraconductrice resultant de la présence de vortex dans le réseau, sous la température critique des îlots supraconducteurs. Bien que le système suive une loi de type BKT, le saut de l'exposant a dans $V = I^a$, attendu à la transition BKT, n'a pas pu être observé, probablement du fait de la nature désordonnée du réseau.

Nous avons principalement étudié l'influence de la morphologie du réseau de billes supraconductrices. Dans le cas d'un réseau peu dense (taux de couverture de 40 %), le fait que le réseau soit constitué de jonctions Josephson plus longues réduit considérablement la température de transition par rapport au cas d'un réseau plus dense (taux de couverture de $70 - 80$ %). Dans le cas du réseau peu dense, un plateau de résistance est observé entre la transition des billes d'étain et le début de la transition BKT, que nous interprétons comme correspondant à la percolation de l'effet de proximité à travers le graphène, à mesure que la température diminue. Un effet similaire à été observé dans les échantillons à base de plomb. Dans ce cas-là, la résistance à l'interface pourrait aussi en être une des causes. Le formalisme BKT doit être adapté pour prendre en compte le fait que le courant critique est exponentiellement réduit près de T_c dans les jonctions SNS longues.

Nous avons également étudié les propriétés dynamiques des réseaux peu denses. Le courant critique et la réponse AC ont été mesurés. Il semble que ces réseaux désordonnés se comportent comme leur joint le plus faible. La dépendence en température du courant critique et le comportement de l'échantillon lors du passage dans l'état normal sont très différents selon que l'on se trouve au-dessous ou au-dessus de $+15$ V sur la grille. Ceci semble indiquer que notre échantillon est dominé par deux joints faibles différents selon la tension de grille. L'effet Josephson alternatif montre un comportement surprenant. En effet, nous avons systématiquement mesuré des pas de Shapiro correspondant à une jonction Josephson unique, lorque

nous attendions des pas multiples du fait de la nature de l'échantillons. Ceci n'est pas nécessairement en contradiction avec notre interprétation en terme de réseau de jonction, et pourrait simplement être dû au fait que le joint le plus faible est suffisamment différent du reste des jonctions pour donner l'illusion qu'il est le seul à répondre à l'excitation AC. Enfin, l'apparition d'un régime s'apparentant à du 'flux-flow' dans l'état normal au-dessus du courant critique reste mysterieuse.

Afin de mieux comprendre le comportement de ces échantillons, un meilleur contrôle du désordre des billes est nécessaire. Nous devons pour ceci laisser tomber la notion d'auto-assemblage et fabriquer le réseau par lithographie électronique. Par ailleurs, les ilôts d'étain doivent être évaporés à basse température pour ne pas démouiller. Cette étude est actuellement en cours dans notre équipe (voir Fig.2.45). Les premières données expérimentales sur ces réseaux montrent une température de transition réduite, ce qui était attendu puisque l'espacement entre bille est plus grand.

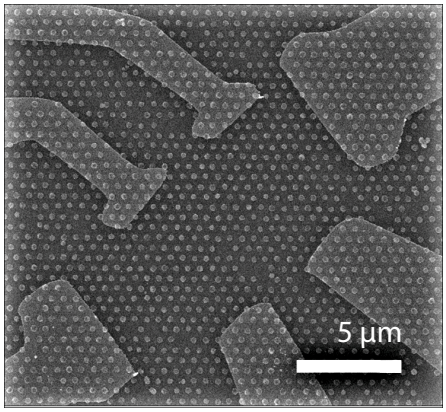

Figure 2.45 – *Image MEB d'un échantillon de graphène sur lequel un réseau régulier d'îlots d'étain a été fabriqué par lithographie électronique suivie d'un dépôt d'étain à basse température. Avec l'aimable autorisation de Zheng Han*

Tous les échantillons testés dans ce chapitre ont été fabriqués avec du graphène exfolié de bonne qualité. Les échantillons avaient tous une résistance par carré de l'ordre du kΩ. Nous nous sommes également intéressés à ce qui se passe dans ces matériaux hybrides lorsque l'on fait varier le désordre du médium, c'est-à-dire du graphène. Ceci sera le sujet de l'étude présentée dans le prochain chapitre.

Conclusion of Chapter 2

In this chapter, we have characterized the influence of Sn adsorbates on the electronic properties of graphene by means of room temperature measurements and Raman spectroscopy. We then explored the low temperature properties of a superconducting hybrid system resulting from the decoration of graphene monolayers by a non-percolating, self-assembled arrays of superconducting islands. Two materials belonging to the family of low-melting-point metals (Sn and Pb) have been successfully tested and give a fully superconducting state above 1 K, by percolation of the proximity effect through the graphene sheet, leading to global phase coherence between the grains.

The transition towards the zero resistance state follows the well-known Berezinski-Kosterlitz-Thouless (BKT) dependence in temperature, characteristic of the presence of phase fluctuations and vortices in 2D superconducting systems. We have explored the influence of surface morphology, revealing that, in the low density case (40 % coverage, the so called " loose-array "), having longer SNS junctions can drastically reduce the transition temperature as compared to the case of high density arrays ($70 - 80$ % coverage so-called " tight-array "). For the loose array samples, a plateau of constant resistivity is seen between the superconducting transition of Sn islands and the onset of the BKT transition, corresponding to the slow percolation of the proximity effect through the graphene layer. A similar behavior is found in the lead decorated sample, a behavior that could be due to the increased contact resistance at the Pb/graphene interface, which depresses the intensity of the proximity effect. We showed that the BKT formalism has to be adapted to account for these length effects.

We then showed that the dynamical properties of the loose networks, such as the critical current or the AC response, seem to be entirely dominated by their weakest link. The critical current, as well as the switching behavior, show two distinct regimes corresponding to gate voltages above or below $+15$ V. We attribute this to the existence of a different weakest link in these two regions of gate. The AC Josephson effect does not follow what popular wisdom tells us about arrays of Josephson junctions. Instead, the array displays the behavior of a single Josephson junction. This does not necessarily contradicts our previous assumption that the system is an array of Josephson junctions. As a matter of fact, it is

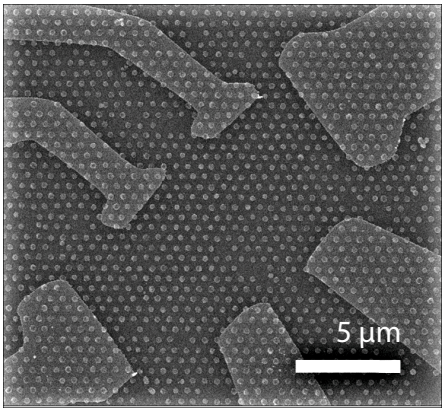

Figure 2.46 – *SEM picture of a sample on top of which a regular array of Sn islands has been deposited. The array was patterned by e-beam lithography and deposition was done at low temperatures. Courtesy of Zheng Han.*

not impossible, if the weakest link of the array is different enough from the others, that the system appears like it is only composed of one Josephson junction. Still, these observations need confirmation and are not fully understood. More studies are also needed in order to better characterize and understand the voltage-carrying state above the critical current.

In order to achieve a quantitative understanding of the properties of these arrays, a better control of the different parameters is necessary. Controlling the morphology is actually quite straightforward. We have started the fabrication of Sn/graphene devices, where the Sn islands are not the result of a self assembly process, but are patterned by e-beam lithography. The result is shown in Fig.2.46. Such arrays have already shown signatures of superconductivity and hold promise for new experiments.

All samples tested in this chapter were based on clean, low-disorder graphene, with a sheet resistance on the order of 1 kΩ. It is now interesting to check what happens to this hybrid system if, instead of varying the nature/density of the adsorbed element, one increases the structural disorder of the graphene medium. This will be the subject of the study presented in the following chapter.

3 Electrostatic control of the superconductor-insulator transition in Sn/graphene hybrids using disordered graphene

Introduction en français

Les systèmes de basse dimensionnalité sont moins enclins à adopter un ordre à longue distance que les systèmes à trois dimensions. Rice (1965) [157] a montré que l'ordre supraconducteur ne peut réellement s'établir à des distances arbitrairement grandes que dans un système tridimensionnel. Par conséquent, même s'ils peuvent sembler supraconducteurs, les systèmes bidimensionnels n'atteignent jamais une résistance parfaitement nulle. Celle-ci est simplement infiniment petite. Little (1967) [158] a ensuite montré que ce sont les fluctuations thermodynamiques de la phase supraconductrices qui empêchent l'ordre à longue distance de s'établir. Ces fluctuations entraînent une variation non pas abrupte, mais graduelle de la résistance avec la température. C'est la transition, aujourd'hui désignée sous le nom de 'BKT', que nous avons étudiée dans le chapitre précédent. Reprenons le système étudié dans ce chapitre. Qu'arriverait-il si la résistance dans l'état normal des jonctions Josephson augmentait ? Leur courant critique diminuerait, diminuant du même coup la température de transition BKT. Si la résistance des jonctions augmente jusqu'au point où l'énergie Josephson couplant un îlot supraconducteur à ses voisins devient inférieure à l'énergie de charge de l'îlot, l'ordre supraconducteur à longue distance est détruit et l'état fondamental du système n'est plus supraconducteur mais isolant [159]. Les propriétés d'un tel état isolant intriguent les physiciens depuis longtemps.

L'amplitude du paramètre d'ordre Δ et la phase supraconductrice φ étant des observables duales, elles sont liées par le principe d'incertitude d'Heisenberg. Ceci implique une forme particulière de dualité dans les supraconducteurs granulaires et les réseaux de jonctions Josephson : lorsque la différence de phase est bloquée (connue),

le système est superfluide, et donc le nombre de paires de Cooper ($n \propto \Delta^2$) présentes dans un îlot à un moment donné est totalement inconnu puisque, par définition, l'état supraconducteur est un état collectif. L'état dual est réalisé lorsque des paires de Cooper sont localisées dans les îlots. Les fluctuations de la phase supraconductrice, c'est-à-dire les vortex, se condensent alors dans un état superfluide [160, 161]. Ce modèle 'bosonique' (car l'état isolant est constitué de paires de Cooper localisées, qui sont des bosons), qui est le modèle canonique de la transition supraconducteur-isolant (TSI) dans les systèmes granulaires, est généralement opposé au modèle 'fermionique', dans lequel la transition supraconducteur-isolant (TSI) résulte de la destruction des paires de Cooper.

Le modèle fermionique a été imaginé pour expliquer la TSI dans les systèmes amorphes, c'est-à-dire dans lesquels le désordre est homogène à une échelle beaucoup plus petites que la longueur de cohérence supraconductrice. Dans ces films, on s'attend à ce que l'ordre supraconducteur soit homogène. Et en effet, le comportement de ces films diffère nettement de celui des films granulaires [162]. Le mécanisme aboutissant à la destruction de la supraconductivité dans le modèle bosonique est la renormalisation de la densité d'état au niveau de Fermi par les interactions coulombiennes [163]. Bien qu'il ait eu quelque succès pour prédire la réduction de T_c dans les films amorphes, ce modèle n'explique pas tout car ces films montrent généralement des signatures liées à la présence de paires de Cooper dans l'état isolant, comme une valeur universelle de la résistance à la transition, prévue par le modèle bosonique [164] ou une magnétorésistance positive géante dans l'état isolant [165, 146]. Récemment, des mesures de spectroscopie tunnel ont montré la persistence d'un gap supraconducteur dans la phase isolante de films minces d'oxide d'indium amorphes [166]. Bien que la TSI revête plusieurs formes, il semble donc que le modèle bosonique soit pertinent dans une majorité des cas. En effet, il apparait aujourd'hui que la TSI dans les systèmes amorphes est marquée par l'émergence d'inhomogénéités électronique dans la phase supraconductrice qui en font de fait un système granulaire à la transition.

Il est à noter que les matériaux granulaires ne montrent en réalité jamais une transition purement bosonique. En effet, ceux-ci sont souvent sujet à ce qu'on appelle des TSI dominées par la dissipation. La présence d'états fermioniques (dissipatifs) telles des quasiparticules à basse énergie a pour effet d'écranter les interactions coulombiennes. Comme ces états sont peuplés thermiquement, leur influence s'estompe à mesure que la température diminue, et la phase isolante reprend alors le dessus. Les films supraconducteurs granulaires et les réseaux de jonctions Josephson montrent souvent ce type de transition [167, 168, 169, 170, 171, 172], dans lesquelles, non seulement les quasiparticules, mais également la présence de degrés de libertés dissipatifs dans l'environnement immédiat peuvent influencer la transition.

Lorsqu'on s'intéresse pour la première fois à la riche littérature sur la TSI, il est difficile de ne pas se perdre. En plus de la classe du matériau considéré, granulaires ou amorphes, il faut distinguer les transitions induites par le champ magnétique [173, 174], l'épaisseur du film [175, 164], le recuit [176, 165], le changement de stœchiométrie dans un alliage [177] ou encore la densité de porteurs [12, 178]. Pour faire simple, on peut distinguer *grosso modo* deux types de transitions (bien qu'il y ait des différences subtiles). D'un côté, faire varier l'épaisseur, recuire l'échantillon, faire varier sa composition chimique ou sa densité de porteur ont tous une influence indirecte sur le paramètre de désordre $k_F l_e$. D'un autre côté, le champ magnétique se manifeste différemment, puisqu'en principe il devrait augmenter la population des vortex jusqu'à ce que ceux-ci forment un condensat superfluide [179]. Cependant, ce mécanisme n'a jamais été clairement établi, l'effet du champ magnétique étant également d'introduire de la dissipation en peuplant le système de quasi-particules.

Récemment, des avancées technologiques ont permis d'induire une TSI dans des films minces supraconducteurs en faisant varier la densité de porteurs de charge à désordre constant [12, 13, 178, 14, 180]. Ces expériences sont devenues populaires car elles sont très attirantes d'un point de vue conceptuel. Comparée au désordre, la densité de porteurs de charge est une grandeur qui peut être manipulée continuement et de manière réversible. Par ailleurs, on peut essayer de la mesurer indépendamment, grâce à des mesures d'effet Hall par exemple. Les TSI en densité de porteurs permettent également l'étude de la limite 'propre', c'est-à-dire de faible désordre [178], ce qui est nouveau. L'une des principales limitations de ces expériences à ce jour reste l'efficacité limitée de la grille. Pour pouvoir influencer la densité de porteurs de manière significative, il faut des films d'épaisseur inférieure à la longueur de Debye, autrement dit de quelques atomes d'épaisseur tout au plus. Même dans ces cas-là, la densité de porteurs étant tout de même relativement importante dans ces matériaux (comparée celle du graphène), la seule manière d'induire une TSI complète est d'utiliser des grilles liquides. Celles-ci sont beaucoup plus efficaces que les grilles classiques (les densités atteintes peuvent être 100 fois plus grandes), mais elles sont également contraignantes puisqu'elles gèlent. Changer la densité de porteur nécessite alors de réchauffer l'échantillon avant de modifier la tension.

Ce chapitre, qui constitue le coeur de cette thèse, est consacré à l'étude de la TSI induite en grille dans des hybrides Sn/graphène fabriqués à base de graphène désordonné (voir Chapitre 1). Grâce à ce graphène, nous avons pu étendre notre contrôle sur la supraconductivité des hybrides décrits au Chapitre 2. Les expériences décrites ici démontrent tout le potentiel du graphène comme médium ajustable dans l'étude des ordres électroniques à deux dimentions. Ils constituent la première réalisation expérimentale d'une TSI induite en grille dans un réseau de jonctions Josephson, et plus généralement dans un système supraconducteur granulaire. Le

couplage inhomogène des îlots supraconducteurs sur le graphène crée *de facto* des corrélations supraconductrices inhomogènes, par l'intermédiaire de l'effet de proximité, au sein des états électroniques du graphène, dont le degré de localisation peut être contrôlé par la grille.

La possibilité d'ajuster le degré de désordre (mesuré par la résistance par carré à température ambiante) en changeant le temps d'attaque du graphène permet d'étudier plusieurs limites. Dans la première partie de ce chapitre, nous nous intéresserons au cas d'un graphène peu désordonné dans lequel la force du couplage supraconducteur sera réduite par l'application d'un champ magnétique. Le résultat est une transition contrôlée en grille entre un état faiblement supraconducteur et un état faiblement localisé, que l'on peut comprendre dans le cadre des fluctuations quantiques de la supraconductivité. Dans la deuxième partie, nous verrons le cas d'un graphène beaucoup plus désordonné qui montre une TSI complète en grille sans l'aide du champ magnétique. La TSI observée dans ce matériau a des propriétés à la fois clairement granulaires, mais par certains côtés très proches de celles de la TSI induite par le désordre dans les films minces amorphes. La valeur universelle de résistance à la transition, ainsi que la signature de paires de Cooper localisées dans l'état isolant indiquent que nous sommes en présence d'un isolant bosonique. La transition elle-même semble dominée par des effets de dissipation à hautes températures, de manière similaire à ce qui a été observé dans certains réseaux de jonctions Josephson, transition qui se mue en un régime de percolation à basse température. Cette transition de percolation a lieu à une valeur de grille constante.

Introduction in english

As a general rule, systems of reduced dimensionality show less aptitude for long-range ordering. Rice (1965) [157] showed that superconducting order at arbitrary distances can only exist in three-dimensional superconductors. Even though they seem superconducting, two-dimensional superconductors never reach a truly zero resistance state. Little (1967) [158] demonstrated that the thermodynamic fluctuations of the superconducting phase would prevent true superconductivity to take place in systems of reduced dimensions. Instead of an infinitely sharp superconducting transition, like those found in type I superconductors, he predicted that 2D superconductors should exhibit a smooth transition with the resistance changing gradually. This is what we saw in Chapter 2 in our Sn/graphene hybrids : being prone to phase fluctuations, they exhibit a BKT transitions, where thermally activated fluctuations of the phase prevent superconductivity. What will happen if one increases the normal state resistances of the junctions in the Sn/graphene devices. This will lower the critical temperature T_C by lowering the Josephson energy. At some point, when the latter becomes lower than the charging energy of the superconducting grains, long-range superconducting ordering is destroyed and the ground state of the system is insulating instead of superconducting [159]. The properties of such an insulating state have intrigued physicists for many years.

In a superconductor, the order parameter's amplitude Δ and superconducting phase φ are dual observables. As such, they are linked by Heisenberg's uncertainty principle. This implies a certain form of duality in granular superconductors and Josephson junctions arrays : when the phase difference is locked (known), the system is superconducting, which means it is impossible to know the number of Cooper pairs ($n \propto \Delta^2$) present in a given island at a given moment, because the superconducting state is by nature a collective mode. Conversely, when the Cooper pairs are localised, the phase fluctuations, *i.e.* the vortices should condense into a superfluid [160, 161]. This so-called 'bosonic' scenario (because the insulating state is composed of localized bosons), is the canonical model for the superconductor-insulator transition (SIT) in systems of granular superconductivity. It is generally opposed to the 'fermionic' model. In the fermionic model, the transition is driven by the destruction of the Cooper pairs, followed by the localization of the electrons.

The fermionic model was imagined to describe the SIT in amorphous thin films, which are films where the disorder is homogeneous down to a scale much smaller than the superconducting coherence length, so that no granularity of the superconducting order is expected. As a matter of fact, the behavior of granular and amorphous films is very different [162]. In the fermionic model, the mechanism driving the transition is the Cooper pair breaking due to the renormalization of the density

of states at the Fermi energy by Coulomb interactions [163]. Although this model had some success in describing the reduction of T_c in some amorphous films near the transition, it does not capture the whole physics. As a matter of fact, even those amorphous films show signatures of the presence of Cooper pairs in the insulating state. Some of them showed a universal resistance at the transition, as predicted by the bosonic scenario [164], as well as a giant positive magnetoresistance, a feature associated with the presence of Cooper pairs in the insulating state [165, 146]. Recently, scanning tunneling spectroscopy [166] revealed a gapped density of states in the insulating phase of amorphous InO_x films, proving unambiguously that the Cooper pairs were already pre-formed there. This indicates that superconducting grains naturally emerge even in the most homogeneous films near the transition and implies that the granular ('bosonic') picture is not completely irrelevant in explaining the zero-temperature transition.

Interestingly, the granular films themselves often exhibit a behavior very different from that predicted by the bosonic model. Instead, they often show a SIT driven by dissipation. Although the bosonic model is canonical to describe granular films and Josephson junctions arrays, the expected signatures of this transition are often overshadowed by effects coming from dissipative degrees of freedom such as temperature-dependent screening of the Coulomb interaction [167, 168, 169, 170, 171, 172]. The presence of thermally populated dissipative electronic states, such as quasi-particles, gives a non-universal, temperature-dependant transition. Apart from quasi-particles, any dissipative degree of freedom to which the system can couple can give such transitions.

Looking at the rich literature on the SIT, it is hard not to get confused. In addition to material morphology, another complication comes from the various ways in which the SIT can be induced. In fact, any physical quantity that can affect the strength of the superconducting order can in principle tune the transition. This includes magnetic field [173, 174], film thickness [175, 164], annealing [176, 165], alloy stoichiometry [177] and carrier density [12, 178]. For the sake of simplicity, it is good to try to categorize things a little bit here. Thickness (through the increased influence of surface roughness), annealing (recrystallization) and stoichiometry indirectly influence the disorder, and thus the mean free path. Carrier density, through the parameter $k_F l_e$, has a similar effect on transport, and should therefore exhibit similar characteristics. Finally, the magnetic field transitions involve a different mechanism. In principle magnetic field should increase the population of vortices up to a point where they condense and become superfluid [179].

Recently, tuning the carrier density of the superconductor by applying an electric field has become a very popular way of inducing SIT's [12, 13, 178, 14, 180]. Despite being technologically challenging, these experiments are very appealing for several

reasons. They are conceptually simpler : instead of indirectly influencing the disorder, we directly change the charge carrier density, keeping all other parameters, such as static disorder, under control. The possibility to induce the transition in a clean system without disorder is finally accessible [178]. Finally, unlike the disorder, carrier density can be swept continuously and reversibly between the insulating and the superconducting state. The main limitation of these experiments, however, is the gating efficiency. To significantly modify the overall carrier density, one needs a system which is two-dimensional, not regarding the superconducting coherence length ξ, but regarding the Debye length, *i.e.* the Fermi wavelength, otherwise the gate-induced charges will be screened in the bulk. This is why only atomically thin systems can be efficiently gated, and even in this case, it is often necessary to resort to the efficient but very restricting technique of liquid-gating with ionic solutions. In view of these considerations, one-atom thick semi-metal graphene seems like a very promising platform to induce an SIT by gate voltage.

This chapter, which constitutes the main course of this thesis, will be devoted to the study of the SIT induced by gate voltage in hybrid Sn/graphene fabricated using disordered graphene. Taking advantage of the large low-temperature gate voltage dynamics offered by the graphene samples with a controllable amount of structural disorder described in Chapter 1, we extended the gate-tunability of the superconducting hybrids described in Chapter 2. The experiments described here demonstrate the potential of graphene as a tunable medium for the study of electronic orders in 2D. They constitute the first experimental demonstration of a gate-induced SIT in a Josephson junction array, and more generally in a granular superconductor. Inhomogeneously coupled superconducting particles *de facto* create inhomogeneous superconducting correlation, through the proximity effect, among the electronic states of the graphene sheet, the degree of localization of which can be tuned by the gate voltage.

The possibility to adjust the amount of disorder, which is reflected by the sheet resistivity at room temperature, by changing the etchant and etching time (see Chapter 1) makes it possible to study different cases. In the first section, a weakly disordered sample is subjected to a magnetic field which reduces the strength of superconducting pairing. This results in a crossover from a weakly superconducting to a weakly insulating behavior, as the gate is swept. This experiment sheds light on the weak disorder limit and can be qualitatively understood in the framework of superconducting fluctuations. In the second part, an experiment done on a much more disordered graphene flake will be presented. There, a full transition from a truly superconducting to a strongly insulating state is observed at zero magnetic field. We observed that the properties of this SIT resemble both those of granular and those of the disorder-tuned SIT in highly disordered amorphous thin films. While the high temperature behavior is dominated by dissipation effects, as is expected in a JJA, the low temper-

ature behavior is characterized by a percolative behavior and universal resistance at the percolation threshold.

Table of contents of Chapter 3

3.1 Competition between Josephson and charging energy

The Hamiltonian we used in Chapter 2 (equation 2.27) for Josephson junctions arrays describes well the 'BKT' transition of superconducting thin films of low normal state resistance. However, it was realized early on that this description fails to capture the behavior of more resistive samples. In that case, the model needs to be extended to include the charging energy [159], because dynamical screening of Coulomb interactions is no longer effective. Solving the problem for a regular lattice involves the following Hamiltonian :

$$H = \frac{1}{2}E_C \sum_i n_i^2 + E_J \sum_{nn}(1 - \cos\Delta\varphi) \tag{3.1}$$

where n_i is the electron number in the ith superconducting grain, the Josephson energy E_J of one junction writes :

$$E_J = \frac{\Phi_0 I_C}{2\pi} \tag{3.2}$$

where $\Phi_0 = h/2e$ is the flux quantum and $I_C \propto \frac{1}{R_N}$ is the (gate-tunable) critical current in one junction, and the charging energy E_C is :

$$E_C = \frac{e^2}{2C} \tag{3.3}$$

where C is the island's total capacitance.

Using this formulation, Simanek [181] showed that the transition between superconducting and insulating ground state occurs for $E_J/E_C \cong 1/z$, where z is the number of nearest neighbours.

Many experiments have been carried out to test this model's predictions. They involved fabricating JJA with various Josephson junctions parameters [182]. The main hurdle in these experiments is often the predominant role played by dissipation. As a matter of fact, the presence of a metallic environment can strongly renormalize the charging energy and influence the ground state [167, 169, 170, 172]. In our case, dissipative degrees of freedom are most probably present in the form of uncorrelated electrons in the graphene sheet. Therefore, constant values of the charging energy E_C, should correspond to constant values of the normal state resistance of the graphene sheet.

Evaluating E_J involves a knowledge of I_C, which has to take into account the influence of localization on the diffusion of Cooper pairs. Fukuyama *et al.* [183] have proposed a theory for the proximity effect in strongly localized 2DEG.

3.2 Gate-tunable transition from positive to negative paraconductivity

As we have seen in Chapter 2, increased inter-island gaps results in a lowered superconducting transition temperature. This suppression of the superconducting transition temperature arises due to a weaker coupling between Sn islands, as captured by the parameter E_J. In this section, we will explore the influence of the magnetic field on the transition temperature. At magnetic fields on the order of but smaller than the critical field, the system exhibits a gate-tunable transition between a regime of positive $\frac{dR}{dT} > 0$ and negative superconducting fluctuations $\frac{dR}{dT} < 0$.

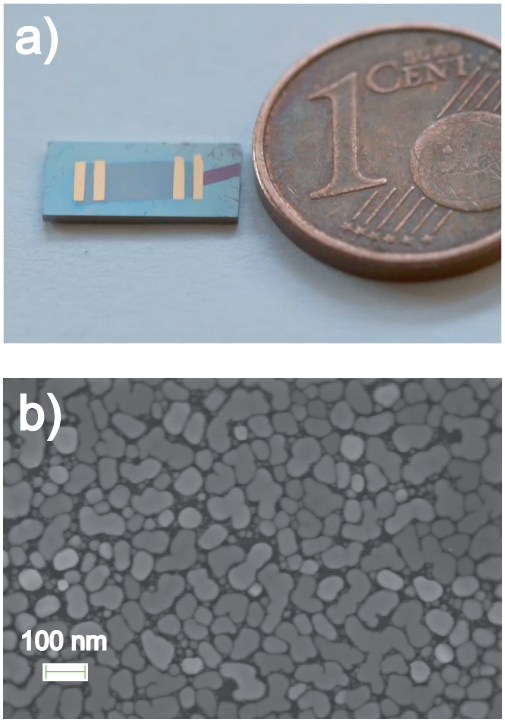

Figure 3.1 – ***Macroscopic CVD sample decorated with Sn SAM-31.*** ***a)*** *Photograph of the sample. The different arrangements of Sn islands on the surface of graphene and on SiO_2 substrate give an enhanced contrast.* ***b)*** *SEM micrograph of the graphene surface showing the ubiquitous tin islands.*

3.2.1 Sample fabrication and first observations

In this section, we have used macroscopic CVD graphene of good quality decorated with Sn islands (sample (SAM-31), see Fig.3.1). CVD graphene was grown on Cu and transferred onto a SiO_2 substrate. Evaporation of Ti/Au electrodes was done using a stencil mask (see §1.3.4.3). Finally, 10 nm of Sn were evaporated on the entire surface. The result is shown in Fig.3.1. The morphology of the obtained Sn islands is similar to the case of the tight array studied in Chapter 2. The electrical coupling to graphene, as inferred from SEM contrast, appears a bit more inhomogeneous. We understand this as stemming from a higher level of surface contamination and roughness due to the transfer process. Inter-island distances can be as small as 5 nm.

The field effect curve at 6.5 K is shown in Fig.3.3. The sample exhibits a behavior similar to that of exfoliated samples. The low mobility and large electron doping arise from the charged impurities created by Sn islands. The overall resistivity is small, indicating good crystalline quality.

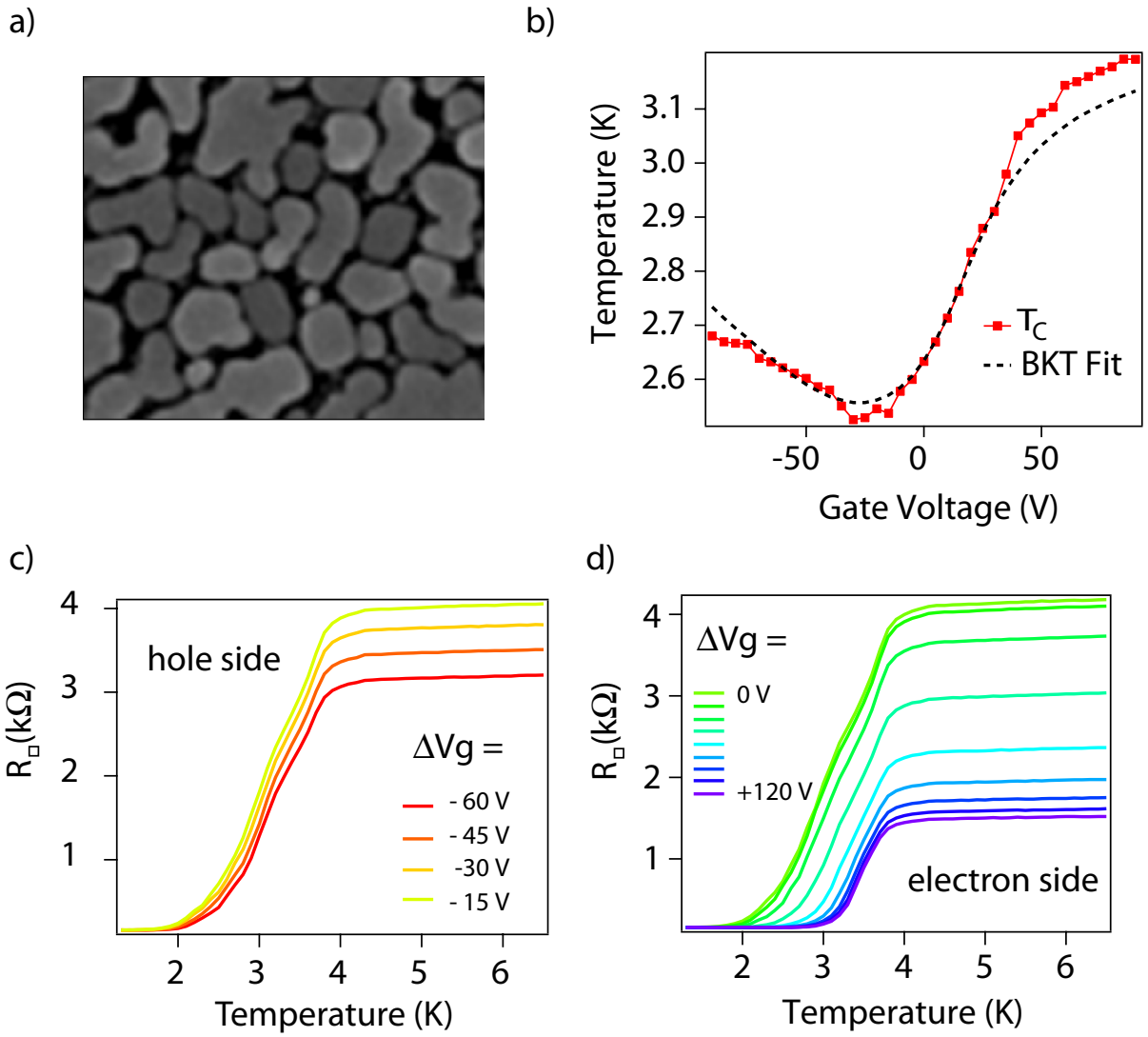

Figure 3.2 – ***Superconducting transition in sample SAM-31 made of CVD graphene.*** ***a)*** *SEM picture of the surface morphology.* ***b)*** *Temperature T_{BKT} extracted from c) and d) using equation (2.32). The dashed line is a fit to equation (2.39) with $\epsilon_\nu = 1.05$.* ***c)*** *Resistance as a function of temperature for various gate voltages on the hole side.* ***d)*** *Same thing on the electrons side.*

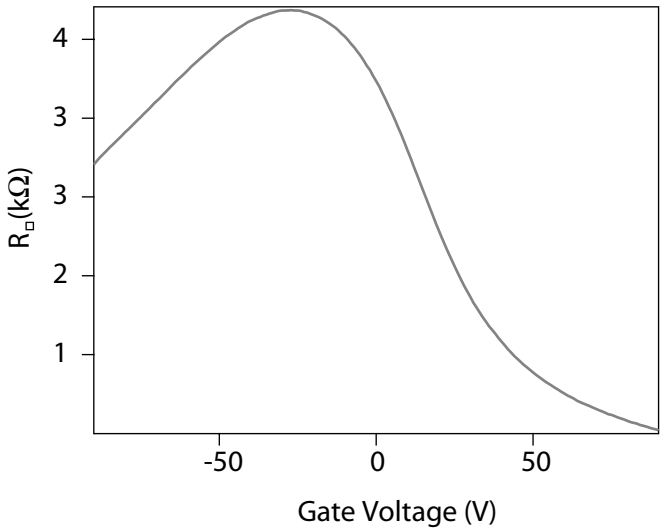

Figure 3.3 – *Sheet resistivity vs gate voltage of sample SAM-31 in the normal state at 6.5K.*

3.2.2 Superconducting transition temperature

Fig.3.2 shows the superconducting transition in sample SAM-31. Similarly to what was observed by [113] in Sn/exfoliated graphene, the superconducting transition temperature is rather high ($\geq$ 2.5 K) as compared to that observed in sample 51-5. The overlap between normal state resistance and critical temperature T_{BKT} is good and equation (2.39) can be used to fit it, yielding a value of the effective dielectric constant, describing the screening of the vortex-antivortex interaction $\epsilon_\nu = 1.05$, similar to values reported in the literature on thin films [149]. We can relate this behavior to the morphology, as was done in the previous chapter. Here we are in the presence of a densely-packed array of islands, connected by very short Josephson junctions, the critical current of which rises quickly below T_{c0}, in contrast to the case of longer junctions in sample 51-5.

3.2.3 Weakening of superconductivity at intermediate magnetic field

3.2.3.1 Destruction of superconductivity in Sn islands by magnetic field

Fig.3.4 shows the field effect curves of sample SAM-31 for different magnetic fields at low temperature ($T = 200$ mK). The field effect curve at $T > T_C$ is shown to give a lower bound to the normal state resistance (which increases slightly at lower temperatures). First of all, it can be seen that superconductivity, understood as zero resistance, survives *at least* up to $B = 0.23$ T for some values of gate voltage. Moreover, regions exhibiting a resistance lower than the normal state resistance survive up to $B_C = 0.63$ T. This indicates the presence of superconducting fluctuations. We do not expect the superconductivity of Sn islands themselves to be affected by the gate voltage. Therefore, we take the presence of these fluctuations as an indication that the

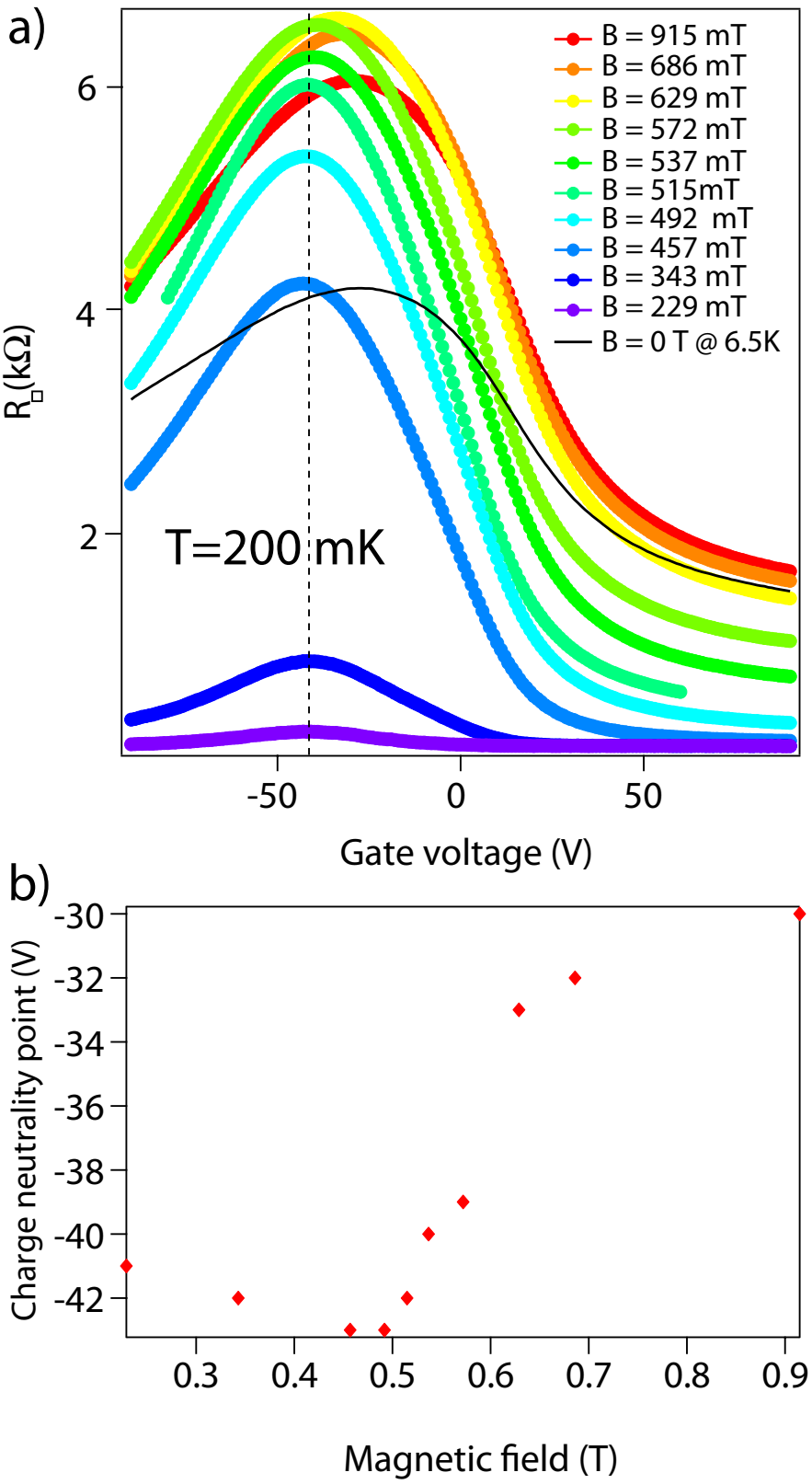

Figure 3.4 – ***Influence of magnetic field on the field effect curve.*** ***a)*** *Sheet resistance of SAM-31 versus gate voltage for various magnetic fields at low temperature (T=200 mK). The zero field resistance at 6.5 K ($T > T_C$) is shown the for comparison (black line). The vertical dashed line shows the position of the charge neutrality point at low fields.* ***b)*** *Position of the charge neutrality point (resistivity maximum) on the curve in a) as a function of magnetic field.*

grains are still superconducting at these fields, the main effect of magnetic field being to weaken the superconducting coupling between them.

This enhanced value of $B_C \approx 0.6$ T $>> B_C^{\text{bulk}}$ is similar to the one recorded in clean graphene devices decorated with Sn in Chapter 2 (see §2.4.1.2).

3.2.3.2 Consequences of the removal of superconductivity on the field effect lines

When the magnetic field is increased beyond 0.6 T, the field effect curves suddenly undergo a dramatic change. First of all, the Dirac point, which was fixed at low fields (see vertical dashed line in Fig.3.4), shifts towards more positive gate voltages and returns to its high temperature position (black curve). The occurence of the shift is concomitant to the recovery of normal state resistance in the highly doped region (see yellow curve). A shift in the Dirac point indicates that the transport is dominated by different regions of the graphene sheet, characterized by different doping. This can be understood as a side effect of removal of superconductivity. When the Sn islands (and the graphene in direct contact with them) are superconducting, the resistivity of the sample is determined by the regions *between* islands, which have a slightly different charge neutrality point. Once in the normal state, the main contribution to the resistivity comes from the tin-covered areas because they constitute the majority of the samples's surface (see §2.1.1.2).

The second striking difference is electron/hole symmetry. The normal state is characterized by very asymmetric field effect curves . Below the critical field, however, field effect curves become very symmetric. Again, this could be explained in terms of transport being dominated by a fraction of the sample's surface where scattering by charged particles is reduced, namely the one which is not covered by Sn. Below Sn islands, the presence of an electrostatic interface potential between graphene and the island (see §2.1.2) could give a carrier-type dependent scattering rate.

3.2.3.3 Superconducting fluctuations near the critical field

The third interesting feature in Fig.3.4 is that the maximum resistivity reached upon sweeping the gate goes through a maximum and decreases in the normal state (as can be seen by comparing the yellow and red curves). This behavior is only seen near the Dirac point. Away from it, the resistivity increases monotonically with magnetic field. As was stated in the previous paragraph, we interpret these as superconducting fluctuations, for the magnitude of the effect is rather small : $\delta g << g$. Note that at such magnetic fields, the weak localization effects should be pretty much suppressed in graphene (see Fig.1.36b), so that the high temperature resistance and the low temperature, high field resistance should coincide.

We can explain this non-monotonic magnetoresistance using the concept of superconducting fluctuations. When one is slightly above the critical temperature or

magnetic field of a superconductor, the superconducting pairing potential Δ is comparable but smaller than the temperature, so that short-lived (virtual) Cooper pairs start to contribute to the transport. This positive contribution to the conductivity is called Aslamasov-Larkin [184] (A-L). The electrons participating in these ephemeral pairs are not available for single-electron tunneling, however. The resulting reduction of the density of states (DOS) gives a negative correction to the conductivity. Finally, Maki [185] and Thomson [186] (M-T) calculated the effect of fluctuations on electron scattering (negative contribution). Together, these contributions give rise to the so-called 'paraconductivity'.

Galitski and Larkin [187] have calculated paraconductivity contributions to the conductivity near the critical field ($B \approx B_C$) and at low temperatures ($T << T_C$) in 2D amorphous superconductors. The same calculation was carried out one year earlier for the case of 3D granular superconductors with large conductance ($g >> 1$) by Beloborodov *et al.* [143]. Both found qualitatively similar results : the corrections to conductivity are dominated by the negative contributions, with DOS and M-T having a similar contribution in the case of [187] and DOS being the only significant term in [143]. However, it should be borne in mind that none of these cases strictly applies to our system, which is granular and 2D with $g \geq 1$.

As predicted by the aforementioned two papers, we do observe an overshoot of the resistance near the critical field in the vicinity of the Dirac point. Away from it, the lack of experimental points does not allow one to say if the resistance is increasing monotonously all the way or if it overshoots. But none of the two calculations mentioned above predicts the A-L contribution to take over the DOS contribution at low temperature *above* the B_C : we should always observe an overshoot of the resistance. What these theories do not explicit is how the corrections above the B_C interpolate to the state of zero resistance below the B_C, *i.e.* when the perturbative treatment is no longer valid. All we know is that, as the Cooper pairs start to have an infinite lifetime, the A-L contribution should diverge. This seems to happen at higher fields for gate voltages far from the Dirac point, hence the crossover between negative and positive paraconductivity upon sweeping the gate voltage.

3.2.4 Temperature dependence at intermediate magnetic field

Fig.3.5 shows how the sheet resistivity evolves at low temperatures when a magnetic field $B = 0.51$ T is applied perpendicular to the film. Remember that at zero magnetic field, the sample is superconducting for all gate voltages. For large electrostatic doping, the resistance continues to drop with decreasing temperature, indicating that positive contributions to the paraconductivity dominate. On the other hand, the region near the Dirac point behaves like an insulator : $\frac{dR}{dT} < 0$. Looking closely, we can see that some curves near the Dirac point show a double re-entrance. At first increas-

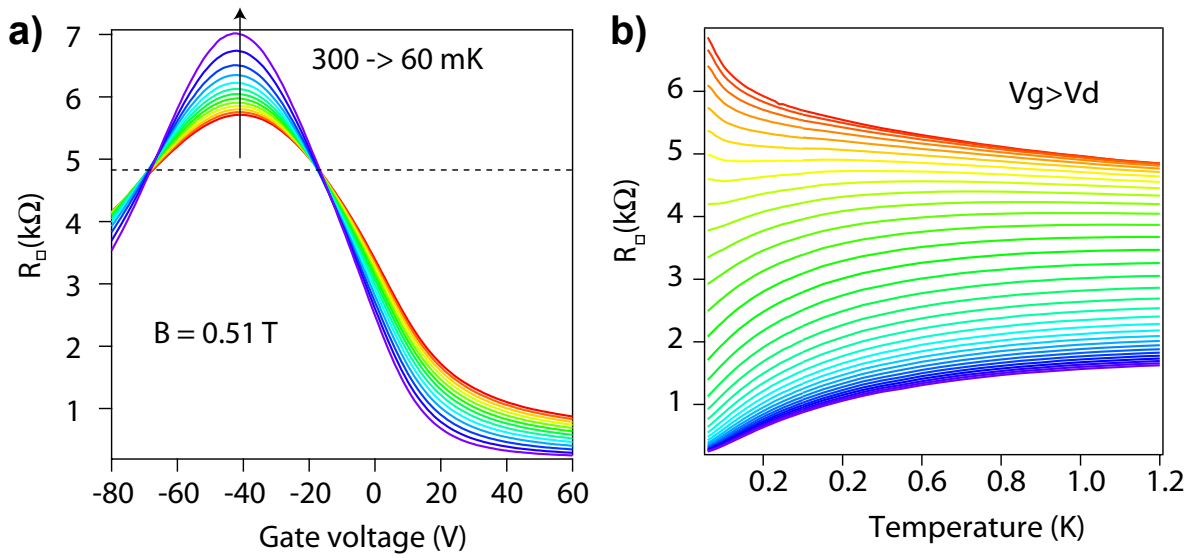

Figure 3.5 – ***Evolution of the sheet resistivity of SAM-31 at low temperatures for intermediate magnetic field*** $B = 0.51$ ***T. a)*** *As a function of gate voltage, at different temperatures.* ***b)*** *As a function of temperature for different gate voltages.*

ing, the curves bend down before going up again at the lowest temperatures. This kind of behavior is typical of granular superconductors [175, 182] and is believed to reflect the competition between the temperature-dependent charging and Josephson energies. This confirms our intuition that Coulomb repulsion is at play here.

The curves taken at different temperatures approximately cross around the same 'critical' point. Such fixed points are of great interest. Their temperature independence means that we can extrapolate the point down to zero temperature. To the right of this point, resistance decreases with decreasing temperature, eventually reaching zero. To the left, it increases to infinity. This is the finite-temperature manifestation of a zero-temperature phase transition, *i.e.* a *quantum* phase transition. A quantum phase transition is a phase transition that happens at zero temperature, and that is driven, not by thermal, but by quantum fluctuations.

3.2.5 Study of the fixed points

The superconductor-insulator transition (SIT) is a kind of quantum phase transition [3, 15]. However, its properties are not yet well understood. Since the pioneering work of A.M. Goldman and his team on the thickness-induced SIT in granular [175] and amorphous [164] films, and a series of theoretical paper by M.P.A. Fisher and co-workers [160, 179, 188] on the 'dirty boson model', one of the central questions in this field concerns the universal value of the resistivity at the quantum critical point, and the scaling exponents of the transition. There has been a lot of contradictory results concerning the critical resistance, most of which involved magnetic-field-induced transitions. Here we do not exactly study the classical magnetic-field-induced SIT.

That would require to record the resistivity versus magnetic field at several temperatures. There are technical reasons for this : because of eddy currents, our fridge has trouble maintaining a constant temperature while sweeping the magnetic field. Instead, we chose to sweep the gate voltage at intermediate magnetic field for different temperatures.

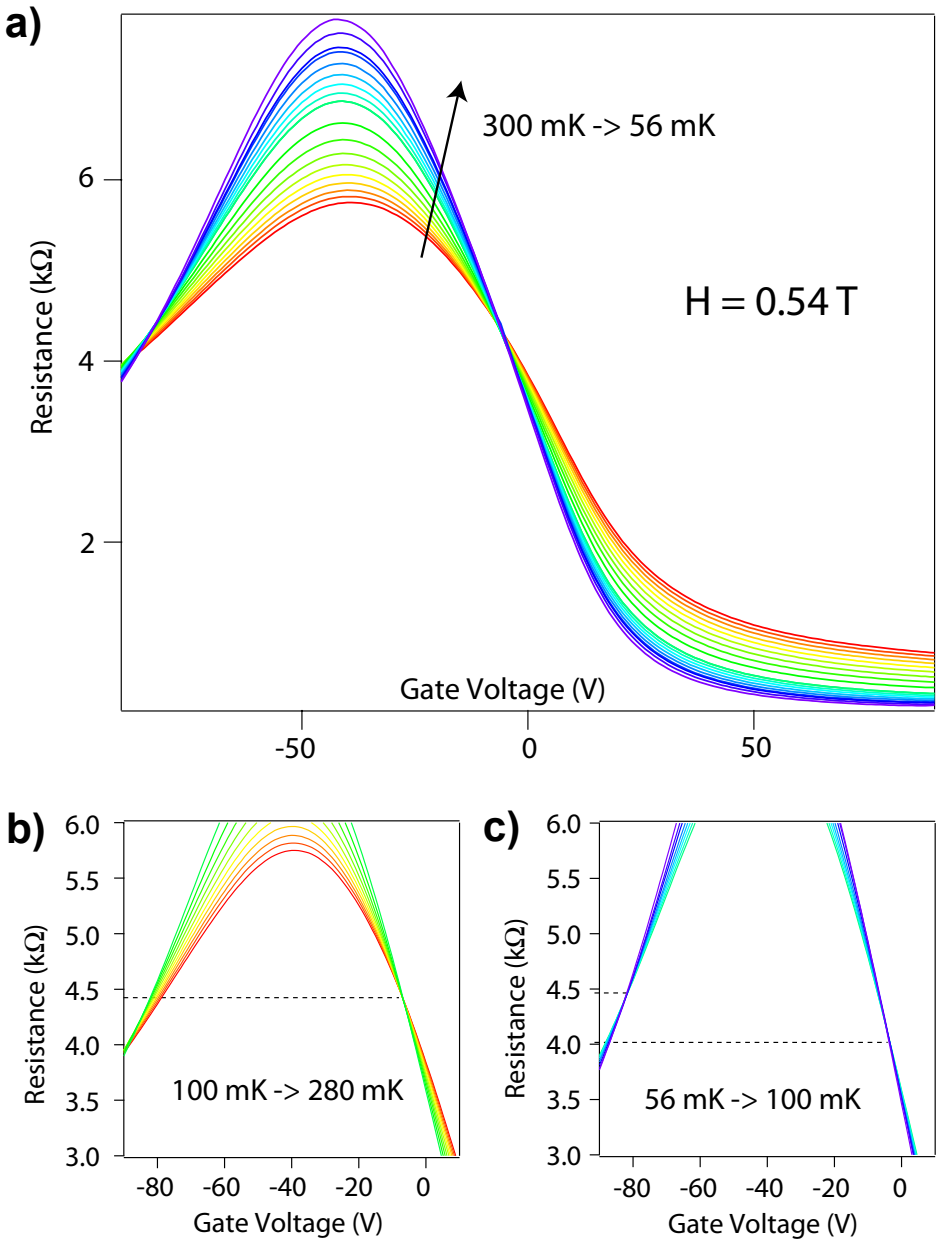

Figure 3.6 – ***Non-universal resistance at the gate-induced transition.*** ***a)*** *Sheet resistance as a function of gate voltage for magnetic field $H = 0.537$ T at different temperatures.* ***b)*** *Zoom on the 2 crossing points in the high temperature range (100 mK$<T<$ 300 mK).* ***c)*** *Zoom on the crossing points for the low temperatures range ($T <$ 100 mK).*

Upon close inspection, Fig.3.5 and 3.6 reveal not one, but two crossing points depending on the temperature range (see Fig.3.6b and c). This inconsistent behavior can be attributed to the renormalization of Coulomb interactions (see also Fig.3.5b). Moreover, the critical resistance is a bit different on the electron side and hole side. Finally, its value is strongly affected by the magnetic field. The different values are summarized in Fig.3.7a. Neglecting the carrier sign and temperature range, we can identify a clear trend towards increasing critical conductance.

Fig.3.7b shows a phase diagram constructed by putting together the results of 5 magnetic-field-induced SIT's in different materials. It shows that all these results pretty much fall onto the same line, which has two branches. If the transition happens at magnetic fields $B_C << B_{C2}(0)$ much smaller than the depairing field, the transition follows the 'dirty boson' model and exhibits a universal conductivity at the transition $G_C = 4e^2/h$. On the other hand, transitions that necessitate a magnetic field close to $B_{C2}(0)$ are characterised by a higher critical conductance, and a transition towards a weakly localized metallic state rather than a real insulating state. When the field required to induce the transition is very close to the depairing field, the quasiparticle DOS starts to increase significantly. These low-energy excitations are able to dynamically screen the Coulomb repulsion, thus giving the phase transition a whole new character. The effect of dissipation on quantum phase transitions has been discussed by Kapitulnik *et al.* [189]. In the presence of dissipation, the quantum phase transition loses its universal and quantum character, at least down to a very low temperature, which could be inaccessible.

We have included our data in the phase diagram of Fig.3.7b. An assumption has been made on the value of $B_{C2}(0)$ in our system. We know that it is higher than 0.69 T because at this field we can still find a gate voltage where $\frac{dR}{dT} > 0$. We took $B_{C2}(0) = 0.76$ T, so that the right-most two points fall onto the curve. There is a rather good agreement between our data and the literature on magnetic-field-induced SIT's.

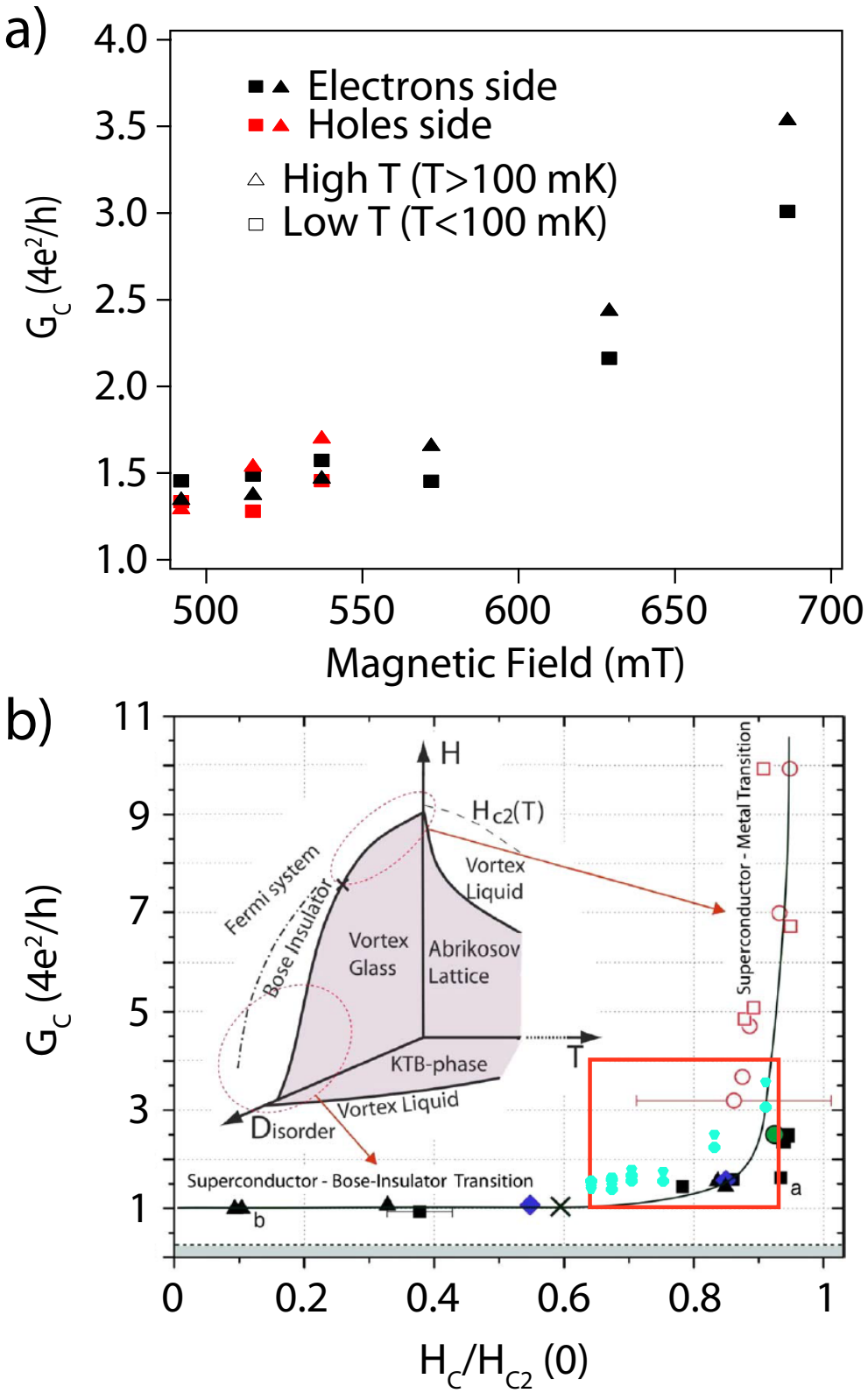

Figure 3.7 – ***Critical resistance at the quantum critical points.*** ***a)*** *Resistivities of the crossing points obtained on SAM-31 by sweeping the gate voltage at various temperatures, as a function of applied magnetic field.* ***b)*** *Diagram summing up the critical resistivities observed in various magnetic-field-driven SIT, in different materials. Taken from [190]. The data shown in a) is laid over the diagram as turquoise blue points inside the red box. Uncertainty remains on the value of* H_{C2}.

3.3 Electrostatically-driven superconductor-insulator transition in decorated highly disordered CVD graphene

In the previous section, we have demonstrated that for lightly disordered systems in a regime of artificially weakened superconductivity, the system can exhibit a transition from a regime of positive superconducting fluctuations to a weakly localized metal. In the coming section, we are going to use a much more disordered graphene sheet, sample SAM-40, that undergoes a transition to a regime of strong localization at low temperatures (see Chapter 1). In this regime, reduced Josephson energy due to the large normal state resistance, and unscreened Coulomb interactions prevent global superconductivity from being established, even though Cooper pairs are present in each superconducting grain. The possibility to tune the transition using the gate voltage at zero magnetic field allows one to get rid of magnetic-field-related problems such as depairing and vortex pinning physics. It will be shown that dissipation still drives the transition at high temperature, but that there is a crossover to a universal regime at lower temperatures. The critical exponent of the quantum phase transition will be extracted. The low-temperature transition shows a percolative behavior and the exponents are close to those predicted by [11] for the percolation of a phase-coherent domain. The insulating behavior is clearly of bosonic nature, and exhibits an Arrhenius-like activation law.

3.3.1 Strong localization crossover temperature in disordered graphene sheets

This time we purposedly choose a graphene sheet exhibiting large sheet resistances at room temperature, in order to have strong localization at low temperature. As we have seen in chapter 1, the amount of disorder can be controlled chemically, and graphene sheets exhibiting a maximum sheet resistance $g \cong 1$ offer the possibility to induce a gate-tunable transition between weak localization and strong localization at very low temperatures. Fig.3.8 shows the sheet resistance of the already-decorated graphene SAM-40 at 300 K and 4 K. From the evolution between room temperature and helium temperature, it is clear that in the region of the Dirac point we are on the verge of strong localization with a maximum sheet resistance already reaching the critical value of $g = 1$ at 4 K.

The mechanism of localization in 2D films has been explained in Chapter 1 (see 1.2.6). We can try to estimate at what temperature the regime of strong localization will set in near the Dirac point. The mean free path l_e can be estimated from the high temperature conductivity using equation 1.24 and assuming that the Dirac peak width

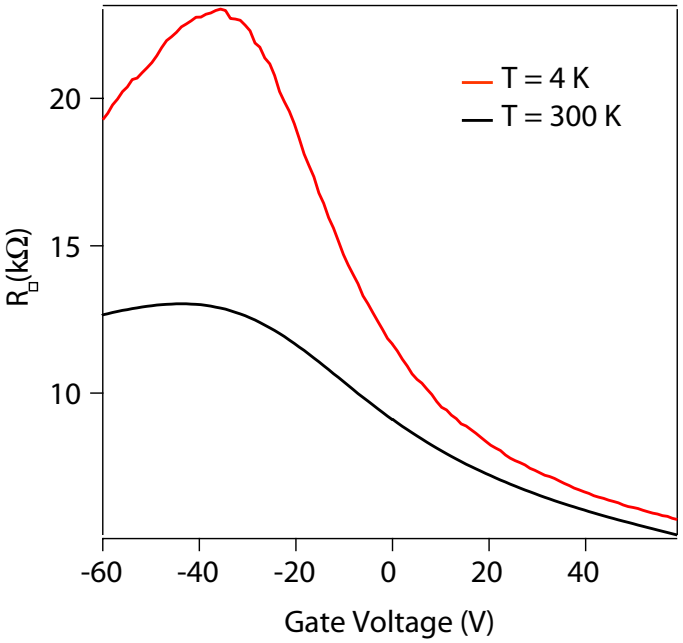

Figure 3.8 – *Field effect curve of a tin-decorated disordered CVD graphene sheet at room temperature and at 4K.*

gives an estimate of the residual carrier density at the Dirac point. For $V_g^{FWHM} = 40$ V, this density is of the order of :

$$n_0 \approx \frac{C_g V_g^{FWHM}}{e} \cong 3 \times 10^{16} \text{ m}^{-2} \tag{3.4}$$

This gives :

$$l_e \cong \frac{1}{\sqrt{\pi n_0}} = 3.25 \text{ nm} \tag{3.5}$$

We can then deduce the localization length using equation 1.35 :

$$\xi_{loc} = l_e \exp(\pi k_F l_e) = 75 \text{ nm} \tag{3.6}$$

Finally, we expect the regime of strong localization to occur when the coherence length $L_\Phi \cong \xi_{loc}$. If the coherence length is limited by electron-electron interactions, we expect this to happen when the temperature reaches the Thouless energy of the localization volume :

$$T_\xi \cong \frac{\hbar D}{k_B \xi_{loc}^2} = \frac{\hbar v_F l_e}{2 k_B \xi_{loc}^2} \cong 2.1 \text{ K} \tag{3.7}$$

This result is in good agreement with our observation that the sheet resistivity reaches $g = 1$ at 4 K. Following the same procedure, we can estimate the transition temperature at high gate voltages ($V_g = +50$ V). Using $g \cong 5$ and $n_0 \cong 6 \times 10^{16}$ m^{-2}, we find $T_\xi = 7 \times 10^{-5}$ K. It is now clear that a metal-insulator transition should happen in the graphene sheet upon changing the gate voltage at low temperatures.

3.3.2 High temperature regime : re-entrant insulating state and the role of dissipation

The temperature dependence of this sample at first resembles that of the previously studied samples (Fig.3.9). The critical temperature of bulk tin can be clearly identified (black dotted line), and is accompanied by a partial drop of the resistance. At lower temperatures, the broad transition towards superconductivity is very reminiscent of the BKT transition. For gate voltages near the Dirac point, however, this time we observe a re-entrant insulating behavior. The turning point is outlined with a red dotted line. Below this point, the insulating curves $\frac{dR}{dT} < 0$ start to diverge exponentially (see Fig.3.10), exhibiting a truly insulating state, as opposed to the weak dependence observed in the previous section.

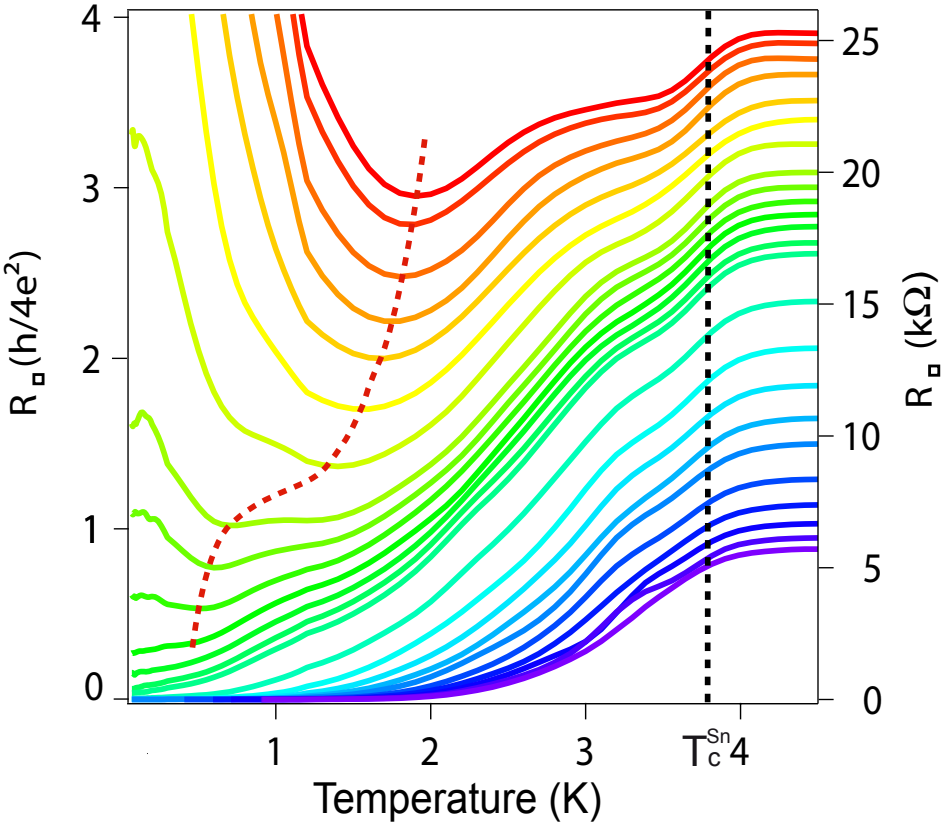

Figure 3.9 – *Evolution of sheet resistance with temperature for different values of gate voltage. From red to purple, $\Delta V = 0V$ to $\Delta V = +96V$*

The non-monotonic temperature dependence of the resistance is a typical signature of near-critical granular systems [175, 182], as opposed to homogeneously disordered films, which usually display a monotonic temperature dependence with a well-defined threshold independent of temperature [164]. The re-entrance is attributed to the temperature dependence of the screening of Coulomb interactions by thermally activated quasiparticles. This observation is in line with our expectations : being com-

posed of 'islands' separated by weak graphene links, our system clearly belongs to the 'granular' family.

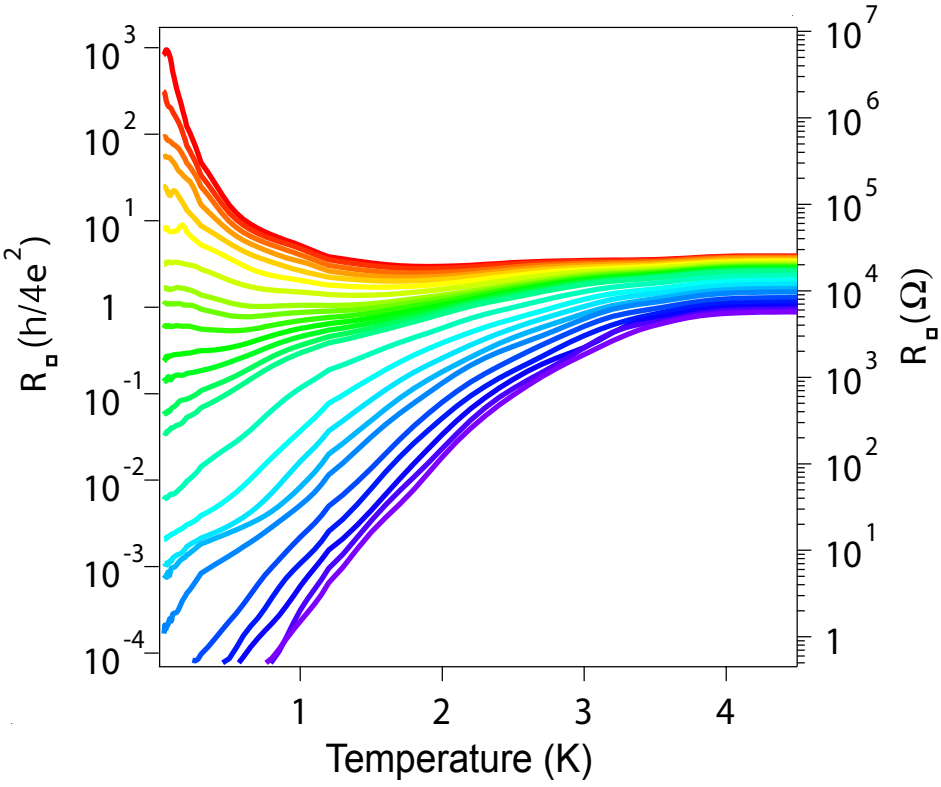

Figure 3.10 – *Sheet resistance versus temperature for different values of gate voltage (the same used in Fig.3.9), plotted on a logarithmic scale.*

From the data of Fig.3.10 we can derive a phase diagram : plotting $\log(\frac{dR}{dT})$, we can easily identify the insulating phase $\log(\frac{dR}{dT} < 0) = -\infty$. The color plot is displayed in Fig.3.11. The re-entrant temperature corresponds to the top of the white 'bell'. It seems related to a constant value of the normal state resistance, as is shown by the black line laid over the diagram. This normal state resistance has been obtained by applying a magnetic field $H = 1$ T to remove all superconductivity (the R_N values obtained that way are plotted in Fig.3.12). It is interesting to note that the phase boundary is related to R_N in the high temperature limit, but that the agreement breaks down at lower temperatures. In the low temperature part it follows a vertical line of constant gate voltage.

3.3.2.1 Role of the tunable dissipative environment

According to the canonical model (see §3.1), the phase boundary between superconducting and insulating behavior should correspond to a constant value of the ratio E_J/E_C. We know that, at temperatures of the order of $T_C/3$, I_cR_N still varies significantly with temperature, even for short Josephson junctions (see Fig.2.13). Therefore, this boundary cannot correspond to a constant value of E_J, which means E_C must be

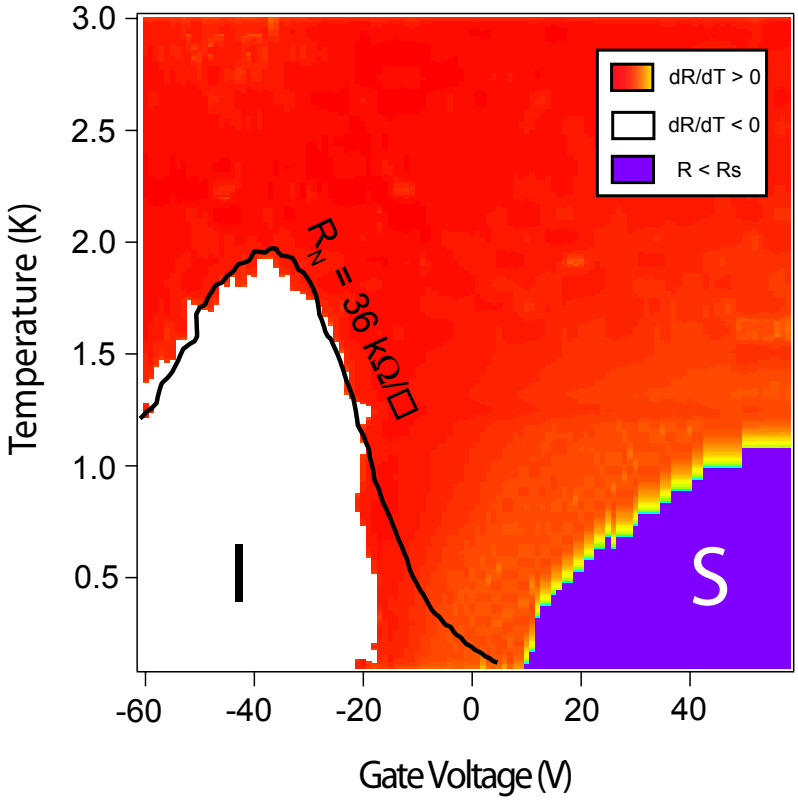

Figure 3.11 – *Color plot of* $ln\left(\frac{dR}{dT}\right)$. *I stands for 'insulating', S for 'superconducting'. The line of constant normal state resistance* $R_N = 36\ k\Omega$ *is laid over.*

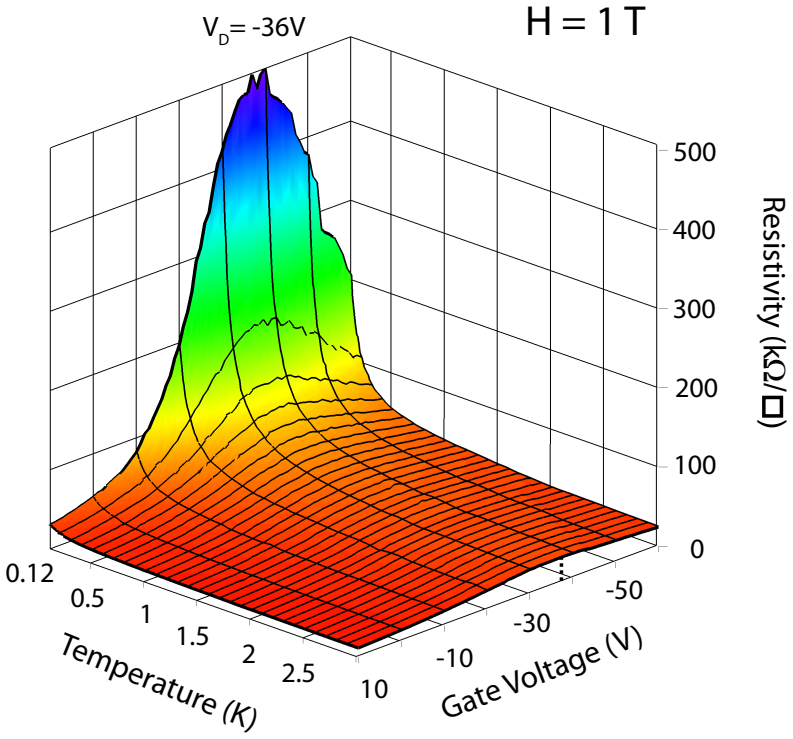

Figure 3.12 – *Normal state sheet resistivity as a function of gate voltage and temperature, obtained by applying a magnetic field of* 1 *T.*

changing as well. Several sources of dissipation can account for this renormalization of the charging energy E_C.

First, thermally activated quasi-particles have often been invoked as a source of screening in arrays of tunneling Josephson junctions, or in granular films [167, 168]. This source is particularly active at high temperatures, close to T_{C0}. However, it should depend on temperature only, and not on R_N, as it is associated to the superconducting Sn islands and not to graphene itself. The presence of a metallic plane nearby is also a known source of screening : electron-electron interactions are cut-off at a distance equal to twice the gate dielectric thickness [57] for example. The effect of this capacitive coupling on the superconductor-insulator transition in 2D arrays of Josephson junctions have been studied both experimentally [169] and theoretically [170]. However, that source of dissipation is constant, since the back-gate's conductivity does not change. Finally, a similar effect can be observed when a resistive shunt is present between the SC islands [172]. The latter explanation seems the most appropriate in our case. As is explained in Fig.3.13, our system is naturally shunted. Takahide *et al.* [172] observed that resistively shunted arrays of Josephson junctions exhibit superconductivity even for very low values of the E_J/E_C ratio and that the SIT was controlled by the value of the shunt resistance. The threshold value of that shunt resistance depends only weakly on the E_J/E_C ratio when $E_J/E_C << 1$. Fisher [191] actually showed that for $E_J/E_C << 1$, the critical shunt resistance below which the superconducting phase is stabilized is universal : $r_n^c = d\frac{h}{4e^2}$, where d is the array's dimensionality. Once renormalized by the aspect ratio W/L of an individual junction, which is typically larger than 1, the value of the normal state resistance $R_N = \frac{W}{L} r_n = 36$ kΩ we found is in good agreement with this theory.

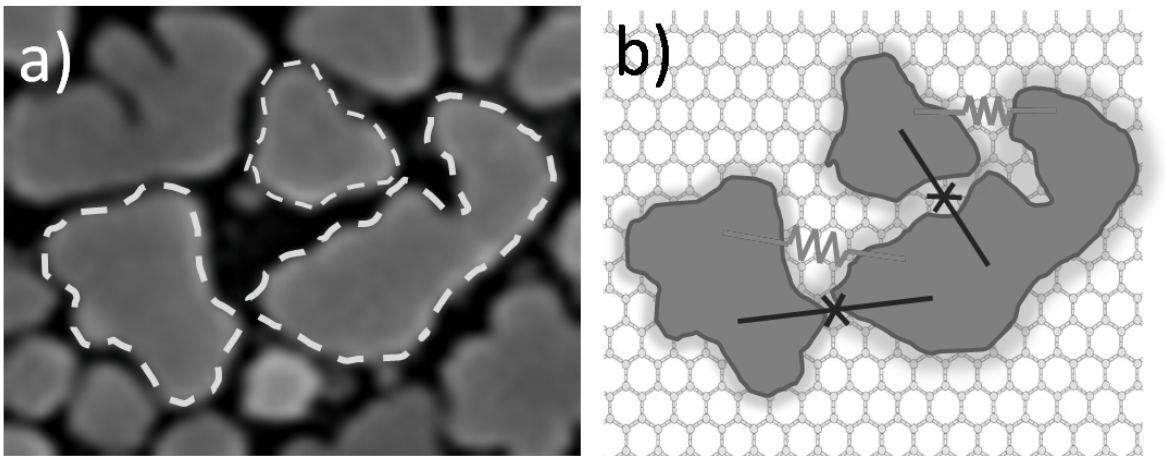

Figure 3.13 – ***A resistively shunted array of Josephson junctions. a)*** *Detail of an SEM micrograph showing several tin islands.* ***b)*** *Equivalent electrical circuit. The blue shaded areas represent the superconducting correlations around the SC islands. Percolation of the blue areas forms Josephson junctions. The remaining (non-shaded) areas act as resistive shunt.*

3.3.3 Low-temperature limit : universal sheet resistance and signs of percolation

As can be seen in Fig.3.11, the low temperature phase boundary no longer follows a constant value of R_N, but takes place at evergrowing values of the normal state resistance. Instead it seems that it should rather be defined by a critical value of gate voltage. This can be more clearly seen in Fig.3.14, where a crossing point is apparent. Interestingly, the resistivity at the critical point is very close to the 'universal' value of $h/4e^2 = 6.45$ kΩ.

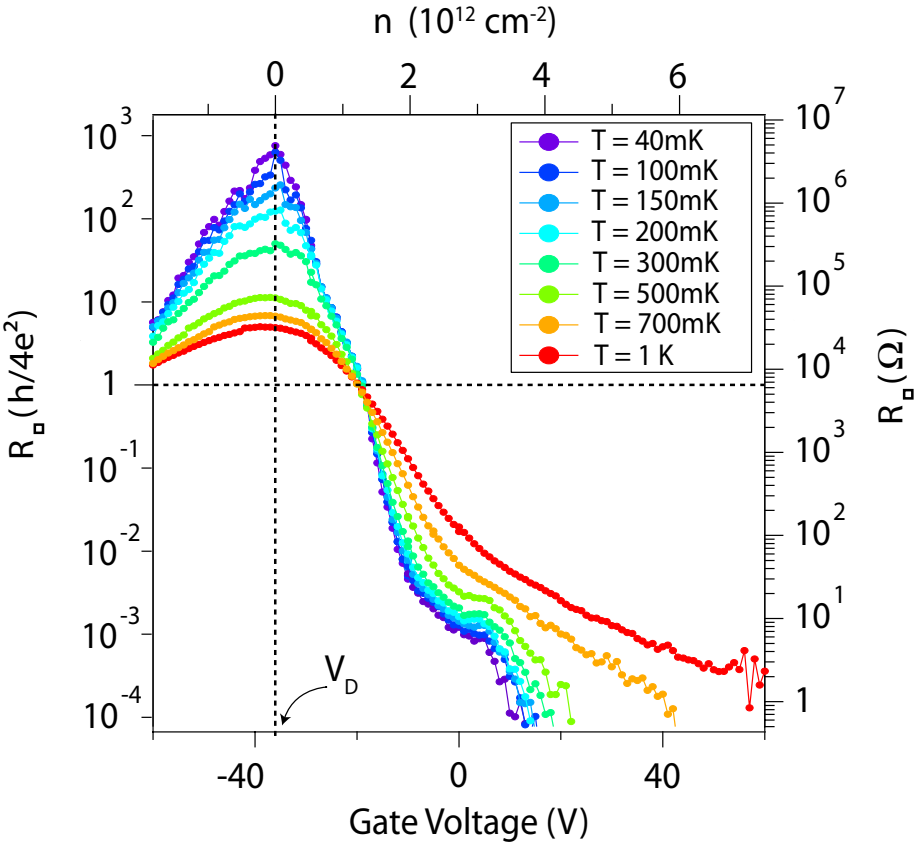

Figure 3.14 – *Low temperature sheet resistance dependence on gate voltage. The crossing point near $V_g = -20V$ is indicated, as well as the position of the Dirac point.*

3.3.3.1 Transition at constant effective disorder

The transition at constant gate voltage $V_g = -20$ V corresponds to a transition at constant value of the effective disorder $k_F l_e$. From Fig.3.8 one can once again extract the localization length, this time for $V_g = -20$ V. We find $\xi_{loc}(-20\text{ V}) \approx 150$ nm, a length which is on the order of the distance between the centers of two Sn islands. This fact is interesting : it seems that one needs to have localized states large enough to bridge two Sn grains in order for global phase coherence to set in. This makes sense,

since the superconducting proximity effect is incompatible with inelastic processes such as a phonon-assisted hopping between localized states.

3.3.3.2 Low temperature current-voltage characteristic

To understand what mechanism underlies this low temperature transition, it is interesting to look at the critical current. Fig.3.15 shows the critical current at various gate voltages measured close to base temperature ($T = 100$ mK). First of all, the critical current density, when compared to the case of exfoliated systems, show a drastic reduction. Near the transition, critical current of $I_C = 50$ nA is observed, which corresponds to critical current densities 2000 times smaller than what we saw in Chapter 2. This indicates that only a few channels transport the supercurrent across the sample.

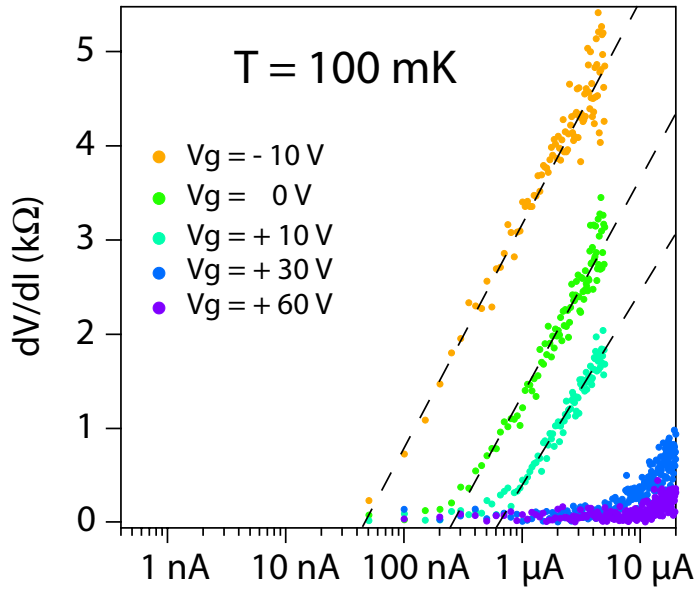

Figure 3.15 – *Differential resistance as a function of applied DC current, for different gate voltages on the right side of the crossing point visible on Fig.3.14 (superconducting side).*

Another interesting feature that is revealed by Fig.3.15 is that $\frac{dV}{dI}(I_b)$ grows logarithmically :

$$\frac{dV}{dI}(I_b) \propto \ln(I_b) \tag{3.8}$$

Let's assume that the current flows along a few 1D chains of Josephson junctions with different critical currents. The distribution of these critical currents defines the system's disorder. Each junction i, when biased above its critical current I_c^i, contributes to the total differential resistance :

$$\frac{dV}{dI} = \sum_{I_c^i < I_b} R_N^i \tag{3.9}$$

We can assume that the critical current of a junction is inversely proportional to its normal state resistance R_N^i. Therefore, the total differential resistance measured at a certain bias current I_b is equal to :

$$\frac{dV}{dI}(I_b) \propto \int_{i=0}^{i=I_b} \frac{f(i)}{i} di \tag{3.10}$$

where $f(I)$ is the critical current distribution of the junctions in the critical path. By equating (3.8) and (3.10), we find $f(i) =$ constant, *i.e.* the critical current distribution is uniform. The low temperature behavior gives us informations about the disorder statistics. It is interesting to compare this result to the model of [192]. This model was developped to explain the measurement of [193] on quench-condensed granular Pb films. These transport measurements show a temperature behavior very similar to ours (see Fig.3.16), with the resistance of the superconducting curves increasing with temperature like $R \propto \exp(T/T_0)$ (see Fig.3.10). In [192], the uniformly distributed value is not the critical current, but the junction's length r_{ij}. The junction's resistance is $R_N \propto \exp(r_{ij}/r_0)$, and therefore the critical current $I_c \propto R_N^{-1}$ follows a linear distribution :

$$f(I_c) = \frac{dN}{dI}(I_c) = \frac{dL}{dI_c}\frac{dN}{dL}(I_c) = \frac{dL}{dI_c} f(L) \tag{3.11}$$

where $f(L)$ is the (uniform) distribution of lengths. Since $I_c \propto exp(-L)$, $L \propto \ln(1/I_c)$ and it follows that $f(I_c) \propto cnst \times \frac{dL}{dI_c} \propto I_c$.

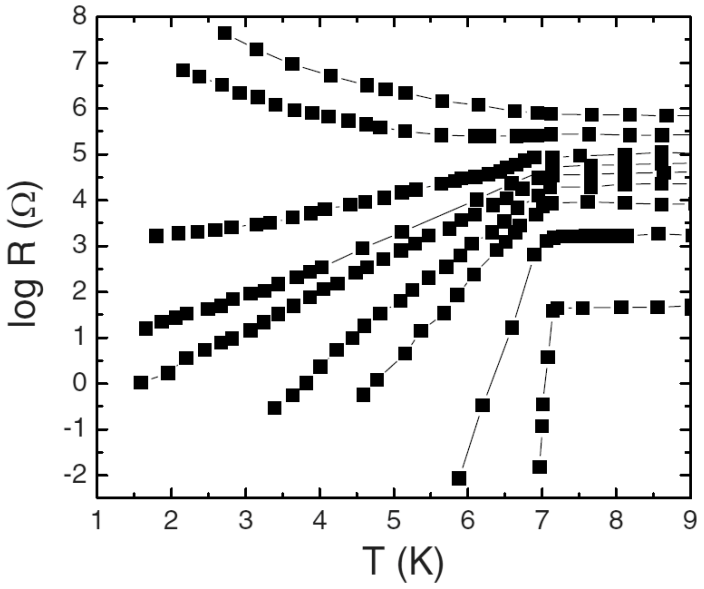

Figure 3.16 – *Resistance versus temperature for different thicknesses of a quench-condensed granular film of Pb (without graphene). Taken from [193].*

Percolation has some universal features, but any percolation treatment necessitates system-specific inputs. Better understanding of the system's disorder has been

inferred from the current-voltage characteristic. Further investigation on this system should involve a specific percolation analysis taking these observations into account.

3.3.4 Characterization of the insulating phase

3.3.4.1 Magnetoresistance and Cooper pair localization

In the field of SIT, magnetic field is one of the most common way to trigger the transition. However, because it involves the complication of vortex physics and spurious depairing effects, it often lacks the universal character of transitions induced by thickness variation. We saw that in the previous experiment with sample SAM-31. SAM-40, on the other hand, is more disordered and offers a unique opportunity to study the superconducting-insulator transition induced by magnetic field in different limits (low and high sheet resistivity) by tuning the carrier density at constant disorder.

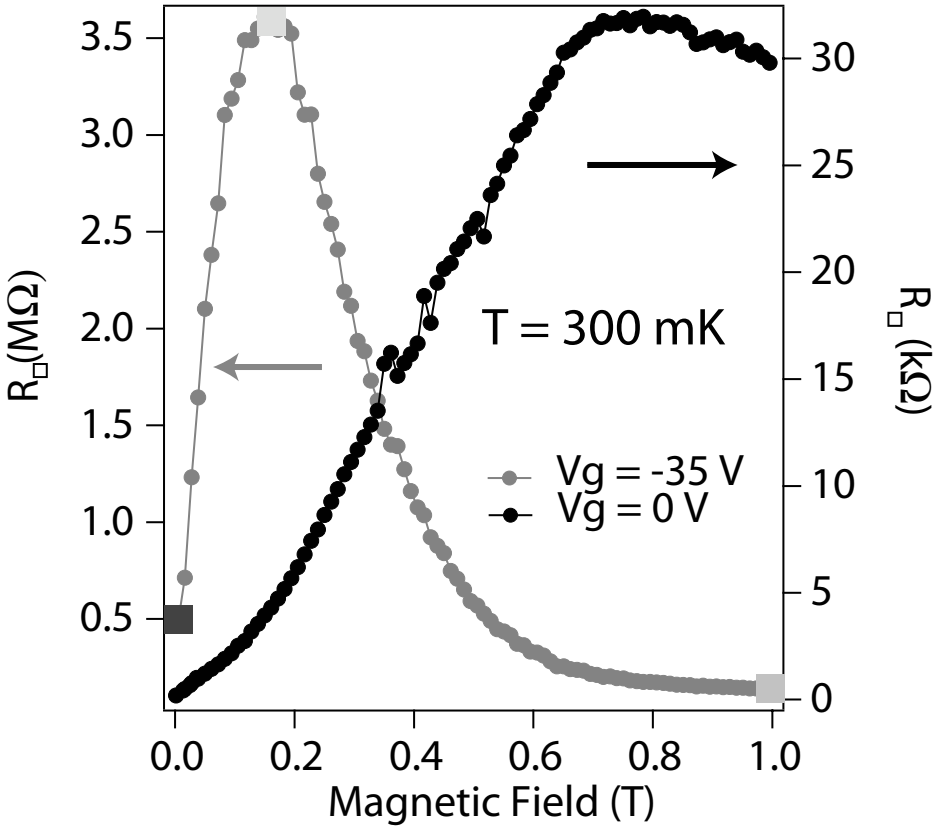

Figure 3.17 – *Sheet resistance as a function of magnetic field, for the gate voltage corresponding to the most insulating state (red curve), and near the transition on the superconducting side (black curve).*

Keeping the sample at $T = 300$ mK, we have varied the gate voltage and magnetic field. Unfortunately, the sample was lost before it could be characterized on the superconducting side. Fig.3.17 therefore only shows the magnetoresistance curves in the insulating state (red curve) and in the intermediate state (black curve). Moreover, we

had no chance to study the magnetic-field-induced transition. Still, the sample's response in the insulating state is very interesting. It shows the same kind of giant magnetoresistance observed in very disordered Bi [146], InO_x [165] and TiN films [174]. The non-monotonic character of the magnetoresistance is usually ascribed to the localization of Cooper pairs (positive magnetoresistance), followed by their destruction (negative slope), and provides a proof of the 'bosonic' character of the insulating phase.

The reason why bosonic insulators are more resistive than single-electrons insulators is because the tunneling probability of a Cooper pair is squared as compared to that of an electron. Therefore, the tunneling regimes is dominated by tunneling of single electrons, the DOS of which is reduced when pairing is effective. This effect is actually the same as the paraconductivity contributions discussed in the previous experiment. Superconducting fluctuations tend to lower the conductance because at $T << T_C$ and intermediate fields, the DOS suppression dominates the Aslamasov-Larkin fluctuations, so that a small magnetic field removes the positive contribution while keeping intact the negative one. Even though this is qualitatively understood, an analytical treatment of this problem is very difficult because it cannot be treated in a perturbative way. Here, the corrections to conductivity diverge (we have recorded resistance overshoot $R_{max}/R(0)$ of up to a factor 10^3 at lower temperatures, see next sections).

In the following, we are going to characterize the insulating state occuring at zero field, intermediate field and strong field, by studying their temperature dependence.

3.3.4.2 Evolution of the resistivity with temperature

On the red curve of Fig.3.17, we can identify three characteristic regions, the temperature dependence of which would be of interest to study. There is the zero field phase (indicated by a blue square), the strongly insulating phase at intermediate field ($B = 0.15$ T, yellow square), and the normal phase ($B = 1$ T, green square).

Insulating state near the Dirac point at $B = 0$ T. Fig.3.18 shows an attempt to fit the resistivity versus temperature of the zero magnetic field phase at the Dirac point ($V_g = -35$ V), with the three usual laws between 1 K and 200 mK. Notice that at temperatures below 200 mK, the resistance starts to saturate, making any fitting impossible. This saturation happens earlier for the least resistive samples. We attribute this saturation to an unfortunate carelessness in the measurement. As a matter of fact, the voltage-biased experiment was carried out using a voltage of 500 μV, a value comparable to the transport gap measured in bare CVD graphene in Chapter 1. In these conditions, it is not surprising to see the resistance saturate. However small the remaining available resistance range is for fitting, the resistance seems to follow

an activation 'Arrhenius' law. While the discrimination between Efros-Shklovskii and Mott variable range hopping regimes is usually controversial and necessitates data spanning many orders of magnitude [55], the Arrhenius activation law has a much steeper divergence of the resistance, and the discrepency is already quite apparent in Fig.3.18.

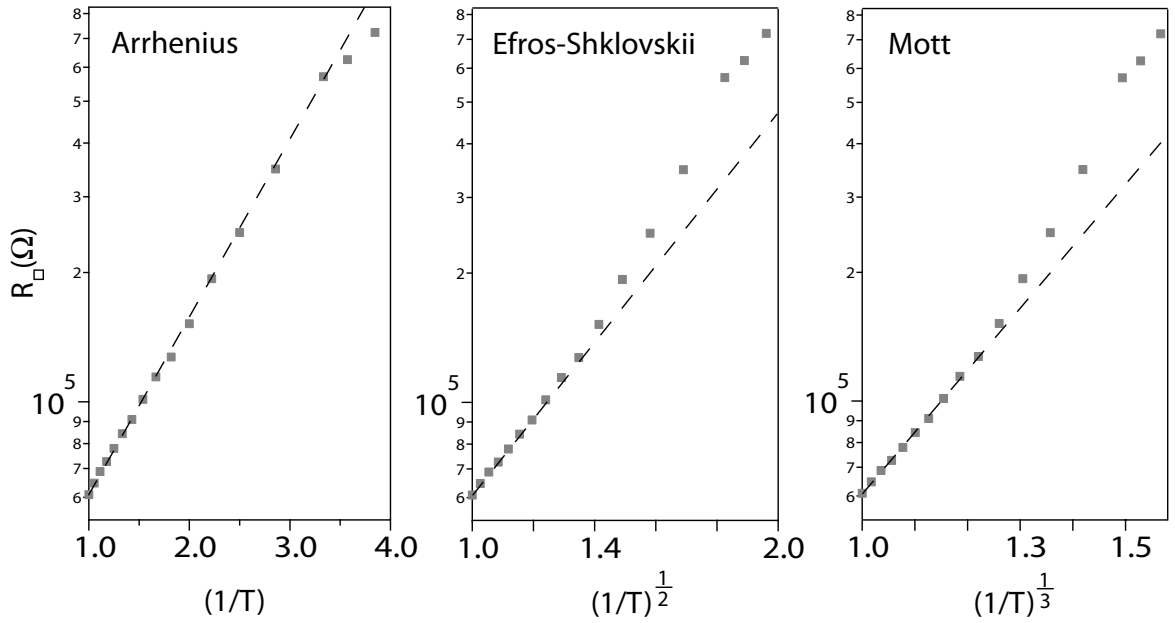

Figure 3.18 – *Sheet resistance at the Dirac point ($V_g = -35$ V) at zero magnetic field, fitted to the three usual laws $R = R_0 \exp\left(\frac{T_0}{T}\right)^{\alpha}$, with $\alpha = 1$ (Arrhenius), $\frac{1}{2}$ (Efros-Shklovskii) and $\frac{1}{3}$ (Mott variable range hopping).*

Strongly insulating state at intermediate field $B = 0.15$ T. Applying a magnetic field of $B = 0.15$ T to maximize the sample's resistance, the system now exhibits a clear activated behavior. Fig.3.19 shows such a fit for different gate voltages in the vicinity of the Dirac point. Again, the resistance saturated at lower temperatures. Because of the low-temperature saturation, we first thought we had identified an Efros-Shklovskii dependence over a large range of resistance [194], but a closer look at the data revealed that there was no possibility to consistently fit the resistance at different gate voltages using that law. Moreover, upon closer inspection (Fig.3.18), the high temperature part of the curve at $V_g = -35$ V does not even follow the ES law, but rather an Arrhenius law.

Temperature dependence of the 'normal' insulator at high field $B = 1$ T. In the high magnetic field limit ($B = 1$ T), resistance is lower than at zero field. The temperature dependence of this 'normal' state is plotted in Fig.3.21. This time, the resistance

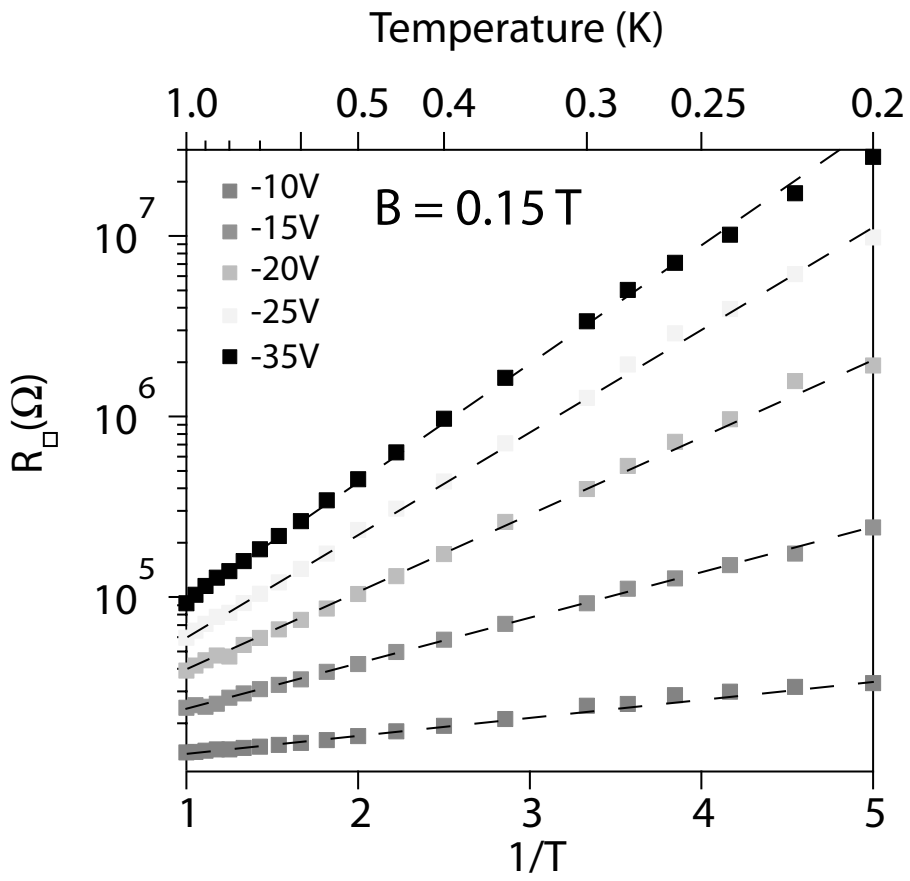

Figure 3.19 – *Temperature dependence in the highly insulating state at magnetic field $B = 0.15$ T for different gate voltages. Dashed lines are fits to the activation law $R = R_0 \exp(\frac{T}{T_0})$ with $T_0 = 1.55$ K, 1.37 K, 1.02 K, 0.87 K, 0.6 K and 0.25 K, respectively.*

clearly fails to follow the activation law, but instead ii seems to behave according to a variable range hopping mechanism (VRH). However, the limited range of temperature does not allow us to discriminate between Mott VRH and Efros-Shklovskii VRH law. This time, we see no saturation, and the data can be fit down to 0.12 K.

3.3.4.3 Discussion

First of all, these data confirm that the insulating state at low and high field are of different natures. There is a stark contrast between the hard gap observed at low fields and the VRH transport at high field. Hard gaps in the transport of 'superconducting' insulators have also been observed in amorphous InO_x [165] and granular quench-condensed films of Bi, Al and Ga [195, 196]. It is predicted by theories pertaining to both granular [197] and amorphous [198] bosonic insulators.

The activation temperatures at $B = 0$ T and $B = 0.15$ T are reported together in Fig.3.20a. The maximum activation temperature is of the order of $T_C/2.4$ similarly to what was observed in InO_x films [165]. There seems to be a good linear relationship between the normal state sheet resistivity and the activation temperature, as is shown

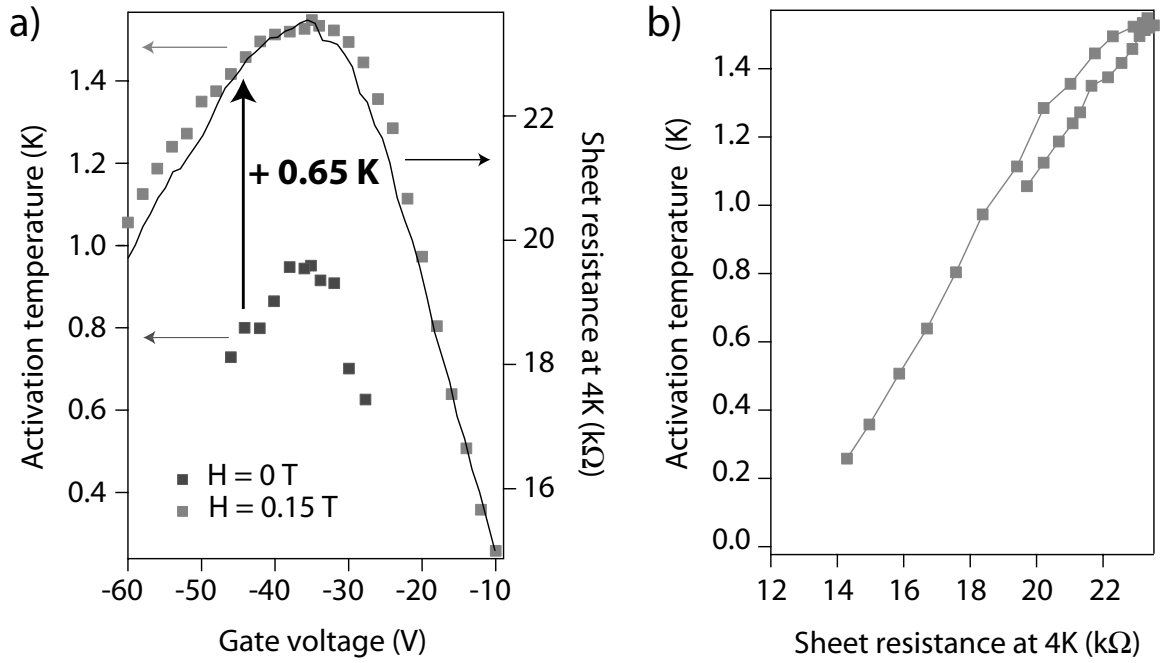

Figure 3.20 – ***Activation temperature extracted from the fit to the Arrhenius law, for*** $B = 0$ ***T and*** $B = 0.15$ ***T. a)*** *As a function of gate voltage. The black line laid over is the normal state sheet resistivity.* ***b)*** *As a function of normal state sheet resistivity.*

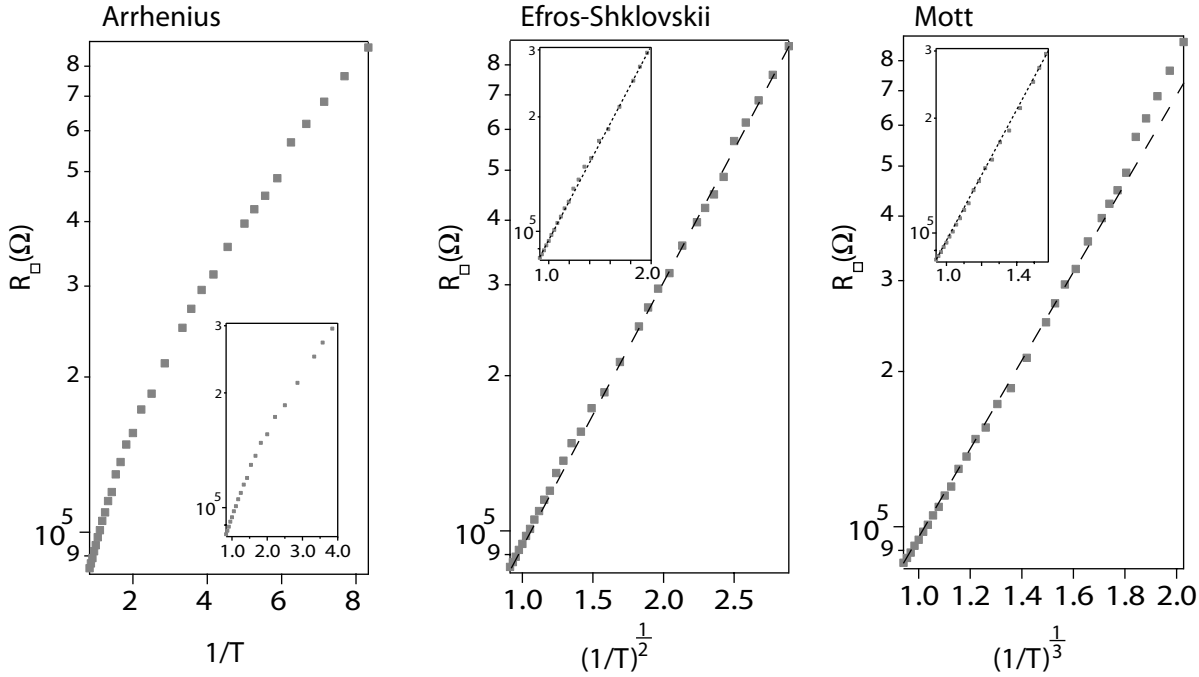

Figure 3.21 – *Temperature dependence of the film resistance in the limit of high magnetic field ($B = 1$ T) at the Dirac point ($V_g = -35$ V), compared to Arrhenius, Efros-Shklovskii and Mott VRH law. Insets the same data, limited to the range used for the previous plots, in case a different behavior would show up at high temperatures.*

on Fig.3.20b for the case of $B = 0.15$ T. As suggested by [197], T_0 could be related to the change in tunneling conductance induced by the gate votlage. Besides, the activation temperatures at $B = 0.15$ T seems shifted upward by 0.65 K as compared to the ones at zero field, meaning that the magnetic field influences indifferently the transport gap of low and high resistance films.

There are different models [199, 197, 198, 200] treating the superconducting insulator. Although choosing the best model is beyond the scope of this manuscript, the model of Beloborodov *et al.* [197] seems to apply quite straightforwardly to our system. They studied the magnetic response of a granular film with inhomogeneous grain sizes. Because grains of different sizes have different critical fields, there exists a range of magnetic field for which two phases coexist : a normal phase and a superconducting phase. Since we are in two dimensions, the theory of on-site percolation states that for some configurations, neither phase percolates. If the tunneling resistance between two grains is low enough, this results in a very insulating phase, with an activation energy proportional to the superconducting gap.

Only a careful examination of experimental data, such as the magnetic field and normal state sheet resistivity influence on the activation temperature, together with a better understanding of the energy levels within the grains and of the coupling between graphene and Sn grains will tell if this model fits our data.

3.3.5 Analysis of the quantum phase transition

As we have seen before (Fig.3.14), in the low temperature regime, the sample starts to exhibit a single crossing point at a critical value of gate voltage. It is always worth trying to extract more information when one sees what appears like a quantum phase transition. Since the seminal papers of Hebard and Paalanen [173] and Fisher [179], it is common practise, when one finds a superconductor-insulator transition, to extract the critical exponents of that transition.

3.3.5.1 Quantum phase transition

Quantum phase transition are continuous phase transition (as opposed to first order phase transitions), which are not driven by thermal fluctuations, but by quantum fluctuations [3]. They occur when a parameter K entering the Hamiltonian is varied continuously beyond a critical value K_C. We need to define an order parameter characterizing the transition. Here both phases are characterized by a finite superconducting order parameter $\Psi = \Delta \exp(j\varphi)$. What distinguishes the superconducting phase from the insulating phase is the long-range order of the superconducting phase φ. The two phases can therefore be defined by the correlation length of the phase φ. It will go to zero in the insulating phase, and diverge at the critical point, where global phase coherence is established. All phase transitions are governed by scaling

laws near their critical point. The correlation length of superconducting phases obeys :

$$\xi \propto \delta^{-\nu} \tag{3.12}$$

where ν is the critical exponent, and $\delta = \frac{|K-K_C|}{K_C}$ is the distance from the critical value of the parameter K. The exponent ν defines the universality class of the phase transition. For quantum phase transitions, in addition to the correlation length, there exists a correlation time ξ_τ reflecting the robustness of the ordered phase against zero point fluctuations. This time also diverges at the transition :

$$\xi_\tau \propto \omega_c^{-1} \propto \xi^z \tag{3.13}$$

where z is called the dynamical critical exponent and ω_c is the cut-off frequency of the fluctuations.

Therefore, the partition function of a quantum system of dimension d can be expressed as that of a thermodynamic system of dimension $d+1$. At zero temperature, the temporal dimension is infinite, but it becomes bounded at finite temperatures, thus limiting the divergence of the correlation time : $\xi_\tau < \hbar/T$. Here we see that at finite temperatures there is a crossover between a regime of quantum fluctuations when $\xi_\tau < \hbar/T$ and a regime of thermodynamic fluctuations when $\xi_\tau = \hbar/T$ (thermal decoherence bounds ξ_τ). The critical point is characterized by a diverging correlation length at zero temperatures, which means infinitely long-range fluctuations $\omega_c \to 0$. Therefore, at finite temperature, there always exists a 'critical region' in the vicinity of the critical point, where the correlation length is cut-off by thermodynamic fluctuations (Fig.3.22). In this 'critical region', the system is again d-dimensional, and the physics is governed by temperature. Even though our system is not governed by quantum fluctuations anymore, we can see by using (3.13) that the temperature-dependent phase correlation length in the critical region $L_\Phi \propto 1/T^{1/z}$ is still governed by the same critical exponent, allowing the characterization of the quantum phase transition at finite temperatures, in a procedure called 'finite-size scaling'.

This can be done because in the vicinity of a quantum phase transition, the physical quantities are all governed by this correlation length. This is the case of the resistance, for example :

$$R(\delta, T) = R_C f(\delta T^{-1/z\nu}) \tag{3.14}$$

The way in which the critical exponents are obtained is by recording the resitance vs parameter K, for example magnetic field, for different temperatures. If the system behaves according to (3.14), then the curves should all collapse onto a single curve when R/R_C is plotted against $|K - K_C|T^{-1/z\nu}$. The parameter $z\nu$ yielding the best collapse is considered the critical exponent of the transition.

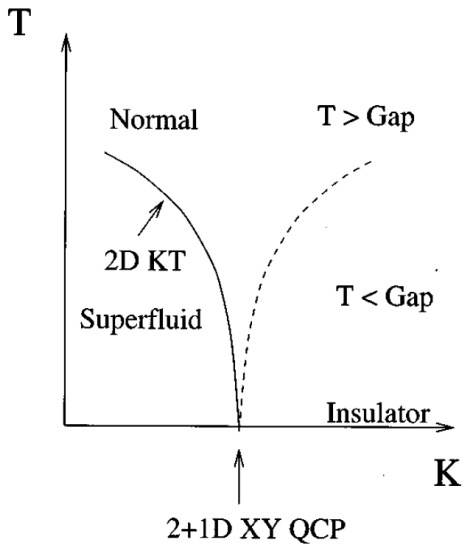

Figure 3.22 – *Phase diagram of a 2D Josephson junction array. The line at zero temperature contains the quantum phase transition, at the quantum critical point. At finite temperatures, the critical region in-between the continuous and dashed line is the critical region, where the thermodynamics dominates. Taken from [3].*

3.3.5.2 Finite-size scaling analysis of the electrostatically-driven transition

Looking more closely at Fig.3.14, we note that not all of the curves cross at the same point. This is pretty obvious if we look at Fig.3.9. There is a second re-entrance temperature below which the system shows more insulating behavior, and the critical values change. At intermediate temperature (0.6 K $< T <$ 1.2 K), however, there is a region where the $R(V_g)$ exhibits a remarkably stable crossing point. This is shown in Fig.3.23. In this range of temperature, not only is the crossing point stable, but the value of the critical resistance is conspicuously close to the value $R_C = h/4e^2$.

We then performed the finite-size scaling analysis, following two methods described in [173, 201]. In the first method, we plot $(R - R_C)$ as a function of $|V_g - V_{gc}|T^{-1/z\nu}$ (Fig.3.24a). The exponent $z\nu$ that gave the best collapse was 1.05 ± 0.1. The second method is shown in Fig.3.24b. It consists in fitting the dependence of the slope $\left(\frac{\partial R}{\partial V_g}\right)_{V_{gc}}$ at the transition as a logarithmic function of temperature. The slope yields the critical exponent $z\nu$. This technique, because it only considers the close vicinity to the critical point, is probably accurate down to lower temperatures, as it is assured to lie within the critical region. The extracted exponent value is 1.18 ± 0.02

3.3.5.3 Discussion

The critical exponents we find definitely lie in the same range as previously reported values. For a review of the exponents reported in the literature, see page 39 of [202] (available online at http://www.csnsm.in2p3.fr/Theses). A thorough study would require an independent determination of the dynamical exponent z, however. This

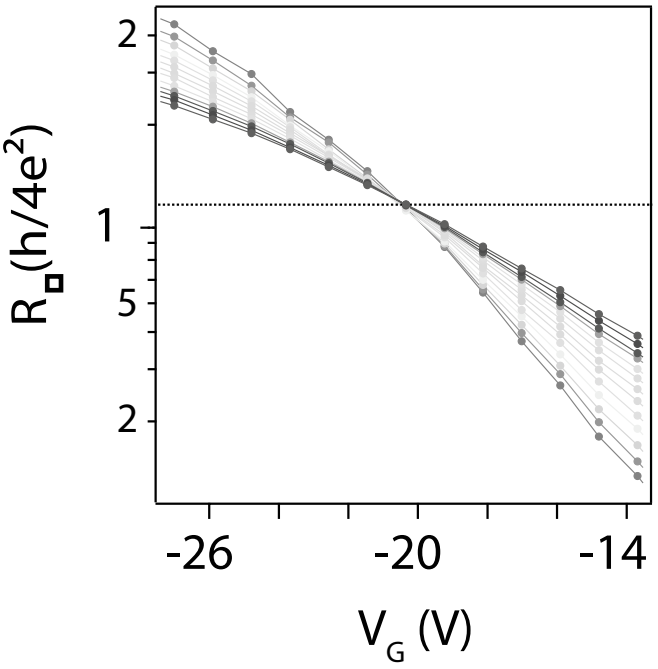

Figure 3.23 – *A subset of the $R(V_g)$ curves from Fig.3.14 showing a stable crossing point. Temperatures range from 0.6 K (red) to 1.2 K (blue) by steps of 0.05 K.*

was done in [173] by comparing the BKT transition temperature to the critical field. Unfortunately, our incomplete measurement did not allow us to do this analysis. The dirty boson model [179] predicts that $z = 1$ and $\nu \geq 1$, where the exact value of ν should depend on the transition mechanism. For example, percolation in 2D should give $\nu = 4/3$. Assuming that we indeed have $z = 1$, then the correlation length exponent we find is none of the well established percolation exponents for classical 2D (4/3), 3D (2/3), or quantum 2D (7/3), but a similar exponent has been reported in thickness-tuned transition in amorphous Bi films [203]. Recent simulations have also predicted similar exponents [11].

3.3.5.4 Breakdown of the finite-size scaling at low temperatures

At lower temperatures, the scaling analysis breaks down because the crossing point shifts. Interestingly, it doesn't start to drift continuously, but instead it settles to another value (Fig.3.25) ($V_g = -17.5V, R_C = 0.42\ h/4e^2$). This is quite remarkable and probably means that a temperature-independent source of dissipation is present. If the only sources of dissipation were graphene and quasi-particles in Sn islands, one would see their effect evolve continuously with the sheet resistivity and with temperature, respectively. This is what we see above 1.2 K (see previous sections). Here, on the contrary, there is a sudden change around 600 mK. After the change, the insulating side is favoured over the superconducting side, which means the dissipation has been cut off. A possible candidate would be the presence of a charged impurity in

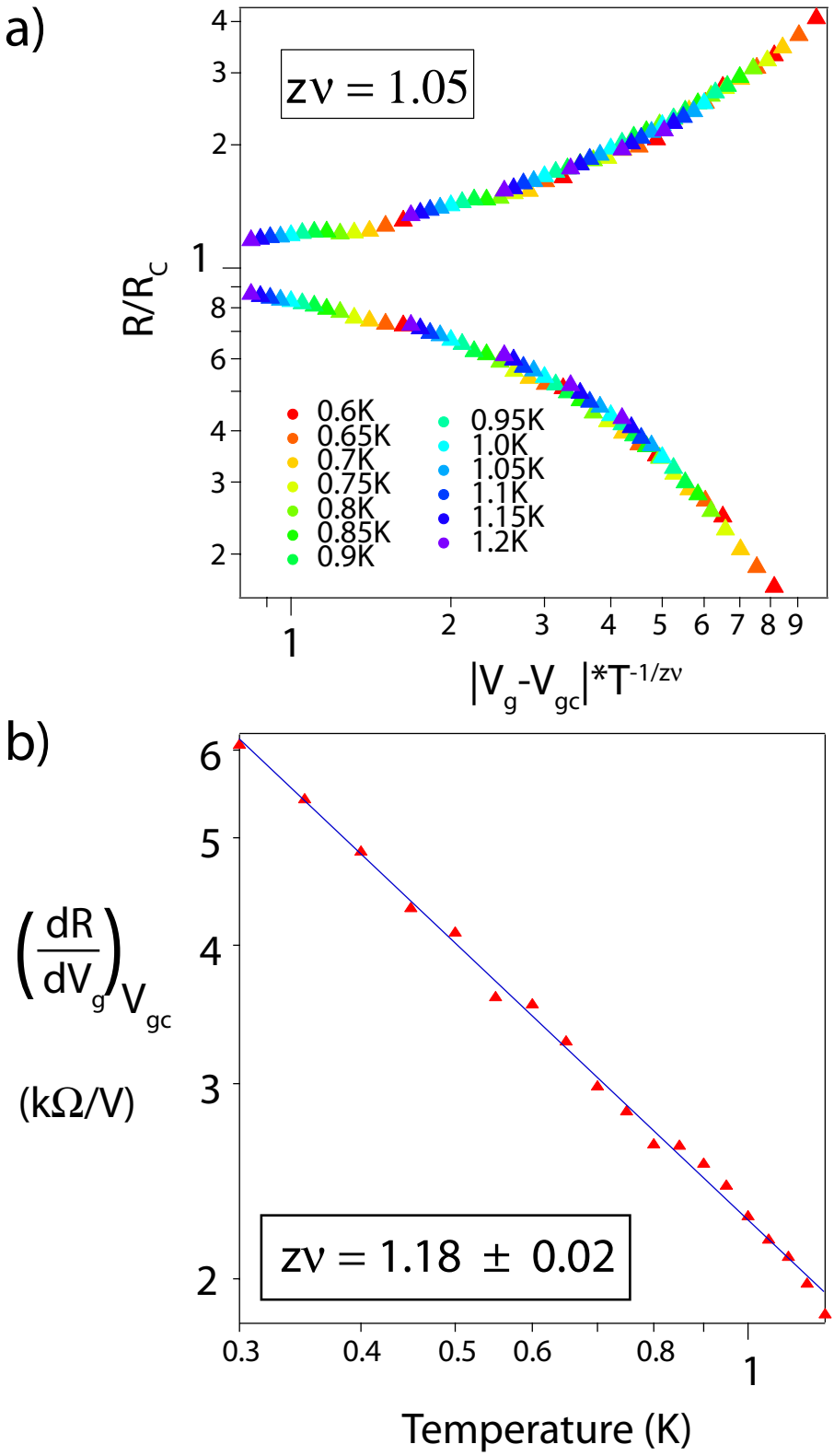

Figure 3.24 – ***Finite-size scaling of the superconductor-insulator transition using the two methods described in [201]. a)*** *Taking all points shown in Fig.3.23, the best collapse of the curves was obtained using the exponent* $z\nu = 1.05$. ***b)*** *Fitting the slope of the* $R(V_g)$ *at the critical point to* $\log(T)$ *yields* $z\nu = 1.18$.

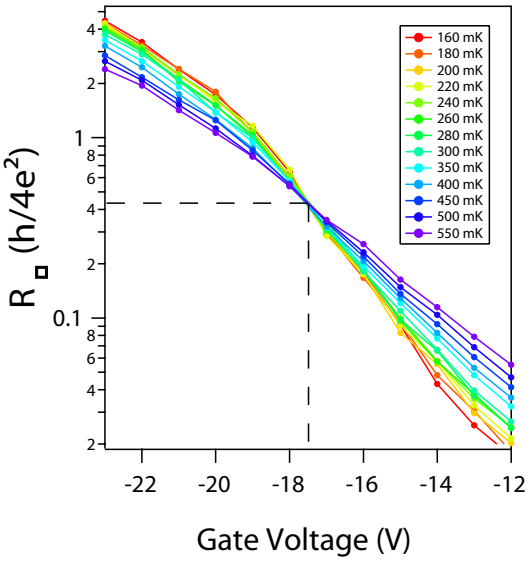

Figure 3.25 – *R(Vg) curves showing a new 'non-universal' crossing point at lower temperatures.*

the gate dielectric that would be freezed below a certain temperature. Unfortunately it was not possible to continue the scaling analysis below 600 mK. Two reasons can be invoked. First, the range of gate voltage showing a universal behavior, that is the quantum critical region, shrinks at low temperatures. Second, the resistance for all gate voltages starts to level off at very low temperatures.

3.3.5.5 Saturation of the curves at very low temperature

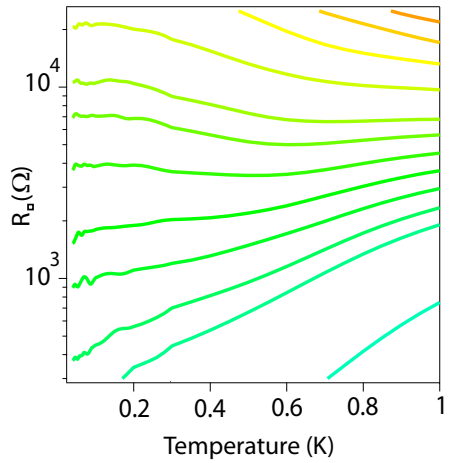

Figure 3.26 – *Resistance as a function of temperature for different gate voltages. Zoom on the critical region at low temperatures showing the level-off.*

The low temperature levelling-off has been observed in many SITs and has raised fundamental questions because such an anomalous metallic phase is not predicted at zero temperature. In our case, this saturation is clearly not related to electron thermalization, because it happens at too high a temperature ($\cong$ 200 mK), and because it only concerns some gate voltages close to the critical point. This problem has been adressed by Mason and Kapitulnik [204], and Kapitulnik *et al.* [189] in the framework of coupling to a bath of dissipative degrees of freedom and its effect on the quantum phase transitions. The metallic back-gate plane indeed provides such a source of gapless excitations [169] and could explain why we observe this behavior.

Conclusion du Chapitre 3

La possibilité d'induire du désordre à différents degrés dans le graphène en utilisant la méthode d'attaque chimique décrite au Chapitre 1 nous a permis de fabriquer des échantillons de Sn/graphène dans lesquels le couplage entre îlots supraconducteurs était plus faible. Nous nous sommes penchés sur deux cas limites de désordre, caractérisés par leur résistance à température ambiante. Les principaux résultats de ce chapitre sont les suivants :

- Dans la limite de faible désordre ($k_F l_e > 1$, localisation faible même à basses températures) la transition induite par la grille en présence de champ magnétique peut se comprendre qualitativement comme étant due à une compétition entre les différentes contributions aux fluctuations supraconductrices.

- Dans la limite de fort désordre, nous avons montré qu'il était possible de transiter d'un état supraconduteur vers un état isolant simplement en faisant varier la densité de porteurs. Cette TSI, qui s'opère à désordre structural constant dans la maille de graphène est très similaire aux TSI induites par la variation d'épaisseur dans les matériaux granulaires.

- Dans l'état isolant, nous avons vu une signature claire de la localisation des paires de Cooper, à la fois dans la magnétorésistance et dans la loi d'activation.

- Le régime de hautes températures est caractéristique d'une transition induite par la dissipation. Le paramètre contrôlant l'état fondamental du système est alors sa résistance dans l'état normal, qui dépend à la fois de la grille et de la température.

- Dans le régime de basses températures, la transition s'opère à voltage/densité de porteurs/$k_F l_e$ constant. La présence d'un courant critique infinitésimal du côté supraconducteur de la transition indique que celle-ci est liée à un phénomène de percolation. Le comportement particulier de la résistance différentielle au-dessus du courant critique nous donne par ailleurs des informations utiles sur la statistique du désordre dans le système.

- Il est intéressant de noter que la résistance à la transition vaut presque exactement le quantum de résistance pour une paire de Cooper $h/4e^2$.

- Les exposant critiques dérivés de l'analyse de la loi d'échelle de la transition ne sont ni ceux d'une percolation classique, ni ceux d'une percolation quantique (entendu qu'ils ne valent pas 7/3 comme attendu par [190]). En revanche, ils se pourrait qu'ils s'accordent avec des calculs récents de groupe de renormalisation, qui ont trouvé des exposants proches pour la percolation quantique de

domaines cohérents en phase sur un réseau aléatoire de grains supraconducteurs à deux dimensions [11].

Ces expériences montrent que le matériau hybride Sn/graphène nous permet d'amener un regard nouveau sur les problématiques de TSI et de localisation de paires de Cooper. Améliorer notre connaissance et notre contrôle du désordre dans ce système nous permettrait probablement d'aller encore plus loin. Ce système pourrait servir à mieux comprendre cette transition, non seulement dans les systèmes granulaires, mais également dans les systèmes amorphes. En effet, la structure de notre système nous permet de contrôler la transition métal-isolant (TMI) du graphène tout en gardant les propriétés supraconductrices constantes, ce qui était jusque-là impossible dans les films minces désordonnés. Il se pourrait bien que l'émergence d'une structure électronique fractale à la TMI induise une TSI de type percolation quantique [11]. Le point le plus urgent auquel il faudrait maintenant s'attaquer est le problème de l'homogénéité du désordre induit dans le graphène. Comme nous l'avons vu au Chapitre 1, les feuilles macroscopiques sont parfois caractérisées par des inhomogénéités à grande échelle. Il faudrait comprendre si la percolation que nous avons observée prend sa source dans des inhomogénéités préexistentes ou émergentes.

Conclusion of Chapter 3

The possibility to obtain different levels of structural disorder within graphene by chemical treatment allowed us to generate Sn/graphene samples where the superconducting coupling between Sn grains was rather weak. In this family of samples, two limits have been investigated, characterized by the square resistance of the graphene sheet being close to or far from the quantum of resistance. The main results of this chapter are :

- In the limit of graphene with weak disorder (weak localization in the graphene sheet), the transition driven by a magnetic field can be qualitatively understood as a competition between the positive and negative contributions to the paraconductivity.
- In the limit of strong disorder, we showed that it is possible to cross the superconductor to insulator transition simply by tuning the carrier density with the gate voltage. This superconductor-insulator transition, which occurs at constant structural disorder of the graphene medium, can be characterized as a quantum phase transition and it bears a strong resemblance with the transitions that occurs in superconducting thin films of granular morphology.
- In the insulating state, we have seen a clear signature of Cooper pair localization, both in the magnetoresistance data and in the activation behavior of the resistance.
- The high-temperature regime seems to be dominated by dissipation effects. The normal state resistance of the graphene sheet, which has a direct influence on the dissipative degrees of freedom, then controls the ground state (superconducting or insulating) of the system.
- In the low temperature regime, the transition happens at constant gate voltage and increasing normal state resistance. The strong suppression of the critical current density in the vicinity of the transition, as compared to what was measured in clean systems in Chapter 2, together with the peculiar logarithmic increase of the voltage with bias current, point towards a percolation transition.
- In an interesting coincidence, at the transition critical point, the system assumes a sheet resistivity equal (within error bars) to the quantum of resistance for Cooper pairs $h/4e^2$.
- The critical exponent derived from the finite-size scaling analysis at the transition are not those of a classical nor quantum percolation (understand that they are not 7/3, as is expected according to [190]). Instead, they seem to agree with

recent renormalization group calculations on the quantum percolation of phase coherence on random 2D lattices [11].

These experiments demonstrate that Sn/graphene hybrids provide an original system to study the localization of Cooper pairs and percolation of superconducting phase coherence across a disordered 2D network of superconducting grains. By improving our knowledge and control of the atomic disorder in the graphene sheet, this system could become a model system and the perfect testbed for the theories of the superconductor-insulator transition in disordered systems. As a matter of fact, by separating the effect of electron localization and superconductivity, this system allows a systematic study of the former while keeping the latter constant. It seems that the emergence of fractality at the metal-insulator transtion leads to a quantum percolative SIT [11]. Further work is needed to characterize in more detail the parameters governing the transition. The most critical point that should be adressed concerns the homogeneity of the structural disorder induced in the graphene sheet. As we saw in Chapter 1, macroscopic samples are sometimes characterized by inhomogeneous disorder at large scales. Understanding if this is the reason for the percolative behavior, if it stems from the randomness in the island's morpholgy, or if it would happen in an homogeneously disordered sample is an important issue.

Graphene nano-electro mechanical systems and suspended Josephson junction

4

Introduction en français

Les systèmes microélectromécaniques (MEMS) sont étudiés depuis au moins 40 ans [205]. Les dispositifs à base de MEMS sont aujourd'hui très répandus dans les objets de tous les jours, sous la forme d'accéléromètres, de capteurs de forces, fitres passe-bande de haute fréquence dans les circuits électroniques ou encore thermomètres. L'une des figures de mérite de ces résonateurs mécaniques est leur fréquence de résonance, qui augmente à mesure que l'on diminue leur taille (voir Fig.4.2a). Réduire le volume d'un résonateur le rend également plus sensible puisque sa masse diminue. C'est pourquoi un effort constant a été fait pour miniaturiser toujours plus ces résonateurs. Depuis $10-15$ ans, le domaine des résonateurs nanoscopiques, les NEMS, est devenu un axe de recherches majeur [206, 207]. En poussant la miniaturisation en-dessous du nanomètre, les chercheurs se sont retrouvés confrontés aux limites intrinsèques de ces objets. Les propriétés sont alors différentes puisqu'on arrive à la frontière entre le monde classique et le monde quantique.

Les nouveaux défis qui se présentent à l'échelle des NEMS et qui sont spécifiques à ceux-ci sont de plusieurs natures. Tout d'abord, le rapport surface/volume allant croissant, la dissipation par les effets de surface (systèmes à deux niveaux, frictions) deviennent de plus en plus importants. Ceci entraîne une diminution du facteur de qualité Q dans les résonateurs nanométriques (voir Fig.4.2b). Une partie des travaux menés sur les NEMS ont donc pour objet une meilleure compréhension des mécanismes dissipatifs et des limitations intrinsèques de ce facteur de qualité [208]. Un autre problème fondamental qui se pose lorsqu'on diminue la taille des résonateurs mécaniques est que, du fait de leur petite taille, il devient de plus en plus difficile d'interagir avec eux. Le problème se manifeste dans les résonnateurs électriques par le fait que la capacité du résonnateur devient très

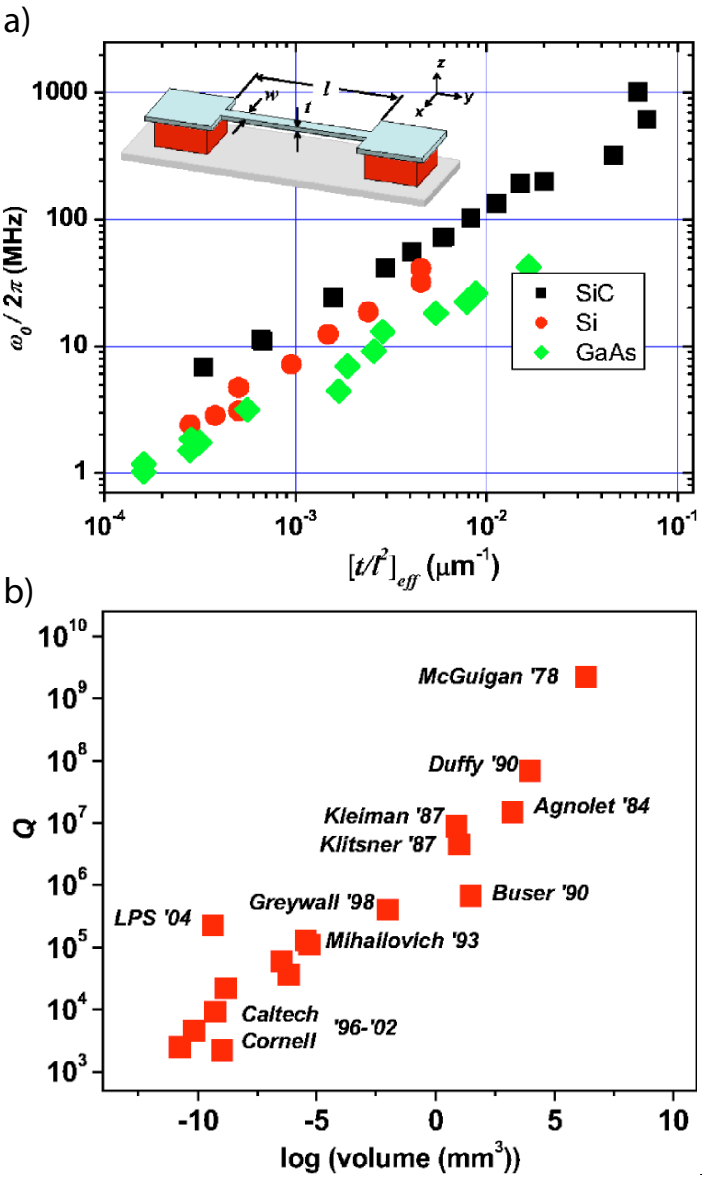

Figure 4.1 – ***Tendances dans la miniaturisation des MEMS. Tiré de [207]. a)*** *A rapport d'aspect constant, la fréquence augmente lorqu'on diminue la taille.* ***b)*** *Le facteur de qualité Q diminue avec la réduction du volume.*

petite devant les capacités parasites, ou, dans le cas d'une détection optique, par l'impossibilité de résoudre un résonateur plus petit que la longueur d'onde de la lumière.

Du fait de leur très grande sensibilité, les NEMS sont sujet à ce qu'on appelle le phénomène de rétro-action, dans lequel le processus de lecture lui-même a pour effet d'exciter le résonateur [209]. Dans la limite quantique, le principe d'incertitude d'Heisenberg constitue une source de rétro-action fondamentale. En effet, celui-ci nous dit qu'il est impossible de mesurer la position du résonnateur sans perturber son moment cinétique [210, 211].

Finalement, un aspect important de la recherche contemporaine sur les NEMS est le fait que, grâce à leur fréquence de résonance élevée, ceux-ci offrent la possibilité d'accéder au régime quantique, dans lequel le taux d'occupation du mode fondamental est inférieur à un. Cette condition est réalisée lorsque $\hbar\omega_0 < k_B T$, où ω_0 est la pulsation du mode fondamental. Un ordre de grandeur qu'il est bon d'avoir en tête est le suivant : si la fréquence de résonance du mode fondamental est de 1 GHz, le résonateur sera dans la limite quantique en-dessous de 50 mK. Dans ce régime, la nature quantique du résonateur devrait devenir manifeste. Un travail colossal a été entrepris dans cette direction depuis une dizaine d'années [212]. Ces expériences suscitent un vif intérêt car, aujourd'hui encore, les modalités de la transition entre le régime quantique et le régime classique sont mal connues. Par ailleurs, ces résonateurs quantiques pourraient servir comme composants dans un hypothétique futur ordinateur quantique. La démonstration récente d'un résonateur dans son état fondamental a donc naturellement provoqué l'émoi de la communauté [213]. Le domaine des NEMS quantiques en est encore à ses balbutiements, et beaucoup d'expériences restent à faire, ne serait-ce que pour valider une bonne fois pour toute la mécanique quantique. Pour certaines expériences sur les NEMS quantiques, les matériaux carbone apparaissent comme d'excellents candidats car l'amplitude de leur mouvement de point zéro est supposément beaucoup plus grande que celle des autres matériaux [212].

Historiquement, les NEMS ont été fabriqués à partir de matériaux massifs (Si, SiC, SiN, GaAs,...) dans lesquels on enlève de la matière pour fabriquer des structures suspendues. Ce procédé, appelé 'bulk micromachining', est une approche de type 'top-down' (de-haut-en-bas), qui a des avantages en termes de production, reproductibilité, et surtout permet de produire des résonateurs d'une grande homogénéité structurale, puisqu'ils sont sculpté dans la masse. Les NEMS carbones à base d'allotropes hybridés sp^2 (nanotubes (NT) et graphène) suspendus ne peuvent pas être fabriqués par une approche top-down. Cependant, leur avantage tient à leurs propriétés mécaniques intrinsèquement supérieures. On évalue la robustesse d'un matériau à sa capacité à supporter son propre poids. Avec une densité très basse ($\rho = 2.7$ g.cm^{-3}) et un module d'Young extrèmement élevé ($E \cong 1$ TPa), les allotropes du carbone sont les matériaux ultimes du point de vue des propriétés mécaniques.

Ces excellentes propriétés mécaniques se traduisent par une fréquence de résonance très élevée :

$$f = 1.05\frac{t}{L^2}\sqrt{\frac{E}{\rho}} \tag{4.1}$$

Les NT et le graphène sont donc très prometteurs pour la réalisation de NEMS à haute fréquence de résonance. Mais ils ont d'autres avantages. Tout d'abord, l'effet du champ électrique sur leur conductivité fait qu'ils peuvent être utilisés pour détecter leur propre mouvement. En surveillant leur conductance, on peut détecter des changement liés à leur déplacement par rapport à une grille maintenue à potentiel fini constant [214, 215, 216]. Celà permet d'utiliser un schéma d'excitation et de détection intégralement électriques ne nécessitant qu'une seule ligne RF. Ces résonateurs ont également la particularité de pouvoir être opérés dans un régime de forte tension. En appliquant entre eux et la grille une tension électrique continue, on induit une force électrostatique qui suffit à induire une grande tension. La fréquence de résonance, qui varie avec la racine carré de cette tension, peut ainsi être réglée électriquement sur de larges gammes de fréquences. Il a d'ailleurs été démontré qu'un nanotube peut à lui seul constituer comme un récepteur radio accordable [217].

Tandis que les NT ont typiquement des fréquences de résonance et des facteurs de qualité plus élevés, le graphène a d'autres atouts à faire valoir. Tout d'abord, son grand rapport surface/volume peut s'avérer utile pour la détection de gaz [215]. Ensuite, la possibilité de faire croître le graphène par CVD ouvre la porte à de la fabrication de type top-down [218]. Enfin, comme nous l'avons vu dans les chapitres prcdents, le graphène peut facilement s'hybrider.

Mesurer un résonateur dans la limite quantique n'est pas une mince affaire. Non seulement il faut réussir à refroidir le résonateur jusqu'à cette limite, mais encore faut-il pouvoir le mesurer sans le perturber outre mesure. Pour celà, de nouvelles techniques de détection ont été développées. Outre les techniques impliquant le couplage à un système à deux niveaux (QuBits) [213], certaines expériences impliquent un couplage entre le résonateur et une cavité résonante, soit optique [219, 220] soit micro-onde [221, 222]. Cette cavité permet alors également de refroidir le résonateur par un phénomène d'absorption stimulée de phonons par la cavité. Les hybrides supraconducteurs Sn/graphène pourraient trouver une application de niche ici, où se combineraient les propriétés mécaniques hors du commun du graphène et la possibilité de coupler ses modes de résonance à ceux de la cavité supraconductrice, voir de la cavité optique qu'il forme avec le substrat [223]. Plus simplement, et sans aller aussi loin que la limite quantique, de tels résonateurs pourraient permettre de réduire la dissipation liée aux électrons et mettre à jour d'autres sources de dissipation à basses températures.

Dans ce chapitre, des résultats préliminaires sur les NEMS graphène, obtenus durant ma première année de thèse, seront présentés. Tout d'abord, les résultats de la littérature [215, 216] ont été reproduits, c'est-à-dire que nous avons mesuré la fréquence de résonance du mode fondamental de flexion de membranes de graphène attachées aux deux extrèmités, en utilisant la technique de mixage hétérodyne du courant [214]. Des échantillons de Sn/graphène suspendus ont ensuite été fabriqués, démontrant la faisabilité et la robustesse de telles structures. Bien qu'aucun signal de résonance mécanique n'ait encore pu être mesuré, nous avons vu que ces membranes étaient bien supraconductrices.

Introduction in english

Microelectromechanical sytems (MEMS) have been studied for at least 40 years [205]. Today, devices based on MEMS such as accelerometers, high frequency band-pass filters in electronic circuits, high-sensitivity force sensors or thermometers are commonly used in the industry. One of the figures of merit for these resonators is their resonant frequency that scales inversely with size (see Fig.4.2a). Reducing the volume of the resonators also makes them more sensitive to mass. Hence the drive towards device miniaturization. Over the past $10-15$ years, the physics of sub-micrometer resonators, *aka* nanoelectromechanical systems (NEMS) [206, 207], has become a subject of intense research. Pushing miniaturization below the micrometer scale, one is faced with fundamental limits, and the ultimate properties of these devices depend on the crossover between the classical and the quantum regime.

The peculiarities and specific challenges pertaining to the sub-micrometer world (as opposed to MEMS) are several-fold. First, the ever-increasing surface-to-volume ratio gives an increasing importance to dissipation by surface defects. This translates into a steady decrease of the quality factor Q (see Fig.4.2b). Part of the NEMS community is therefore concerned with understanding the dissipation mechanisms and fundamental limitations of the quality factor [208]. Another important issue when shrinking the size of these devices comes from the reduced coupling to their environment, which makes them difficult to address : electrical actuation schemes become increasingly dominated by parasitic capacitances, while optical schemes are intrinsically limited by the light's wavelength. Because their sensitivity becomes so high, NEMS start to be influenced by the forces involved in the read-out process itself [209]. This back-action has a fundamental lower limit set by the Heisenberg uncertainty principle [210, 211], which states that the position of the resonator cannot be measured without disturbing its motion.

Finally, with their increased resonant frequency, NEMS open the possibility to reach the quantum regime, where the phonon occupation number in the fundamental mode is less than one (for $\hbar\omega_0 < k_B T$, where ω_0 is the frequency of the fundamental mode). In this regime, the quantum-mechanical nature of the oscillator manifests. There is a keen interest in these experiments, as the transition from the quantum to the classical world is not yet well understood. The recent demonstration of a macroscopic resonator in its quantum ground state of motion has caused a big stir [213], for it has been a long-standing quest [212]. The field of quantum NEMS is still in its infancy, with a lot more experiments to do to test the limits of quantum mechanics. With this in mind, people are now trying to use carbon allotropes to realize quantum NEMS.

Historically, NEMS have been fabricated from bulk material (Si, SiC, SiN, GaAs,...) by a process called bulk micromachining. This top-down approach offers good reproducibility, as well as structural homogeneity. Carbon NEMS, which are mechan-

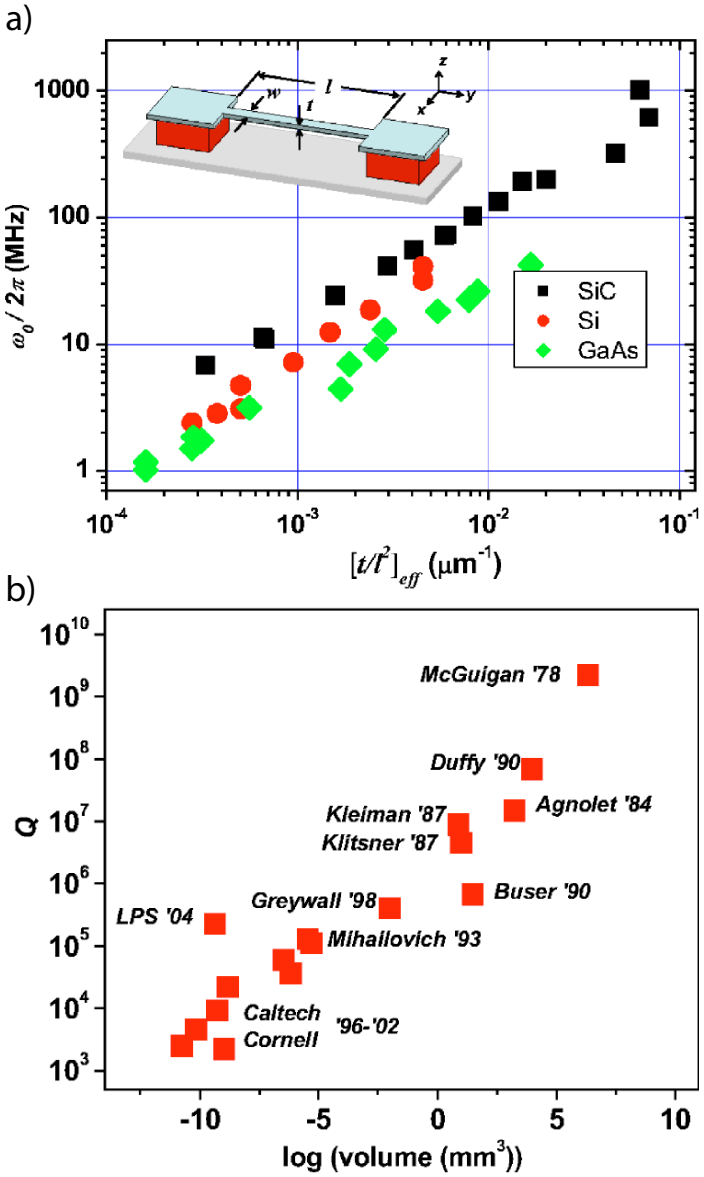

Figure 4.2 – ***Trends in MEMS miniaturization. Taken from [207]. a)*** *Increasing frequency with decreasing size.* ***b)*** *Decreasing Q factor with decreasing volume.*

ical resonator fabricated out of sp^2 carbon allotropes carbon nanotubes (CNT) and graphene, cannot be fabricated by micromachining, but their advantage lies in their intrisincally superior properties. The strength of a mechanical structure is measured by its ability to support its own weight. For that, it needs to be rigid and light. With their low mass density $\rho = 2.7$ g.cm^{-3} and extremely high Young's modulus $E = 1$ TPa, sp^2 carbon allotropes are the ultimate structural materials. And as far as NEMS are concerned, the stronger structures have a higher resonant frequency :

$$f = 1.05\frac{t}{L^2}\sqrt{\frac{E}{\rho}} \tag{4.2}$$

CNTs and graphene are therefore ideal materials for NEMS. But they have other advantages. First of all, because their electrical conductivity is gate-tunable, they can detect their own motion with respect to a metallic back-gate plane [214, 215, 216], allowing a fully electrical actuation and measurement using only one RF line for the excitation. Second, these resonators can be operated in the strained regime. Applying a DC voltage on the gate electrode is enough to strain them significantly. The resonant frequency of strained resonators scales as the square root of the strain, thus making these NEMS's resonance frequency gate-tunable. Use of nanotubes as tunable radio receivers has been demonstrated [217].

While CNTs exhibit the larger resonant frequencies and Q factors, graphene has other qualities. First, graphene resonators present the ultimate surface-to-volume ratio, which would be an interesting property for example for gas sensing [215]. Second, it offers the possibility to prepare batches of resonators using CVD graphene and a top-down fabrication approach [218]. And third, graphene can be easily hybridized.

Measuring a resonator in its quantum ground state of motion is a very difficult experiment. In order to cool down the fundamental mode and measure the motion while keeping perturbation at a minimum (quantum-limited) level, novel detection schemes have been devised, which involve coupling the resonator to an optical [219, 220] or microwave [221, 222] cavity. The resonant frequency of the cavity is modulated by the motion of the mechanical resonator, and the coupling to the cavity allows sideband cooling. Superconducting Sn/graphene hybrid could find a niche application here, as graphene's exceptional mechanical properties could be coupled to superconductivity to create novel quantum NEMS. More simply, these superconducting NEMS could be used to implement a dissipationless magnetomotive actuation/detection scheme, which would allow to get rid of an important source of dissipation at low temperatures.

In this chapter, preliminary results on graphene NEMS obtained during the first year of my PhD will be shown. First, the results of [215, 216] were reproduced by measuring the resonant frequency of graphene resonators actuated and detected us-

ing the heterodyne mixing current technique [214]. Suspended hybrid Sn/graphene devices were then fabricated, the mechanical resonance signal of which could not be measured using the same technique. Nevertheless, a preliminary study of their superconducting properties at low temperatures has been carried out.

Table of contents of Chapter 4

4.1 Suspension of graphene membranes

We have fabricated suspended graphene membranes with electrical contacts using exfoliated graphene, by following the method pioneered by Bolotin *et al.* [9]. The exfoliation procedure is explained in Chapter 1 (see §1.3.1.2). E-beam lithography using the method described in §1.3.4.1 was used to define the contacts and a bilayer of 5 nm Cr + 100 nm Au was evaporated as electrodes. The use of thick electrodes ensured the mechanical rigidity of the structure. Suspension was then achieved by removal of the substrate. For that, the sample was dipped in a buffered HF solution.

4.1.1 Substrate underetching by HF

HF is known to etch almost all inorganic oxides, including SiO_2, as well as most metals, with the exception of Au, Ag, Cr, Pd, and Pt. This is a major problem for making suspended graphene membranes with superconducting contacts. Buffered HF (BHF) is a mixture of HF and NH_4F. NH_4F is a buffer agent, which helps maintain the solution's pH constant. BHF has a lower, but more controllable etch rate than pure HF. Fig.4.3 shows the underetching process. During the HF dip, the gold electrodes act as a protective cap and prevent the SiO_2 underneath them to be etched. It is important to etch sufficiently to ensure that the structure is fully released from the substrate. At the same time, etching SiO_2 completely would be detrimental, as it would introduce risks of electrical shunt between graphene and the back-gate. Since the etching is isotropic, it creates an overhang below the electrodes, weakening the structure.

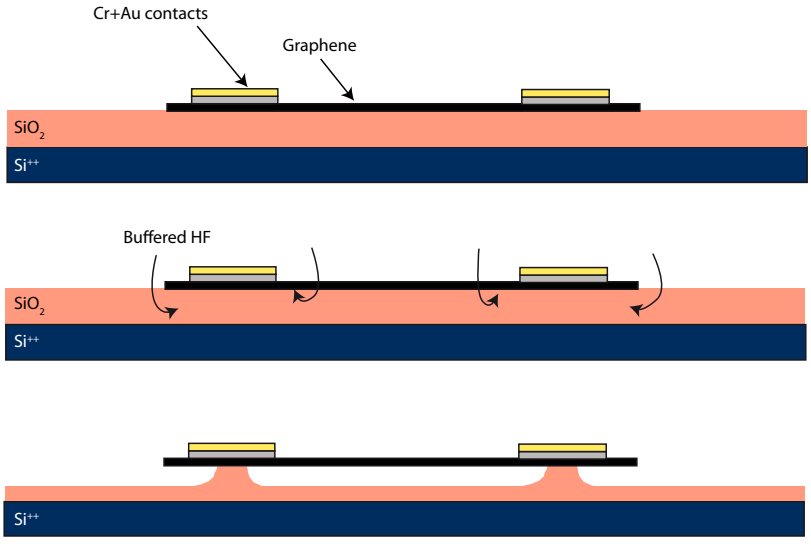

Figure 4.3 – *HF etching of the substrate on the pre-patterned device. The isotropic etching releases the membrane and results in electrodes underetching.*

As was first noticed by [215] and [216] the etching rate is enhanced in the vicinity of graphene. This was revealed by sonicating a suspended device to remove the graphene membrane and look below (Fig. 4.4). The etching is not homogeneous : the region covered by graphene has been etched much faster, and has no pillar left to maintain it. This feature has advantages and drawbacks. On the one hand, one can suspend very large graphene surfaces, larger than the dielectric thickness without risking a shunt to the back-gate. On the other hand, the resulting structures are very weak. Graphene is actually only held by the electrode it is stuck to. This is why we used thicker electrodes. After underetching, the sample was transferred to several water baths for rinsing. Finally, it was put into isopropanol and transferred to a commercial supercritical dryer Tousimis Autosamdri-815 Series B.

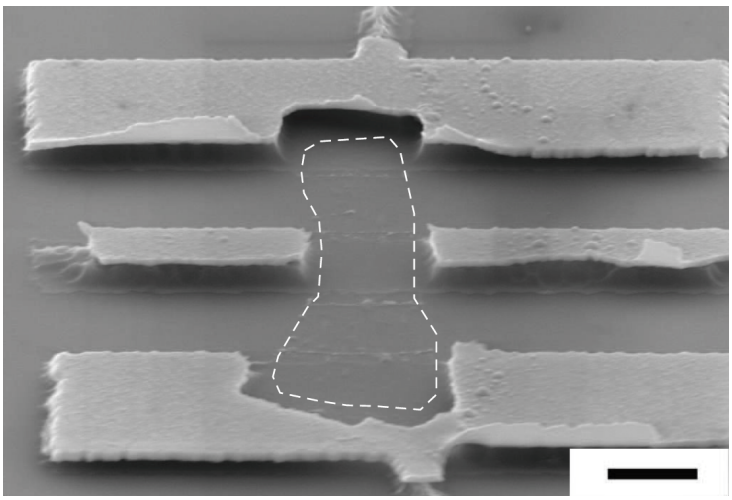

Figure 4.4 – *SEM picture of a the underlying structure after the suspended membrane has been removed by sonication. Image taken during my undergraduate internship in TIFR Mumbai. From [216].*

4.1.2 Supercritical drying

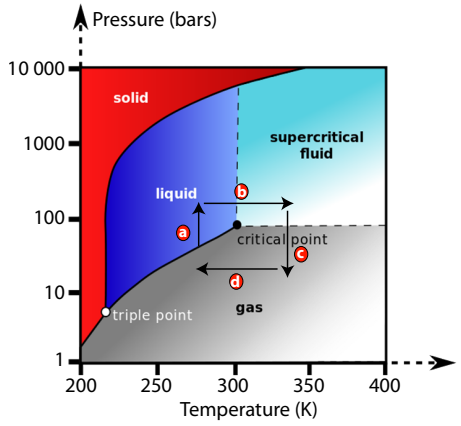

Figure 4.5 – *Principle of the supercritical drying. The phase diagram of CO_2 is shown. The drying sequence is indicated by arrows.*

Supercritical drying is routinely used in the MEMS and biology industry. Microscopic suspended structures are very prone to collapsing during the drying procedure, due to capillary force at the liquid/gas interface. The idea of supercritical drying is to heat up the liquid at high pressure beyond the critical point. Commercially available supercritical dryers use CO_2, which has a rather low critical point (in temperature and pressure). Isopropanol is first gradually replaced by (pressurized) liquid CO_2 in the chamber at 0°C (Fig.4.5 arrow a). Then it is heated beyond the critical point (Fig.4.5 arrow b). The pressure is

then released (Fig.4.5 arrow c) and the temperature decreased (Fig.4.5 arrow d). The phase transition proceeded smoothly without discontinuity. When the chamber is full of liquid CO_2, it is heated up and then the pressure is decreased.

4.1.3 Successfully suspended membranes

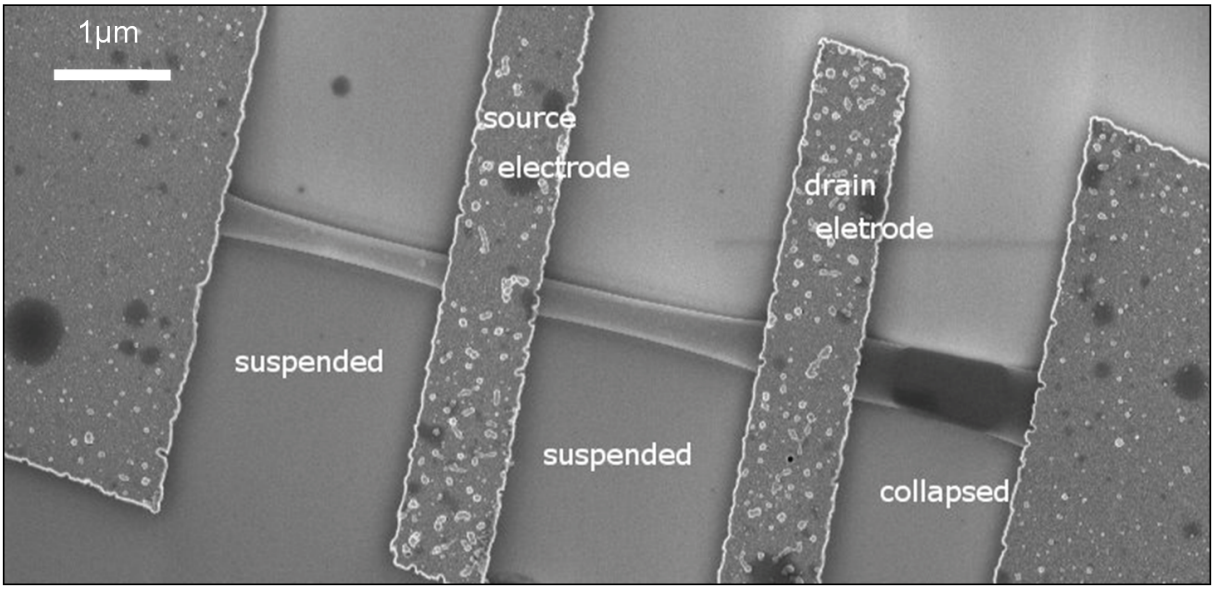

Figure 4.6 – *SEM picture of a suspended graphene membrane. The rightmost membrane is partially collapsed.*

We successfully suspended membranes of about $2-3\mu m$ in length and $1\mu m$ in width (see Fig. 4.6). Beyond these values, our membranes were systematically collapsed.

4.2 Ballistic transport in suspended graphene

Micron-sized flakes of graphene obtained by exfoliation are supposedly perfectly crystalline. Two sources of scattering can be identified as being prominent in such perfect graphene : charged impurities, and rippling. On SiO_2 substrates, these mechanisms find their origin in the substrate itself, which contains trapped charges, and it very rough (at an atomic scale). Suspension of graphene allows one to get rid of the detrimental influence of the substrate on the electronic mobility. The only impurities left are the resist residues situated on the flake itself, and these can be removed by in-situ cleaning using Joule annealing. The highest reported room-temperature mobilities ($120,000\ \mathrm{cm}^2.\mathrm{V}^{-1}.\mathrm{s}^{-1}$) in graphene (and in any 2DEG, see Fig.1.4) have been recorded in such Joule-annealed suspended graphene membranes [9, 224]. This section will present measurements of such suspended membrane showing ballistic transport at low temperatures and well-defined quantum Hall plateaus at low magnetic fields. But first, the method which is a mandatory prerequisite if one wants to obtain such high mobilities samples will be described : current annealing.

4.2.1 Cleaning of suspenses membranes using current annealing

Even though getting rid of the substrate is necessary, it is not sufficient to get ultrahigh mobilities in graphene as long as residues of PMMA and other contaminants are present on the surface, that are likely to scatter electrons. Current annealing was first introduced by Moser *et al.* [225] and has since then been widely adopted in the field. The big advantage of current annealing over furnace annealing is that the heating can be much more intense and localized in the graphene flake. It has been shown [77] that the electronic temperature can be as high as 2000K when graphene is biased with high current densities in the saturation regime. This treatment proves exfoliated graphene's high crystalline purity and structural robustness.

Voltage biasing was used for the annealing. An example of such an sequence of annealing steps with some field effect curves taken before and after is shown in Fig.4.7. Each step consists first of ramping up the voltage until the resistance changes, maintain this voltage until it stabilizes, then ramping it down to the opposite voltage, and go back to zero. Field effect curves are recorded between each annealing step, to check if the transport properties have improved. During the first annealing steps, we witness a huge decrease in the overall resistance, which we attribute to the improvement of the contact resistance. Further annealing removes the adsorbates by Joule evaporation and brings the Dirac point back near $V_g = 0V$. The voltage biasing is actually designed to be safer in these later stages of annealing. When the Dirac point suddenly shifts towards zero, the resistance increases, and the dissipated power $P = U^2/R$ suddenly drops in a self-limiting process. The opposite occurs if the sample experienced a current bias. Of course, in the early steps the diminishing

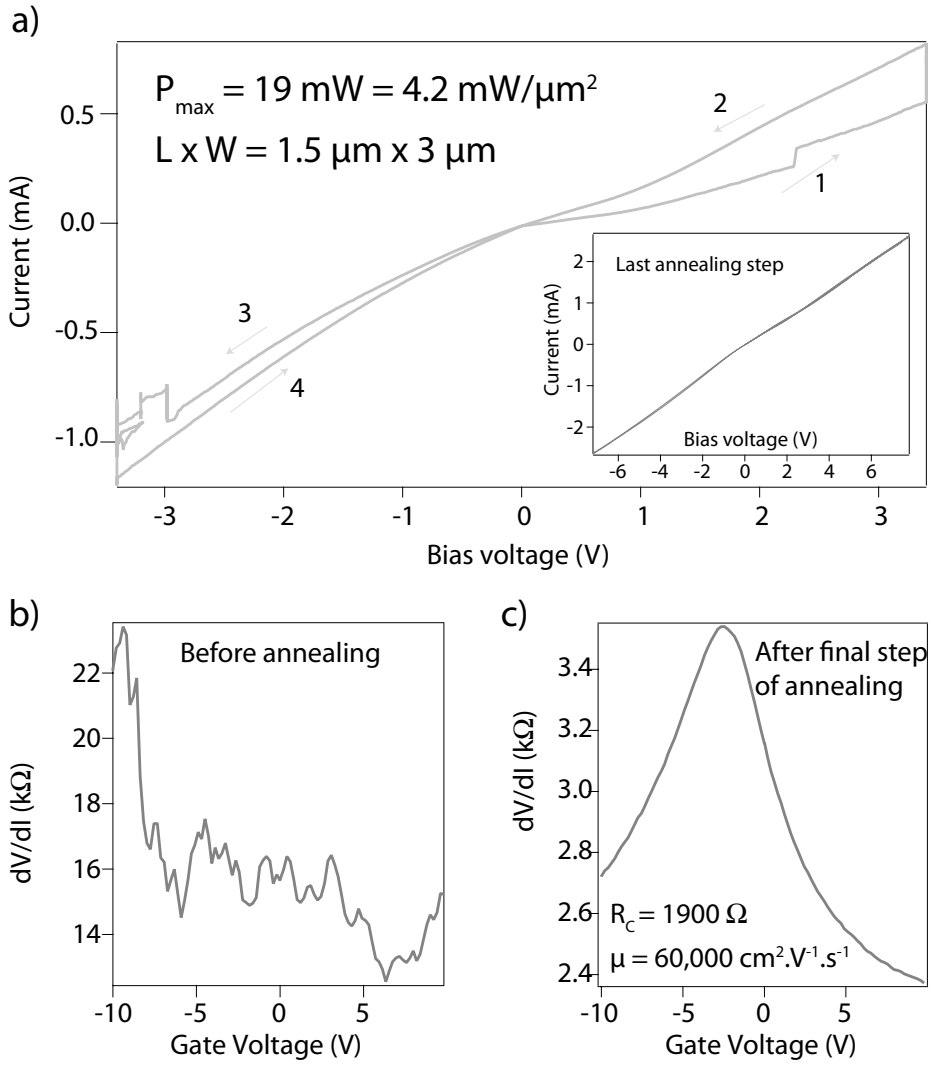

Figure 4.7 – ***Joule heating steps and their effect on mobility at*** 4 ***K. a)*** *Typical I(V) curve recorded during the annealing process. The vertical lines correspond to places where the voltage ramping was paused to let the system get clean.* ***Inset*** *: last annealing step. It is sometimes necessary to go as high as* 7 *to* 10 *V in order to thoroughly clean the sample. The maximum dissipated power was* 19 *mW.* ***b)*** *Field effect curve prior to annealing.* ***c)****Field effect cureve after the last annealing step.*

contact resistance makes it dangerous to voltage-bias the sample, but this happens at much lower dissipated power, and is considered safe. The anneling shown in Fig.4.7 involves 13 steps, only two of which are shown. At the final step, the dissipated power is about 4.2 mW/m^2 of graphene. Note that this sample was two-probe, so the mobility fit shown in Fig.4.7c uses the contact resistance as a fitting parameter, making this value unreliable. In the next section, transport properties of a 4-probes device that exhibits low-temperature mobilities in excess of $100,000\ cm^2.V^{-1}.s^{-1}$ after current annealing will be presented.

4.2.2 Characterization of ultrahigh mobility samples

Not all suspended samples can exhibit ultrahigh mobility. This can be due to the presence of crystalline defects or imperfect edges. Fig. 4.8 shows what can be obtained in a very good sample.

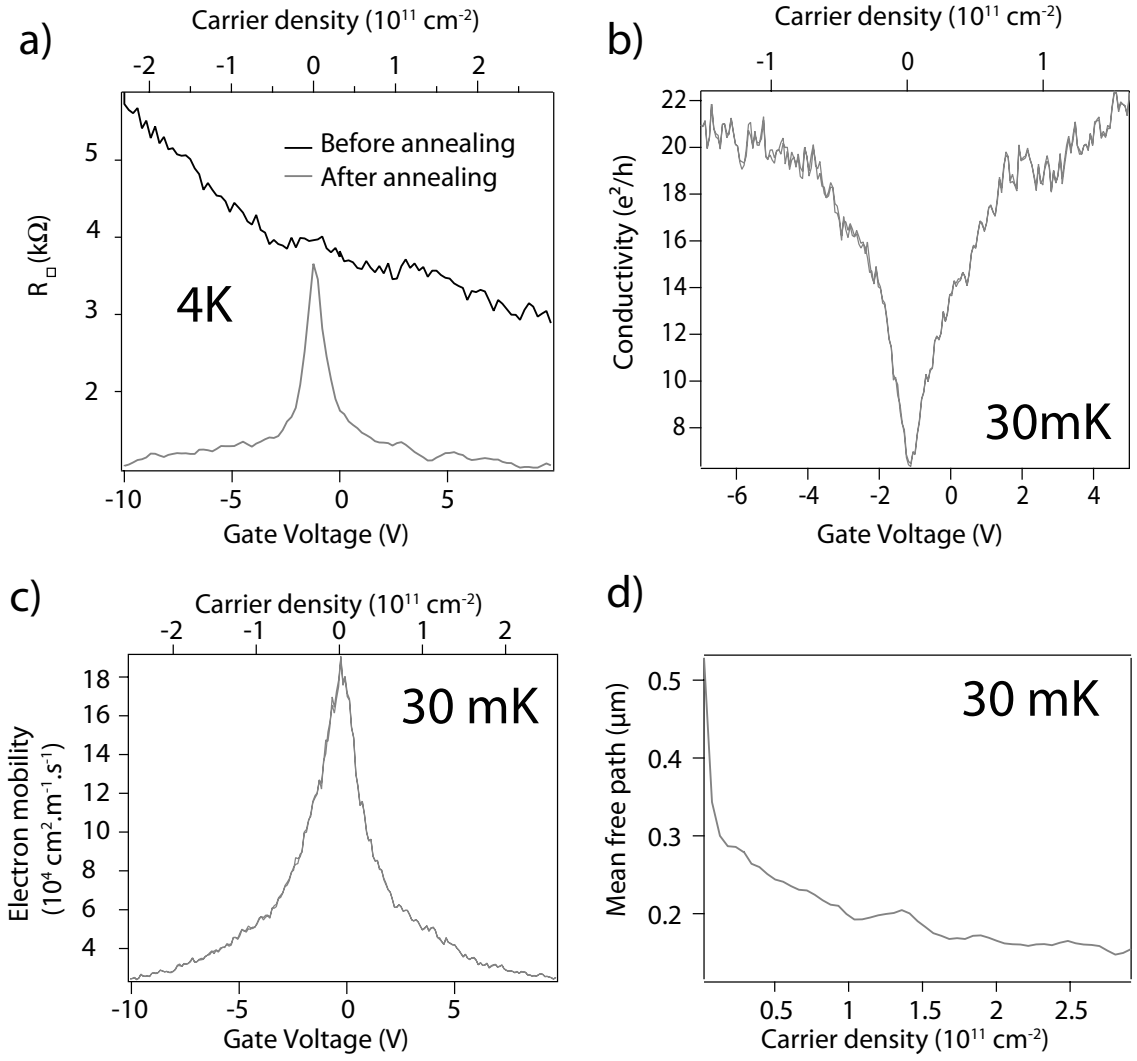

Figure 4.8 – ***Ultrahigh mobility suspended sample.*** ***a)*** *Field effect curve before and after the current annealing at 4K.* ***b)*** *Conductivity at 30 mK after annealing.* ***c)*** *Field effect mobility calulated using Drude's formula (1.19).* ***c)*** *Mean free path estimated using Einstein's relation (1.24).*

Fig. 4.8a shows the sheet resistance versus gate voltage before and after current annealing. The carrier density is assessed from the sample's geometry. The membrane is suspended about 180 nm above the substrate, which is still 100 nm thick. Therefore, the capacitance to the gate is $C_g = 4,3.10^{-5}$ F.m^{-2}.

Unlike the case of graphene on SiO_2, the conductivity is not proportional to carrier density (as can be seen in Fig. 4.8b)), but instead shows a $\sigma \propto \sqrt{n}$ dependence, as already observed by [24]. This is expected in ballistic samples [24]. Therefore, fitting this curve with equation (1.21) makes no sense. Instead, we can use Drude's formula (equation 1.19) to find the gate-dependent mobility (Fig. 4.8c). Taking as a residual carrier density the width of the region of gate-independent resistivity near the charge neutrality point $n_0 \approx 10^{10}$ cm^{-2}, we find mobilities as high as $180,000$ cm^{2}V^{-1}s^{-1} near the Dirac point and about as low as $20,000$ cm^2.V^{-1}.s^{-1} at higher densities, much like what was reported by [224], who used the same geometry, with 4 probes going across the sample.

Whereas the linear dependence in non-suspended sample is usually ascribed to charged impurity scattering [46], the square root dependence observed here is indicative of ballistic transport. In the ballistic regime, the conductivity is given by the number of channels, which is given by :

$$\sigma_{bal} = \frac{4e^2}{h}N = \frac{4e^2}{h}\frac{W}{\lambda_F} = \frac{4e^2}{h}\frac{Wk_F}{\pi} \propto \sqrt{n} \tag{4.3}$$

where W is the device's width and λ_F and $k_F = \frac{\pi}{\lambda_F}$ is the Fermi wavelength and wavenumber, respectively.

Fig. 4.8d shows the mean free path, estimated using Einstein's relation for graphene (1.24). The mean free path is always higher than 200 nm, a value which is of the order of the sample size ($L = 1.4$ μm). This confirms that we are close to the ballistic limit. However, the minimum conductivity is still much higher than the predicted value for ballistic sample in the limit of evanescent ballistic modes $\sigma_{min} = 4e^2/h\pi$ [36, 224].

4.2.3 Quantum Hall effect in suspended devices

We also performed quantum Hall effect measurement on this high mobility suspended sample. The result is shown in Fig. 4.9a and b. Because the sample's geometry is not a regular Hall bar (Fig. 4.9c), the σ_{xx} and σ_{xy} both contribute to the total conductance. As was shown by Abanin and Levitov [226], the relative contributions depend on the sample's aspect ratio. Fig. 4.9d shows their prediction for different sample aspect ratios. We can see that our sample indeed shows plateaus that correpond to the expected values of the Hall conductance σ_{xy} for monolayer graphene $4(n + 1/2)G_0$. Between these plateaus, the contribution of σ_{xx} gives peaks, as predicted by Abanin and Levitov for the case of samples of aspect ratio $L < W$.

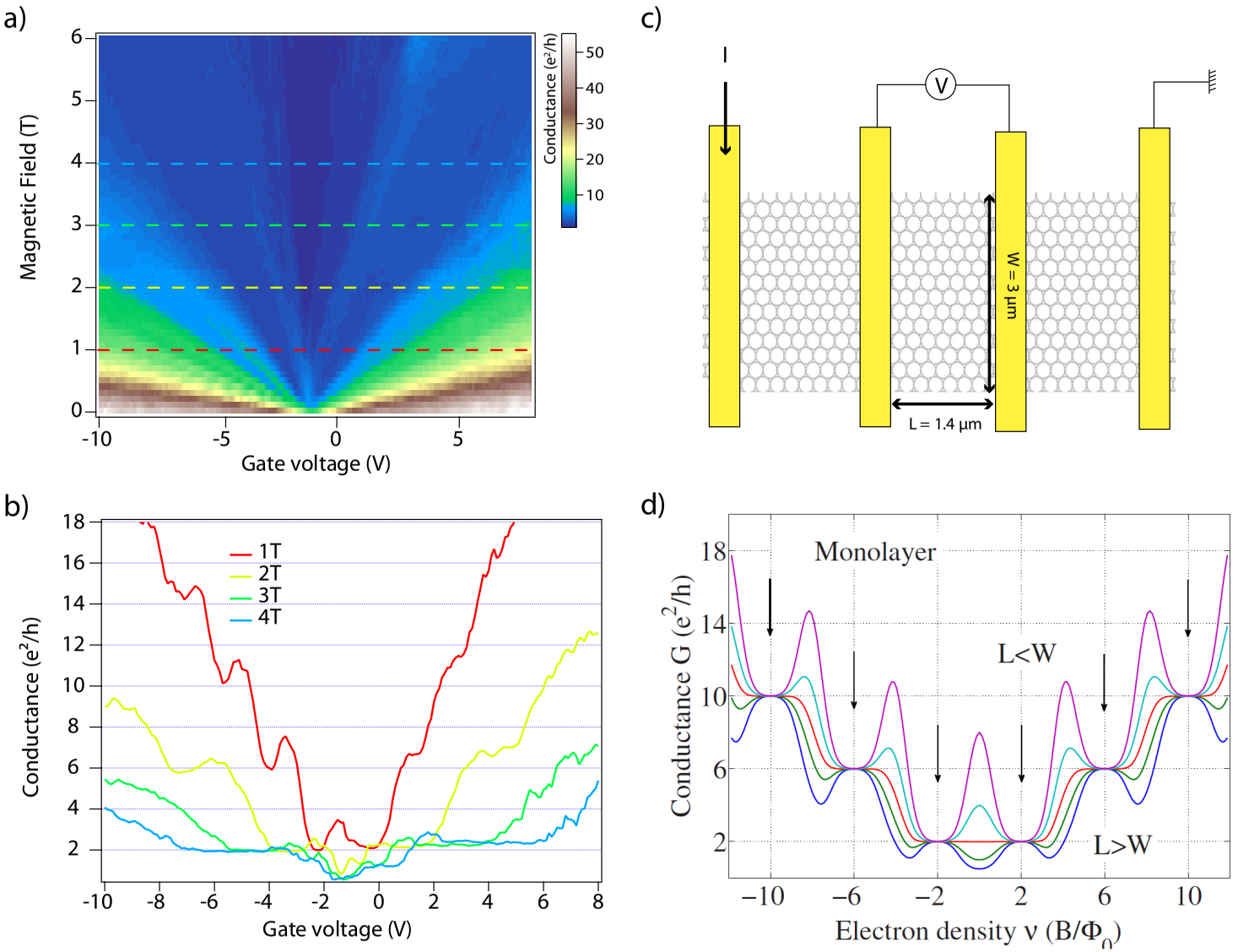

Figure 4.9 – ***Quantum Hall effect in high mobility suspended graphene at*** $T = 1$ ***K. a)*** *Colorplot of the conductance as a function of gate voltage and magnetic field.* ***b)*** *Curves taken along the dashed lines in a. Plateaus at values of conductance* $2e^2/h$, $6e^2/h$ *and* $10e^2/h$, *typical of monolayer graphene, can clearly be identified.* ***c)*** *Device geometry.* ***d)*** *Theoretical predictions of Abanin and Levitov [226] for the quantum Hall effect in a rectangular sample (as opposed to a regular Hall bar), for different aspect ratios* L/W.

4.3 Probing the mechanical motion of suspended graphene membranes

Apart from their exceptional electronic properties, suspended graphene membranes are very interesting from a purely mechanical viewpoint. As a matter of fact, graphene combines a unique set of properties. On the one hand, it is one of the stiffest known materials, with a Young modulus of about 1 TPa, and it can withstand elastic strain up to 20 % [21]. On the other hand, its 2-dimensionality makes it extremely light. In a very crude approximation, one can model a mechanical resonator as a suspended spring, where the resonant frequency is proportional to $\sqrt{k/m}$, where k stiffness and m the mass. In this respect, one can see that graphene has an excellent figure of merit for making high frequency resonators. Finally, unlike carbon nanotubes, graphene has a very large surface to volume ratio (actually the ultimate, with two surfaces and no bulk), which makes it extremely promising for mass sensing applications. In this section, it will be shown that the field effect of graphene allows the detection of mechanical vibrations using a fully electrical scheme. Gate voltage and temperature dependences of the resonant frequency within the framework of a string under tension will be explained.

4.3.1 High-speed readout of high impedance systems

When measuring a device with a high impedance, one is faced with a fundamental problem of bandwidth. The electrical circuit formed by the high impedance (R) device under test (DUT) and unavoidable stray capacitance C has an intrinsic cutoff frequency $f_{\text{cutoff}} = 1/2\pi RC$, which seriously hampers the achievable reading speed. This problem is universal and of particular importance at the nanoscale. Because ot this, STM measurements suffer from a low operation speed [227]. It is also a limiting factor for the electrical readout of quantum dots [228], carbon nanotubes [229] and graphene. Let's take a graphene sheet for example. Its typical resistance (including contact resistance) is $R = 10$ kΩ. The stray capacitance (due to contact pads mostly) is typicaly of the order of 10 pF. Approximating the circuit as a low-pass filter, we see that the cutoff frequency $f \cong 1.6$ MHz is too small to measure resonance frequencies in the tens of megahertz.

There are several ways around this problem. For example, one can couple the DUT to a resonant LC circuit (tank) circuit. The tank circuit will be calibrated to have an impedance of about 50 Ω for a fast readout. At the same time, its coupling to the DUT allows its resonant frequency to be modulated when the DUT's state changes. The reading is thus done by looking at the reflectance of the LC circuit. This technique has been used for the fast readout of SET [228] and STM [227]. Another method is to reduce the stray capacitance by using local gates. This was done by Xu *et al.* [230]

on graphene. This way, they could directly measure the resonance frequency using a network analyser, improving drastically the measurement speed.

A third method will be used here. This is a method that was devised by Sazonova *et al.* in order to measure the high-frequency mechanical resonance of carbon nanotubes [229]. The principle is that the product of two high frequency signals close in frequency produces a low frequency signal containing the information. This is called 'mixing down' the signal.

4.3.2 Heterodyne mixing technique

Following the method introduced by Sazonova *et al.* [214] for carbon nanotubes resonators, we used a fully electrical actuation and readout technique based on signal mixing. This technique is suitable for a resonator which has non-linear transport characteristics. It has been reported for the measurement of graphene resonators [215, 216]. The principle is to use the graphene's sensitivity to gating to detect its motion at the resonant frequency through its effect on the gating. The resonator is actuated using the electrostatic force created by a radio-frequency voltage at frequency ω. The total back-gate voltage is therefore the sum of an AC and a DC voltage :

$$V_g = V_g^{DC} + \delta V_g^{\omega} \tag{4.4}$$

The effect of the AC voltage on the conductance of graphene is two-fold : there is a purely electrical response, and an electromechanical one. The purely electrical signal is simply due to the modulation of the carrier density by the time-varying voltage.

$$\delta q^{el} = C_g \delta V_g^{\omega} \tag{4.5}$$

Where C_g is the graphene's capacitance to gate. The electromechanical contribution comes from the mechanical motion of the membrane. Letting $z(\omega)$ be the frequency-dependent amplitude of the membrane's motion, the capacitance is modulated with amplitude :

$$\delta C_g(\omega) = C_g' z(\omega) \tag{4.6}$$

So that to a good approximation, the total carrier density modulation at frequency ω is :

$$\delta q = C_g V_g^{\omega} + \delta C_g(\omega) V_g^{DC} = C_g V_g^{\omega} + C_g' z(\omega) V_g^{DC} \tag{4.7}$$

Where we have neglected the higher order terms in $\delta C_g \delta V_g^{\omega}$. This in turn gives a conductance modulation :

$$\delta G = \frac{dG}{dq}\delta q \tag{4.8}$$

We can see that the modulation will be a maximum when the slope of the field effect curve $\frac{dG}{dq}$ is a maximum, in other words it will vanish at the Dirac point. We can also see that the electromechanical term, which is the term proportional to $z(\omega)$ will vanish if the DC gate voltage is zero. This is fairly easy to understand : if there is no gating, there can be no modulation of the gating (to first order).

The structures we will be studying typically have resonant frequencies in the range of tens, or even hundreds of megahertz. This has to be compared to the cutoff frequency of the circuit. A rough estimate gives a capacitance to ground of about 5 pA, mainly due to the contribution of the contact pads, and a typical device resistance of order 10 kΩ. The cutoff frequency of the circuit is therefore of the order of 20 MHz. To extract the signal at high frequency, we will therefore use a mixing technique. The principle is to bias the sample at a frequency slightly different $\omega + \delta\omega$. The resulting drain source current will be :

$$I_{ds} = G(\omega)V_{ds}(\omega + \delta\omega) \tag{4.9}$$

This product of two sine functions naturally has a component at the sum frequency $2\omega + \delta\omega$ and a component at the difference frequency $\delta\omega$, both containing the information we need (the proportionality to $z(\omega)$). Using lock-in detection, we can extract the signal at frequency $\delta\omega = 10$ kHz, a frequency that we have chosen to suit our setup. Not only does this allow us to avoid the cutoff frequency problem, but it also allows us to work with a low frequency lock-in.

4.3.3 FM technique

The heterodyne mixing technique described above is essentially an amplitude modulation (AM) technique. The voltage applied to the source electrode actually achieves both the biasing (V_{sd}) and the gating (V_{sg}) of the device. Therefore, the previously discussed scheme is equivalent to having a single AM signal applied directly to the source, with amplitude modulated at frequency $\delta\omega$ ([229]). An alternative technique to extract the electromechanical signal has recently been demonstrated by [231]. Unlike the previous one it involves frequency modulation (FM). It has the great advantage to avoid the purely electrical background signal. In this setup we apply an FM signal to the source electrode :

$$V^{FM}(t) = V_c \cos(\psi(t)) \tag{4.10}$$

where $\psi(t) = \omega_c t + (\omega_\Delta/\omega_L)\sin(\omega_L t)$. Here, ω_c is the carrier frequency, which is modulated at a frequency ω_L and with an amplitude ω_Δ. The second-order Taylor

expansion of the current flowing through the device around $z = z_0$ and $V_{sd} = 0V$ writes :

$$I(V(t), z_0 + \delta z(t), V_g^{DC}) = I(0, z_0, V_g^{DC}) + \frac{\partial I}{\partial V_{sd}} V(t) + \frac{\partial I}{\partial z}\delta z(t) + \frac{1}{2}\frac{\partial^2 I}{\partial V_{sd}^2}(V(t))^2 + \frac{\partial^2 I}{\partial z \partial V_{sd}} V(t)\delta z(t) + \frac{1}{2}\frac{\partial^2 I}{\partial z^2}(\delta z(t))^2 \quad (4.11)$$

Where the first, third and last terms are zero because no current flows without source-drain voltage. The second term gives only high frequency signals. The FM signal can be decomposed using the Jacobi-Anger expansion :

$$V^{FM}(t) = V_c \left[\mathrm{J}_0\left(\frac{\omega_\Delta}{\omega_L}\right) \cos(\omega_c t) + \sum_{n=1}^{\infty} \mathrm{J}_n\left(\frac{\omega_\Delta}{\omega_L}\right) \left(\cos((\omega_c - n\omega_L)t) + (-1)^n \cos((\omega_c + n\omega_L)t)\right) \right] \quad (4.12)$$

where $\mathrm{J_n}$ is the n^{th} Bessel function. The square of this expression contains no term at the modulation frequency ω_L, and therefore, at the modulation frequency ω_L, we are left with only mechanical terms. Finally, the current detected by the lock-in at frequency ω_L is not a lorentzian, like in the AM technique, but the derivative of a lorentzian. It is proportional to :

$$F(\omega_c) = \frac{2\omega_c \left(\omega_c^2 - \omega_0^2 - \frac{\omega_0^2}{Q}\right)\left(\omega_c^2 - \omega_0^2 + \frac{\omega_0^2}{Q}\right)}{\left[(\omega_0^2 - \omega_c^2)^2 + \left(\frac{\omega_0 \omega_c}{Q}\right)^2\right]^2} \quad (4.13)$$

where ω_0 is the resonant frequency and Q is the quality factor.

4.3.4 Measurement circuits

Measurement of the mechanical resonance were carried out in a Lakeshore cryogenic probe station under vacuum. The RF signal was generated using an Agilent E4421B RF signal generator. For the low frequency modulation, the internal oscillator of our Stanford Research 830 lock-in was used. Modulation can directly be achieved by the RF signal generator, but the lock-in detection works better when the lock-in uses its own oscillator.

The two setup (AM and FM) are depicted in Fig.4.10. For the AM detection setup (Fig.4.10a), the RF signal was duplicated using a signal splitter. One end was directly plugged to the gate electrode, sourcing the actuation signal at frequency ω. The DC voltage was added to it using a bias tee. An RF frequency mixer was used to generate the source-drain voltage at frequency $\omega + \delta\omega$, by mixing the RF signal with

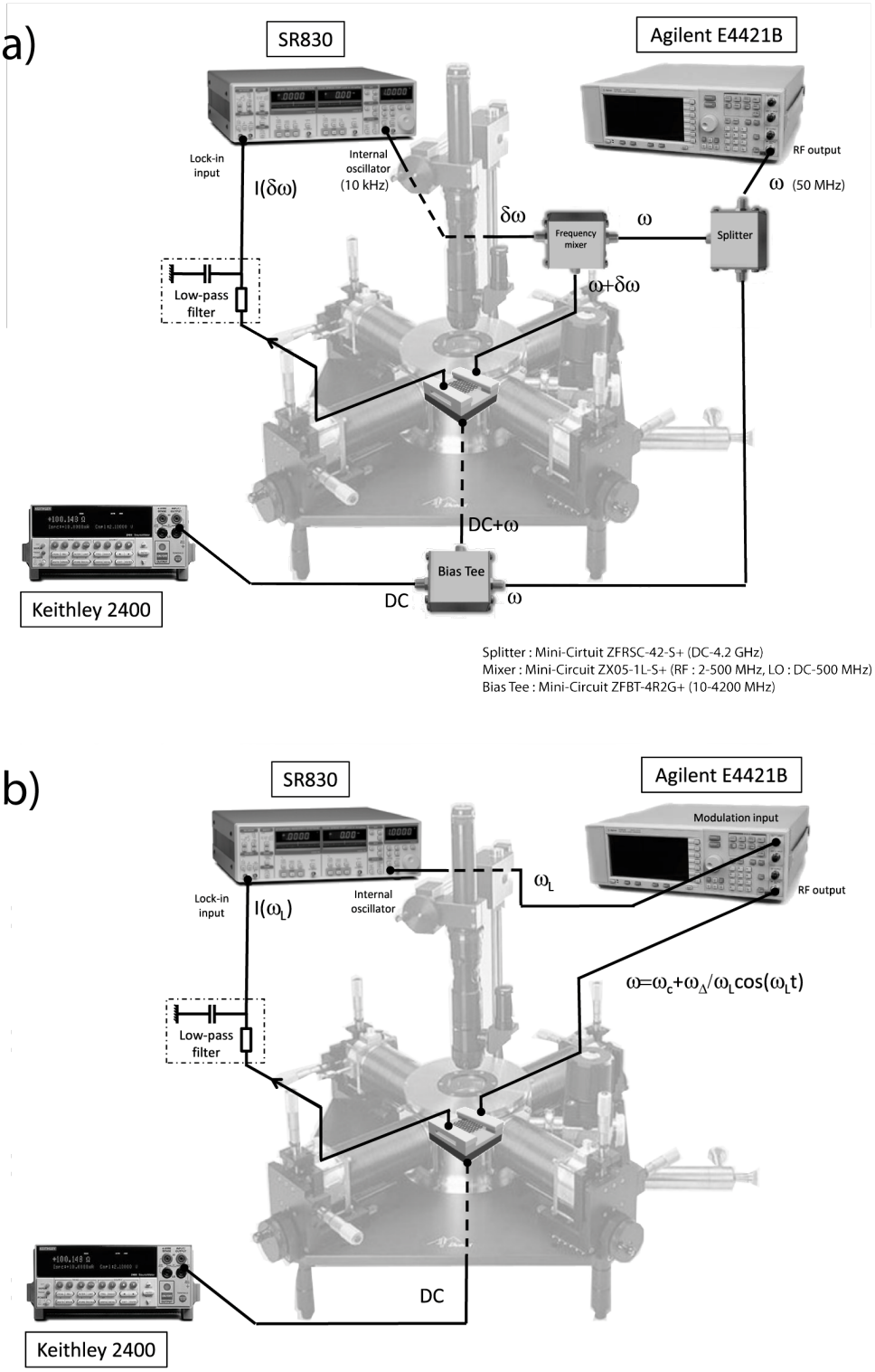

Figure 4.10 – ***NEMS measurement setup. a)*** *AM setup.* ***b)*** *FM setup.*

the internal oscillator signal of the lock-in at $\delta\omega$. The drain electrode was connected to the input of the lock-in which was set to current detection mode. Spurious high-frequency signals were filtered out of the lock-in input using a home-made low-pass filter's cutoff frequency $f_c = 100kHz$). In the FM configuration (Fig.4.10b), a single RF signal is applied to the source electrode, while only DC voltage is applied to the gate. The modulation frequency is set by the lock-in's internal oscillator and the frequency excursion is set by the RF generator.

4.3.5 Resonance signal

Fig. 4.11 shows the current recorded by the lock-in as a function of carrier frequency ω when using the AM (Fig.4.11a) and FM setup (Fig.4.11b). We can see that the FM setup gives better results, as the background signal is almost inexistent and therefore the signal is much more prominent. The results discussed in the following were obtained using the AM technique, unless specified otherwise. There are two ways to assess the mechanical origin of the sharp peak. First, according to equation (4.7), the mechanical signal should be proportional to V_g^{DC} and vanish near zero gate voltage. Second, because electrostatic forces induce tension in the membrane, the resonant frequency should be gate voltage-dependent.

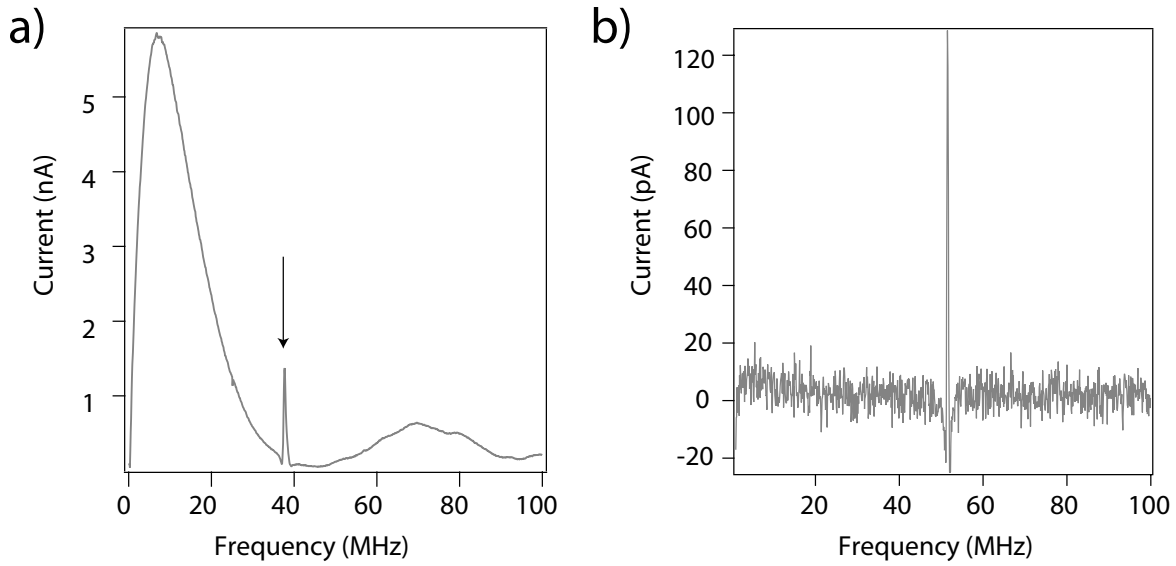

Figure 4.11 – ***Mixing signal detected by the lock-in (Gate voltage*** $V_g = -6V$***). a)*** *Using the AM setup.* ***b)*** *Using the FM setup.*

Fig.4.12a shows the gate voltage evolution of the resonance peak found in Fig.4.11a. The behavior of the peak definitely points towards a mechanical origin. Fig.4.12b shows cuts along the colored lines in Fig.4.12a. The change from a dip to a peak with varying gate voltage corresponds to crossing of the Dirac point, the po-

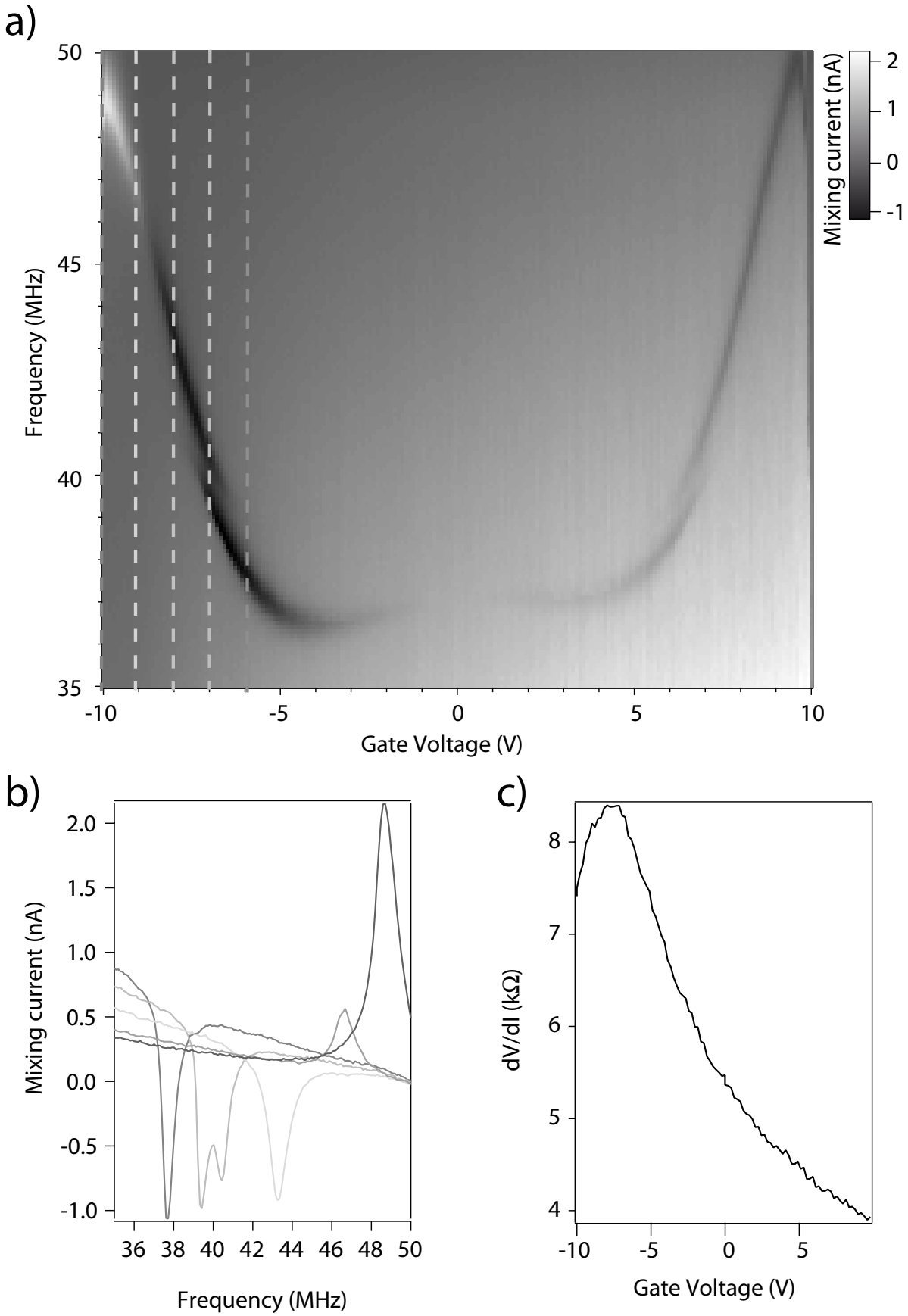

Figure 4.12 – ***Gate dependence of the mechanical resonance signal. a)*** *Intensity plot of the mixing current as a function of gate voltage and frequency. The colored dashed lines correspond to the different linescans showed in panel* ***b)****.* ***c)*** *Field effect of the device showing that the Dirac point aroung -8V indeed corresponds to the change of sign in the mechanical signal.*

sition of which is shown in Fig.4.12c. This is in good agreement with equation (4.8), which further confirms that this feature is related to the graphene flake.

4.3.6 Gate dependence of the resonant frequency

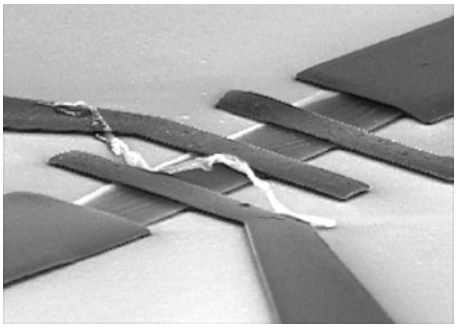

Figure 4.13 – *SEM image of a suspended graphene membrane. The fabrication method induces a lot of stress, as can be seen from the rippling of the surface.*

Because their cross section is extremely small (atomic thickness), a moderate electrostatic force is sufficient to impart large strain in graphene or CNT resonators, allowing for a wide tunability of their resonant frequency [214, 215]. The ability to tune in situ the resonant frequency is of technological interest for the realization of broadband adjustable band-pass filters [217]. Moreover, because they are metallic, CNT and graphene can be stressed using electrostatic forces. Unlike CNTs, it is commonly admitted [215, 216, 232] that graphene NEMS fabricated using the method described here have a built-in stress, which explains the rather high resonant frequency of order 50 MHz that are typically measured. This can actually be seen on some SEM images, where ripples are visible (see Fig.4.13), indicating stress. In this regime of tension, the resonant frequency is dictated by the stress, like in the case of a guitar string :

$$f_{res} = \frac{1}{2L}\sqrt{\frac{T_0 + T_e(V_g)}{\rho w}} \tag{4.14}$$

Where T_0 and $T_e(V_g)$ are the built-in and electrostatically-induced tension, respectively, L and w the length and width of the flake, and ρ is its surface density.

The electrostatic force induced by the gate voltage writes :

$$F = \frac{1}{2}\frac{\partial C_g}{\partial z}V_g^2 \tag{4.15}$$

Where C_g is the capacitance between the gate and the membrane. Following the approach of [215], we can model our device as an elastic membrane with Young's modulus 1 TPa and relate the tension in the membrane to the applied voltage :

$$T \approx \frac{T_0}{3} + \alpha V_g^{4/3} \tag{4.16}$$

Where α is a constant, so that, at high V_g ($T_e >> T_0$) the resonant frequency increases as $V_g^{2/3}$. At low V_g, the electrostatic force has practically no effect on the total tension. The negative dispersion of the resonant frequency, that can be seen at low V_g on Fig.4.12a, comes from the contribution of the electrostatic potential energy, which softens the effective spring constant [233]. If the membrane if modelled as

a spring of stiffness k and equilibrium position z_0, the potential landscape in the presence of a gate voltage is

$$E_{tot}(z) = E_{spring} + E_{elec} = \frac{1}{2}k(z - z_0)^2 - \frac{Q}{4\pi\epsilon_0 z} \tag{4.17}$$

Where Q is the total charge induced by the gate voltage. Applying a gate voltage therefore brings the equilibrium position z_0, which minimizes E_{tot}, closer to zero, and the effective spring constant $k_{eff} = \left(\frac{\partial^2 E_{tot}}{\partial z^2}\right)_{z_0}$ is softened.

4.3.7 Additional features : anti-crossing and slightly assymetric gate dependence

Apart from these features Fig.4.12 exhibits an anticrossing near $V_g = -7V$ and $+6V$. This kind of feature has been attributed to the resonance mode of the suspended gold pads [215]. The asymmetry in gate voltage can be attributed to trapped charges in the oxide, which add an offset to the gate voltage. Finally, our devices systematically show a small asymmetry in the frequency, which is an interesting albeit strange result.

4.3.8 Quality factor at room temperature

Applying a low excitation, we have measured the resonance signal in the linear regime in order to extract the room temperature quality factor. The frequency scan at $V_g = -6V$ is shown in Fig.4.14.

This measured value of $Q = 174$ compares favorably with other reported values in single-layer doubly-clamped graphene NEMS ($Q = 78$ in [234] and $Q = 125$ in [215]).

4.3.9 Evolution of the resonant frequency at low temperatures

Fig.4.15a shows the evolution of the dispersion curve of the resonance frequency as the temperature is lowered. Fitting these dispersion with the model of [215] described above (dashed lines in Fig.4.15a), we can extract the surface density and built-in tension of the resonator as a function of temperature (shown in Fig.4.15b,c and d). After an abrupt drop between 300K and 275K, the frequency steadily increases with decreasing temperature, and the dispersion becomes more and more negative. The fitting parameters indicate a sharp increase of the surface density during the first stages of cooling (probably due to cryosoption) (Fig.4.15c), accompanied by a steady increase in the tensile stress throughout the cooling process (Fig.4.15d). The stress partially originates from thermal contraction of the electrodes (which is larger than the thermal expansion of graphene) [216].

This fitting procedure demonstrates the wealth of information that can be extracted

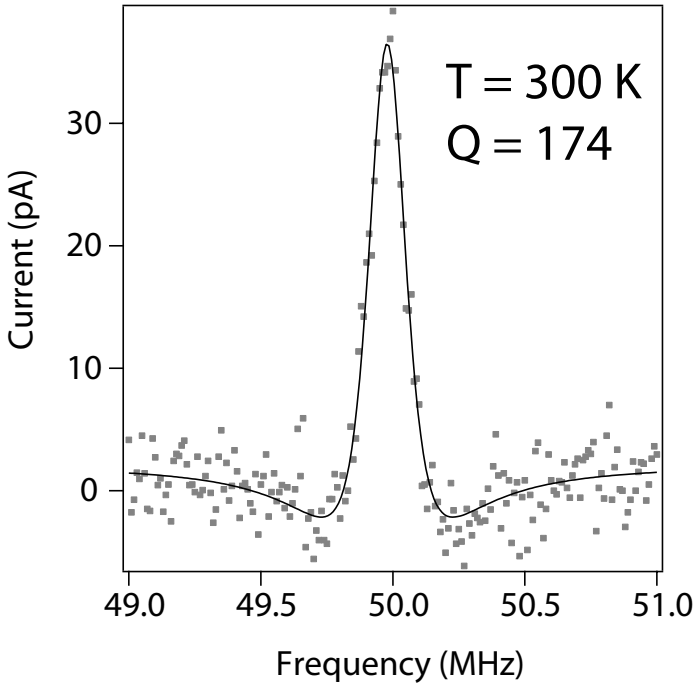

Figure 4.14 – ***Red squares*** *: electrical response as a function of frequency using the FM setup showing the resonance for* $V_g = -6V$ *at* $T = 300$ *K.* ***Black curve*** *: the resonance lineshape was fitted using equation (4.13) from [231] to find the quality factor Q.*

from a measurement of the combined effect of electrostatic force and temperature on the resonant frequency in doubly clamped graphene membranes.

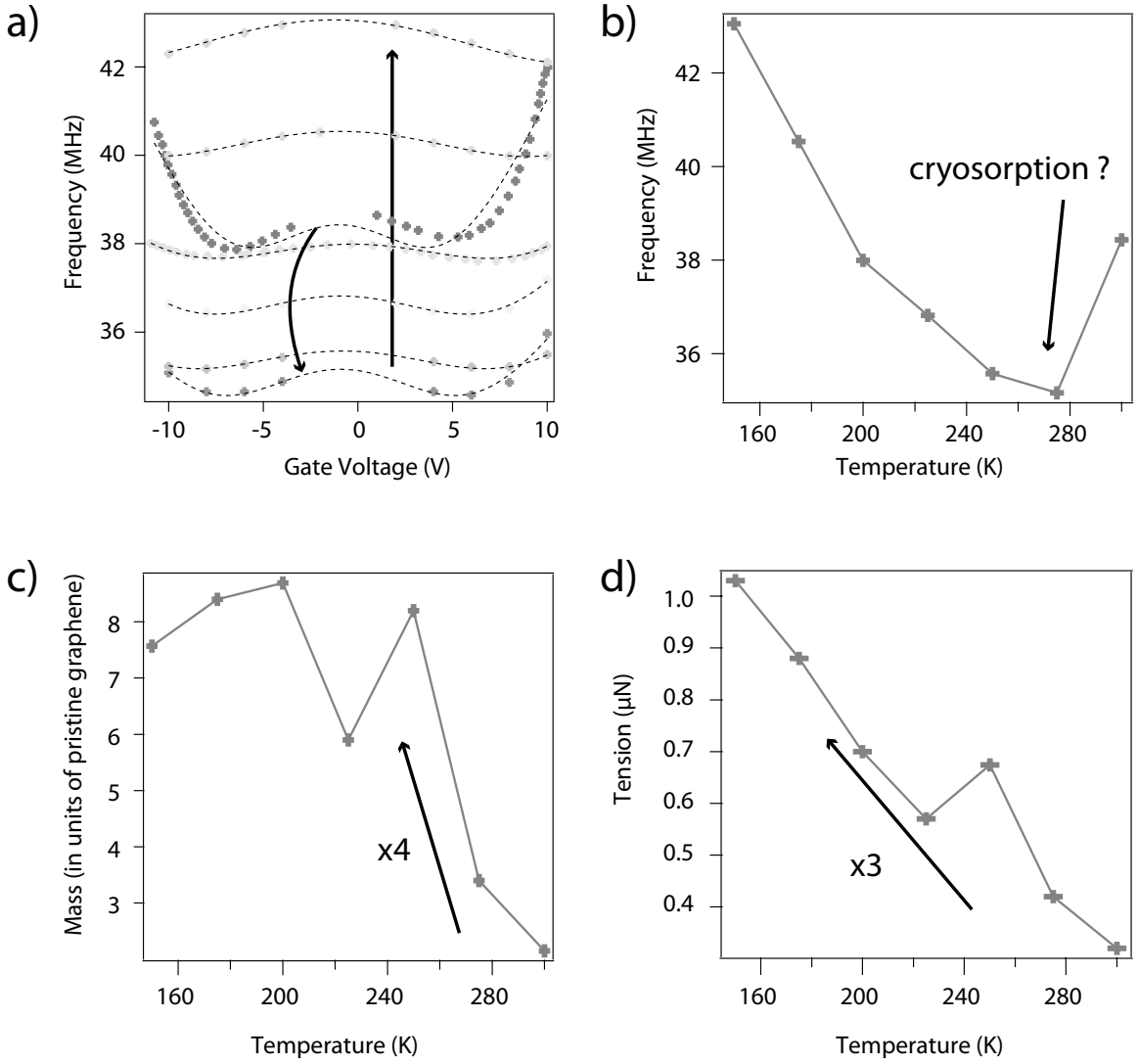

Figure 4.15 – ***Low temeperature study of the mechanical resonance.*** ***a)*** *Resonance frequency as a function of gate voltage for different temperatures. Red to green : 300K, 275K, 250K, 225K, 200K, 175K. Dotted lines are fits using the model of [215]* ***b)*** *Resonant frequency at zero gate voltage as a function of temperature.* ***c)*** *Areal density of the graphene sheet as a function of temperature.* ***d)*** *Built-in tension as a function of temperature.*

4.4 Superconducting suspended hybrids

Seoanez *et al.* have shown [208] that low-energy electronic excitations are an important source of dissipation in graphene NEMS. Coupling the nice mechanical and electronic properties of suspended graphene with the superconducting properties of hybrid Sn/graphene, one could realize a low-dissipation NEMS. Moreover, Sonne *et al.* [235] have proposed a novel cooling scheme for Josephson junction NEMS based on the coupling of Andreev bound states to the mechanical modes.

Despite their promises, suspended graphene Josephson junctions have been impossible to fabricate so far. There is a technical hassle in that hydrofluoric acid, which is the best method to get electrically connected suspended graphene, is not compatible with any commonly-used superconductor, making the fabrication of suspended graphene SNS junction a problem. In this section it will be shown that gate-tunable superconductivity in a suspended graphene membrane can be obtained by evaporating Sn nanoparticles on top of already-suspended graphene flakes. Some preliminary results on the superconducting transport will be discussed.

4.4.1 Sample fabrication and morphology

Suspended graphene membranes are prepared using the same technique described in the previous sections. In the last step of fabrication, 10 nm of Sn is evaporated on the whole surface after suspension. Fig.4.16 shows the device characterization by AFM and STM. The sample does not collapse after the evaporation, but we can see that the graphene flake's edges bend. Fig.4.16e is an SEM picture taken under large tilting angle and reveals the shadow region below the flake, where no tin has reached the substrate. Fig.4.16f shows that this shadow region actually extends a bit beyond the current flake position, indicating that the flake was actually flatter prior to evaporation and that bending happens after the tin is deposited. This curling of the edges is probably unrelated to the stress induced by the tin's weight. In the previous section, the room temperature built-in stress, inferred from the dispersion of the resonant frequency, was about $F = 3.10^{-7}$ N in bare suspended graphene. We can evaluate the total gravitational force exerted by tin :

$$F = mg = \rho V g = 2.10^{-15}\ \text{N} \tag{4.18}$$

Where $g = 9.81$, $\rho = 7300$ kg.m^{-3} is the mass density of tin, and $V = 10$ nm x 4μ m x 0.7μ m is the total volume of tin on top of the suspended membrane. This value is clearly negligible. The curling probably originates from electrostatic or van der Waals forces.

Fig.4.17 shows for comparison an SEM micrograph of suspended multilayer graphene on top of which the Sn does not induce the same kind of bending, most likely because of the higher bending rigidity of multilayered structures.

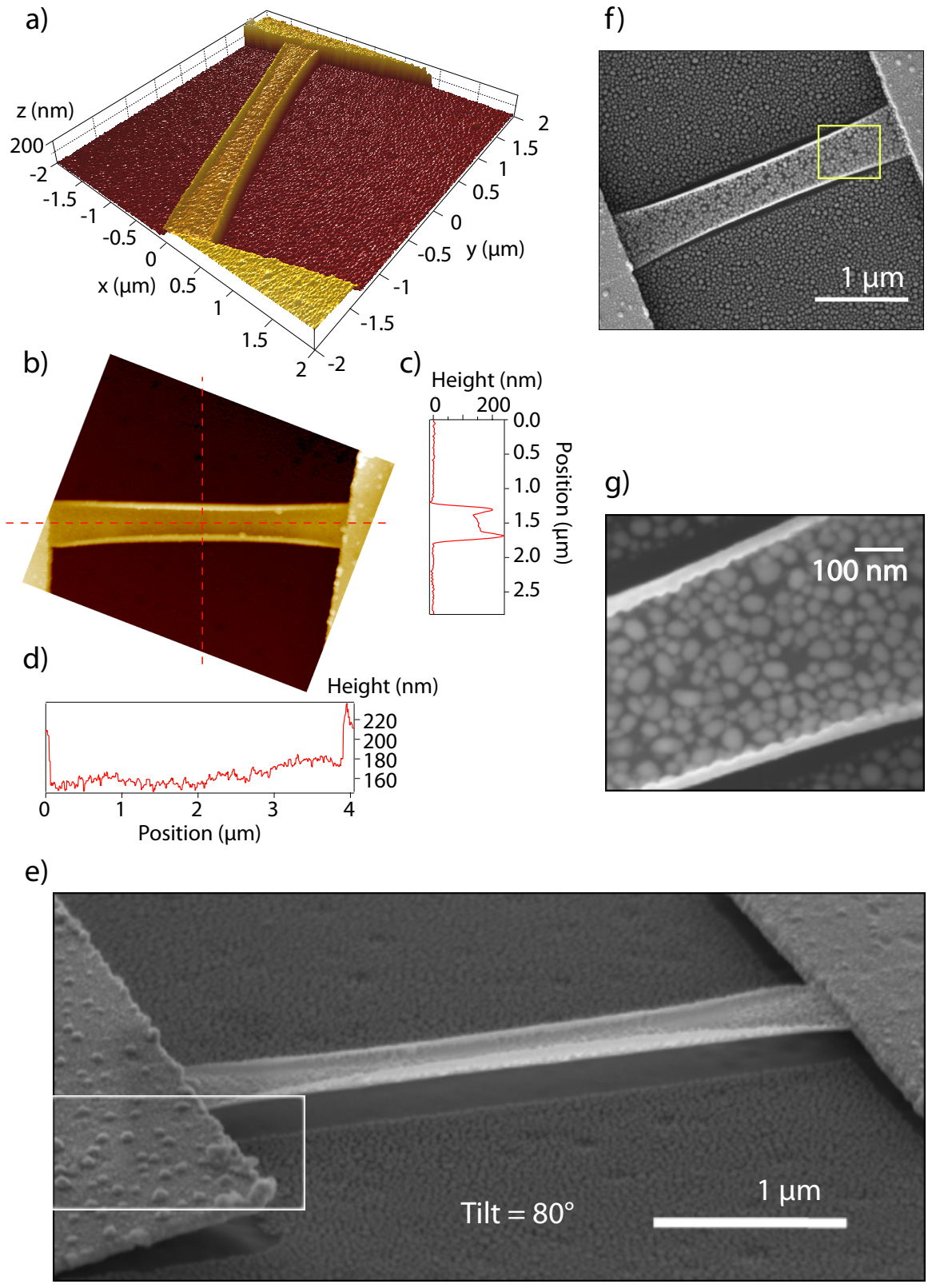

Figure 4.16 – ***Suspended hybrid Sn/graphene.*** ***a)*** *3D reconstruction of the AFM image in b).* ***b)*** *Amplitude signal of the AFM scan of the suspended sample. AFM was used in tapping mode.* ***c)*** *and* ***d)*** *Profiles along the red dotted lines in b).* ***e), f and g)*** *SEM images. g) is a zoom of the squared region in f).*

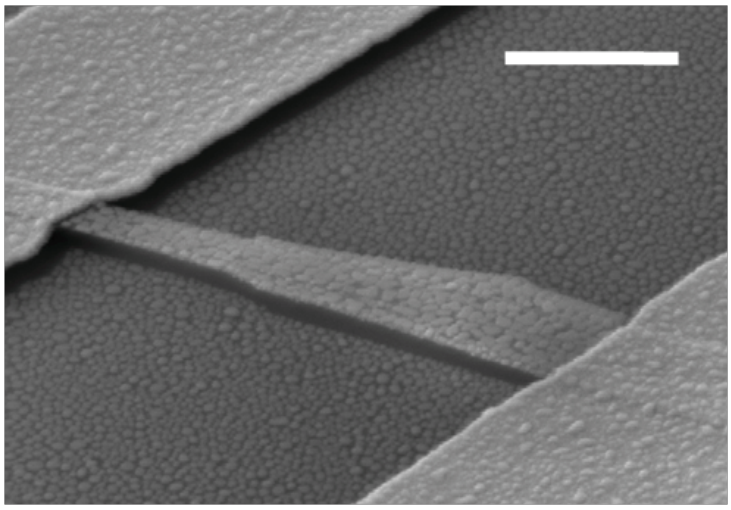

Figure 4.17 – *Tilted SEM image of suspended flake of multilayer graphene covered with Sn grains. Multilayer graphene sheets are much stiffer than monolayer and have higher resonant frequencies [236]. Due the increased stiffness, the sheet doesn't bend when Sn is evaporated on it. Scale bar is* 1 *µm.*

Finally, the size of Sn islands is greatly reduced as compared to what we observed on supported devices. As can be seen in Fig.4.16g, the typical diameter falls well below the superconducting coherence length of tin, with the largest grains reaching 50 nm and the average grain around 30nm.

4.4.2 Low temperature transport and superconductivity

The sample was cooled down in the dilution refrigerator to record its superconducting properties.

Fig.4.18 shows the superconducting transition at low temperatures. To prevent mechanical collapse of the sample, gate voltage was swept within ±15 V, preventing the observation of the Dirac point. The superconducting transition temperature is considerably reduced when compared to that of supported samples. We do not expect superconductivity to be affected by confinement in Sn grains of this size [237] (see§2.4.1.1). Instead, this weak superconductivity could be the effect of an enhanced electrical barrier at the graphene/Sn interface. As a matter of fact, the increased tendency to dewet from the surface is likely associated with a weaker electrical coupling. Unfortunately, we have not recorded the resistance near 3.7 K and cannot tell for sure that there is no depletion of the superconducting gap. It should also be noted that the system does not undergo a full transition, as a residual resistance of about 50 Ω remains at 50 mK. Surprisingly, the resistance starts to increase at low temperature after the superconducting transition at gate voltages where the critical temperature is higher. The low temperature current and magnetic field dependence is plotted in Fig.4.19. The critical current of about 20nA and the critical field of 1.5 mT are extremely weak as compared to supported samples.

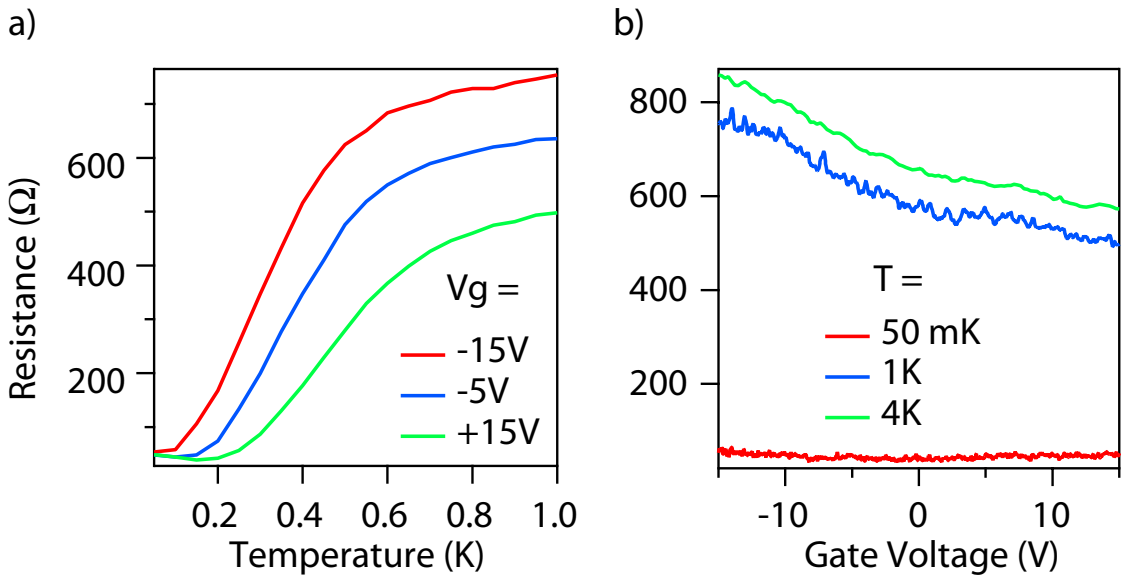

Figure 4.18 – ***Superconducting transition in suspended hybrid Sn/graphene.*** ***a)*** *Temperature dependence of the resistance for 3 gate voltages.* ***b)*** *Field effect curve at 3 different temperatures.*

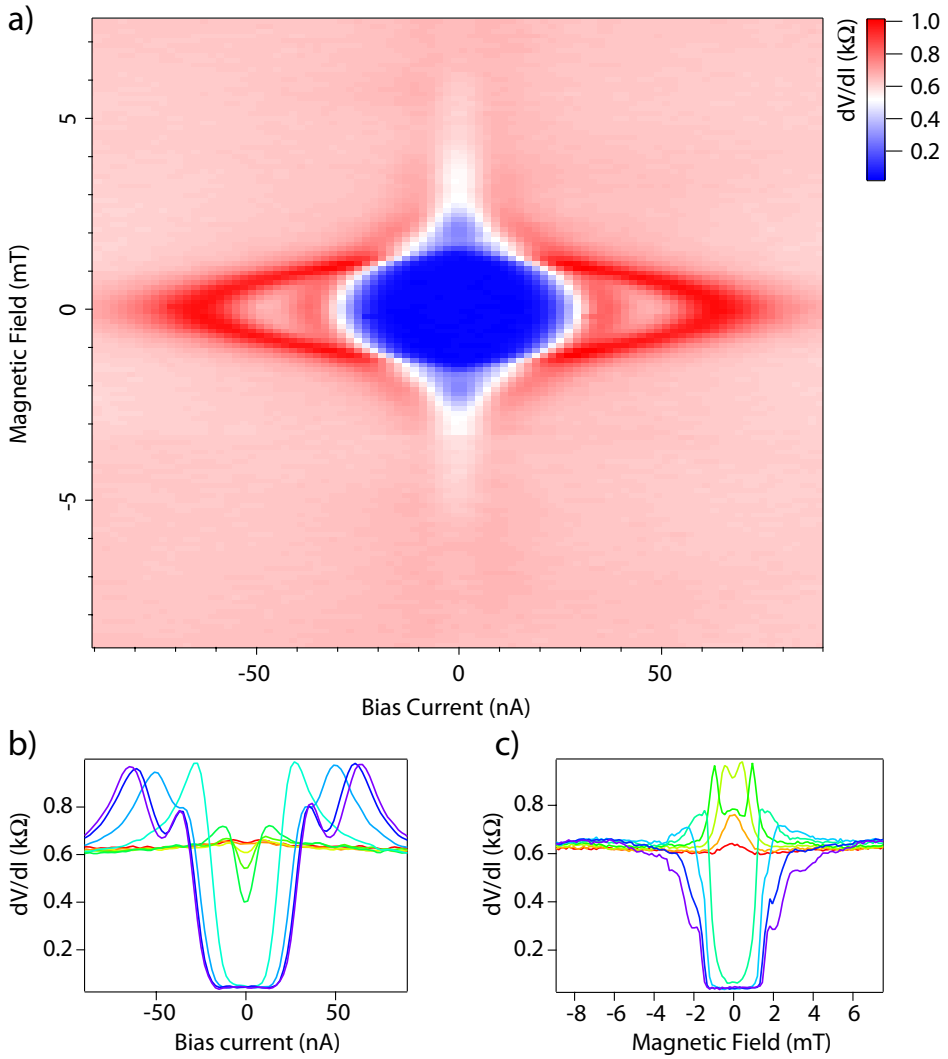

Figure 4.19 – ***Low temperature critical current and critical field.*** ***a)*** *Map of the differential resistance as a function of injected current and magnetic field.* ***b)*** *Cuts of the a) along constant values of magnetic fields.* ***b)*** *Cuts at constant bias current.*

Conclusion du Chapitre 4

Dans ce chapitre, nous avons vu que les propriétés mécaniques exceptionnelles du graphène permettent la réalisation de membranes suspendues. Nous avons montré qu'une fois maitrisée, cette technique de fabrication représente une amélioration technologique significative, avec deux conséquences importantes : de meilleures propriétés électroniques, et des propriétés mécaniques.

- Les deux surfaces du graphène (supérieure et inférieure) peuvent être nettoyée par auto-échauffement en passant du courant, ce qui permet au graphène de recouvrer ses propriétés intrinsèques, et en particulier sa mobilité de porteurs de charges exceptionnelle. Dans le cas de nos échantillons de graphène exfolié, nous avons ainsi pu ramener le point de neutralité de charge très proche de $V_g = 0$ V , ce qui indique que les impuretés chargées ont pu être efficacement nettoyées, et une mobilité électronique de l'ordre de 10^5 cm^2.V^{-1}.s^{-1} à basses températures.

- La géométrie des échantillons doublement attachés et suspendus au-dessus d'un plan métallique permet une détection des modes de vibration basée sur le couplage capacitif et l'effet de champ dans le graphène. Ceci nous a permis de mesurer la fréquence de résonance du mode fondamental de flexion de la membrane de manière entièrement électrique.

- Le facteur de qualité du mode fondamental est de l'ordre de quelques centaines à température ambiante et la fréquence de résonance peut être ajustée grâce au voltage de grille, qui contrôle la tension dans la membrane. Un modèle de mécanique des milieux continus permet d'ajuster la fréquence de résonance obtenue pour différentes tensions de grille et différentes températures pour en déduire des informations sur la tension dans la membrane et la masse effective du mode fondamental de flexion.

Finalement, dans la perspective de fabriquer des résonateurs mécanique supraconducteurs, nous avons montré que les membranes de graphène suspendues étaient compatibles avec une décoration à l'étain similaire à ce qui a été montré au Chapitre 2. Ces membranes ont des propriétés supraconductrices semblables, bien que le courant et le champ magnétique critiques soient réduits. Cependant, nous n'avons pas été en mesure de détecter la résonance mécanique de ces membranes en utilisant la technique de couplage capacitif. Il reste maintenant à trouver une signature des modes de vibrations, et si possible en tirant parti des propriétés supraconductrices.

Pour des applications nécessitant de hautes fréquences de résonnance, des échantillons à base de graphène multicouche pourraient se révéler plus appropriés du fait de leur grande rigidité. Finalement, ces matériaux sont également prometteurs

pour l'implémentation de méthodes de détection non-dissipatives dans les NEMS, mais également pour toute application nécessitant de minimiser l'interaction avec le substrat.

Conclusion of Chapter 4

In this chapter, we saw that the outstanding mechanical properties of graphene allow the realization of suspended devices. We have shown that, once mastered, this fabrication method represents a technological improvement with two important consequences : better electronic properties, and new mechanical properties.

- First, both top and bottom surfaces of graphene can be efficiently cleaned by self-heating, restoring the exceptional electronic properties of pristine graphene. In the case of exfoliated graphene, the charge neutrality point can be found close to zero volt on the gate, indicating a strong reduction of the residual charge carrier density, and the electronic mobility can exceed 10^5 $cm^2.V^{-1}.s^{-1}$.

- Second, this geometry allows to couple the transport of electrons to mechanical degrees of freedom. The graphene forms an atomically thin vibrational membrane, the motion of which can be probed by monitoring the variation of conductance. This make it possible to probe electrically the resonant frequency of the fundamental flexural mode.

- The mechanical resonance has been measured to have a quality factor in the range of hundreds at room temperature, and the resonant frequency can be tuned upon the application of stress via the electrostatic force induced by the back-gate voltage. The combined temperature- and gate-dependence of the resonant frequency allow us to extract information on both the stress in the membrane and the effective mass of the flexural mode.

Finally, as a perspective towards the realization of superconducting resonators, we have shown that suspended graphene membranes can be decorated by tin nanoparticles in a fashion similar to what has been shown for substrate supported systems (see Chapter 2). The resulting devices exhibit a rather similar superconducting behavior with a reduced critical current but no mechanical resonance was detected for the decorated sample. Further work is needed to explore the signature of mechanical motion within the superconducting properties of the systems. Such samples could implement very high frequency dissipation-less detection schemes. Furthermore, suspended graphene membranes appear promising for the realization of other type of hybrid devices for which the interaction with a substrate has to be minimized.

Conclusions et perspectives

Dans le Chapitre 1, une nouvelle méthode chimique permettant d'introduire du désordre dans le graphène a été décrite. Le résultat de cette attaque est un graphène dans lequel nous pouvons induire une transition en grille entre des états faiblement et fortement localisés à basses températures. Les mesures de spectroscopie Raman indiquent que les défauts introduits sont de type hybridisation sp^3. Le transport à basses températures est caractérisé par un régime de saut à distance variable en présence d'interactions coulombiennes (régime d'Efros-Shklovskii).

Le Chapitre 2 s'est concentré sur les propriétés supraconductrices d'échantillons hybrides Sn/graphène et Pb/graphène, obtenus en utilisant des feuilles de graphène structurellement intactes. Les mesures Raman montrent que le dépôt de métal n'induit pas de désordre structurel dans la maille. Néanmoins, celui-ci a pour effet de doper fortement le graphène en déplaçant son niveau de Fermi. Ces observations peuvent être comprises de manière semi-quantitatives par le modèle de Giovannetti *et al.* [115]. Les propriétés de transport à basses températures de ces hybrides ont été mesurées. Elles ont montré l'influence déterminante de la propreté de surface dans la morphologie des grains, et par là dans les propriétés supraconductrices globales. Ces matériaux se comportent comme des réseaux de jonctions Josephson. Ils transitent vers l'état supraconducteur suivant un mécanisme typiquement bidimensionnel appelé BKT, dans lequel dominent les fluctuations de la phase supraconductrice. Le courant critique et la réponse AC de ces réseaux sont eux déterminés par le joint le plus faible. Ceci est une manifestation du désordre morphologique.

Dans le Chapitre 3, la décoration de graphène désordonné avec des billes d'étain nous a permis d'obtenir un matériau hybride montrant une TSI contrôllable en grille. Les propriétés de cette transition ont été étudiées dans les cas limites de faible et de fort désordre. Dans la limite de fort désordre, l'état isolant porte les signatures d'un isolant de Bose, c'est-à-dire que les paires de Cooper y pré-existent et sont localisées. La transition vers l'état isolant semble alors être de type percolatif à basses températures et contrôlée par la dissipation à hautes températures. Ce nouveau système hybride pourrait améliorer notre compréhension de la TSI dans les supraconducteurs granulaires. En effet, les propriétés du médium (graphène) et du matériau supraconducteur peuvent y être contrôlés indépendamment et continuement, faisant du matériau Sn/graphène un système modèle pour l'étude de la TSI à deux dimensions.

Le Chapitre 4 a introduit d'autres voies de recherche. Nous avons étudié la possibilité d'utiliser de tels hybrides pour la résalisation de NEMS supraconducteurs. Nous avons fabriqué avec succès des membranes de graphène suspendues et avons pu mesurer la fréquence de résonance du mode de vibration fondamental à l'aide de la technique de mixage hétérodyne du courant, reproduisant les résultats de la littérature. Des membranes suspendues supraconductrices ont également été fabriquées, et nous avons mesuré leurs propriétés de transport à basse températures.

Principaux résultats

- Une nouvelle manière d'introduire du désordre dans le graphène par voie chimique a été découverte.
- Le rôle de la morphologie des billes d'étain dans les propriétés supraconductrices a été mis en évidence.
- Un nouveau système montrant la TSI a été découvert. Il s'agit du premier exemple de TSI induite en grille dans un système supraconducteur granulaire.
- Les résultats de la litérature sur les NEMS graphène ont été reproduits.
- La possibilité de fabriquer des membranes suspendues de Sn/graphene conservant des propriétés supraconductrices a été démontrée.

Questions ouvertes et perspectives concernant la transition supraconducteur-isolant

Quelle est la nature des défauts induits par l'attaque chimique utilisée au Chapitre 1 ?

Il y a de bonnes raisons de penser que ces défauts sont en réalité une hybridisation partielle de type sp^3 de la maille de graphène. Cependant, seules des mesures en champ proche pourront nous dire avec certitude qu'il ne s'agit pas de vacances. Ce genre de mesures pourrait également nous donner une estimation indépendante de la densité de défauts. Enfin, des mesures de spectroscopie par photoémission X pourraient nous renseigner sur la nature des liens chimiques présents et donc sur les espèces chimiques attachées.

Le désordre est-il homogène, comment le savoir, et comment faire pour qu'il le soit ?

Une cartographie Raman sur de grandes surfaces pourrait être réalisée afin de mesurer la variation d'intensité de la bande D qui est proportionnelle à la densité de défauts. Il serait intéressant de mener une étude comparative entre du graphène attaqué avec des solutions ayant des concentrations différentes (pour le même degré général de désordre). Nous avons remarqué que la solution $(NH_4)_2S_2O_8$ (la 'bonne' solution pour enlever le Cu sans induire de défauts) induit en fait des défauts si on la laisse agir suffisamment longtemps. Peut-être ces défaut sont-ils différents, plus homogènes ?

Dans quelle mesure la transition de percolation observée au Chapitre 3 est-elle liée à l'inhomogénéité du désordre ? Y aurait-il une percolation dans le cas d'un désordre homogène à l'échelle de la longueur de cohérence supraconductrice, et si oui, aurait-elle les mêmes caractéristiques ?

Cette question est celle de l'universalité de la transition que nous avons observé. Il y a bien entendu une différence entre une percolation à travers des inhomogénéités pré-existantes, qui devrait dépendre de l'échantillon considéré, et une percolation à travers des inhomogénéités émergeant à la transition, qui devrait porter quelque part un caractère plus universel.

Contrôler le désordre dans notre système est donc très important. Celà implique une meilleure compréhension et un contrôle plus strict de l'homogénéité du désordre dans le graphène, mais également au niveau des îlots d'étain. Le taux de couverture ainsi que le couplage étain/graphène devraient être constants sur toute la suface de l'échantillon. Les progrès faits en matière de nettoyage de la contamination de surface,

ainsi que la fabrication de réseaux réguliers nous permettront peut-être d'améliorer ce point. Ceci nous permettrait peut-être d'établir un lien avec la théorie de la supraconductivité fractale à la TSI dans les films d'oxide d'indium amorphe [238].

Quelle est la valeur de la résistance d'Andreev ? Comment pourrait-on caractériser cette interface ?

Dans les expériences de transport, il est impossible d'avoir une lecture directe de ce paramètre. De plus, le désordre d'ordre morphologique rend toute mesure indirecte très imprécise. Deux solutions s'offrent à nous. Le prochain thésard sur le sujet, Zheng Han, est actuellement en train d'étudier des réseaux réguliers fabriqués par lithographie électronique. Dans un réseau régulier, le problème a été traité théoriquement par Feigel'man *et al.* [112], qui ont donné la relation entre T_{BKT} et cette résistance d'interface. Une autre approche serait évidemment d'utiliser des techniques de champ proche. La technique de la sonde de Kelvin [239] permet de lire directement le potentiel de la surface, ce qui pourrait nous donner de précieuses informations sur le couplage électrique Sn/graphène. Par ailleurs, des mesures de courant tunnel à travers des nanoparticules de Pb ont été utilisées par Brun *et al.* pour estimer la résistance d'interface ainsi que la capacité de ces nanoparticules [**?**]. Cette méthode semble toute indiquée.

Pourquoi nos échantillons montrent-ils un seul pas de Shapiro au lieu de pas de Shapiro géants comme il est prévu dans les réseaux de jonctions Josephson ?

Ceci est probablement un effet de l'inhomogénéité dans les jonctions. Si le joint le plus faible est très différent des autres, il est possible que seule sa réponse soit visible. Nous aimerions néanmoins nous en assurer et pour celà, les réseaux ordonnés sont de bons candidats. Si notre interprétation est la bonne, ceux-ci devraient montrer des pas de Shapiro géants.

Perspective : le graphène comme plateforme médiatrice des interactions électroniques

Lorsque des nanoparticules supraconductrices de plomb et d'étain sont adsorbées à la surface du graphène, le matériau qui en résulte est un hybride qui combine les propriétés supraconductrices de l'adsorbat et la grande sensibilité au champ électrique du graphène. Celui-ci agit alors comme une plateforme ajustable qui contrôle l'établissement de l'ordre supraconducteur global. Lorsque du désordre est introduit dans le graphène, il devient sujet à une transition métal-isolant contrôlée en grille. Cette plateforme désordonnée offre un contrôle plus étendu des interactions électroniques par la tension de grille.

Le travail présenté dans cette thèse peut être considéré comme une démonstration du concept plus général de graphène comme médium ajustable contrôlant l'établissement de phases électroniques à longue distance. Nous pouvons d'ores et déjà imaginer une expérience similaire, dans laquelle les matériaux supraconducteurs seraient remplacés par des matériaux ferromagnétiques. Par effet de proximité [240], le ferromagnétisme des îlots se transmettrait aux électrons du graphène, qui deviendraient les vecteurs de l'interaction ferromagnétique entre îlots par un processus de type RKKY. Ce système permettrait d'étudier le modèle d'Ising à 2 dimensions, avec des applications possibles en spintronique.

Par ailleurs, il ne faut pas oublier que le graphène possède deux surfaces. En remplaçant le substrat neutre SiO_2 par un oxyde ferromagnétique par exemple, et en décorant la surface du dessus avec des supraconducteurs, il serait possible d'étudier comment et dans quelle mesure ces deux ordres électroniques antagonistes peuvent coexister à deux dimensions.

Finalement, les systèmes hybrides à base de graphène possèdent un potentiel immense que nous commençons à peine à entrevoir. De récents travaux ont par exemple prédit l'émergence d'états électroniques topologiques lorsque du graphène est décoré d'atomes lourds comme l'indium ou le thallium. Ces atomes adsorbés introduisent un fort couplage spin-orbite, normalement absent dans le graphène, ce qui pourrait donner lieu à un effet Hall quantique de spin [241].

Perspective : Sn/graphène comme membrane mécanique robuste et transparente compatible avec la supraconductivité

Ces dernières années, la recherche en nanomécanique a beaucoup investi pour atteindre la limite quantique. Ceci passe par des techniques de mesures et de refroidissement impliquant de coupler le résonateur à une cavité optique [220], supraconductrice [222], ou à un système à deux niveaux [213]. Les chercheurs s'intéressent aujourd'hui de près à la possibilité d'utiliser le graphène et les nanotubes de carbone pour la réalisation de tels résonateurs quantiques car ceux-ci ont à la fois de haute fréquence de résonance (nécessaires pour atteindre la limite $\hbar\omega > k_B T$) et un mouvement de point zero de grande amplitude [212] (voir Fig.4.20). Il a par ailleurs été montré récemment que le graphène suspendu formait avec le substrat de SiO_2 une cavité optique car le graphène est semi-transparent [223]. Ajoutons à celà la possibilité d'induire de la supraconductivité, nous voyons que le matériau Sn/graphène possède un fort potentiel pour les applications de nanomécanique puisqu'il est naturellement couplé à une cavité optique et à une cavité supraconductrice. Plus simplement, le simple fait d'être supraconducteur pourrait permettre l'implémentation d'un schéma de mesure sans dissipation du mouvement du résonateur, ce qui pourrait améliorer le facteur de qualité.

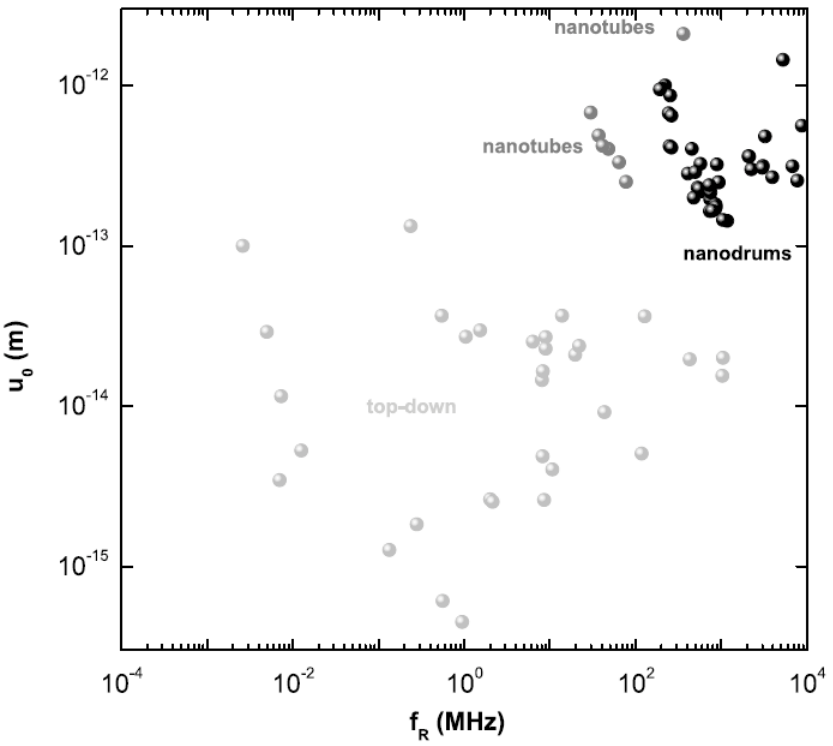

Figure 4.20 – *Figure de mérite des résonateurs quantiques montrant la fréquence de résonance et l'amplitude de mouvement de point zero dans plusieurs types de résonateurs. Les résonateurs à base de nanotubes et de tambours de graphène (fabriqués en utilisant une approche bottom-up, opposées ici aux résonateurs fabriqués dans la masse par une approche top-down) possèdent des propriétés supérieures en termes de fréquence et d'amplitude. Tiré de [212].*

Conclusions and perspectives

In Chapter 1, a new chemical route to induce disorder in graphene has been described. The resulting graphene sheets exhibit a gate-tunable transition between a weakly and a strongly localized state at low temperatures. Raman spectroscopy indicates that these defects are sp^3 hybridizations of the carbon lattice. Low-temperature transport is characterized by variable range hopping with Coulomb interactions (Efros-Shklovskii).

Chapter 2 focused on the superconducting properties of Sn/graphene and Pb/graphene obtained using structurally intact graphene flakes. Sn does not introduce any structural defect in graphene, as was shown by Raman spectroscopy. However, it induces a significant shift in the Fermi energy that can be semi-quantitatively accounted for by the DFT calculations of Giovannetti *et al.* [115]. The low temperature transport properties of these hybrids have been investigated, showing the predominant role played by surface cleanliness in determining the morphology, and thereby the superconducting properties. These materials behave like arrays of Josephson junctions. They undergo a BKT transition, where the intermediate temperature regime is characterized by fluctuations of the superconducting phase. The critical current and the AC Josephson effect are dominated by the response of the array's weakest link.

In Chapter 3, the combination of disordered graphene and Sn nanoparticles resulted in a hybrid superconductor exhibiting a gate-tunable superconductor-insulator transition (SIT). The properties of this transition have been investigated for the case of low and high disorder. In the high disorder limit, the insulating state bears the characteristic signatures of a Cooper pair insulator. The transition seems to be driven by percolation at low temperatures and by dissipation at high temperatures. This novel hybrid system allows for a better understanding of the physics of the SIT in granular superconductors. As a matter of fact, the properties of the insulating medium and superconducting grains can be controlled independently and continuously, thus making Sn/graphene a model system for the study of SIT in two dimensions.

Chapter 4 explored new avenues of research, namely the possible use of such hybrid Sn/graphene membranes to implement superconducting NEMS. Graphene nanomechanical resonators have been successfully fabricated and measured, reproducing the results from the literature . Superconducting suspended membranes of Sn/graphene have also been fabricated and measured, demonstrating that Sn/graphene membranes are compatible with nanomechanics.

Main results

- A novel chemical way to introduce disorder in graphene has been discovered.
- The role of Sn islands morphology in the superconducting properties of Sn/graphene hybrids has been highlighted.
- A new system showing the superconductor-insulator transition has been studied. It is the first example of a gate-tunable SIT in a granular system.
- Results from the literature on graphene NEMS have been reproduced.
- The fabrication of suspended membrane of Sn/graphene with superconducting properties has been demonstrated.

Open questions and perspectives concerning superconducting hybrids and the superconductor-insulator transition

What is the nature of the defects induced by the chemical solution used in Chapter 1 ?

There is strong evidence supporting the fact that these defects are the result of a partial sp^3 hybridization of the graphene lattice. However, only STM mapping could give confirmation that the defects are indeed sp^3 and not vacancies. It could also give an independent and reliable estimate of the defect density. Finally, X-ray photoemission spectroscopy (XPS) could give useful informations about the nature of the chemical bonds.

How inhomogeneous is this disorder, and how could it be made more homogeneous ?

A systematic mapping of the large-scale spatial variations of the D band could answer this question. It could be interesting to study graphene treated with the same solution but in different concentrations (for the same total amount of disorder). $(NH_4)_2S_2O_8$ (the 'good' etchant) also induces defects, although much more slowly. Using it instead of $Na_2S_2O_8$ might induce a more homogeneous defect density.

To what extent is the percolative transition observed in Chapter 3 related to disorder inhomogeneity ? Would there be a percolative transition, and if yes, would it bear the same scaling exponents if the disorder was homogeneous at a scale smaller than the superconducting coherence length ?

This question relates to the universality of the transition we have probed. There is a difference between a percolation through pre-existing inhomogeneities, which should be sample-dependent, and percolation through emerging inhomogeneities, which should bear some universal character.

Controlling the disorder in our system involves both a better control of the defect density in graphene, and of the island's morphologies, by making sure for example that the surface coverage does not vary and that the Sn/graphene coupling is constant throughout the sample. Recent progress in this direction involve a better cleaning procedure of the resist residues at the surface of transferred CVD graphene and the fabrication of regular arrays of Sn islands. Achieving this would maybe allow us to draw a line between our system and the so-called amorphous superconducting thin films such as InO_x, where fractal superconductivity has been predicted at the threshold [238].

What is the value of the Andreev resistance ? How could we characterize the Sn/graphene interface

In the present state of the experiments, the problem is that we have no way to read it directly, and its effect on the superconducting properties is overshadowed by the system's disorder. Two solution are currently being explored. The next PhD student on this project, Zheng Han, is currently measuring artificially-patterned regular arrays of Sn islands on graphene. Recording the transition temperature T_{BKT} of such arrays will allow us to give an estimate of the Andreev resistance, by application of the model of Feigel'man *et al.* [112]. An alternative and complementary route is to use local probes. Kelvin Probe Microscopy (KPM) [239] allows a direct readout of the surface potential, thus giving interesting informations about the electrical coupling between Sn and graphene. Moreover, recent STM experiments on Pb nanoparticles by Brun *et al.* [242] have demonstrated the possibility to read directly the interface resistance and nanoparticle's capacitance by analyzing the spectroscopic measurement.

Why did our samples exhibit single Shapiro steps when giant steps are expected in arrays of Josephson junctions ?

This is probably an effect of junction's inhomogeneities. Simulations using a RSJ model show that the Shapiro steps amplitude are very dependent on shunt resistance. Neverthesless, this question deserves further investigation, which is another reason

why samples with regularly spaced Sn islands are currently under study. If our current understanding is right, these should normally exhibit giant Shapiro steps.

Perspective : graphene as a tunable platform mediating interactions

When superconducting nanoparticles of Sn or Pb are adsorbed on the surface of graphene, the resulting material is a hybrid that combines the superconducting properties of the adsorbate with the fine electrostatic tunability of the graphene substrate. The latter acts as an adjustable platform that mediates the establishment of global superconducting order. When structural disorder is introduced in the graphene medium, it undergoes a gate-controlled transition between a metallic and an insulating state. This disordered platform allows an even more extensive control of the superconducting order by the gate voltage.

The work presented in this manuscript can be considered as a proof of concept for the more general use of graphene as an adjustable medium controlling long-range electronic ordering. An anolog experiment can be envisioned, involving ferromagnetic instead of superconducting islands. By a similar proximity effect [240], the ferromagnetic islands would induce spin polarization of the graphene's electrons and the graphene sheet would mediate the interaction between the magnetic moments of ferromagnetic nanoparticles by means of the gate-tunable RKKY interaction. This could be a nice system to study the 2D Ising model, with possible applications in the realm of spintronics.

Moreover, the existence of two (top and bottom) surfaces in graphene opens vast possibilities for studying the interplay between superconductivity and ferromagnetism. For example, one may wonder what happens if one replaces the SiO_2 substrate with a ferromagnetic oxide and decorate the top surface with superconducting nanoparticles.

Finally, hybrid systems based on graphene have an immense potential that we are only starting to understand. For example, recent proposals have pointed out the fact that spin-orbit interactions, naturally weak in graphene, can also be induced by adsorption of heavy atoms of In or Tl. This has been predicted to introduce new topological electronic order in graphene, such as a quantum spin Hall state [241].

Perspective : Sn/Graphene as a robust and transparent mechanical membrane supporting superconductivity

In recent years, experiments reaching the quantum limit in nanomechanics have involved coupling the resonator to an optical cavity [220], superconducting cavity [222], or superconducting Qubit [213]. Researchers are now turning to carbon nanotubes and graphene as good candidates to observe the quantum ground state of motion, as these resonators have both a high resonant frequency (necessary to reach the quantum limit $k_B T < \hbar\omega$) and a large amplitude zero-point motion [212] (see Fig.4.21). Suspended sheets of few-layer-graphene have been shown to form an optical cavity above the SiO_2 substrate [223] and now Sn/graphene can achieve superconductivity in a suspended structure. This system therefore has enormous potential for quantum nanomechanics applications, because in addition to being mechanically superior, graphene optical and superconducting cavities open the possibility to implement sideband cooling schemes [243]. More simply, the mere fact that Sn/graphene is superconducting allows the implementation of dissipationless actuation and detection schemes based either on the capacitive or on the magnetomotive technique, which could greatly improve the low-temperature quality factor of these devices and unveil the influence of other sources of dissipation.

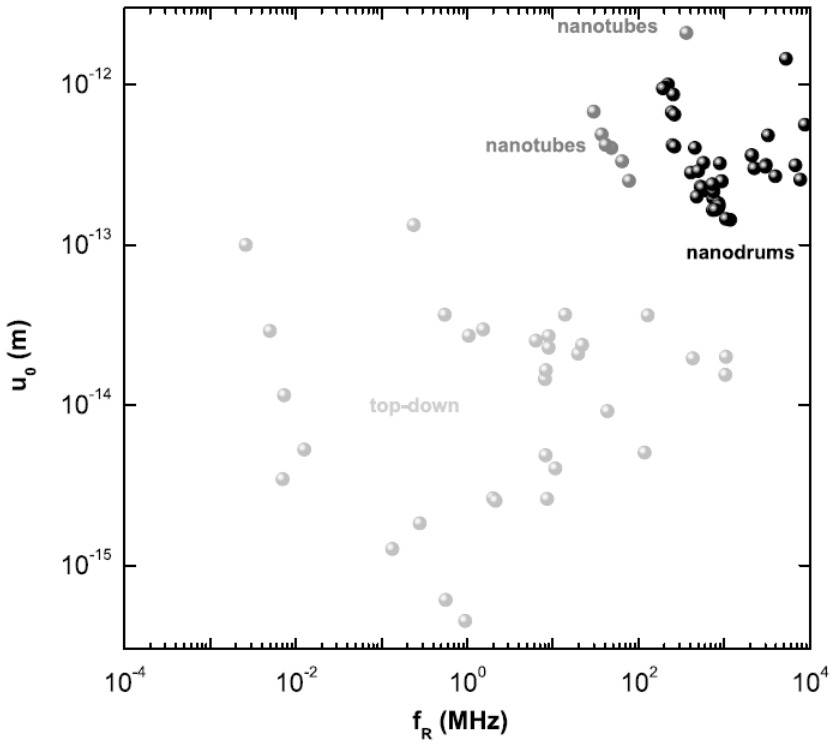

Figure 4.21 – *Comparison of the zero-point motion amplitude and resonant frequency of different NEMS systems. Bottom-up systems such as nanotubes and graphene nanodrums have both a higher frequency and a larger zero-point motion amplitude than classical top-down-fabricated NEMS devices.Taken from [212].*

Bibliography

[1] Ando, T., Fowler, A. B., and Stern, F. *Reviews of Modern Physics* **54**(2), 437–672 April (1982). (Cited pages 2 et 12.)

[2] Abrahams, E., Anderson, P. W., Licciardello, D. C., and Ramakrishnan, T. V. *Physical Review Letters* **42**(10), 673–676 March (1979). (Cited pages 2, 12, 38 et 41.)

[3] Sondhi, S. L., Girvin, S. M., Carini, J. P., and Shahar, D. *Reviews of Modern Physics* **69**(1), 315 January (1997). (Cited pages 3, 12, 162, 180 et 182.)

[4] Kosterlitz, J. M. and Thouless, D. J. *Journal of Physics C: Solid State Physics* **6**(7), 1181–1203 April (1973). (Cited pages 3, 13 et 111.)

[5] Beasley, M. R., Mooij, J. E., and Orlando, T. P. *Physical Review Letters* **42**(17), 1165–1168 April (1979). (Cited pages 3, 13, 111 et 119.)

[6] Geim, A. K. and Novoselov, K. S. *Nat Mater* **6**(3), 183–191 March (2007). (Cited pages 4, 13, 20 et 24.)

[7] Novoselov, K. S., Geim, A. K., Morozov, S. V., Jiang, D., Katsnelson, M. I., Grigorieva, I. V., Dubonos, S. V., and Firsov, A. A. *Nature* **438**(7065), 197–200 November (2005). (Cited pages 4, 13, 37 et 46.)

[8] Novoselov, K. S., Geim, A. K., Morozov, S. V., Jiang, D., Zhang, Y., Dubonos, S. V., Grigorieva, I. V., and Firsov, A. A. *Science* **306**(5696), 666 –669 October (2004). (Cited pages 4, 13, 19, 24 et 46.)

[9] Bolotin, K., Sikes, K., Jiang, Z., Klima, M., Fudenberg, G., Hone, J., Kim, P., and Stormer, H. *Solid State Communications* **146**(9-10), 351–355 June (2008). (Cited pages 4, 13, 20, 24, 200 et 203.)

[10] Morozov, S. V., Novoselov, K. S., Katsnelson, M. I., Schedin, F., Elias, D. C., Jaszczak, J. A., and Geim, A. K. *Physical Review Letters* **100**(1), 016602 January (2008). (Cited pages 4, 13, 20 et 24.)

[11] Iyer, S., Pekker, D., and Refael, G. *Physical Review B* **85**(9), 094202 March (2012). (Cited pages 5, 14, 166, 183, 187 et 189.)

[12] Parendo, K. A., Tan, K. H. S. B., Bhattacharya, A., Eblen-Zayas, M., Staley, N. E., and Goldman, A. M. *Physical Review Letters* **94**(19), 197004 May (2005). (Cited pages 5, 14, 148 et 151.)

[13] Caviglia, A. D., Gariglio, S., Reyren, N., Jaccard, D., Schneider, T., Gabay, M., Thiel, S., Hammerl, G., Mannhart, J., and Triscone, J.-M. *Nature* **456**(7222), 624–627 December (2008). (Cited pages 5, 14, 148 et 151.)

[14] Leng, X., Garcia-Barriocanal, J., Bose, S., Lee, Y., and Goldman, A. M. *Physical Review Letters* **107**(2), 027001 July (2011). (Cited pages 5, 14, 148 et 151.)

[15] Gantmakher, V. F. and Dolgopolov, V. T. *Physics-Uspekhi* **53**(1), 1–49 January (2010). (Cited pages 13 et 162.)

[16] Wallace, P. R. *Physical Review* **71**(9), 622–634 May (1947). (Cited pages 19, 24 et 30.)

[17] McClure, J. W. *Physical Review* **104**(3), 666–671 November (1956). (Cited pages 19 et 24.)

[18] Yan, Z., Lin, J., Peng, Z., Sun, Z., Zhu, Y., Li, L., Xiang, C., Samuel, E. L., Kittrell, C., and Tour, J. M. *ACS Nano* September (2012). (Cited pages 19, 24 et 46.)

[19] Mayorov, A. S., Gorbachev, R. V., Morozov, S. V., Britnell, L., Jalil, R., Ponomarenko, L. A., Blake, P., Novoselov, K. S., Watanabe, K., Taniguchi, T., and Geim, A. K. *Nano Letters* **11**(6), 2396–2399 June (2011). (Cited pages 20, 21, 24 et 26.)

[20] Balandin, A. A. *Nature Materials* **10**(8), 569–581 July (2011). (Cited pages 20 et 25.)

[21] Lee, C., Wei, X., Kysar, J. W., and Hone, J. *Science* **321**(5887), 385–388 July (2008). (Cited pages 20, 25 et 208.)

[22] Gannett, W., Regan, W., Watanabe, K., Taniguchi, T., Crommie, M. F., and Zettl, A. *Applied Physics Letters* **98**(24), 242105–242105–3 June (2011). (Cited pages 21 et 26.)

[23] Dean, C. R., Young, A. F., Meric, I., Lee, C., Wang, L., Sorgenfrei, S., Watanabe, K., Taniguchi, T., Kim, P., Shepard, K. L., and Hone, J. *1005.4917* May (2010). (Cited pages 21 et 26.)

[24] Bolotin, K. I., Sikes, K. J., Hone, J., Stormer, H. L., and Kim, P. *Physical Review Letters* **101**(9), 096802 (2008). (Cited pages 21, 26 et 206.)

[25] Betz, A. *Elastic and inelastic scattering in graphene studied by microwave transport and noise*. PhD thesis, Universite Paris VI, Paris, (2012). (Cited pages 21 et 26.)

[26] Shon, N. H. and Ando, T. *Journal of the Physical Society of Japan* **67**(7), 2421–2429 (1998). (Cited pages 20 et 25.)

[27] Suzuura, H. and Ando, T. *Physical Review Letters* **89**(26), 266603 December (2002). (Cited pages 20, 22, 25 et 40.)

[28] Morozov, S. V., Novoselov, K. S., Katsnelson, M. I., Schedin, F., Ponomarenko, L. A., Jiang, D., and Geim, A. K. *Physical Review Letters* **97**(1), 016801 July (2006). (Cited pages 22, 25, 40 et 47.)

[29] Aleiner, I. L. and Efetov, K. B. *Physical Review Letters* **97**(23), 236801 December (2006). (Cited pages 22 et 25.)

[30] McCann, E., Kechedzhi, K., Fal'ko, V. I., Suzuura, H., Ando, T., and Altshuler, B. L. *Physical Review Letters* **97**(14), 146805 October (2006). (Cited pages 22, 25, 40 et 78.)

[31] Elias, D. C., Nair, R. R., Mohiuddin, T. M. G., Morozov, S. V., Blake, P., Halsall, M. P., Ferrari, A. C., Boukhvalov, D. W., Katsnelson, M. I., Geim, A. K., and Novoselov, K. S. *Science* **323**(5914), 610 –613 January (2009). (Cited pages 22, 25 et 75.)

[32] Castro Neto, A. H., Guinea, F., Peres, N. M. R., Novoselov, K. S., and Geim, A. K. *Reviews of Modern Physics* **81**(1), 109 January (2009). (Cited page 29.)

[33] Bena, C. and Montambaux, G. *New Journal of Physics* **11**(9), 095003 September (2009). (Cited page 33.)

[34] Martin, J., Akerman, N., Ulbricht, G., Lohmann, T., Smet, J. H., von Klitzing, K., and Yacoby, A. *Nat Phys* **4**(2), 144–148 February (2008). (Cited page 35.)

[35] Katsnelson, M. I., Novoselov, K. S., and Geim, A. K. *Nature Physics* **2**(9), 620–625 August (2006). (Cited page 35.)

[36] Miao, F., Wijeratne, S., Zhang, Y., Coskun, U. C., Bao, W., and Lau, C. N. *Science* **317**(5844), 1530–1533 September (2007). (Cited pages 35 et 206.)

[37] Adam, S., Hwang, E. H., Galitski, V. M., and Sarma, S. D. *Proceedings of the National Academy of Sciences* **104**(47), 18392–18397 November (2007). (Cited pages 35 et 37.)

[38] Cheianov, V. V., Falko, V. I., Altshuler, B. L., and Aleiner, I. L. *Physical Review Letters* **99**(17), 176801 October (2007). (Cited page 35.)

[39] Ponomarenko, L. A., Geim, A. K., Zhukov, A. A., Jalil, R., Morozov, S. V., Novoselov, K. S., Grigorieva, I. V., Hill, E. H., Cheianov, V. V., Falko, V. I., Watanabe, K., Taniguchi, T., and Gorbachev, R. V. *Nature Physics* **7**(12), 958–961 (2011). (Cited pages 35 et 106.)

[40] Adam, S., Hwang, E., and Das Sarma, S. *Physica E: Low-dimensional Systems and Nanostructures* **40**(5), 1022–1025 March (2008). (Cited pages 37 et 67.)

[41] Hwang, E. H. and Das Sarma, S. *Physical Review B* **77**(19), 195412 May (2008). (Cited page 37.)

[42] Tan, Y.-W., Zhang, Y., Bolotin, K., Zhao, Y., Adam, S., Hwang, E. H., Das Sarma, S., Stormer, H. L., and Kim, P. *Physical Review Letters* **99**(24), 246803 December (2007). (Cited page 37.)

[43] Chen, J.-H., Jang, C., Adam, S., Fuhrer, M. S., Williams, E. D., and Ishigami, M. *Nat Phys* **4**(5), 377–381 May (2008). (Cited page 37.)

[44] Jang, C., Adam, S., Chen, J.-H., Williams, E. D., Das Sarma, S., and Fuhrer, M. S. *Physical Review Letters* **101**(14), 146805 October (2008). (Cited pages 37 et 67.)

[45] Nomura, K. and MacDonald, A. H. *Physical Review Letters* **98**(7), 076602 February (2007). (Cited page 37.)

[46] Peres, N. M. R. *Reviews of Modern Physics* **82**(3), 2673 (2010). (Cited pages 37, 68 et 206.)

[47] Monteverde, M., Ojeda-Aristizabal, C., Weil, R., Bennaceur, K., Ferrier, M., Gueron, S., Glattli, C., Bouchiat, H., Fuchs, J. N., and Maslov, D. L. *Physical Review Letters* **104**(12), 126801 March (2010). (Cited page 37.)

[48] Couto, N. J. G., Sacp, B., and Morpurgo, A. F. *Physical Review Letters* **107**(22), 225501 November (2011). (Cited page 37.)

[49] McEuen, P. L., Bockrath, M., Cobden, D. H., Yoon, Y.-G., and Louie, S. G. *Physical Review Letters* **83**(24), 5098–5101 December (1999). (Cited pages 40 et 103.)

[50] Morpurgo, A. F. and Guinea, F. *Physical Review Letters* **97**(19), 196804 November (2006). (Cited page 40.)

[51] Lee, P. A. and Ramakrishnan, T. V. *Reviews of Modern Physics* **57**(2), 287–337 April (1985). (Cited page 42.)

[52] Miller, A. and Abrahams, E. *Physical Review* **120**(3), 745–755 November (1960). (Cited page 42.)

[53] Mott, N. F. *Philosophical Magazine* **19**(160), 835–852 (1969). (Cited page 43.)

[54] Efros, A. L. and Shklovskii, Boris, I. *Electronic Properties of Doped Semiconductors*. Springer-Verlag, Berlin, (1984). (Cited pages 43, 44, 45 et 74.)

[55] Mason, W., Kravchenko, S. V., Bowker, G. E., and Furneaux, J. E. *Physical Review B* **52**(11), 7857–7859 (1995). (Cited pages 43, 45, 72 et 177.)

[56] Mott, N., Pepper, M., Pollitt, S., Wallis, R. H., and Adkins, C. J. *Proceedings of the Royal Society of London. A. Mathematical and Physical Sciences* **345**(1641), 169–205 August (1975). (Cited page 44.)

[57] Aleiner, I. L. and Shklovskii, B. I. *Physical Review B* **49**(19), 13721–13727 May (1994). (Cited pages 45 et 171.)

[58] Berger, C., Song, Z., Li, T., Li, X., Ogbazghi, A. Y., Feng, R., Dai, Z., Marchenkov, A. N., Conrad, E. H., First, P. N., and de Heer, W. A. *J. Phys. Chem. B* **108**(52), 19912–19916 (2004). (Cited page 46.)

[59] Berger, C., Song, Z., Li, X., Wu, X., Brown, N., Naud, C., Mayou, D., Li, T., Hass, J., Marchenkov, A. N., Conrad, E. H., First, P. N., and Heer, W. A. D. *Science* **312**(5777), 1191–1196 May (2006). (Cited page 46.)

[60] Stankovich, S., Dikin, D. A., Piner, R. D., Kohlhaas, K. A., Kleinhammes, A., Jia, Y., Wu, Y., Nguyen, S. T., and Ruoff, R. S. *Carbon* **45**(7), 1558–1565 June (2007). (Cited page 46.)

[61] Li, D., Muller, M. B., Gilje, S., Kaner, R. B., and Wallace, G. G. *Nat Nano* **3**(2), 101–105 February (2008). (Cited page 46.)

[62] Yu, Q., Lian, J., Siriponglert, S., Li, H., Chen, Y. P., and Pei, S.-S. *Applied Physics Letters* **93**(11), 113103–113103–3 September (2008). (Cited page 46.)

[63] Kim, K. S., Zhao, Y., Jang, H., Lee, S. Y., Kim, J. M., Kim, K. S., Ahn, J.-H., Kim, P., Choi, J.-Y., and Hong, B. H. *Nature* **457**(7230), 706–710 February (2009). (Cited page 46.)

[64] Reina, A., Jia, X., Ho, J., Nezich, D., Son, H., Bulovic, V., Dresselhaus, M. S., and Kong, J. *Nano Letters* **9**(1), 30–35 January (2009). (Cited page 46.)

[65] Li, X., Cai, W., An, J., Kim, S., Nah, J., Yang, D., Piner, R., Velamakanni, A., Jung, I., Tutuc, E., Banerjee, S. K., Colombo, L., and Ruoff, R. S. *Science* **324**(5932), 1312–1314 June (2009). (Cited pages 46 et 50.)

[66] Gao, L., Ren, W., Xu, H., Jin, L., Wang, Z., Ma, T., Ma, L.-P., Zhang, Z., Fu, Q., Peng, L.-M., Bao, X., and Cheng, H.-M. *Nature Communications* **3**, 699 February (2012). (Cited page 46.)

[67] Bae, S., Kim, H., Lee, Y., Xu, X., Park, J.-S., Zheng, Y., Balakrishnan, J., Lei, T., Kim, H. R., Song, Y. I., Kim, Y.-J., Kim, K. S., zyilmaz, B., Ahn, J.-H., Hong, B. H., and Iijima, S. *Nature Nanotechnology* **5**(8), 574–578 (2010). (Cited page 46.)

[68] Wang, H., Wang, G., Bao, P., Yang, S., Zhu, W., Xie, X., and Zhang, W.-J. *J. Am. Chem. Soc.* **134**(8), 3627–3630 (2012). (Cited page 46.)

[69] Petrone, N., Dean, C. R., Meric, I., van der Zande, A. M., Huang, P. Y., Wang, L., Muller, D., Shepard, K. L., and Hone, J. *Nano Letters* **12**(6), 2751–2756 June (2012). (Cited page 46.)

[70] Cai, J., Ruffieux, P., Jaafar, R., Bieri, M., Braun, T., Blankenburg, S., Muoth, M., Seitsonen, A. P., Saleh, M., Feng, X., Mllen, K., and Fasel, R. *Nature* **466**(7305), 470–473 July (2010). (Cited page 46.)

[71] Kosynkin, D. V., Higginbotham, A. L., Sinitskii, A., Lomeda, J. R., Dimiev, A., Price, B. K., and Tour, J. M. *Nature* **458**(7240), 872–876 April (2009). (Cited page 46.)

[72] Roddaro, S., Pingue, P., Piazza, V., Pellegrini, V., and Beltram, F. *Nano Letters* **7**(9), 2707–2710 (2007). (Cited page 49.)

[73] Han, Z., Kimouche, A., Allain, A., Arjmandi-Tash, H., Reserbat-Plantey, A., Pairis, S., Reita, V., Bendiab, N., Coraux, J., and Bouchiat, V. *arXiv:1205.1337* May (2012). (Cited pages 50 et 52.)

[74] Mohiuddin, T. M. G., Lombardo, A., Nair, R. R., Bonetti, A., Savini, G., Jalil, R., Bonini, N., Basko, D. M., Galiotis, C., Marzari, N., Novoselov, K. S., Geim, A. K., and Ferrari, A. C. *Physical Review B* **79**(20), 205433 May (2009). (Cited pages 55 et 96.)

[75] Yan, J., Zhang, Y., Kim, P., and Pinczuk, A. *Physical Review Letters* **98**(16), 166802 April (2007). (Cited pages 55, 96 et 97.)

[76] Berciaud, S., Ryu, S., Brus, L. E., and Heinz, T. F. *Nano Letters* **9**(1), 346–352 January (2009). (Cited page 55.)

[77] Berciaud, S., Han, M. Y., Mak, K. F., Brus, L. E., Kim, P., and Heinz, T. F. *Physical Review Letters* **104**(22), 227401 June (2010). (Cited pages 55 et 203.)

[78] Koh, Y. K., Bae, M.-H., Cahill, D. G., and Pop, E. *ACS Nano* **5**(1), 269–274 January (2011). (Cited page 55.)

[79] Tuinstra, F. *The Journal of Chemical Physics* **53**(3), 1126 (1970). (Cited pages 56 et 65.)

[80] Cancado, L. G., Jorio, A., Ferreira, E. H. M., Stavale, F., Achete, C. A., Capaz, R. B., Moutinho, M. V. O., Lombardo, A., Kulmala, T. S., and Ferrari, A. C. *Nano Letters* **11**(8), 3190–3196 (2011). (Cited pages 56, 57 et 65.)

[81] Malard, L., Pimenta, M., Dresselhaus, G., and Dresselhaus, M. *Physics Reports* **473**(5-6), 51–87 April (2009). (Cited pages 56, 57 et 58.)

[82] Araujo, P. T., Terrones, M., and Dresselhaus, M. S. *Materials Today* **15**(3), 98–109 March (2012). (Cited page 63.)

[83] Eckmann, A., Felten, A., Mishchenko, A., Britnell, L., Krupke, R., Novoselov, K. S., and Casiraghi, C. *Nano Letters* (2012). (Cited page 65.)

[84] Das Sarma, S., Adam, S., Hwang, E. H., and Rossi, E. *Reviews of Modern Physics* **83**(2), 407 May (2011). (Cited page 67.)

[85] Wu, X., Sprinkle, M., Li, X., Ming, F., Berger, C., and de Heer, W. A. *Physical Review Letters* **101**(2), 026801 July (2008). (Cited page 72.)

[86] Joung, D. and Khondaker, S. I. *arXiv:1210.1876* October (2012). (Cited pages 72, 75 et 76.)

[87] Moser, J., Tao, H., Roche, S., Alzina, F., Sotomayor Torres, C. M., and Bachtold, A. *Physical Review B* **81**(20), 205445 May (2010). (Cited pages 72, 75 et 78.)

[88] Reed, J. P., Uchoa, B., Joe, Y. I., Gan, Y., Casa, D., Fradkin, E., and Abbamonte, P. *Science* **330**(6005), 805–808 May (2010). (Cited page 74.)

[89] Rosenbaum, R. *Physical Review B* **44**(8), 3599–3603 August (1991). (Cited page 74.)

[90] Liang, S.-Z. and Sofo, J. O. *arXiv:1208.5026* August (2012). (Cited page 75.)

[91] Gmez-Navarro, C., Weitz, R. T., Bittner, A. M., Scolari, M., Mews, A., Burghard, M., and Kern, K. *Nano Letters* **7**(11), 3499–3503 November (2007). (Cited page 75.)

[92] Eda, G., Mattevi, C., Yamaguchi, H., Kim, H., and Chhowalla, M. *The Journal of Physical Chemistry C* **113**(35), 15768–15771 September (2009). (Cited page 75.)

[93] Kaiser, A. B., Gmez-Navarro, C., Sundaram, R. S., Burghard, M., and Kern, K. *Nano Letters* **9**(5), 1787–1792 May (2009). (Cited page 75.)

[94] Hong, X., Cheng, S.-H., Herding, C., and Zhu, J. *Physical Review B* **83**(8), 085410 February (2011). (Cited pages 75 et 78.)

[95] Withers, F., Russo, S., Dubois, M., and Craciun, M. *Nanoscale Research Letters* **6**(1), 526 September (2011). (Cited page 75.)

[96] Matis, B. R., Bulat, F. A., Friedman, A. L., Houston, B. H., and Baldwin, J. W. *Physical Review B* **85**(19), 195437 May (2012). (Cited pages 75 et 78.)

[97] Chuang, C., Puddy, R., Lin, H.-D., Lo, S.-T., Chen, T.-M., Smith, C., and Liang, C.-T. *Solid State Communications* **152**(10), 905–908 May (2012). (Cited page 75.)

[98] Chen, J.-H., Cullen, W. G., Jang, C., Fuhrer, M. S., and Williams, E. D. *Physical Review Letters* **102**(23), 236805 June (2009). (Cited page 75.)

[99] Archanjo, B. S., Barboza, A. P. M., Neves, B. R. A., Malard, L. M., Ferreira, E. H. M., Brant, J. C., Alves, E. S., Plentz, F., Carozo, V., Fragneaud, B., Maciel, I. O., Almeida, C. M., Jorio, A., and Achete, C. A. *Nanotechnology* **23**(25), 255305 June (2012). (Cited page 75.)

[100] Zhou, Y.-B., Liao, Z.-M., Wang, Y.-F., Duesberg, G. S., Xu, J., Fu, Q., Wu, X.-S., and Yu, D.-P. *The Journal of Chemical Physics* **133**(23), 234703–234703–5 December (2010). (Cited page 75.)

[101] Tikhonenko, F. V., Horsell, D. W., Gorbachev, R. V., and Savchenko, A. K. *Physical Review Letters* **100**(5), 056802 February (2008). (Cited pages 77 et 78.)

[102] Tikhonenko, F. V., Kozikov, A. A., Savchenko, A. K., and Gorbachev, R. V. *Physical Review Letters* **103**(22), 226801 November (2009). (Cited page 77.)

[103] Hsu, S.-Y. and Valles, J. *Physical Review Letters* **74**(12), 2331–2334 March (1995). (Cited page 78.)

[104] Uchoa, B. and Castro Neto, A. H. *Physical Review Letters* **98**(14), 146801 April (2007). (Cited pages 83 et 86.)

[105] Nandkishore, R., Levitov, L. S., and Chubukov, A. V. *Nature Physics* **8**(2), 158–163 (2012). (Cited pages 83 et 86.)

[106] Heersche, H. B., Jarillo-Herrero, P., Oostinga, J. B., Vandersypen, L. M. K., and Morpurgo, A. F. *Nature* **446**(7131), 56–59 March (2007). (Cited pages 83, 86, 103 et 104.)

[107] Du, X., Skachko, I., and Andrei, E. Y. *Physical Review B* **77**(18), 184507 May (2008). (Cited pages 83, 86 et 104.)

[108] Schapers, T. *Superconductor/Semiconductor Junctions*. Springer, September (2001). (Cited pages 83, 86 et 103.)

[109] Titov, M. and Beenakker, C. W. J. *Physical Review B* **74**(4), 041401 July (2006). (Cited pages 83, 86 et 133.)

[110] Beenakker, C. W. J. *Physical Review Letters* **97**(6), 067007 (2006). (Cited pages 83, 86 et 104.)

[111] Rickhaus, P., Weiss, M., Marot, L., and Schonenberger, C. *Nano Letters* **12**(4), 1942–1945 April (2012). (Cited pages 83, 86 et 104.)

[112] Feigelman, M. V., Skvortsov, M. A., and Tikhonov, K. S. *JETP Letters* **88**(11), 747–751 May (2009). (Cited pages 84, 86, 231 et 236.)

[113] Kessler, B. M., Girit, C. O., Zettl, A., and Bouchiat, V. *Physical Review Letters* **104**(4), 047001 January (2010). (Cited pages 87, 93, 95, 113, 115, 119 et 158.)

[114] Shaw, R. W., Mapother, D. E., and Hopkins, D. C. *Physical Review* **120**(1), 88–91 October (1960). (Cited pages 90 et 114.)

[115] Giovannetti, G., Khomyakov, P. A., Brocks, G., Karpan, V. M., van den Brink, J., and Kelly, P. J. *Physical Review Letters* **101**(2), 026803 July (2008). (Cited pages 93, 94, 95, 104, 228 et 234.)

[116] Kessler, B. M. *Hybrid two-dimensional electronic systems and other applications of sp-2 bonded light elements*. PhD thesis, UNIVERSITY OF CALIFORNIA, BERKELEY, September (2010). (Cited pages 93, 115, 120 et 128.)

[117] Li, W., He, Y., Wang, L., Ding, G., Zhang, Z.-Q., Lortz, R. W., Sheng, P., and Wang, N. *Physical Review B* **84**(4), 045431 July (2011). (Cited page 96.)

[118] Josephson, B. *Physics Letters* **1**(7), 251–253 July (1962). (Cited page 98.)

[119] Anderson, P. W. and Rowell, J. M. *Physical Review Letters* **10**(6), 230–232 March (1963). (Cited page 98.)

[120] Clarke, J. and Braginski, A. I., editors. *The SQUID Handbook: Fundamentals and Technology of SQUIDs and SQUID Systems, Volume I*. May (2005). (Cited page 98.)

[121] Golubov, A. A., Kupriyanov, M. Y., and Il'ichev, E. *Reviews of Modern Physics* **76**(2), 411 April (2004). (Cited page 98.)

[122] Josephson, B. *Reviews of Modern Physics* **36**(1), 216–220 January (1964). (Cited page 98.)

[123] Belzig, W., Wilhelm, F. K., Bruder, C., Schon, G., and Zaikin, A. D. *Superlattices and Microstructures* **25**(5), 1251–1288 May (1999). (Cited pages 99 et 102.)

[124] DE GENNES, P. G. *Reviews of Modern Physics* **36**(1), 225–237 January (1964). (Cited pages 99 et 100.)

[125] Andreev, A. F. *Soviet Physics JETP* **19**, 1228 (1964). (Cited page 99.)

[126] Courtois, H., Charlat, P., Gandit, P., Mailly, D., and Pannetier, B. *Journal of Low Temperature Physics* **116**(3), 187–213 (1999). (Cited page 100.)

[127] Dubos, P., Courtois, H., Pannetier, B., Wilhelm, F. K., Zaikin, A. D., and Schon, G. *Physical Review B* **63**(6), 064502 January (2001). (Cited pages 101, 102 et 122.)

[128] Kulik, I., O. and Omelyanchuk, A., N. *JETP Letters* **21**(4), 96 (1975). (Cited pages 101 et 102.)

[129] Ambegaokar, V. and Baratoff, A. *Physical Review Letters* **10**(11), 486–489 June (1963). (Cited page 102.)

[130] Likharev, K. K. *Reviews of Modern Physics* **51**(1), 101 January (1979). (Cited pages 102 et 133.)

[131] Takayanagi, H. and Kawakami, T. *Physical Review Letters* **54**(22), 2449–2452 June (1985). (Cited page 104.)

[132] Ojeda-Aristizabal, C., Ferrier, M., Gueron, S., and Bouchiat, H. *Physical Review B* **79**(16), 165436 April (2009). (Cited page 104.)

[133] Komatsu, K., Li, C., Autier-Laurent, S., Bouchiat, H., and Gueron, S. *Physical Review B* **86**(11), 115412 September (2012). (Cited pages 104, 106 et 134.)

[134] Beenakker, C. W. J. *Reviews of Modern Physics* **80**(4), 1337 October (2008). (Cited page 105.)

[135] Tinkham, M. *Introduction to Superconductivity: Second Edition*. Dover Publications, June (2004). (Cited pages 109, 115 et 129.)

[136] Lobb, C. J., Abraham, D. W., and Tinkham, M. *Physical Review B* **27**(1), 150–157 January (1983). (Cited pages 111 et 122.)

[137] Likharev. *Dynamics of Josephson Junctions and Circuits*. Taylor & Francis, August (1986). (Cited page 111.)

[138] Barone, A. and Patern, G. *Physics and Applications of the Josephson Effect*. John Wiley & Sons, (1982). (Cited page 112.)

[139] Anderson, P. *Journal of Physics and Chemistry of Solids* **11**(12), 26–30 September (1959). (Cited page 113.)

[140] Halperin, W. P. *Reviews of Modern Physics* **58**(3), 533–606 July (1986). (Cited page 113.)

[141] Bose, S., Garcia-Garcia, A. M., Ugeda, M. M., Urbina, J. D., Michaelis, C. H., Brihuega, I., and Kern, K. *Nat Mater* **9**(7), 550–554 July (2010). (Cited pages 114 et 137.)

[142] Wang, X.-L., Feygenson, M., Aronson, M. C., and Han, W.-Q. *The Journal of Physical Chemistry C* **114**(35), 14697–14703 (2010). (Cited page 114.)

[143] Beloborodov, I. S., Efetov, K. B., and Larkin, A. I. *Physical Review B* **61**(13), 9145–9161 April (2000). (Cited pages 114 et 161.)

[144] Cren, T., Serrier-Garcia, L., Debontridder, F., and Roditchev, D. *Physical Review Letters* **107**(9), 097202 August (2011). (Cited page 114.)

[145] Larkin, A. *Soviet Physics JETP* **21**(1), 153 (1965). (Cited page 114.)

[146] Nguyen, H. Q., Hollen, S. M., Stewart, M. D., Shainline, J., Yin, A., Xu, J. M., and Valles, J. M. *Physical Review Letters* **103**(15), 157001 October (2009). (Cited pages 115, 147, 151 et 176.)

[147] Resnick, D. J., Garland, J. C., Boyd, J. T., Shoemaker, S., and Newrock, R. S. *Physical Review Letters* **47**(21), 1542 November (1981). (Cited pages 118 et 125.)

[148] van der Zant, H. S. J., Webster, M. N., Romijn, J., and Mooij, J. E. *Physical Review B* **42**(4), 2647–2650 August (1990). (Cited pages 118 et 125.)

[149] Epstein, K., Goldman, A. M., and Kadin, A. M. *Physical Review B* **26**(7), 3950 October (1982). (Cited pages 119 et 158.)

[150] Reyren, N., Thiel, S., Caviglia, A. D., Kourkoutis, L. F., Hammerl, G., Richter, C., Schneider, C. W., Kopp, T., Retschi, A.-S., Jaccard, D., Gabay, M., Muller, D. A., Triscone, J.-M., and Mannhart, J. *Science* **317**(5842), 1196–1199 August (2007). (Cited pages 125 et 126.)

[151] Benfatto, L., Castellani, C., and Giamarchi, T. *Physical Review B* **80**(21), 214506 December (2009). (Cited page 125.)

[152] Repaci, J. M., Kwon, C., Li, Q., Jiang, X., Venkatessan, T., Glover, R. E., Lobb, C. J., and Newrock, R. S. *Physical Review B* **54**(14), R9674–R9677 October (1996). (Cited page 126.)

[153] Tang, L.-H. and Chen, Q.-H. *Physical Review B* **67**(2), 024508 January (2003). (Cited page 126.)

[154] Gurevich, A. and Vinokur., V. M. *Physical Review Letters* **100**(22), 227007 June (2008). (Cited page 126.)

[155] Clarke, J. *Physical Review B* **4**(9), 2963–2977 November (1971). (Cited pages 129 et 131.)

[156] Reinel, D., Dieterich, W., Wolf, T., and Majhofer, A. *Physical Review B* **49**(13), 9118–9124 April (1994). (Cited page 129.)

[157] Rice, T. M. *Physical Review* **140**(6A), A1889–A1891 December (1965). (Cited pages 146 et 150.)

[158] Little, W. A. *Physical Review* **156**(2), 396–403 April (1967). (Cited pages 146 et 150.)

[159] Abeles, B. *Physical Review B* **15**(5), 2828–2829 March (1977). (Cited pages 146, 150 et 155.)

[160] Fisher, M. P. A., Weichman, P. B., Grinstein, G., and Fisher, D. S. *Physical Review B* **40**(1), 546–570 July (1989). (Cited pages 147, 150 et 162.)

[161] Phillips, P. and Dalidovich, D. *Science* **302**(5643), 243 –247 October (2003). (Cited pages 147 et 150.)

[162] Frydman, A. *Physica C: Superconductivity* **391**(2), 189–195 August (2003). (Cited pages 147 et 150.)

[163] Finkel'stein, A. *Physica B: Condensed Matter* **197**(14), 636–648 March (1994). (Cited pages 147 et 151.)

[164] Haviland, D. B., Liu, Y., and Goldman, A. M. *Physical Review Letters* **62**(18), 2180–2183 May (1989). (Cited pages 147, 148, 151, 162 et 168.)

[165] Sambandamurthy, G., Engel, L. W., Johansson, A., and Shahar, D. *Physical Review Letters* **92**(10), 107005 March (2004). (Cited pages 147, 148, 151, 176 et 178.)

[166] Sacepe, B., Dubouchet, T., Chapelier, C., Sanquer, M., Ovadia, M., Shahar, D., Feigel/'man, M., and Ioffe, L. *Nat Phys* **7**(3), 239–244 March (2011). (Cited pages 147 et 151.)

[167] Chakravarty, S., Kivelson, S., Zimanyi, G. T., and Halperin, B. I. *Physical Review B* **35**(13), 7256 May (1987). (Cited pages 147, 151, 155 et 171.)

[168] Fazio, R. and Schon, G. *Physical Review B* **43**(7), 5307 March (1991). (Cited pages 147, 151 et 171.)

[169] Rimberg, A. J., Ho, T. R., Kurdak, ., Clarke, J., Campman, K. L., and Gossard, A. C. *Physical Review Letters* **78**(13), 2632 March (1997). (Cited pages 147, 151, 155, 171 et 185.)

[170] Wagenblast, K.-H., van Otterlo, A., Schon, G., and Zimanyi, G. T. *Physical Review Letters* **79**(14), 2730 October (1997). (Cited pages 147, 151, 155 et 171.)

[171] Wagenblast, K.-H., van Otterlo, A., Schon, G., and Zimanyi, G. T. *Physical Review Letters* **78**(9), 1779 March (1997). (Cited pages 147 et 151.)

[172] Takahide, Y., Yagi, R., Kanda, A., Ootuka, Y., and Kobayashi, S.-i. *Physical Review Letters* **85**(9), 1974 (2000). (Cited pages 147, 151, 155 et 171.)

[173] Hebard, A. F. and Paalanen, M. A. *Physical Review Letters* **65**(7), 927 (1990). (Cited pages 148, 151, 180, 182 et 183.)

[174] Baturina, T. I., Islamov, D. R., Bentner, J., Strunk, C., Baklanov, M. R., and Satta, A. *Journal of Experimental and Theoretical Physics Letters* **79**, 337–341 April (2004). (Cited pages 148, 151 et 176.)

[175] Jaeger, H. M., Haviland, D. B., Orr, B. G., and Goldman, A. M. *Physical Review B* **40**(1), 182 July (1989). (Cited pages 148, 151, 162 et 168.)

[176] Shahar, D. and Ovadyahu, Z. *Physical Review B* **46**(17), 10917 November (1992). (Cited pages 148 et 151.)

[177] Crauste, O., Marrache-Kikuchi, C. A., Berg, L., Stanescu, D., and Dumoulin, L. *Journal of Physics: Conference Series* **150**(4), 042019 March (2009). (Cited pages 148 et 151.)

[178] Bollinger, A. T., Dubuis, G., Yoon, J., Pavuna, D., Misewich, J., and Boovi, I. *Nature* **472**(7344), 458–460 April (2011). (Cited pages 148, 151 et 152.)

[179] Fisher, M. P. A. *Physical Review Letters* **65**(7), 923 (1990). (Cited pages 148, 151, 162, 180 et 183.)

[180] Biscaras, J., Bergeal, N., Hurand, S., Grossetłte, C., Rastogi, A., Budhani, R. C., LeBoeuf, D., Proust, C., and Lesueur, J. *Physical Review Letters* **108**(24), 247004 June (2012). (Cited pages 148 et 151.)

[181] imnek, E. *Physical Review B* **22**(1), 459–462 July (1980). (Cited page 155.)

[182] van der Zant, H. S. J., Elion, W. J., Geerligs, L. J., and Mooij, J. E. *Physical Review B* **54**(14), 10081 October (1996). (Cited pages 155, 162 et 168.)

[183] Fukuyama, H. and Maekawa, S. *Journal of the Physical Society of Japan* **55**(6), 1814–1817 (1986). (Cited page 155.)

[184] Aslamasov, L. and Larkin, A. *Physics Letters A* **26**(6), 238–239 February (1968). (Cited page 161.)

[185] Maki, K. *Progress of Theoretical Physics* **40**(2), 193–200 (1968). (Cited page 161.)

[186] Thompson, R. S. *Physical Review B* **1**(1), 327–333 January (1970). (Cited page 161.)

[187] Galitski, V. M. and Larkin, A. I. *Physical Review B* **63**(17), 174506 April (2001). (Cited page 161.)

[188] Fisher, M. P. A., Grinstein, G., and Girvin, S. M. *Physical Review Letters* **64**(5), 587 January (1990). (Cited page 162.)

[189] Kapitulnik, A., Mason, N., Kivelson, S. A., and Chakravarty, S. *Physical Review B* **63**(12), 125322 March (2001). (Cited pages 164 et 185.)

[190] Steiner, M. A., Breznay, N. P., and Kapitulnik, A. *Physical Review B* **77**(21), 212501 June (2008). (Cited pages 165, 186 et 188.)

[191] Fisher, M. P. A. *Physical Review B* **36**(4), 1917–1930 August (1987). (Cited page 171.)

[192] Strelniker, Y. M., Frydman, A., and Havlin, S. *Physical Review B* **76**(22), 224528 December (2007). (Cited page 174.)

[193] Frydman, A., Naaman, O., and Dynes, R. C. *Physical Review B* **66**(5), 052509 (2002). (Cited page 174.)

[194] Allain, A., Han, Z., and Bouchiat, V. *Nature Materials* **11**(7), 590–594 (2012). (Cited page 177.)

[195] Dynes, R. C., Garno, J. P., and Rowell, J. M. *Physical Review Letters* **40**(7), 479–482 February (1978). (Cited page 178.)

[196] Lin, Y.-H. and Goldman, A. M. *Physical Review B* **82**(21), 214511 December (2010). (Cited page 178.)

[197] Beloborodov, I. S., Fominov, Y. V., Lopatin, A. V., and Vinokur, V. M. *Physical Review B* **74**(1), 014502 July (2006). (Cited pages 178 et 180.)

[198] Feigelman, M. V., Ioffe, L. B., Kravtsov, V. E., and Yuzbashyan, E. A. *Physical Review Letters* **98**(2), 027001 January (2007). (Cited pages 178 et 180.)

[199] Galitski, V. M., Refael, G., Fisher, M. P. A., and Senthil, T. *Physical Review Letters* **95**(7), 077002 (2005). (Cited page 180.)

[200] Vinokur, V. M., Baturina, T. I., Fistul, M. V., Mironov, A. Y., Baklanov, M. R., and Strunk, C. *Nature* **452**(7187), 613–615 March (2008). (Cited page 180.)

[201] Markovicacute, N., Christiansen, C., Mack, A. M., Huber, W. H., and Goldman, A. M. *Physical Review B* **60**(6), 4320 (1999). (Cited pages 182 et 184.)

[202] Marrache-Kikuchi, C. *Effets dimensionnels dans un système désordonné au voisinage des transitions métal-isolant et supraconducteur-isolant.* PhD thesis, Universite Paris-Sud XI, (2006). (Cited page 182.)

[203] Markovi, N., Christiansen, C., and Goldman, A. M. *Physical Review Letters* **81**(23), 5217–5220 December (1998). (Cited page 183.)

[204] Mason, N. and Kapitulnik, A. *Physical Review Letters* **82**(26), 5341 June (1999). (Cited page 185.)

[205] Newell, W. E. *Science* **161**(3848), 1320–1326 September (1968). (Cited pages 190 et 195.)

[206] Craighead, H. G. *Science* **290**(5496), 1532–1535 November (2000). (Cited pages 190 et 195.)

[207] Ekinci, K. L. and Roukes, M. L. *Review of Scientific Instruments* **76**(6), 061101 (2005). (Cited pages 190, 191, 195 et 196.)

[208] Seonez, C., Guinea, F., and Castro Neto, A. H. *Physical Review B* **76**(12), 125427 (2007). (Cited pages 190, 195 et 219.)

[209] Steele, G. A., Huttel, A. K., Witkamp, B., Poot, M., Meerwaldt, H. B., Kouwenhoven, L. P., and van der Zant, H. S. J. *Science* **325**(5944), 1103–1107 August (2009). (Cited pages 192 et 195.)

[210] Naik, A., Buu, O., LaHaye, M. D., Armour, A. D., Clerk, A. A., Blencowe, M. P., and Schwab, K. C. *Nature* **443**(7108), 193–196 (2006). (Cited pages 192 et 195.)

[211] Hertzberg, J. B., Rocheleau, T., Ndukum, T., Savva, M., Clerk, A. A., and Schwab, K. C. *Nature Physics* **6**(3), 213–217 (2010). (Cited pages 192 et 195.)

[212] Poot, M. and van der Zant, H. S. *Physics Reports* **511**(5), 273–335 February (2012). (Cited pages 192, 195, 232, 233 et 238.)

[213] OConnell, A. D., Hofheinz, M., Ansmann, M., Bialczak, R. C., Lenander, M., Lucero, E., Neeley, M., Sank, D., Wang, H., Weides, M., Wenner, J., Martinis, J. M., and Cleland, A. N. *Nature* **464**(7289), 697–703 April (2010). (Cited pages 192, 193, 195, 232 et 238.)

[214] Sazonova, V., Yaish, Y., Ustunel, H., Roundy, D., Arias, T. A., and McEuen, P. L. *Nature* **431**(7006), 284–287 September (2004). (Cited pages 193, 194, 197, 198, 209 et 215.)

[215] Chen, C., Rosenblatt, S., Bolotin, K. I., Kalb, W., Kim, P., Kymissis, I., Stormer, H. L., Heinz, T. F., and Hone, J. *Nat Nano* **4**(12), 861–867 December (2009). (Cited pages 193, 194, 197, 201, 209, 215, 216 et 218.)

[216] Singh, V., Sengupta, S., Solanki, H. S., Dhall, R., Allain, A., Dhara, S., Pant, P., and Deshmukh, M. M. *Nanotechnology* **21**(16), 165204 April (2010). (Cited pages 193, 194, 197, 201, 209, 215 et 216.)

[217] Jensen, K., Weldon, J., Garcia, H., and Zettl, A. *Nano Letters* **7**(11), 3508–3511 November (2007). (Cited pages 193, 197 et 215.)

[218] Zande, A. M. v. d., Barton, R. A., Alden, J. S., Ruiz-Vargas, C. S., Whitney, W. S., Pham, P. H. Q., Park, J., Parpia, J. M., Craighead, H. G., and McEuen, P. L. *Nano Letters* **10**(12), 4869–4873 December (2010). (Cited pages 193 et 197.)

[219] Metzger, C. H. and Karrai, K. *Nature* **432**(7020), 1002–1005 December (2004). (Cited pages 193 et 197.)

[220] Arcizet, O., Cohadon, P.-F., Briant, T., Pinard, M., and Heidmann, A. *Nature* **444**(7115), 71–74 February (2006). (Cited pages 193, 197, 232 et 238.)

[221] Teufel, J. D., Donner, T., Castellanos-Beltran, M. A., Harlow, J. W., and Lehnert, K. W. *Nature Nanotechnology* **4**(12), 820–823 (2009). (Cited pages 193 et 197.)

[222] Teufel, J. D., Donner, T., Li, D., Harlow, J. W., Allman, M. S., Cicak, K., Sirois, A. J., Whittaker, J. D., Lehnert, K. W., and Simmonds, R. W. *Nature* **475**(7356), 359–363 July (2011). (Cited pages 193, 197, 232 et 238.)

[223] Reserbat-Plantey, A., Marty, L., Arcizet, O., Bendiab, N., and Bouchiat, V. *Nature Nanotechnology* **7**(3), 151–155 (2012). (Cited pages 193, 232 et 238.)

[224] Du, X., Skachko, I., Barker, A., and Andrei, E. Y. *Nat Nano* **3**(8), 491–495 (2008). (Cited pages 203 et 206.)

[225] Moser, J., Barreiro, A., and Bachtold, A. *Applied Physics Letters* **91**(16), 163513 (2007). (Cited page 203.)

[226] Abanin, D. A. and Levitov, L. S. *Physical Review B* **78**(3), 035416 July (2008). (Cited pages 206 et 207.)

[227] Kemiktarak, U., Ndukum, T., Schwab, K. C., and Ekinci, K. L. *Nature* **450**(7166), 85–88 November (2007). (Cited page 208.)

[228] Schoelkopf, R. J., Wahlgren, P., Kozhevnikov, A. A., Delsing, P., and Prober, D. E. *Science* **280**(5367), 1238–1242 May (1998). (Cited page 208.)

[229] Sazonova, V. A. *A tunable carbon nanotube resonator*. PhD thesis, June (2006). (Cited pages 208, 209 et 210.)

[230] Xu, Y., Chen, C., Deshpande, V. V., DiRenno, F. A., Gondarenko, A., Heinz, D. B., Liu, S., Kim, P., and Hone, J. *Applied Physics Letters* **97**(24), 243111 (2010). (Cited page 208.)

[231] Gouttenoire, V., Barois, T., Perisanu, S., Leclercq, J.-L., Purcell, S. T., Vincent, P., and Ayari, A. *Small* **6**(9), 10601065 (2010). (Cited pages 210 et 217.)

[232] Eichler, A., Moser, J., Chaste, J., Zdrojek, M., Wilson-Rae, I., and Bachtold, A. *Nature Nanotechnology* **6**(6), 339–342 May (2011). (Cited page 215.)

[233] Solanki, H. S., Sengupta, S., Dhara, S., Singh, V., Patil, S., Dhall, R., Parpia, J., Bhattacharya, A., and Deshmukh, M. M. *Physical Review B* **81**(11), 115459 March (2010). (Cited page 215.)

[234] Bunch, J. S., van der Zande, A. M., Verbridge, S. S., Frank, I. W., Tanenbaum, D. M., Parpia, J. M., Craighead, H. G., and McEuen, P. L. *Science* **315**(5811), 490–493 January (2007). (Cited page 216.)

[235] Sonne, G., Pea-Aza, M. E., Gorelik, L. Y., Shekhter, R. I., and Jonson, M. *Physical Review Letters* **104**(22), 226802 June (2010). (Cited page 219.)

[236] Poot, M. and van der Zant, H. S. J. *Applied Physics Letters* **92**(6), 063111–063111–3 February (2008). (Cited page 221.)

[237] Strongin, M., Thompson, R. S., Kammerer, O. F., and Crow, J. E. *Physical Review B* **1**(3), 1078–1091 February (1970). (Cited page 222.)

[238] Feigel'man, M., Ioffe, L., Kravtsov, V., and Cuevas, E. *Annals of Physics* **325**(7), 1390–1478 July (2010). (Cited pages 231 et 236.)

[239] Yu, Y.-J., Zhao, Y., Ryu, S., Brus, L. E., Kim, K. S., and Kim, P. *Nano Letters* **9**(10), 3430–3434 October (2009). (Cited pages 231 et 236.)

[240] Haugen, H., Huertas-Hernando, D., and Brataas, A. *Physical Review B* **77**(11), 115406 March (2008). (Cited pages 232 et 237.)

[241] Weeks, C., Hu, J., Alicea, J., Franz, M., and Wu, R. *Physical Review X* **1**(2), 021001 October (2011). (Cited pages 232 et 237.)

[242] Brun, C., Muller, K. H., Hong, I.-P., Patthey, F., Flindt, C., and Schneider, W.-D. *Physical Review Letters* **108**(12), 126802 March (2012). (Cited page 236.)

[243] Aspelmeyer, M., Meystre, P., and Schwab, K. *Physics Today* **65**(7), 29–35 (2012). (Cited page 238.)